

STUDY OF NANOSCALE MATERIALS USING POSITRON ANNIHILATION SPECTROSCOPY

By

PRIYA MAHESHWARI
CHEM01200904007

Bhabha Atomic Research Centre, Mumbai

*A thesis submitted to the
Board of Studies in Chemical Sciences
In partial fulfillment of requirements
For the Degree of*

DOCTOR OF PHILOSOPHY

of

HOMI BHABHA NATIONAL INSTITUTE



AUGUST, 2013

HOMI BHABHA NATIONAL INSTITUTE

Recommendations of the Viva Voce Board

As members of the Viva Voce Board, we certify that we have read the dissertation prepared by **Priya Maheshwari** entitled “**Study of Nanoscale materials Using Positron Annihilation Spectroscopy**” and recommend that it may be accepted as fulfilling the dissertation requirement for the Degree of Doctor of Philosophy.

Date:

Chairman: Prof. A. Goswami

Date:

Guide: Prof. P. K. Pujari

Date:

Member 1: Prof. G. Amarendra

Date:

Member 2: Prof. B. S. Tomar

Date:

Member 3: Prof. S. Kapoor

Final approval and acceptance of this dissertation is contingent upon the candidate's submission of the final copies of the dissertation to HBNI.

I hereby certify that I have read this dissertation prepared under my direction and recommend that it may be accepted as fulfilling the dissertation requirement.

Date:

Place:

STATEMENT BY AUTHOR

This dissertation has been submitted in partial fulfillment of requirements for an advanced degree at Homi Bhabha National Institute (HBNI) and is deposited in the Library to be made available to borrowers under rules of the HBNI.

Brief quotations from this dissertation are allowable without special permission, provided that accurate acknowledgement of source is made. Requests for permission for extended quotation from or reproduction of this manuscript in whole or in part may be granted by the Competent Authority of HBNI when in his or her judgment the proposed use of the material is in the interests of scholarship. In all other instances, however, permission must be obtained from the author.

Priya Maheshwari

DECLARATION

I, hereby declare that the investigation presented in the thesis has been carried out by me. The work is original and has not been submitted earlier as a whole or in part for a degree /diploma at this or any other Institution / University.

Priya Maheshwari

Dedicated to

***My Grandparents
&
Parents***

List of Publications

REFFEREED JOURNALS

1. Study of iron phthalocyanine organic semiconductor thin films using slow positron beam
P. Maheshwari, D. Dutta, S. Samanta, A. Singh, D. K. Aswal, A. V. R. Reddy and P. K. Pujari
Phys. Stat. solidi c 6,11, (2009) 2589-2591.
2. Microstructure study of supported liquid membranes using slow positron beam
P. K. Pujari, **P. Maheshwari**, S. K. Sharma, D. Dutta, K. Sudarshan and A. V. R. Reddy
Phys. Stat. solidi c 6,11, (2009)2417-2419.
3. Effect of interfacial hydrogen bonding on the freezing/melting behavior of nano-confined liquids
P. Maheshwari, D. Dutta, S. K. Sharma, K. Sudarshan, P. K. Pujari, M. Majumdar, B. Pahari, B. Bandyopadhyay, K. Ghosharay and A. Ghosharay
J. Phys. Chem. C, 114 (2010) 4966.
4. Study of interfaces in organic semiconductor heterojunctions
P. Maheshwari, D. Dutta, K. Sudarshan, S. K. Sharma, S. Samanta, A. Singh, D. K. Aswal and P. K. Pujari,
Journal of Physics: Conference Series 262 (2011) 012036.
5. Defect depth profiling in organic semiconductor multilayers
Priya Maheshwari, P. K. Pujari, S. K. Sharma, K. Sudarshan, D. Dutta, S. Samanta, A. Singh, D. K. Aswal, R. Ajay Kumar and I. Samajdar
Organic Electronics, 13 (2012)1409.
6. Phase transition of water confined in Saponites using Positron annihilation spectroscopy
Priya Maheshwari, S. K. Sharma, D. Dutta, K. Sudarshan, P. K. Pujari
Mat. Sci. Forum, 733 (2013) 111.

7. Phase transition of nanoconfined water in clay: Positron annihilation, Nuclear magnetic resonance and Dielectric relaxation studies
Priya Maheshwari, P. K. Pujari, S. K. Sharma, D. Dutta, K. Sudarshan, V. S. Mithu, P. K. Madhu, S. K. Deshpande, P. N. Patil and N. Raje
J. Phys. Chem. C, 117 (2013) 14313.

8. Depth dependent inhomogeneities in nanoscale OSC films: PAS and XRR study
Priya Maheshwari, D. Bhattacharya, S. K. Sharma, S. Mukherjee, S. Basu and P. K. Pujari
(Communicated)

9. Direct evidence of linkage between pore interconnectivity and permeability of metal ions in PTFE supported liquid membranes: A slow positron beam study
Priya Maheshwari, D. Dutta, K. Sudarshan, S. K. Sharma, P. K. Mohapatra, P. U. Sastry and P. K. Pujari
(Communicated)

SYMPOSIUM

1. Study of pore architecture in track etched polycarbonate membranes using slow positron beam
P. Maheshwari, S. K. Sharma, D. Dutta, K. Sudarshan, and P. K. Pujari
Proceedings of Nuclear and Radiochemistry symposium (NUCAR)- 2011.

2. Study of phase transition of 2D confined water
Priya Maheshwari, S. K. Sharma, D. Dutta, K. Sudarshan, P. N. Patil and P. K. Pujari
Proceedings of Nuclear and Radiochemistry symposium (NUCAR)- 2013.

ACKNOWLEDGEMENTS

This thesis would not have been possible without the support and encouragement of many people who contributed and extended their valuable assistance in the completion of the research work. I feel short of words in expressing my appreciation for their help at various stages of this work.

First and foremost, I would like to express my sincere gratitude to my thesis advisor Prof. P. K. Pujari for his continuous support to my work, his patience, encouragement, enthusiasm and immense knowledge. His intellectual ideas and guidance helped me in my research work and writing this thesis. He has always been a source of motivation for me in difficult times in research or otherwise. I express my deep sense of appreciation for his support and for energizing me to overcome all the hurdles.

Besides my advisor, I would like to thank members of my doctoral committee; Prof. A. Goswami, Prof. B. S. Tomar, Prof. G. Amarendra and Prof. S. Kapoor for their encouragement, insightful comments and fruitful ideas during the course of the thesis work which have been useful for the progress of the work. I would like to express my gratitude to Dr. D. Dutta, Dr. K. Sudarshan and Dr. S. K. Sharma for helping me in learning the instrumentation and experimental techniques. I share the credit of my work with them for helping me in carrying out the experiments round the clock and sharing the ideas. I would also like to thank my lab mates Dr. S. Mukherjee and Dr. P. N. Patil for their timely help.

I cannot find words to express my gratitude to Dr. Suparna Sodaye who has been there all the times to encourage and motivate me to work cheerfully. Her constant support and presence have been an emotional support for me to overcome all the hurdles on my path. I would also like to thank my senior colleagues Dr. R. Acharya and Dr. Rahul Tripathi for

their encouragement and advice during the course of the research work. I also owe a great debt of gratitude to my collaborators Dr. S. K. Deshpande (UGC-CSIR, BARC), Dr. P. K. Madhu (TIFR), Mr. V. S. Mitthu (TIFR), Dr. N. Raje (ACD, BARC), Dr. N. Padma (TPD, BARC), Dr. D. Bhattacharya (SSPD, BARC), Dr. S. Basu (SSPD, BARC) and Dr. D. K. Aswal (TPD, BARC) for their help and fruitful discussions during the course of the work. My heartfelt appreciation goes to Dr. Soumen Samanta for his friendship and constant support in carrying out work on organic semiconductor thin films.

Apart from the intellectual support, an emotional support is always needed to conquer the hardships. For this, I would like to thank, from the bottom of my heart, my friends Alka, Megha, Chun Mei, Sanhita, Manish, Gayatri, Divya and Kanishka for their warm friendship.

Last but not the least, my deepest gratitude is to my family for their warm support which brings belief and hope into my life; to my beloved parents, who have been so caring and supportive of me all the time and my grandparents, who have always been a source of inspiration towards achieving the goals in life. Immense love and affection of my sisters and brothers have been invaluable in the journey towards my goal.

Apart from all the people mentioned in this acknowledgment, there are many others who have helped me in various ways during the course of this thesis work. My sincere thanks and apologies to all those I may have forgotten to mention.

Priya Maheshwari

CONTENTS

	Page No.
SYNOPSIS	1
LIST OF FIGURES	24
LIST OF TABLES	33
<i>CHAPTER-I</i>	
INTRODUCTION	34
1.1. Positron and its discovery	35
<i>1.1.1. Positron Annihilation</i>	36
1.2. The Positronium atom	36
1.3. Positron sources	38
1.4. Positron annihilation spectroscopy	39
<i>1.4.1. Positron lifetime spectroscopy (PALS)</i>	40
<i>1.4.2. Doppler broadening spectroscopy (DBS)</i>	42
<i>1.4.3. Coincidence Doppler broadening spectroscopy (CDB)</i>	43
<i>1.4.4. Age-momentum correlation technique (AMOC)</i>	43
1.5. Positron/Ps annihilation spectroscopy: A tool to probe condensed matter	44
1.6. Nanoscale materials	45
1.7. Positron annihilation spectroscopy: Characterization tool for nanoscale materials	49
1.8. Scope of the present work	51
<i>1.8.1. Nanodroplets</i>	
<i>1.8.2. Pore architecture of membranes</i>	56
<i>1.8.3. Nanostructure characterization in organic semiconductor thin films</i>	59
<i>CHAPTER-II</i>	
Experimental Techniques and Data Analysis	
(Positron annihilation spectroscopy)	64
2.1. Positron sources	65
<i>2.1.1. Conventional techniques</i>	65
<i>2.1.2. Beam based techniques</i>	67

2.2. Positron annihilation lifetime spectroscopy	69
2.2.1. Lifetime spectrometer	69
2.2.2. Lifetime spectrum analysis	72
2.3. Doppler broadening spectroscopy	74
2.3.1. Doppler broadening set up	74
2.3.2. Data analysis	75
2.4. Depth profiling using slow positron beam	78
2.4.1. Variable Energy Positron Fit (VEPFIT) analysis	79

CHAPTER-III

Nanodroplets: Phase transitions in nanoconfined fluids	82
3.1. Sample preparation	87
3.1.1. Ethylene glycol and isopropanol confined in ZSM 5 zeolite	87
3.1.2. Saponite clay	88
3.2. Experimental techniques	89
3.2.1. X-ray Diffraction	89
3.2.2. Thermogravimetric and Evolved Gas Analysis	90
3.2.3. Attenuated total reflection- Fourier transform Infra-red spectroscopy	90
3.2.4. Differential scanning calorimetry	91
3.2.5. Positron annihilation spectroscopy	92
3.2.5a. <i>Ethylene glycol and isopropanol</i>	
3.2.5b. <i>Water confined in saponite clay</i>	
3.2.6. Nuclear magnetic resonance	93
3.2.6a. <i>Chemical shift and relaxation time</i>	94
3.2.6b. <i>Static and Magic angle spinning</i>	95
3.2.6c. <i>Ethylene glycol and isopropanol</i>	97
3.2.6d. <i>Water confined in saponite clay</i>	97
3.2.7. Dielectric relaxation spectroscopy	98
3.2.7a. <i>The dielectric constant and polarization</i>	99
3.2.7b. <i>Relaxation Times</i>	99
3.2.7c. <i>Instrumentation and measurement technique</i>	100
3.2.7d. <i>Water confined in clay</i>	101

3.3. Results and Discussion	
I. Freezing/melting behavior of ethylene glycol and isopropanol confined in ZSM 5	103
3.3.1. Ethylene glycol and isopropanol confined in ZSM 5	103
3.3.1a. PAS results	
3.3.1b. NMR results	108
3.3.1c. Discussion	113
II. Phase transitions of water confined in clay nanopores	115
3.3.2. Water confined in saponite clay	116
3.3.2a. TG-EGA results	116
3.3.2b. ATR-FTIR results	118
3.3.2c. DSC results	120
3.3.2d. PAS results	121
3.3.2e. NMR results	127
3.3.2f. DRS results	131
3.3.2g. Discussions	137
3.4. Conclusions	139
CHAPTER-IV	141
Pore architecture of membranes	141
4.1. Materials	145
4.2. Experimental Techniques	146
4.2.1. Conventional characterization of the membranes	146
4.2.2. Small angle X-ray scattering	147
4.2.3. Positron annihilation lifetime spectroscopy	147
4.2.4. Doppler broadening and $3\gamma/2\gamma$ annihilation radiation measurements	148
4.2.5. Transport properties (permeability of metal ions)	148
4.3. Results and discussion	149
4.3.1. Polytetrafluoroethylene Supported liquid membranes	149
4.3.1a. Surface morphology and chemical nature	150
4.3.1b. Small angle X-ray scattering	150
4.3.1c. Positron annihilation life time spectroscopy	152

4.3.1d. Doppler broadening and $3\gamma/2\gamma$ annihilation spectroscopy	153
4.3.1.e. Permeability of metal ions and transport properties	156
4.3.2. Track etched polycarbonate membranes	159
4.3.2a. Surface morphology	159
4.3.2b. Doppler broadening and $3\gamma/2\gamma$ annihilation spectroscopy	159
4.4. Conclusions	163

CHAPTER-V

Nanostructure characterization in Organic Semiconductor thin films	165
5.1. Material and sample preparation	168
5.2. Experimental Techniques	172
5.2.1. Grazing incidence X-ray diffraction (GIXRD)	172
5.2.2. Atomic force microscopy (AFM)	172
5.2.3. Doppler broadening spectroscopy	172
5.2.4. Current-voltage measurement (<i>J-V</i> characteristics)	173
5.2.5. X-ray reflectivity (XRR)	174
5.3. Results and Discussion	
5.3.1. Effect of substrate temperature and thickness of the film	175
5.3.1a. Surface morphology and crystallinity	175
5.3.1b. Doppler broadening spectroscopy	177
5.3.1c. Discussion	179
5.3.2. Effect of post deposition annealing treatment	180
5.3.2a. Surface morphology and crystallinity	180
5.3.2b. Doppler broadening spectroscopy	182
5.3.2c. VEPFIT analysis	183
5.3.2d. S-W Analysis	185
5.3.2e. Depth profiling using X-ray reflectivity	186
5.3.2e. Discussion	189
5.3.3. Defect profiling in organic semiconductor heterostructures	191
5.3.3a. Grazing incidence X-ray diffraction	191
5.3.3b. Doppler broadening spectroscopy	192
5.3.3c. S-W Analysis	196

5.3.3d. <i>VEPFIT analysis</i>	198
5.3.3e. <i>Analysis of the effect of intrinsic electric field and defects at the interfaces (VEPFIT modeling)</i>	201
5.3.3f. <i>Mobility of positrons and charge carriers in OSC layers</i>	203
5.3.4. Interface engineering: Modification of dielectric surface using self assembled monoayers (SAM)	205
5.3.4a. <i>Crystallinity and surface morphology of the films</i>	205
5.3.4b. <i>Depth profiling using slow positron beam</i>	207
5.3.4c. <i>Field effect mobility of charge carriers</i>	211
5.3.4d. <i>Discussion</i>	212
5.4. Conclusions	213
SUMMARY	216
BIBLIOGRAPHY	221

SYNOPSIS

Positron annihilation spectroscopy (PAS) is a powerful nuclear probe to study open volumes and defects in solids. It is known as one of the sensitive defect spectroscopic techniques due to the propensity of positron to get trapped in low electron density regions like free volume hole, voids, vacancy defect etc. Positron, antiparticle of electron was first postulated by P. M. A. Dirac as the “negative” energy extension of his theory of electron energy levels [Dirac, 1930 and 1935]. Later, Anderson discovered positron experimentally in the cloud chamber experiments [Anderson, 1933]. Positrons are mainly produced from the radioisotope decay and pair production process. When a positron enters the solid, it loses its momentum rapidly and thermalizes within a few picoseconds. After thermalization, it diffuses for few hundreds of picoseconds in the medium before annihilating from an electron of the Bloch state (in perfect crystals). However, in the presence of defects, positron gets trapped in the defects and then annihilates with the electrons in the vicinity of the defect. The gamma radiation emitted after the electron-positron annihilation carries information about the electron density and momentum distribution and thus, enables identification of various properties of the material. The rate of annihilation depends on the electron density and hence, annihilation rate from the delocalized state is higher than the trapped state. The positron lifetime (inverse of the annihilation rate) can be correlated to the size of the defect and the corresponding intensity can be correlated to defect concentration [Brandt et al., 1981]. The momentum distribution of annihilating electron-positron pair can be obtained from the annihilation gamma radiation through Doppler broadening and deviation from anti-linearity. Positron being in thermalized state, Doppler broadening of annihilation radiation is caused by the kinetic energy of the electron and hence, it helps in measuring electron momentum distribution. This information is also useful for the identification of

chemical surrounding of the trapping site through the coincidence measurement of annihilation gamma radiation i.e. coincidence Doppler broadening spectroscopy [Ashoka-Kumar et al., 1996].

In some materials, especially molecular solids, positron may bind with an electron to form a quasi-bound state, namely, “positronium (Ps) atom”. The subsequent fate of positron is then determined by the interaction of Ps with the surrounding medium. The formation mechanism of Ps in the medium has been explained by different models viz. “spur model” and “ore model” [Ore and Powell, 1949, and Mogensen, 1974]. The Ps atom is identical to hydrogen atom except the magnitude of the masses. Similar to hydrogen atom, Ps exists in two spin states viz. “*para*” and “*ortho*” for singlet and triplet states, respectively. Statistically, the formation probability of *ortho*-Ps (*o*-Ps) to *para*-Ps (*p*-Ps) is 3:1. The intrinsic lifetime of *o*-Ps and *p*-Ps are 142 ns and 125 ps, respectively [Schrader and Jean, 1988].

Positron/Ps both are used as probes to study atomic and molecular properties of condensed matter. In metallic systems, due to negligible Ps formation, positron annihilation is mainly indexed to examine the defects like vacancies, vacancy clusters, dislocations etc. [West et al., 1973; Brandt et al., 1983; Seeger et al., 1974]. On the other hand, in molecular solids like polymers, the trapping of *o*-Ps in free volume nanoholes and pores in porous materials can provide information about the size and environment of the trapping site [Ito et al., 1998, 1999a and 2000 and Bandzuch et al., 2000]. The trapped *o*-Ps annihilates with an electron of opposite spin from the surrounding via two photon annihilation, process known as “*pick-off*” annihilation, with a reduced lifetime which is correlated to the size of the defect/free volume nanoholes through Tao-Eldrup equation [Tao, 1972 and Eldrup et al., 1981]. In addition to molecular solids, Ps annihilation in liquids can be correlated to various properties of the liquid. Ps annihilation and its

lifetime in liquids have been explained by bubble model proposed by Ferrel to account for long lifetimes in liquids as compared to solids [Ferrell, 1957].

The ability to get monoenergetic positrons (positron beam technique) has enabled characterization of surfaces and depth profiling of microstructure in thin films [Puska and Nieminen, 1994]. The image potential well at the surface acts as a two-dimensional defect for positron and may trap the positrons. This enables identification of structural imperfections (like steps, islands, surface vacancy etc.) on the surface using low energy positrons. It is thus, possible to characterize surfaces, especially at the nanometer scale where, finite size and reduced dimensionality induced effects are predominant. Depth profiling using positron beam is used to extract positron/Ps diffusion length or mobility in the material which is correlated to the nanostructure especially in thin films. Defect depth profiling has also opened a possibility to characterize buried interfaces in heterostructures as well as characterization of modified interfaces [Zubiaga et al., 2011; Makkonen et al., 2010].

The current thesis work involves positron annihilation studies in nanoscale materials. These materials are categorized into two classes viz. nanopores in porous materials and nanoscale thin films. In the context of porous materials, the nanopores are used as confining media for liquids and the properties of these liquids under nanoscale confinement are studied. This includes phase behavior of liquids viz. freezing/melting under nanoscale confinement. The study mainly aims at understanding the effect of interfacial interaction between the liquid and the wall of the confining geometry on the freezing/melting behavior of confined liquids. The structural and dynamical parameters obtained from different techniques (PAS, nuclear magnetic resonance and dielectric relaxation spectroscopy) are indexed to probe phase transitions of the confined liquids. Here, the freezing/melting behavior of ethylene glycol and isopropanol confined in ZSM

5 and the phase behavior of water confined in slit-like pores of saponite clay have been studied. Pore structure of porous materials dictates various properties of the material like transport and permeability in membranes, exchange capacity in zeolites etc. The sensitivity of PAS for pore characterization is utilized to study the pore architecture in porous membranes. The diffusion/mobility of positron/Ps in the medium (porous network) is indexed to investigate the pore architecture in terms of pore interconnectivity in microporous membranes where 3γ annihilation is the dominating annihilation mechanism. The diffusion length of Ps is obtained from $3\gamma/2\gamma$ profile using VEPFIT analysis. The correlation between Ps diffusion length and transport properties of the membranes is examined. In the area of nanoscale films, nanostructural modification in organic semiconductor (OSC) thin films as a function of different growth parameters and post growth annealing treatment has been studied. Defect depth profiling is carried out to extract positron/Ps diffusion length to probe defect microstructure of thin films. The study also entails investigation of buried interfaces in OSC heterostructures where heteroepitaxy between different materials leads to the appearance of interfacial region consisting of defect/disorder. The effect of surface modification using self-assembled monolayer (SAM) on the nanostructure of the grown OSC thin film has also been studied.

Comprehensive details of the work are described in the respective chapters of the thesis. A brief overview of the structure of the thesis is described in the following.

CHAPTER I: Introduction

This chapter concentrates on the overview of PAS in material science. A brief account of the process of positron annihilation in materials, Ps formation and its annihilation characteristics and different techniques involved in PAS is described in this chapter. The sensitivity of each technique to specific property/characteristics of the material is also discussed. The application of PAS to study various properties of

condensed matter like free volume nanoholes in polymers, atomic defects in metals/alloys, electronic structure of defects, Fermi surfaces of materials etc. are discussed. This chapter also includes the scope of the present thesis work with a brief review of literature in the current area of research. The thesis entails positron annihilation study in nanoscale materials. Different varieties of nanoscale materials and their properties are briefly described with a highlight on the techniques generally used for the characterization of these properties. The sensitivity of PAS for the characterization of nanoscale materials and its advantage over other techniques is explained subsequently. In the present thesis work, nanoscale materials are categorized into two classes: nanopores in porous materials and nanoscale thin films.

Nanopores of the porous materials have been used as a medium to confine fluids (nanoscale confinement). The properties of fluids are significantly different than the bulk when confined at nanoscale dimensions where surface interaction plays the dominant role owing to the increased surface to volume ratio. The fundamental scientific interest in this area is to understand the new physics that results from finite-size effects, varying dimensionality, and surface forces. Confined fluids exhibit deviation in freezing/melting point, glass transition temperature, existence of different phases not prevailing in the bulk, peculiar thermodynamic properties etc. Plenty of experimental studies have been performed to address the science and phenomenon behind the deviation of physical and thermodynamical properties of nanoconfined fluids from their bulk counterparts [Alba-Simionesco, et al. 2003; Kimmich et al., 2002]. The experimental results together with simulations have depicted the role of fluid-wall interfacial energy and the size of confining geometry on the shift in freezing/melting points [Miyahara et al., 1997; Radhakrishnan et al., 2002]. In addition, the direction of shift (increase/decrease in phase transition temperature) depends upon whether the pore wall favours the confined solid

phase or confined fluid phase. However, the experimental and theoretical work in the area of confinement i.e. phase behavior in pores are beset with significant difficulties. On the experimental side, the morphology of confining matrix i.e. poor knowledge of the exact distribution of pore size, shapes, connectivity impose difficulties in the interpretation of the observed data. On the other hand, in theoretical work, simulating the exact morphology of the porous material considering the presence of impurities (might present in real system and can produce spurious result) and the presence of metastable states leads to significant deviation from the experimentally observed results.

Despite a wealth of research, the field is experimentally and empirically driven and a lot of work needs to be carried out to gain complete understanding of the effect of confinement. This can be achieved by probing the properties of confined phase and investigation under different conditions/parameters (temperature, size, and nature of the confining matrix). For this, the structural and dynamical properties of confined phase (liquid) are seen to be sensitive indices to probe the change in phase behavior or phase transitions. In this thesis work, a comprehensive study has been carried out using PAS, NMR and DRS to probe variation of structural and dynamical properties associated with the phase behavior of nanoconfined fluids. The sensitivity of PAS to electron density and momentum distribution (lifetime and Doppler broadening spectroscopy, respectively) has been utilized to investigate nanostructural alterations (surface chemistry, change of density, free volume etc.) following the transitions. PAS has been used to study the phase behavior of number of gases and fluids confined in porous materials [Duffy et al., 2000; Bartos et al., 2001; Wilkinson et al., 1992] and mobility of glass forming liquids under confinement effect [Kilburn et al., 2008]. In addition, the dependence of dynamics of molecules (relaxation mechanism) on the intermolecular forces and surrounding molecular configurations enables probing the phase transitions. The dynamical properties

have been studied using spin-spin and dipolar relaxation times obtained from nuclear magnetic resonance (NMR) and dielectric relaxation spectroscopy (DRS), respectively. The main objective of the work is to understand the role of confining geometry and surface interactions between the fluid and wall of the confining geometry on the phase behavior/transitions of confined fluids.

PAS is a well established and sensitive tool to characterize nanostructure in polymers by providing information about the pore size, its distribution and fraction of free volume nanoholes. These nanostructural properties are deterministic measures for various thermo-mechanical properties of the polymeric systems. The triplet Ps state (*o*-Ps) plays the key role in probing porous materials through its reduced lifetime which can be correlated to the size of the pores through Tao-Eldrup equation [Tao, 1972 and Eldrup et al., 1981]. Another important aspect in the characterization of porous materials is to understand the pore growth mechanism which mainly deals with the length scale over which the pores are interconnected depending upon the porogen loading. This has important implication in the context of generation of porous matrices for various applications where the amount of porogen loading dictates not only the porosity but the network/interconnectivity between the pores. There are number of studies pertaining to porous structure in low k-dielectric films, porous membranes etc. [Lynn et al., 2006; Gidley et al., 2007; Sun et al., 2002], providing information about the pore size, its distribution and porosity. Most of these studies on the characterization of pore structure are focused on the identification of nanopores/nanoholes. Host of techniques such as small angle X-ray/neutron scattering, gas absorption techniques, ellipsometric porosimetry, electron microscopy that can characterize the size as well as pore fraction, however, they fail to evaluate the extent of pore interconnectivity. In this regards, slow positron beam profiling is a sensitive technique to determine the extent of pore

interconnection through the evaluation of positron/Ps mobility in porous materials. The ability of positron/Ps to diffuse within the porous network i.e. the mean free path of Ps (diffusion length) in the pores gives an idea about the length scale over which pores may be interconnected thus providing a complete picture of the pore architecture [Gidley et al., 2006]. In this work, PAS has been utilized for the characterization of pore architecture in microporous membranes (micron size pores) viz. supported liquid membrane (polytetrafluoroethylene (PTFE)) and track-etched polycarbonate membrane. For larger pores, Ps life-time will reach saturation value of 142 ns and is not useful for pore size measurement. Depth profiling using $3\gamma/2\gamma$ spectroscopy using a slow positron beam has provided a new approach to study the pore interconnectivity in microporous membranes. The correlation of pore interconnectivity and permeation property of the membranes is also examined.

Thin films are basic building block of all the electronic devices like solar, photovoltaic cells, transistors, light emitting diodes etc. The structure and morphology of the film play key role to ascertain working mechanism and performance of the device. For instance, defects (vacancy, lattice, structural defects like grain boundaries etc.) are seen to influence charge transport and optical properties of the device. The structure and morphology of nanoscale films are highly dependent on the deposition techniques and conditions (nature of substrate, its temperature etc.). In addition, the interfaces between various components of the device are crucial for device performance. In this regards, the structural characterization plays a pivotal role in thin film research and essential to realize perspectives for the next generation electronic industry. Hence, there is a need for the fundamental understanding from atomic and nanoscale characterization techniques to examine bulk, surfaces, sub-surfaces and interfacial regions in thin films. Defect profiling using slow positron beam is a sensitive and non-destructive technique to characterize

nanostructure in thin films. There has been plethora of work related to defect characterization in semiconductor thin films (single and multilayers) [Zhao et al., 1996; Brauer et al., 2002; Ferragut et al., 2010], thin high k-dielectric films on Si substrates [Uedono et al., 2007], metal-oxide semiconductor (MOS) structures [Uedono et al., 1988], Si/SiO₂ interfaces [Kauppinen et al., 1997] etc. All these work relate to silicon or compound semiconductor materials. In this thesis, slow positron beam has been used for the first time to study the nanostructure of OSC thin films. Due to low charge carrier mobility of OSC in contrast to inorganic semiconductors, efforts are being made to achieve best possible mobility in these materials. Owing to large anisotropy in shape and the structure of OSC, good quality film is a challenge and essential to make best use of these materials for organic electronic devices. The main objective of the present work is to study the nanostructure of OSC thin films as a function of different growth parameters like nature of the substrate, deposition temperature and post deposition annealing treatment. Further, interfacial characteristics between different components of the device (organic and inorganic) and at modified surfaces have also been studied. These interfaces are crucial for the high efficiency of the devices. The present study has revealed that depth profiling using slow positron beam has great potential owing to its capability to probe sub-surface regions and buried interfaces at nanoscale.

CHAPTER II: Experimental techniques and data analysis

This chapter covers the instrumentation and experimental set up of PAS techniques viz. lifetime and Doppler broadening spectroscopy, being utilized for the present thesis work. For the study of nanodroplets, conventional PAS techniques using radioisotope ²²Na source have been utilized. The conventional fast-fast coincidence circuit utilizing two BaF₂ detectors has been used for the lifetime measurements. The time resolution of the spectrometer is 290 ps. The lifetime spectra are analyzed using routine

PATFIT-88 having programs RESOLUTION and POSITRONFIT [Kirkegaard et al., 1981 and 1989; Kirkegaard and Eldrup, 1972]. The algorithm for the fitting analysis is described in this chapter. Doppler broadening measurement has been performed using HPGe detector with energy resolution of ~ 2.0 keV at 1332 keV photopeak of ^{60}Co . The analysis of Doppler broadening shape (S) and wing (W) parameters is also described.

For the study of pore architecture in membranes and nanostructure of thin OSC films, depth profiling has been carried out using slow positron beam. The full description of the beam components and transport of positrons is described in this chapter. Doppler broadening measurement is carried out in positron energy range of 200 eV to 20 keV. The S -parameter and $3\gamma/2\gamma$ ratio are calculated by taking integral counts within an energy window of ~ 1.2 keV around 511 keV and energy window of 385-485 keV and 501-522 keV of the energy spectrum of annihilation gamma radiation for 3γ and 2γ contributions, respectively. The annihilation profiles have been fitted using “variable energy positron fit” (VEPFIT) program to evaluate positron/Ps diffusion length, S -parameter corresponding to different layers of the sample and thickness of the layers, as the case may be [van Veen et al., 1990].

Other complementary techniques like atomic force microscopy, differential scanning calorimetry, thermogravimetric and evolved gas analysis, grazing incidence X-ray diffraction, nuclear magnetic resonance, dielectric relaxation spectroscopy and X-ray reflectivity (XRR) are also used in the present thesis work. The details of the techniques are described in the respective chapters. In addition to the experimental techniques used, the details of sample preparation are also described in the respective chapters.

CHAPTER III: Nanodroplets: Phase transitions in nanoconfined liquids

This chapter deals with the effect of interfacial interactions on the phase behavior of nanoconfined fluids. The freezing/melting behavior of two liquids viz. ethylene glycol

(EG) and isopropanol (IP) confined in the nanopores of ZSM 5 zeolite have been studied using PAS and NMR in order to examine the role of interfacial hydrogen bonding between the liquids and the wall surface of the confining pore. Positron lifetime and Doppler broadening measurements have been carried out as a function of temperature. The change of slope/discontinuity in positron annihilation parameters viz. o -Ps lifetime (τ_3), intensity (I_3) and S -parameter are signature of phase transitions of the confined liquid. An elevation in freezing/melting point has been observed in the case of EG and IP. This is in contrast to benzene confined in the same matrix [Dutta et al., 2008] wherein, a depression was observed. This has been attributed to the role of interfacial interactions on the direction of the shift in freezing/melting point. The fluid-wall interaction is attractive in the case of EG and IP unlike benzene, which experiences weakly attractive/repulsive interaction with the pore wall. In addition, the extent of shift in freezing/melting point is observed to be different in the two cases. The elevation in phase transition temperature EG is only 3.8%, whereas in IP shift of 7.5% relative to their respective bulk freezing temperature has been observed. This has been explained on the basis of distinct interfacial interaction or the surface energy. The strength of fluid-wall interaction is different due to the distinct nature of hydrogen bonding in these liquids. IP [CH3CH(OH)CH3] has intermolecular hydrogen bonding and strong attractive interfacial interaction with the pore surface whereas, EG [(CH2OH)2] experiences both intra- and inter-molecular hydrogen bonding, resulting in the reduction in the strength of interfacial interaction towards the surface. The spin-spin relaxation time (T_2) measured from NMR is also seen to be sensitive to phase transitions through its dependence on molecular configuration/environment which affects the relaxation process. In the case of EG, T_2 decay curve is expressed as a sum of two distinct components exhibiting Gaussian decay unlike IP where, a sum of three components exhibiting Lorentzian decay is required. The

different time scale for these components has indicated different physical environment of the molecules pertaining to different interfacial interactions in these cases. The temperature dependence of T_2 components (I(1) and I(2)) in both the cases has revealed phase transition at an elevated temperature, consistent with PAS study.

The effect of confinement on the phase behavior of water confined in slit-like pores of saponite clay has also been studied. Water confined in a nanoscale environment exhibits peculiar properties differing from the bulk. The anomalous behavior of water in confined systems has been attributed to the effect of surface interactions which modify the hydrogen-bonded network of water resulting in the formation of new phases and emergence of transitions otherwise, not prevailing in the bulk. Confinement of water in nano domains is therefore, sometimes regarded as a trick to experimentally assess the bulk water properties within the inaccessible low-temperature region and may provide answers to many open questions concerning the properties of supercooled water. A comprehensive study using PAS, NMR and DRS in corroboration with other conventional characterization techniques has been carried out to examine the phase behavior of nanoconfined water. The amount of water in the pores has been determined from thermogravimetric and evolved gas analysis which corresponds to two layer of water inside the pores. Temperature dependent PAS has indicated the presence of two phase transitions viz. above (high temperature transition, HTT) and below (low temperature transition, LTT) the bulk freezing temperature of water as revealed from the change of slope of S -parameter. This has been attributed to the presence of different regimes of water experiencing distinct interfacial interactions and undergoes transition at different temperatures. The presence of these transitions has also been confirmed from NMR and DRS. The ^1H chemical shift analysis and spin-spin relaxation times have revealed the presence of HTT. The variation of chemical shift has shown the alteration in hydrogen-

bonded network of water molecules at HTT, whereas, the variation of spin-spin relaxation times has been correlated to the immobilization of water molecules (faster relaxation) close to the platelet surface (bound molecules) as compared to the slower relaxation of molecules away from the platelet surface. On the other hand, DRS is seen to be sensitive to LTT through the variation of dipolar relaxation times. The study has indicated that LTT is associated with the incomplete freezing of water or depression in the freezing/melting point of water as confirmed from PAS, differential calorimetry and DRS. The evidence of HTT, in addition to LTT for supercooled water is the first experimental report on the phase behavior of nanoconfined water. The present study manifests the role of surface interaction on the phase behavior of confined liquids.

Chapter IV: Pore architecture of microporous membranes

This chapter primarily deals with the characterization of pore architecture of the membranes having pore size in the range of few microns. For such larger pore size, lifetime analysis is insensitive due to the saturation of *o*-Ps lifetime (142 ns). However, knowledge about the pore architecture in terms of porosity (open and close) and pore interconnectivity in these microporous membranes can be obtained by indexing Ps diffusion/mobility in the membranes. The study seeks to examine the correlation between pore architecture and transport (permeability) properties of the membranes. In this work, $3\gamma/2\gamma$ profiling using slow positron beam has been utilized to study the pore architecture of supported liquid membrane (SLM) namely Polytetrafluoroethylene (PTFE) and track-etched polycarbonate membranes having pore size in the range of 200-5000 nm and 30-400 nm, respectively. PTFE membranes have been characterized by scanning electron microscopy (SEM) and Fourier transform infrared spectroscopy to examine the morphology and chemical nature of the membranes, respectively. All the membranes have similar chemical nature but, distinct morphology. On the basis of surface

morphology, the membranes are categorized into two classes: Membranes A (200 nm) and B (450 nm) show granular structure with small pores, whereas membranes C (1200 nm) and D (5000 nm) show fibre like structure with large open pores. Small angle X-ray scattering and positron lifetime data have revealed the fact that so far as smaller pores are concerned, they are identical in all the membranes and larger pores would be responsible for the variations in other measured experimental parameters. The $3\gamma/2\gamma$ profiling has been used to evaluate Ps diffusion length in the membranes using VEPFIT analysis. A systematic increase in Ps diffusion length from A to D with the exception of C has been observed. The transport properties of the membranes have been studied through the permeability of Pu^{+3} and Am^{+3} with TODGA as extractant with n-dodecan as solvent and nitric acid in feed as well as receiver cells. A systematic decrease in permeability is seen from A to D (with increase in pore size) under identical condition which is contrary to the expected increase in permeability with the pore size. In addition to this, an inverse relation has been seen between the permeability and Ps diffusion length indicating the decrease in permeability with the increase in the length scale of pore interconnection. The high porosity in membrane C and D (observed from SEM and porosity measurement) may modify $3\gamma/2\gamma$ profiles due to the escape of Ps from the membrane surface. Therefore, in order to get better insight into this, surface of the membranes B and C (one from each category) is capped with ~ 10 nm gold layer which prevents Ps to escape from the surface and makes them coral within the porous network. This would help in identifying true pore architecture of the membranes. It is seen that the $3\gamma/2\gamma$ profiles, both the magnitude as well as curvature (hence, Ps diffusion length) are modified in the case of gold capped membranes. Ps diffusion length is much larger in gold capped membranes as compared to pristine, indicating the high interconnectivity of pores in these membranes which is considered as the microscopic origin for the decrease in permeability. The large

difference in $3\gamma/2\gamma$ ratio and Ps diffusion length, especially in membrane C indicates high open porosity in this membrane as compared to others and is responsible for exceptionally small Ps diffusion length measured for its pristine form. The study reveals a linkage between pore architecture and the permeability of metal ion in microporous membrane. Similar measurements have also been carried out in track etched polycarbonate membranes (pristine and gold capped) having pore sizes 30, 200 and 400 nm. A large difference in Ps diffusion length for pristine and gold capped membranes has been seen revealing modification of $3\gamma/2\gamma$ profile pertaining to open porosity and large pore size. The interconnectivity is seen to be high in the case of membrane with 30 nm pore size unlike others, reflected from the large value of Ps diffusion length in the former as compared to latter. The Ps diffusion length is of the order of pore size in all membranes except that of 30 nm pore size which indicates that Ps diffusion length is the signature of pore cross-section in these cases. The study demonstrates the advantages of positron beam characterization of pore interconnectivity in the design/development of membranes with tailored transport properties.

Chapter V: Nanostructure characterization of organic semiconductor thin films

This chapter deals with the characterization of nanostructure of thin OSC films. Defect depth profiling using slow positron beam has been used to examine the nanostructural characteristics of these films as a function of different growth parameters. The structure and morphology of OSC film are highly dependent on the nature of substrate, deposition temperature and rate, thickness of the film as well as post deposition annealing treatment. Metal phthalocyanine (OSC) films grown at different substrate temperature and of different thicknesses have been studied to examine the nanostructure and morphology of the films as a function of above mentioned growth parameters. The

surface morphology has been characterized using AFM and the quantitative analysis of the defect/disorder in the film has been carried out by fitting the experimental S -parameter profiles using VEPFIT analysis to obtain bulk S -parameter and diffusion length of positron. The study has revealed the effect of interaction between the substrate and the molecules as well as between the two molecules on the growth behavior of OSC molecules. The study has indicated difference in the morphology of the films grown at different temperatures and of different thicknesses. In addition to optimized growth parameter for well ordered and defect free films, post deposition annealing treatment is also seen to improve the ordering of OSC molecules. For this, the effect of post deposition annealing treatment on the nanostructure of Cobalt phthalocyanine films grown on quartz substrate has been studied. AFM has revealed the modification in the morphology of the films with the annealing treatment. Depth profile study (PAS and XRR) however, has shown the presence of a region with large defects/disorder i.e. inhomogeneity in the nanostructure across the depth of the film. In addition to defect microstructure of the bulk film, interfaces are also crucial for device performance. For efficient charge transport and conductivity between different components of the device, structural defects should be minimized across the interfaces. Heteroepitaxy between different types of materials is the main cause of the origin of defects at the interfaces. Interfacial properties can be tailored by wettability or adhesion between different materials or modifying the electronic structure of the materials. For example, the dielectric interface (between dielectric and organic layer) is modified by polymers or self-assembled monolayers (SAM) which has influence on the growth behavior of OSC molecules. In this regards, depth profiling has been carried out to examine the defect microstructure of buried interfaces in OSC heterostructures. Multilayer structure of different OSC materials (p and n -type) consisting of interfaces between organic materials

and organic and inorganic materials have been characterized using slow positron beam. The S -parameter profile has revealed the presence of defects/disorder at these interfaces. The study also highlights the type of defects at the interfaces between different materials through S - W analysis. The effect of modification of dielectric surface using self assembled monolayer on the interfacial characteristics and growth behavior of OSC molecules has also been studied using PAS and AFM. In addition to the characterization of nanostructural properties, charge conductivity has also been measured for the single layer OSC film. The charge carrier mobility (determined from current-voltage characteristics) in OSC film is seen to be comparable to positron mobility, evaluated from the diffusion length of positron in the films. Though the scattering mechanism of electron and positron could be different, the dependence of mobility (in both the cases) on structural defects enables comparison between the mobilities of the two particles. This property can be used to get a prior idea of the charge transport characteristic of the devices. The study has highlighted the sensitivity of the technique for nanostructure of thin films and buried interfaces. Depth profiling using slow positron beam opens an avenue for the characterization of devices in electronic industry.

Summary

The present work highlights the sensitivity and capability of positron annihilation spectroscopic (PAS) techniques to probe atomic and molecular level properties in nanoscale materials. Two categories of nanoscale materials viz. porous matrices and nanoscale thin films have been studied in the present work. PAS has been utilized to study variety of properties ranging from phase transition of nanoconfined liquids to the characterization of nanostructure of porous membranes and thin films. The sensitivity of positron annihilation parameters to electron density and electron momentum distribution helps in identifying minute structural alterations following the phase transitions. An

elevation in the freezing/melting point has been observed in ethylene glycol and isopropanol confined in ZSM 5 nanopores which has been attributed to the role of surface interactions between the liquids and wall of the pores. Interestingly, the extent of the shift has been seen to be different in the two cases owing to the difference in the strength of interaction between the liquid and the wall surface pertaining to distinct nature of hydrogen bonding in these liquids. PAS study has been corroborated with NMR wherein, dynamics of the molecules (spin-spin relaxation) has been utilized to index phase transitions. The different time scale for relaxation indicates different physical environment of the molecules pertaining to different interfacial interactions in these cases. The structural and dynamical properties have been probed to investigate the phase behavior of nanoconfined water in saponite clay (slit-like pores) using PAS, NMR and DRS. An experimental evidence of a new phase transition (above the bulk freezing point of water) in nanoconfined water, in addition to the low-temperature transition in supercooled water has been reported. The study reveals it to be a structural rearrangement of water molecules associated with modification of hydrogen-bonded network. Evidence has also suggested the dynamical arrest/immobilization of water layer near the clay platelet surface (bound water molecules) to be associated with this transition. The above study on phase behavior of liquids confined in nanopores provides evidence of the role of surface interactions on the phase transitions of liquids.

Positron/Ps diffusion length in the material has been utilized to examine the pore architecture of microporous membranes. For larger pore size, lifetime analysis is insensitive due to the saturation of *o*-Ps lifetime (142 ns). Ps diffusion length evaluated from $3\gamma/2\gamma$ profiles has been indexed as a measure of the length scale of interconnection of pores in the membranes. The comparison of $3\gamma/2\gamma$ ratio in pristine and gold capped membranes has helped in examining the true pore architecture of the membranes by

preventing Ps escape from the surface of the membranes owing to high open porosity. In the case of supported liquid PTFE membranes, the pore architecture of membranes has been correlated to the transport properties of the membranes in terms of the permeability of different ions through the membranes. An inverse relation has been seen between the permeability and Ps diffusion length indicating the decrease in permeability with the increase in the length scale of pore interconnection. In the case of track etched polycarbonate membranes, Ps diffusion length obtained in the case of gold capped membranes has been seen to provide length scale of interconnection for smaller pores as well as cross-section of the pores for larger pores indicating small degree of interconnection in the latter case. The study demonstrates the advantages of positron beam characterization of pore interconnectivity in the design/development of membranes with tailored transport properties.

The sensitivity or localization of positron in the low electron density region enables identification of defects/disorder in materials. This capability has been utilized for the characterization of nanostructure of thin OSC films. Depth profiling using slow positron accelerator has been used for the characterization of defect microstructure in these films as a function of different growth parameters like deposition temperature, thickness of the films and post deposition annealing temperature. The bulk S -parameter and positron diffusion length evaluated from VEPFIT analysis have been indexed for the analysis of defect/disorder. The effect of interaction between the molecules and substrate on the growth modes has been observed, as revealed from the variation of the nanostructure of the films grown at different temperatures and of varying thicknesses. The post deposition annealing has been seen to modify the morphology of room temperature deposited film from island like to granular form as seen from AFM. However, inhomogeneity in the nanostructure i.e. a region with more defects/disorder as

compared to rest of the film has been observed from PAS as well as XRR. Defect depth profiling has also been carried out for characterizing buried interfaces between different organic (*p* and *n*-type) and inorganic materials (*p* or *n*-type and substrate) in OSC heterostructures. The study reveals the effect of heteroepitaxy between different materials which leads to more defects/disorder at the interfaces between different materials. Interface engineering using self assembled monolayer has been employed to minimize defect/disorder at the interface between OSC and substrate. The mobility of positron determined from the measured positron diffusion length has been seen to be comparable to charge carrier mobility in OSC thin films. This has significant implication towards the determination of charge mobility in OSC materials without the actual device configuration. Depth profiling using slow positron accelerator opens an avenue for the characterization of nanostructure of organic devices.

REFERENCES

1. Alba-Simionesco, C.; Dosseh, G.; Dumont, E.; Geil, B.; Morineau, D.; Frick, B.; Teboul, V., and Xia, Y., **2003**. *Eur. Phys. J. E* 12, 19.
2. Anderson, C.D., **1933**. *Phys. Rev.*, 43, 491.
3. Asoka-Kumar, P.; Alatalo, M.; Ghosh, V.J.; Kruseman, A.C.; Nielsen, B., and Lynn, K.G., **1996**. *Phys. Rev. Lett.*, 77, 2097.
4. Bandzuch, P.; Kristiak, J.; Sausa, O., and Zrubcova, J., **2000**. *Phys. Rev. B*. 61(13), 8784.
5. Bartos, J.; Sausa, O.; Kristiak, J.; Blochowicz, T., and Rossler, E., **2001**. *J. Phys.: Condens. Matter* 13, 11473.
6. Brandt, W., and Dupasquier, A., (Eds.) **1981**. *Positron Solid State Physics: Proceedings of the International School of Physics "Enrico Fermi", Course LXXXIII*, July 1981.
7. Brandt, W., and Dupasquier, A., **1983**. "Positron solid state Physics", North-Holland, Amsterdam.
8. Brauer, G.; Anwand, W.; Skorupa, W.; Revesz, A.G., and Kuriplach, J., **2002**. *Phys. Rev. B* 66, 195331.
9. Dirac, P.A.M., **1930**. *Proc. Camb. Phil. Soc.*, 26, 361.
10. Dirac, P.A.M., **1935**. *The Principles of Quantum Mechanics*, Oxford University Press.
11. Duffy, J. A., and Alam, M. A., **2000**. *Langmuir* 16, 9513.
12. Dutta, D.; Pujari, P.K.; Sudarshan, K., and Sharma, S.K., **2008**. *J. Phys. Chem. C* 112, 19055.
13. Eldrup, M.; Lightbody, D., and Sherwood, J.N., **1981**. *Chem. Phys.* 63, 51.
14. Ferragut, R.; Calloni, A.; Dupasquier, A., and Isella, G., **2010**. *Nano. Res. Lett.* 5, 1942.
15. Ferrell, R.A., **1957**. *Phys. Rev.* 108, 167.

16. Gidley, D.W.; Peng, H.G., and Vallery, R.S., **2006**. *Ann. Rev. Mater. Res.* 36, 49.
17. Gidley, D. W.; Vallery, R. S.; Liu, M., and Peng, H. –G. **2007**. *Phys. Stat. Solidi (c)* 4, 3796.
18. Ito, K.; Ujihira, Y.; Yamashita, T., and Horie, K., **1998**. *J. Polymer Sci. B* 36, 1141.
19. Ito, K.; Ujihira, Y.; Yamashita, T., and Horie, K., **1999a**. *Polymer* 40, 4315.
20. Ito, K.; Ujihira, Y.; Yamashita, T., and Horie, K., **2000**. *J. Polymer Sci. B* 38, 922.
21. Kauppinen, H.; Corbel, C.; Liskay, L.; Laine, T.; Oila, J.; Saarinen, K.; Hautojärvi, Barthe, P.; M-F., and Blondiaux, G., **1997**. *J. Phys.: Condens. Matter* 9, 10595.
22. Kilburn, D., **2008**. *Appl. Phys. Lett.* 92, 033109.
23. Kimmich, R., **2002**. *Chem. Phys.* 284, 253.
24. Kirkegaard, P., and Eldrup, M., **1972**. *Comp. Phys. Comm.* 3, 240.
25. Kirkegaard, P.; Eldrup, M.; Mogensen, O.E., and Pedersen, N.J, **1981**. *Comp. Phys. Comm.* 23, 307
26. Kirkegaard, P.; Pedersen, N.J., and Eldrup, M., **1989**. PATFIT-88: A data-processing system for positron annihilation spectra on mainframe and personal computers, RISO-M-2740, RISO National Laboratory, Denmark.
27. Makkonen, I.; Snicker, A.; Puska, M. J.; Mäki, J.-M., and Tuomisto, F., **2010**. *Phys. Rev. B.* 82, 041307(R).
28. Miyahara, M., and Gubbins, K. E., **1997**. *J. Chem. Phys.* 106, 2865.
29. Mogensen, O.E., **1974**. *J. Chem. Phys.* 60, 998.
30. Ore, A., and Powell, J. L., **1949**. *Phys. Rev.* 75(11), 1696.
31. Puska, M., and Nieminen, R., **1994**. *Rev. Mod. Phys.* 66 (3).
32. Radhakrishnan, R.; Gubbins, K. E., and Sliwinska-Bartkowiak, M., **2002**. *J. Chem. Phys.* 116, 1147.
33. Seeger, A., **1974**. *Appl. Phys.* 4, 183.

34. Schrader, D.M., and Jean, Y.C., (Eds.) **1988**. *Positron and Positronium Chemistry*, Elsevier, New York
35. Tao S.J., **1972**. *J. Chem. Phys.* 56, 5499.
36. Uedono, A.; Tanigawa, S., and Ohji, Y., **1988**. *Phys. Lett. A* 133, 82.
37. Uedono, A.; Naito, T.; Otsuka, T.; Ito, K.; Shiraishi, K.; Yamabe, K.; Miyazaki, S.; Watanabe, H.; Umezawa, N.; Chikyow, T.; Ohdaira, T.; Suzuki, R.; Akasaka, Y.; Kamiyama, S.; Nara, Y., and Yamada, K., **2007**. *Japan. J. Appl. Phys.* 46, 3214.
38. van Veen, A.; Schut, H.; Vries, J. De; Hakvroot, R.A., and Ijpma, M.R., **1990**. *AIP conf. Proc.* 218, 171.
39. West, R.N., **1973**. *Adv. Phys.* 12, 263
40. Wilkinson, N. J.; Alam, M. A.; Clayton, J. M.; Evans, R.; Fretwell, H. M., and Usmar, S. G, **1992**. *Phys. Rev. Lett.* 69, 3535.
41. Zhao, X., Itoh, Y., Aoyagi, Y., Sugano, T., Hirata, K., Kobayashi, Y., Ohdaira, T., Suzuki, R. and Mikado, T., **1996**. *J. Radioanal. Nuc. Chem.* 211, 31.
42. Zubiaga, A.; Garcia, J. A.; Plazaola, F.; Zuñiga-Perez, J., and Muñoz-Sanjose, V., **2011**. *J. of Phys: Conference Series* 265, 012004.

LIST OF FIGURES

	Page No.
 CHAPTER-I	
Figure 1.1: Principle of techniques in Positron annihilation spectroscopy	40
Figure 1.2: Schematic representation of annihilation γ -rays	42
 CHAPTER-II	
Figure 2.1: The decay scheme of ^{22}Na	66
Figure 2.2: The positron energy spectrum in ^{22}Na decay	67
Figure 2.3: Slow positron accelerator at Radiochemistry Division (SPARC), BARC, Mumbai.	68
Figure 2.4: Positron implantation profile on a film of density 1 g/cc (figure taken from reference [Gidley et al., 2006]	69
Figure 2.5: Block diagram of the positron lifetime spectrometer	71
Figure 2.6: The lifetime spectrum measured using ^{60}Co γ -rays for obtaining the time resolution of the positron lifetime spectrometer	72
Figure 2.7: Block diagram of Doppler broadening spectroscopy set up	75
Figure 2.8: Schematic representation of evaluation of Doppler broadening parameters from DBS spectrum	76
Figure 2.9: The energy spectrum of positron/Ps annihilation	77
 CHAPTER-III	
Figure 3.1: Schematic of typical smectite clay (T_d : tetrahedral; O_h : octahedral)	89
Figure 3.2: One-Dimensional ^1H spectrum of water confined inside clay	

- nanopores, when the sample is static (grey) and spinning at 5 kHz at magic angle (black) inside the 700 MHz NMR spectrometer. The peak at 0 ppm in MAS spectrum corresponds to Si-OH group in the clay platelets. Peaks with stars on top of them are MAS side bands of the water and Si-OH peaks. **96**
- Figure 3.3:** The schematic of the measurement of dielectric response **101**
- Figure 3.4:** The Variation of S -parameter with temperature during cooling and heating cycle for ethylene glycol in ZSM-5. The solid lines are for eye-guide. **104**
- Figure 3.5:** The variation of pick-off lifetime (τ_p) and intensity (I_p) during cooling cycle for ethylene glycol in ZSM-5. The solid lines are for eye guide. **105**
- Figure 3.6:** The variation of S -parameter with temperature during cooling and heating cycle for isopropanol in ZSM-5. The solid lines are for eye guide. **106**
- Figure 3.7:** The variation of pick-off lifetime (τ_p) and intensity (I_p) during cooling cycle for isopropanol in ZSM-5. The solid lines are for eye guide. **107**
- Figure 3.8:** Decay of NMR signal intensity for ^1H spin-spin relaxation in ethylene glycol in ZSM-5 at 267 and 240 K. Inset: two distinct fractional intensities ($I(1)$ and $I(2)$) of spin-spin relaxation time (T_2) are shown at 267 K. **109**
- Figure 3.9:** Temperature variation of fractional intensities of the molecular components having two different mobilities observed in ^1H NMR of ethylene glycol in ZSM-5. **110**
- Figure 3.10:** ^1H spin-spin relaxation time (T_2) at various temperatures of the molecular components with two different mobilities in ethylene glycol in ZSM-5. **110**

- Figure 3.11:** Decay of NMR signal intensity for ^1H spin-spin relaxation in isopropanol at 220 K. **111**
- Figure 3.12:** Temperature variation in fractional intensities of the molecular components with three different mobilities observed in ^1H NMR of isopropanol in ZSM-5. **112**
- Figure 3.13:** ^1H spin-spin relaxation time (T_2) at various temperatures of the molecular components with three different mobilities in isopropanol in ZSM-5. **113**
- Figure 3.14:** (a) Mass (%) loss as a function of temperature (mass-temperature curve) for dry and hydrated clay as measured from TG-EGA. Inset shows FTIR spectrum of the evolved gas. (b) DW profile for hydrated clay as obtained from mass-temperature curve. **117**
- Figure 3.15:** ATR-FTIR spectra of dry and hydrated clay. Inset shows the deconvoluted OHS band of water (3000-3600 cm^{-1}). OHS band is deconvoluted into four peaks (a, b, c and d). **119**
- Figure 3.16:** Heat flow per unit mass in dry and hydrated clay in cooling and heating scans. The inset shows the apparent heat capacity (C_p) of confine water obtained by subtracting C_p of dry clay from the hydrated clay. **121**
- Figure 3.17:** Variation of S -parameter with temperature for dry clay. **123**
- Figure 3.18:** Variation of S -parameter with temperature for hydrated clay in cooling (\circ) and heating (\bullet) cycle. **123**
- Figure 3.19:** Variation of o -Ps *pick-off* lifetime (τ_3) and intensity (I_p) as a function of temperature. **124**
- Figure 3.20:** Variation of free volume fraction (f_v) with temperature. **125**
- Figure 3.21:** ^1H chemical shift (δ) of water as a function of temperature

when the clay sample is spinning at 5 kHz at magic angle inside NMR spectrometer. Temperature dependence data from 245-280 K and 290-325 K is fitted to two independent straight lines, yielding temperature coefficient (g) values of -12.08 and -4.35 ppb K⁻¹. **128**

Figure 3.22: Transverse relaxation times (T_2^* and T_2') of water as a function of temperature when clay sample is (a) static and (b) spinning at 5 kHz at magic angle inside NMR spectrometer. Dotted lines in both the plots indicate inflection points in the measured T_2' values as a function of temperature. **129**

Figure 3.23: Transverse relaxation time (T_2') of water as a function of temperature obtained in the static mode. Solid and dashed lines (eye guides) represent the likely scenario of the freezing phenomenon of water layers. **131**

Figure 3.24: Three dimensional representation of temperature and frequency dependence of imaginary part of the dielectric permittivity ($\epsilon''(f)$) or dielectric loss for (a) hydrated and (b) dry clay. **132**

Figure 3.25: Dielectric response of hydrated and dry clay at $T = 278$ K. **133**

Figure 3.26: Dielectric response ($\epsilon''(f)$ vs. f) for hydrated clay at 250 K. The solid line represents the fit to the response using sum of power law and HN function; dotted and dash-dot curves represent the main relaxation process and d.c. conductivity contribution, respectively. **134**

Figure 3.27: Temperature dependence of relaxation time (τ) for the main relaxation process in hydrated clay, fitted to Arrhenius (210-235 K) and Vogel-Fulcher (240-300 K) functions. **136**

CHAPTER-IV

Figure 4.1: SLM based three phase extraction system **143**

Figure 4.2: Schematic of positron/Ps behavior in a porous membrane containing closed, open and interconnected pores [Gidley et al., 2006]	145
Figure 4.3: SEM images of PTFE SLMs; A (0.2 μm), B (0.45 μm), C (1.2 μm) and D (5.0 μm)	149
Figure 4.4: ATR-FTIR spectra of PTFE SLMs	150
Figure 4.5: Experimental corrected SAXS profiles	151
Figure 4.6: Fit to the experimental SAXS profile for membrane A; inset shows the obtained pore size distribution	152
Figure 4.7: The S-parameter profile for pristine PTFE SLMs. Error on the data is indicated on one of the data points in the figure.	153
Figure 4.8: The $3\gamma/2\gamma$ profiles for pristine PTFE SLMs	154
Figure 4.9: VEPFIT analysis of $3\gamma/2\gamma$ ratio for PTFE SLMs. Solid lines represent fit to the experimental data. Solid lines represent fit to the experimental data.	155
Figure 4.10: The $3\gamma/2\gamma$ profiles for Pristine and goldcoated PTFE membranes B and C	155
Figure 4.11: Permeability of Pu (III) and Am (III) through PTFE membranes	157
Figure 4.12: Correlation between Permeability of ions in PTFE membranes and Ps diffusion length	157
Figure 4.13: Impression of pore architecture in porous membranes	158
Figure 4.14: SEM images of (a) track etched PC and, (b) fibrous PTFE SLM	159
Figure 4.15: The S-parameter profile for pristine track etched PC membranes; membrane 1 (0.03 μm), membrane 2 (0.2 μm) and membrane 3 (0.4 μm)	160
Figure 4.16: The $3\gamma/2\gamma$ profiles for pristine track etched PC membranes	161

Figure 4.17: The S -parameter profile for goldcoated PC membranes	161
Figure 4.18: The $3\gamma/2\gamma$ profiles for goldcoated PC membranes	162
CHAPTER-V	
Figure 5.1: The structure of Metal Phthalocyanine molecule.	169
Figure 5.2: Schematic of (a) OSC grown on self assembled monolayer (SAM) modified SiO_2/Si substrate; (b) PTS; (c) OTS.	171
Figure 5.3: A schematic of in-plane charge transport measurement geometry.	173
Figure 5.4: GIXRD pattern for FePc films grown on ITO-glass substrate at 30°C (amorphous) and 300°C (crystalline).	176
Figure 5.5: AFM images and height profiles of FePc films.	177
Figure 5.6: The S -parameter profile for 100 nm thick amorphous and crystalline FePc films grown at 30 and 300°C , respectively.	178
Figure 5.7: The S -parameter profile for FePc films of different thicknesses. Arrows represent the interface between film and the substrate.	179
Figure 5.8: GIXRD pattern of CoPc films.	180
Figure 5.9: AFM images of CoPc films: (a) as-prepared; (b) annealed at 140°C ; (c) annealed at 200°C .	181
Figure 5.10: S -parameter profiles for Film 1: as-prepared; Film 2: annealed at 140°C and Film 3: annealed at 200°C .	182
Figure 5.11: VEPFIT fitted S -parameter corresponding to different layers of the films.	183
Figure 5.12: S - W curves for CoPc films; solid lines represent the slope of (S, W) points of respective films.	185

- Figure 5.13:** Fits (continuous lines) to the XRR data (open circles) of as-deposited and annealed films. Top panel (a) highlights the specific features obtained for Film 1. Middle panel (b) shows absence of these features in Film 2 and increased roughness. Bottom panel (c) shows the best fit for Film 3 obtained with a 3-layer model. **187**
- Figure 5.14:** Comparison of SLD profiles of (a) as-deposited (Film 1; black line), (b) film annealed at 140 °C (Film 2; blue line) and (c) film annealed at 200 °C (Film 3; red line). Respective fitted parameters are indicated. **188**
- Figure 5.15:** GIXRD pattern for single layer films of *n* and *p*-type OSC materials on quartz substrate. **191**
- Figure 5.16:** GIXRD pattern for bilayer films of *p-n* and *p-p*-type OSC materials on quartz substrate. **192**
- Figure 5.17:** The *S*-parameter profile for single layer film of *n*-type OSC material deposited on quartz substrate. The solid line represents the best fit to data using VEPFIT. **193**
- Figure 5.18:** The *S*-parameter profile for single layer film of *p*-type OSC material deposited on quartz substrate. The solid line represents the best fit to data using VEPFIT. **194**
- Figure 5.19:** The *S*-parameter profile for *p-n* bilayer. The solid line represents the best fit to data using VEPFIT. **194**
- Figure 5.20:** The *S*-parameter profile for *p-p* bilayer. The solid line represents the best fit to data using VEPFIT. **195**
- Figure 5.21:** The *S*-parameter profile for *n-p-n* trilayer. **196**
- Figure 5.22:** *S-W* correlation for *p-n* and *p-p* bilayers. **197**
- Figure 5.23:** *S-W* correlation for *p-n*, *p-p* and *n-p-n* multilayers. **197**

Figure 5.24: <i>S</i> -parameter profiles for a <i>p-n</i> heterostructure as obtained from Positron diffusion modeling considering different scenarios for the effect of defects and electric field at the interface.	202
Figure 5.25: Current density-voltage (<i>J-V</i>) characteristics in single layer OSC film.	204
Figure 5.26: GIXRD pattern of CuPc films grown on unmodified and SAM modified substrates; (a) SiO ₂ (200 nm)/Si; (b) PTS/SiO ₂ (200 nm)/Si; (c) OTS/SiO ₂ (200 nm)/Si	206
Figure 5.27a: AFM images of CuPc films (30 nm) grown on unmodified and SAM modified substrates; (a) SiO ₂ (200 nm)/Si; (b) PTS/SiO ₂ (200 nm)/Si; (c) OTS/SiO ₂ (200 nm)/Si	206
Figure 5.27b: AFM images of CuPc films (~ 2 nm) grown on SiO ₂ (200 nm)/Si substrate at (a) Room temperature; (b) 225°C temperature	206
Figure 5.28: <i>S-E</i> profile for CuPc film grown on <i>native</i> and thermally grown oxide silicon substrate	208
Figure 5.29: <i>S-E</i> profile for CuPc film grown on <i>native</i> and thermally grown oxide silicon substrate; patterned region indicates the interface between OSC layer and substrate	208
Figure 5.30: <i>S-E</i> profile for CuPc film grown on SiO ₂ (200 nm)/Si at temperatures; room temperature (RT) and 225°C	209
Figure 5.31: <i>S-E</i> profile for CuPc films grown on SiO ₂ (200 nm)/Si and SAM (PTS) modified SiO ₂ (200 nm)/Si substrates	210
Figure 5.32: <i>S-E</i> profile for CuPc films grown on SAM (PTS and OTS) modified substrates	211

Figure 5.33: Transfer characteristics of OFETs on unmodified and SAM modified SiO₂(200 nm)/Si

212

LIST OF TABLES

	Page No.
CHAPTER-I	
Table 1.1: Some commonly used experimental techniques in positron annihilation spectroscopy	41
CHAPTER-III	
Table 3.1: Positron lifetime and intensities at room temperature for the hydrated and dry clay sample	122
Table 3.2: Fitting parameters for hydrated clay; Arrhenius fit ($T < 240$ K) and Vogel-Fulcher fit ($T > 240$ K)	136
CHAPTER -IV	
Table 4.1: Physical parameters of PTFE membrane A, B, C and D	146
Table 4.2: <i>o</i> -Ps life lifetime, Intensity and calculated pore size (PALS measurement)	153
CHAPTER-V	
Table 5.1: <i>S</i> -parameter and diffusion length (L_+) of positron in FePc layer calculated by VEPFIT.	179
Table 5.2a: VEPFIT analysis: Two layer fitting results for film 1 and 2.	184
Table 5.2b: VEPFIT analysis: four layers fitting results for film 3	184
Table 5.3: XRR fitting parameters for film 1 and film 3	189
Table 5.4: Fitted values of <i>S</i> -parameter and positron diffusion length (L_+) in single layer of <i>n</i> and <i>p</i> -type OSCs.	199
Table 5.5: Fitted values of <i>S</i> -parameter and positron diffusion length (L_+) in <i>p-n</i> and <i>p-p</i> bilayers	199

CHAPTER-I

INTRODUCTION

1.1. Positron and its discovery

Positron, an antiparticle of electron was first theoretically predicted by P. M. A. Dirac and latter experimentally discovered by Anderson in the cloud chamber experiments [Anderson, 1933]. Dirac in the course of solving the equation consisting of relationship between the energy E and momentum p of a free particle of mass m considering the relativistic effect into account, encountered an energy spectrum comprising of two energy states separated by an interval of $2mc^2$ [Dirac, 1930 and 1935]. The two energy states obtained by solving the Dirac's equation,

$$E^2 = p^2c^2 + m_0^2c^4 \quad (1.1)$$

are given by $E = \pm c\sqrt{p^2 + m_0^2c^2}$. The negative energy state was explained on the basis of theory of holes wherein, the negative energy state was considered as a completely filled infinite sea of electrons under normal conditions. The photon of energy $E > 2mc^2$ can excite one of these negative energy electrons to the positive energy state creating a hole (positron) in the infinite negative energy sea with a positive energy $+E$. This process is referred to as pair production i.e. creation of particle and its antiparticle. The inverse process viz. emission of radiation as a result of trapping of an electron by a hole (positron) in the negative energy sea is termed as electron-positron pair annihilation.

Positron is a fermion belonging to "leptons" group of fundamental particles and obeys Fermi-Dirac statistics. Electrons, muons, taus, neutrinos and the corresponding antiparticles belong to the lepton group. The lepton number of positron is -1, opposite to that of electron. The physical properties of positron are seen to be slightly different than electron [Schrader and Jean, 1988 and Schwinger et al., 1981]. The only difference is the sign of the charge and attendant properties (orbital and spin magnetic moments) of the two particles.

1.1.1. Positron Annihilation

The annihilation of positron with an electron of the medium results in the emission of radiation photons. The electron-positron annihilation event is governed by quantum electrodynamics. Any number of photons can be produced in any annihilation event under the constraints of spin conservation and the corresponding probability depends on the momentum conservation. The probabilities of zero-photon and one-photon emissions are very small due to the fact that two extra bodies for zero-photon and one extra body for one-photon annihilation are required for the momentum transfer. This is in contrast to, two-photon annihilation where all the conservation laws are satisfied by the two emitted photons. The cross section for three-photon annihilation has been observed to be less than two-photon by a factor of α (fine structure constant) and is given as,

$$\sigma_3 = \frac{4}{3\pi}(\pi^2 - 9)\alpha\sigma_2 \approx \frac{\sigma_2}{371.3} \quad (1.2)$$

where, σ_2 and σ_3 are two-photon and three-photon annihilation cross sections, respectively. In any medium, positron rapidly thermalizes by inelastic collisions and then annihilate with one of the electrons of the medium. At lower energies, the annihilation rate (λ) of positron of velocity ' v ' in an environment with electron density ρ is given by,

$$\lambda = \sigma_2 v \rho = \pi r_0^2 c \rho \quad (1.3)$$

The positron life time (inverse of λ) can provide information about the electron density at the site of annihilation.

1.2. The Positronium atom

In some materials, especially molecular solids, positron may bind with an electron to form a quasi-bound state “positronium atom (Ps)”. The subsequent fate of positron is then determined by the interaction of Ps with the surrounding medium. The formation

mechanism of Ps in the medium has been explained by different models viz. “spur model” and “ore model” [Ore and Powell, 1949, and Mogensen, 1974]. The Ps atom is identical to hydrogen atom except the magnitude of the masses. Similar to hydrogen atom, Ps exists in two spin states viz. “para” and “ortho” for singlet and triplet, respectively. The annihilation characteristics of Ps are governed by similar selection rules and cross section as that of free positron. According to the selection rule,

$$(-1)^{l+s} = (-1)^n \quad (1.4)$$

where, l and s are orbital and spin angular momentum of Ps state and n is the number of photons emitted in self-annihilation, the singlet state (*para*-Ps, *p*-Ps) annihilates into an even number of photons and the triplet state (*ortho*-Ps, *o*-Ps) annihilates into an odd number of photons. Hence, in ground state *p*-Ps and *o*-Ps annihilate by two- and three-photon emission, respectively. The intrinsic lifetime of *p*-Ps and *o*-Ps in vacuum is 125 ps and 142 ns, respectively.

In some condensed phases or molecular solids, *o*-Ps may get trapped in low electron density regions such as free volumes in polymers, pores of the porous systems like zeolites etc. and annihilate with an electron of opposite spin from the medium rather than its own partner via two-photon mode. The process is termed as “*pick-off*” annihilation which reduces the intrinsic lifetime of *o*-Ps. The *pick-off* lifetime of *o*-Ps can be used to determine the size of the cavity *o*-Ps is being trapped and annihilated using a semi-empirical relation, Tao-Eldrup equation, given as [Tao, 1972 and Eldrup et al., 1981],

$$\begin{aligned} \lambda_{pick-off} &= \left[\frac{1}{4} \lambda_s + \frac{3}{4} \lambda_T \right] \cdot P \\ &= 2 \cdot \left[1 - \frac{R}{R + \Delta R} + \frac{1}{2\pi} \sin \left(\frac{2\pi R}{R + \Delta R} \right) \right] \end{aligned} \quad (1.5)$$

where, λ_S , λ_T , R and ΔR are the singlet and triplet Ps self-annihilation rates, radius of the cavity (assuming spherical) and an empirical parameter, respectively. The value of the empirical parameter ΔR has been determined as 0.166 nm. Ps formation is higher in molecular solids as compared to metals and semiconductors owing to low electron density in molecular solids as compared to the latter. In addition, *o*-Ps formation probability and its lifetime vary due to the chemical reactions in the medium [Duplatre et al., 2003].

Ps annihilation and its lifetime in liquids have been explained by bubble model proposed by Ferrel to account for long lifetimes in liquids as compared to solids [Ferrel, 1957]. The strong repulsive interaction between the electron belonging to Ps and the electrons of the medium leads to the formation of a bubble which results in considerable increase in Ps lifetime. The annihilation rate of self-trapped Ps in the bubble is determined by the overlap integral between the Ps wave function spreading outside the bubble into the electronic wave function of the medium. Good correlations have been observed between Ps lifetime in pure liquids and bubble quantities such as surface tension and bubble size [Mogensen, 1988 and 1989]. Ps formation in liquids is a unique phenomenon which has driven the development of Ps chemistry.

1.3. Positron sources

Positrons can be obtained from the radioactive decay of neutron deficient radio-isotope and from pair-production by high energy γ -rays. Radio-isotope positron sources are convenient for most of the laboratory applications whereas, pair production is mainly used for positron beams where high flux is required. The choice of the radio-isotope as a positron source depends on the positron annihilation technique being used. For example, ^{22}Na is mainly used for positron lifetime spectroscopy (PALS) where the prompt γ -ray emitted in coincidence with the positron emission is considered as the birth signal of positron and one of the annihilation γ -ray serves as death of the positron. These two

signals are used to determine the lifetime of positron in the medium. ^{68}Ge radio-isotope can be used for Doppler broadening spectroscopy (DBS), which does not require any prompt γ -ray signal. Depth profile studies require monoenergetic positrons which cannot be obtained from the radio-isotopes owing to the fact that the energy of positrons emitted in β^+ decay of radio-isotopes is not constant but ranges from zero to β_{max} . Therefore, monoenergetic positrons are mainly obtained by either monochromatizing the positrons emitted from radioisotopes or by using the accelerator based positron sources mainly via pair production.

1.4. Positron annihilation spectroscopy

The unique aspect of Positron annihilation spectroscopy (PAS) lies in the fact that the photons emitted in electron-positron annihilation events contain information about the electron density and momentum distribution of the medium. This information can be used to study variety of molecular properties of condensed matter. PAS comprises of different techniques which can be utilized to study different aspects like defects, free volume/pore size and their distribution and correlated nanostructural properties in molecular systems. Each technique provides specific information about the material under study. PAS comprises of three major experimental techniques viz. Positron lifetime spectroscopy (PALS), Doppler broadening spectroscopy (DBS) and angular correlation of annihilation radiation (ACAR) (schematic shown in Figure 1.1). There are other hybrid techniques (summarized in Table 1.1) which utilize correlated or combined information obtained from these techniques. The principle and experimental details of some of these techniques are described in the following. The instrumentation and detailed analysis for PALS and DBS are described in chapter II.

The techniques utilizing the positrons emitted from radio-isotope source directly, provide bulk information of the material owing to the energy distribution of the emitted

positrons. On the other hand, depth dependent information can be obtained by varying the energy of positrons (monoenergizing). This purpose is achieved by positron beam which can provide low to high energy positrons enabling surface and depth profiling in thin films. The details of different beam components and analysis of the data are also described in chapter II.

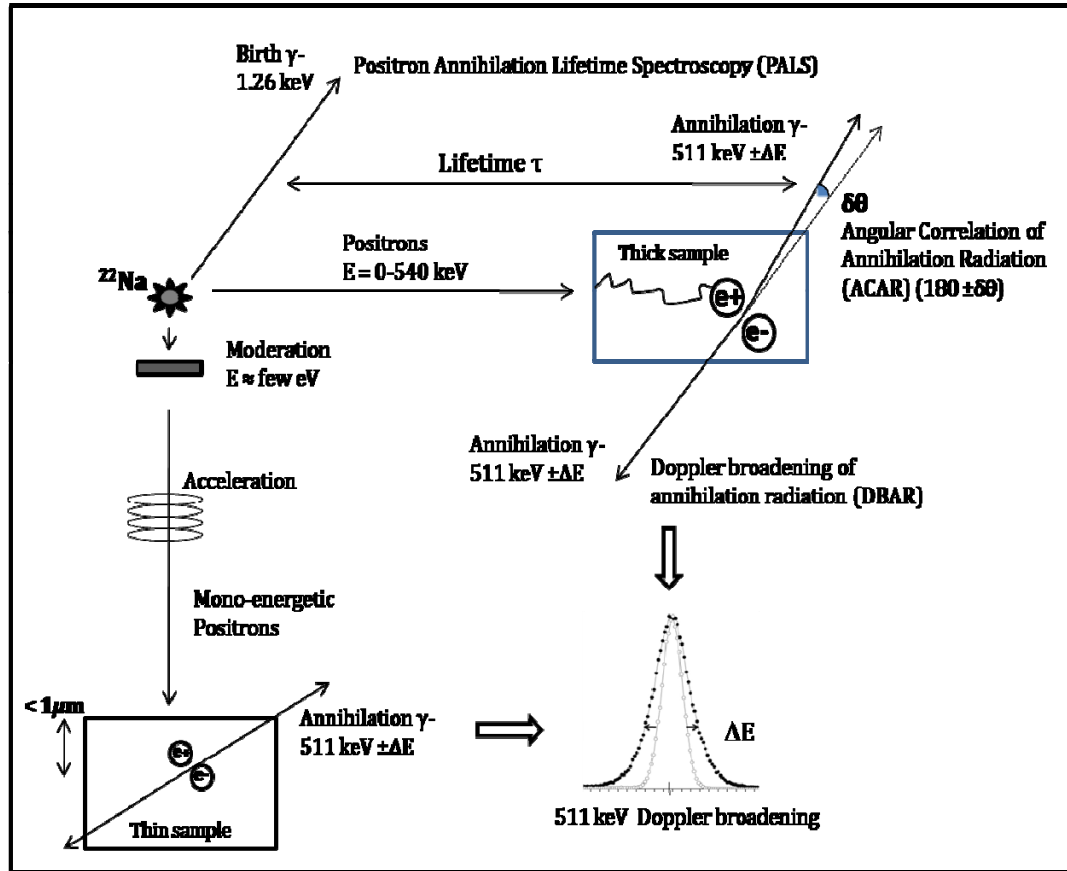


Figure 1.1: Principle of techniques in Positron annihilation spectroscopy.

1.4.1. Positron lifetime spectroscopy (PALS)

PALS involves measuring positron/Ps annihilation characteristics (annihilation γ -rays) in time domain. The lifetime of positron/Ps in a medium is measured by measuring the time interval between the implantation of positron in the medium (birth signal) and its annihilation (death signal). In PALS using radio-isotope source (^{22}Na), the prompt γ -ray

(1275 keV) emitted in coincidence with the positron is indexed as the “birth signal” and one of the annihilation γ -rays (511 keV) as “death signal”.

Table 1.1. *Some commonly used experimental techniques in positron annihilation spectroscopy.*

Technique	Quantities measured
Positron Annihilation Lifetime Spectroscopy (PALS)	Time difference between the birth of positron (signaled by prompt gamma ray) and annihilation gamma ray
Doppler Broadening of Annihilation Radiation (DBAR)	Energy spectrum of annihilation gamma ray to monitor its deviation from 511 keV
Angular Correlation of Annihilation Radiation (ACAR)	Angular deviation of the two annihilation gamma rays from 180° .
Age-MOMentum Correlation (AMOC)	Both PALS and DBAR in correlated mode
$3\gamma/2\gamma$ -ratio	Energy spectrum of the annihilation gamma ray
2-detector Coincidence Doppler Broadening (CDB) measurement	Energy spectra of both the annihilation γ -rays in coincidence

The typical positron annihilation lifetime spectrum is a combination of many exponential decay curves (corresponding to different positron states in the medium) convoluted with time resolution function of the spectrometer. The width of the instrumental resolution function puts a limit on the measured lifetimes. Lifetimes shorter than one-third of the resolution cannot be measured accurately. The positron lifetime (inverse of annihilation rate) in a medium depends on the electron density at the annihilation site. Together with the ability to get trapped in defects/open volumes, PALS

becomes a sensitive defect spectroscopy technique. The detailed instrumentation and analysis will be discussed in chapter II.

1.4.2. Doppler broadening spectroscopy (DBS)

DBS involves measurement of energy spectrum of annihilation γ -rays which is sensitive to the momentum of electron-positron annihilation pair. The measured momentum is primarily determined by the momentum of annihilation electron and hence, can probe the electronic and physical environment at the annihilation site. The finite momentum of electron-positron pair leads to deviation from anti-collinearity and Doppler broadening of annihilation γ -rays. The shift in the energy and the direction of emitted annihilation γ -ray in the laboratory frame can be expressed as (Figure 1.2),

$$\delta\theta \approx \frac{P_T}{m_0 c} \quad (1.6)$$

where, angle of deviation $\delta\theta$ (Figure 1.2) is related to the transverse component (P_T) of electron momentum P and m_0 and c are the rest mass of electron and velocity of light, respectively.

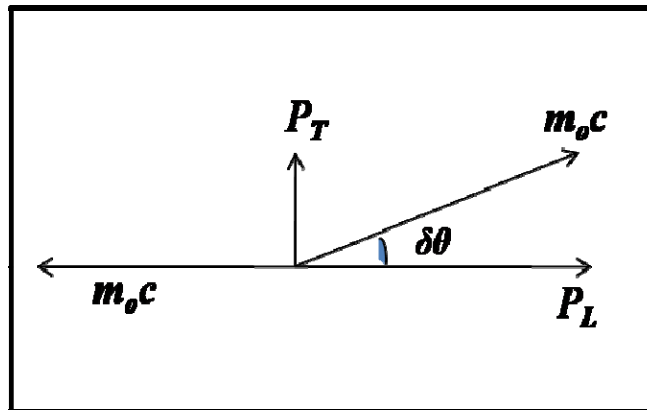


Figure 1.2: Schematic representation of annihilation γ -rays.

The energy of photons in laboratory frame is given as,

$$E_\gamma = \frac{1}{2} E_T \left(1 \pm \frac{v}{c} \cos \theta\right) \quad (1.7)$$

Therefore, the energy of annihilation photon can be written in terms of its rest mass energy as (neglecting the small deviation),

$$E_\gamma = E_0 \pm \delta E = m_0 c^2 \pm c \frac{P_L}{2} \quad (1.8)$$

where, P_L is the longitudinal component of the momentum i.e. component along the emission direction of annihilation photons (taken as z -axis). The Doppler broadened spectrum corresponds to the longitudinal momentum density given by,

$$W(E) = \text{const.} \iint \rho(p_x, p_y, p_z) dp_x dp_y \quad (1.9)$$

where ρ is the electron momentum space density and z -axis is the line joining the detector and source. The detailed instrumentation and analysis will be discussed in chapter II.

1.4.3. Coincidence Doppler broadening spectroscopy (CDB)

This technique involves measurement of both the annihilation γ -rays in coincidence. The coincidence measurement offers better signal to noise ratio as compared to conventional Doppler broadening technique, especially in the high momentum region of the Doppler broadened spectrum. This facilitates identification of chemical surroundings at the annihilation site by indexing the annihilation with core electrons that contribute to the high momentum region. The technique also provides better energy resolution as compared to conventional DBS.

1.4.4. Age-momentum correlation technique (AMOC)

This technique is the hybrid of two conventional positron annihilation techniques. This technique involves correlated measurement of positron lifetime (positron age) and momentum of the annihilating electron-positron pair. The correlated measurement

provides time resolved information about the positron states, helping unambiguous interpretation of data with respect to positron and Ps chemical reactions, positron trapping etc. [Dauwe et al., 2003; Suzuki et al., 2003; Schneider et al., 1997].

1.5. Positron/Ps annihilation spectroscopy: A tool to probe condensed matter

PAS is a powerful technique to study variety of properties of condensed matter. The atomic order sensitivity of positron/Ps and the propensity to get trapped in low electron density regions (free volume hole, voids, vacancy defect etc.) enable PAS to probe atomic and molecular properties in materials. The uniqueness of PAS arises from the fact that annihilation γ -rays carry electronic information (density and momentum) of the site of electron-positron annihilation. It is thus possible to investigate local structures embedded in bulk of the materials like vacancies, dislocations, electronic structure of defect, its size and concentration, superlattices and device structure. There are several reviews on the application of PAS to study material properties [Siegel et al., 1980; Seeger et al., 1974]. PAS has been extensively used to study variety of materials viz. metal/alloys, molecular solids, semiconductors, polymers and biomaterials. In soft condensed matter like polymers and biomaterials, *o*-Ps *pick-off* lifetime enables probing the nanostructural properties viz. free volume distribution and correlated properties such as glass transition, mechanical strength and stability [Ito et al., 1998, 1999a and 2000; Bandzuch et al., 2000 and Mallon et al., 2003]. On the other hand, the obtained momentum distribution (DBS, CDB, ACAR) together with positron/Ps lifetime helps in the investigation of electronic structure, Fermi surface of materials [Smedskjaer et al., 1998; Bansil et al., 1988 and Chan et al., 1992] and defects [West et al., 1973; Brandt et al., 1983; Seeger et al., 1974]. PAS enables unambiguous identification and quantification of vacancy defects, their charge states and electronic environment in semiconductors [Gebauer et al., 2002; Slotte et al., 2003 and Krause-Rehberg et al., 1999; Tuomisto et al.,

2007 & 2008]. Defect profiling and interfacial characteristics in semiconductor heterostructures [Zubiaga et al., 2011; Makkonen et al., 2010] using PAS has emerged as a novel technique for the investigation of nanostructural characteristics of semiconductor devices. Beam based PAS is used as a porosimetry technique in wide range of nanoporous films and membranes with an ability to provide pore architecture (pore interconnectivity) and hidden porosity beneath dense layers [Gidley et al., 2006]. Characterization of porous materials of technological importance like zeolites, silica [Miranda et al., 1993], aerogels [Miranda et al., 2006] etc. is another application of porosimetry using PAS. In addition to the characterization of nanostructural properties of materials, other physical properties pertaining to nanoscale confinement are recently being studied using PAS. This includes phase behavior of liquids confined in nanocavities [Dutta et al., 2006 and 2008] and glass transition temperature of polymer thin films [Keddie et al., 1994; Dalnoki-Veress et al., 2001]. A review of general applications of positron/Ps in probing molecular substances can also be found in literature [Jean et al., 2003].

In the present thesis PAS has been used to probe nanostructural properties of different kinds of nanoscale materials. The main aim is to explore the effect of reduced size on the structural and related properties of nanoscale materials. An introduction to nanoscale materials, their properties and characterization tools is described in the following section.

1.6. Nanoscale materials

Nanoscale materials are defined as the materials with at least one dimension restricted to nanometer length scale (~ 100 nm) and possess unique optical, electrical and magnetic properties. Within this length scale, properties of materials (such as strength, resistivity, conductivity etc.) are significantly different than their bulk counterparts owing

to the dominant role of surface energy. With the advancement in science and technology, especially towards miniaturization of electronic devices, manipulating matter at the level of atomic orders and characterization of the properties at nanoscale has gained intense interest in the last two decades. The characterization and understanding of material properties is of utmost importance in order to develop new materials with potential applications in the area of science, engineering, technology and medicines. Nanoparticles, semiconductor nanocrystals, porous materials (fullerenes, carbon nanotubes and fibres, zeolites, silica, metal organic frameworks etc.) and thin films (~ few nm thickness) are few of the many examples of nanoscale materials. Some of these nanoscale materials are already being commercially available for many applications in industry and medical sciences. In addition to their technological relevance, these materials are topic of current research for fundamental studies related to the effect of reduced dimensionality on the properties of materials. In the present thesis work, the studied nanoscale materials are categorized into two classes: (i) nanopores in porous materials and, (ii) nanoscale thin films. The nanopores of porous materials are employed as confining geometry for different liquids and the properties of liquids under nanoscale confinement is the main subject of study under porous materials category. Pore structure of porous materials dictates various properties of the material like transport and permeability in membranes, exchange capacity in zeolites etc. In this regards, pore architecture in porous membranes in terms of pore interconnectivity has been investigated by making use of mobility of positron/Ps in the medium (porous network). In the area of nanoscale thin films, modification of nanostructure of organic semiconductor (OSC) thin films as a function of different growth parameters and post growth annealing treatment has been studied. In addition, defect depth profiling has been carried out to probe interfacial characteristics in OSC heterojunctions as well as self-assembled monolayer (SAM) modified surfaces in

organic field-effect transistors. A broader discussion on these aspects is given in the following.

The study of properties of materials and their different phases has been an area of fundamental research for decades. Confinement leads to significant change in material properties as compared to its bulk owing to increased surface to volume ratio due to reduced dimensionality. In this regards, study of properties of liquids confined in nano sized cavities has attracted interest due to their significance not only for fundamental research, but also for the advancement of technology especially in the areas related to lubrication, adhesion, catalysis, fabrication of nanomaterials and nanotribology. It has been observed that properties of liquids confined in nanodomains significantly differ from their bulk properties. Confined liquids exhibit peculiar thermodynamic properties, shift in freezing/melting behavior and existence of different phases. The interaction with the solid surface organizes/put constraints on the confined liquid, thus, modifying physical (density, layering, wettability with the surface etc.) and dynamical (relaxation, diffusion) properties. Therefore, understanding the phase behavior of liquids in confinement is desirable not only to understand fundamental physics behind the phase behavior (i.e. role of surface interactions and size of confining geometry) but for their crucial role in various biological and physical processes. Different techniques are being used to study structural, dynamical and thermodynamical properties of confined liquids. Calorimetry (differential scanning and adiabatic) are mainly used for the determination of heat flow and heat capacity; Fourier transform infra-red, X-ray and neutron diffraction and scattering techniques provide information about the structure and density of the confined phase whereas, the dynamical properties are mainly studied using nuclear magnetic resonance (NMR), solvation dynamics and dielectric relaxation spectroscopy (DRS).

Apart from providing a confining region for liquids or other materials, porous materials are important for catalysis, separation processes and ion exchange. Therefore, characterization of porous materials is another important field in nanoscale technology. Pores in the membranes act as sieve and govern transport and permeability properties of the membranes. Tuning the membrane properties like pore size, porosity and chemical nature can provide high selectivity and efficient permeability for separation processes. These properties however, depend on the microstructural characteristics of the membranes or pore architecture. Pore architecture refers to the quantification of pore size, porosity and the length scale over which the pores are connected to each other. Therefore, characterization of pore architecture of the membranes is essential in order to customize membrane properties for variety of applications. Varieties of techniques are available to characterize pores having their sensitivity to different length scales. Gas/solvent adsorption is the most popular technique for the determination of pore size and distribution. Among other techniques, small angle neutron scattering, ellipsometry porosimetry and electron microscopy are being used to characterize size as well as pore fraction. However, these techniques are limited by their sensitivity to hidden, closed and interconnected pores.

Thin film technology is pervasive in many applications, including microelectronics, optics, magnetic, hard and corrosion resistant coatings, micro-mechanics, etc. Thin films (single and multilayers) are basic building block of all the electronic devices like solar, photovoltaic cells, transistors, light emitting diodes etc. The ability to selectively and controllably deposit thin films and characterization of morphology/nanostructure of the films is a prerequisite in order to develop devices with specified electronic and optical properties. The structure and morphology of the film play key role to ascertain working mechanism and performance of the device. In this regards,

defects (vacancy, lattice, structural defects like grain boundaries etc.) are seen to influence charge transport and optical properties of the device. For example, these defects act as charge traps and recombination centers thus, reducing the efficiency of the device. Different growth parameters like the nature of substrate, deposition temperature, deposition rate etc. are seen to influence nanostructure of the grown film. Different nanostructural configuration (nanorods, nanocrystals, nanoribbons etc.) can be achieved by the combination of different growth parameters and deposition techniques. These nanostructural characteristic (configurations and orientation of grains) can be tailored to achieve high efficiency and better performance of the devices. In addition to structure and morphology of the film, interfaces between various components of the device are also crucial for device performance. Heteroepitaxy between different materials leads to structural defects or disorder at the interfaces which influence the charge transport and light absorption/emission characteristics of the device. Therefore, control over growth mechanism and characterization of structural properties is crucial for the development of efficient and high performance devices for technological applications. Surface morphology of thin films is mainly characterized by atomic force and scanning electron microscopy whereas, structural properties like lattice structure of the grown film is investigated using X-ray diffraction/grazing incidence X-ray diffraction. Depth dependent structural properties are mainly studied using X-ray reflectivity, near edge X-ray absorption fine structure, sputter-ion based X-ray photoelectron spectroscopy and secondary ion mass spectrometry techniques.

1.7. Positron annihilation spectroscopy: Characterization tool for nanoscale materials

PAS is a sensitive technique to probe atomic scale structural properties in condensed matter. When a positron enters the solid, it loses its momentum rapidly and

thermalizes within a few picoseconds. After thermalization, it diffuses for few hundreds of picoseconds before finding an electron followed by annihilation. The gamma radiation emitted after the electron-positron annihilation carries information about the electron density and momentum distribution and thus, enables identification of various properties of the material. The unique ability of positron to get trapped in low electron density regions like voids, vacancies, open/free volumes etc. provides sensitivity to probe atomic order defects in materials. The lifetime of positron/Ps at the trapping site can be correlated to the size of the trap, whereas, Doppler broadening of annihilation gamma radiation contains information about the chemical environment at the annihilation site. Thus, PAS can be employed to probe structural characteristics in materials at nanoscales. PAS is used to probe vacancy defects in metals/alloys and semiconductors and sub-nanometer voids termed as free volumes in polymers. This provides an unambiguous identification of vacancy clusters or nanocrystallites formed in metals/metal oxides and nanostructural characteristics in polymers and polymer nanocomposites. This information can be correlated to various physical, opto-electronic and thermal properties of materials.

The ability to get monoenergetic positrons (positron beam technique) has enabled characterization of surfaces and depth profiling of microstructure in thin films. The image potential well at the surface acts as a two-dimensional defect for positron and may trap the positrons. This enables identification of structural imperfections (like steps, islands, surface vacancy etc.) on the surface using low energy positrons. It is thus, possible to characterize surfaces, especially at the nanometer scale where, finite size and reduced dimensionality induced effects are predominant. Depth profiling using positron beam has also opened a possibility to characterize buried interfaces in heterostructures as well as characterization of modified interfaces. Defect free surfaces and interfaces are essential for fabrication of all the electronic devices. With above mentioned capabilities, PAS has

emerged out as a sensitive characterization technique in the area of nanoscience and nanotechnology.

1.8. Scope of the present work

1.8.1. Nanodroplets

Nanodroplets refer to liquid confined in nano domain. Liquids under confinement at nanoscale exhibit significantly different phase behavior/properties as compared to the bulk. The introduction of surface forces, and the competition between fluid–wall and fluid–fluid interaction, can lead to interesting surface-driven phase changes. The fundamental scientific interest in this area is to understand the new physics that results from finite-size effects, varying dimensionality, and surface forces. When the pore width is of the order of the range of the intermolecular forces, a large fraction of the confined molecules experience a reduction in the number of nearest-neighbour molecules, leading to large shifts in phase coexistence curves and a lowering of critical points. Plenty of experimental studies have been performed to address the science and phenomenon behind the deviation of physical and thermodynamical properties of liquids confined at nanoscale dimensions from their bulk counterparts. For this, different topics of condensed matter physics have been considered in confined geometry including H-bonded liquids, polymer physics, phase transitions, critical phenomena, and the glass transition temperature. In the area of phase transition studies, freezing/melting behavior of confined liquids has been studied extensively. It has been established that the first-order transition, i.e. freezing/melting point (T_f), for a bulk material differs from that of the same when it is confined in porous systems. The effect of size on T_f has been studied for organic molecules [Jackson et al., 1996], metal particles [Couchman et al., 1977] and polymer lamellae of different thicknesses [Cheng et al., 1987]. The observed shift in T_f has been

explained from classical thermodynamics Gibbs-Thomson relationship [Thomson et al., 1871; Defay et al., 1966; Evans et al., 1987] given by,

$$\Delta T_f = T_{pore} - T_{bulk} = -\frac{2(\sigma_{sw} - \sigma_{lw})T}{H\rho R} \quad (1.10)$$

where, σ_{sw} and σ_{lw} are the interfacial free energies per unit area for the solid-wall and liquid-wall interfaces, respectively, H is the melting enthalpy of the solid, ρ is its density and R is the radius of the confining pore. However, this classical relationship breaks down for small pores, as the concept of surface tension is not well defined and the bulk values of melting enthalpy and density of solid may no longer be valid in small size pores. In addition to the shift in T_f , direction of the shift i.e. elevation or depression in T_f , has also been observed. The direction of shift depends upon whether the pore wall favours the confined solid phase or confined fluid phase. If the solid-wall interfacial free energy (σ_{sw}) is higher than liquid-wall interface (σ_{lw}) then, ΔT_f is negative or, depression in freezing/melting temperature is observed and vice-versa [Miyahara et al., 1997; Radhakrishnan et al., 2002]. There are number of experimental studies employing variety of techniques such as differential scanning calorimetry [Zheng et al. 2007], nuclear magnetic resonance [Kimmich et al., 2002], dielectric spectroscopy [Barut et al., 1998], neutron scattering [Alba-Simionesco, et al. 2003] etc. and a range of confined systems to explore the effect of pore size and role of fluid-wall interaction energy on the shift/direction of freezing/melting point. In addition to experimental studies, subsequent molecular dynamics studies [Miyahara et al., 1997; Radhakrishnan et al., 2002] have also shown that T_f is strongly affected by the strength of attractive interaction between the liquid molecules and the pore wall.

In the light of the reported experimental results and molecular dynamics simulations on the phase transition behavior of confined liquids, we have employed

positron/Ps annihilation spectroscopy to investigate the freezing/melting behavior of a variety of liquids confined in different nano geometries. The main objective of the work is to understand the role of confining geometry as well as the surface interactions between the liquid and wall of the confining geometry on the phase transitions of confined liquids. PAS has been used to study the phase behavior of number of gases and liquids confined in porous materials [Duffy et al., 2000; Bartos et al., 2001; Wilkinson et al., 1992] and mobility of glass forming liquids under confinement effect [Kilburn et al., 2008]. Bristol positron group has studied the phase diagram of CO₂ confined in vycor glass [Fretwell et al., 1996]. Our positron group has also been involved in the studies related to the phase transition of different liquids confined in silica and zeolites for the past few years [Dutta et al., 2006 and 2008]. In all those studies, the main focus was on the effect of pore size on the freezing/melting point of the liquid (benzene) confined in silica and zeolite pores. The depression in freezing/melting point of benzene was observed in both silica and zeolite pores. However, the extent of the shift was seen to be different depending upon the size of the pore. The negative shift observed in the pore was attributed to the slightly repulsive interaction of benzene with the pore walls. In continuation with these studies, to examine the role of interactions between the liquid and wall of the confining geometry on the phase transitions of confined liquids, two other liquids viz. ethylene glycol and isopropanol confined in zeolite nanopores has been studied in the present work. These two liquids experience attractive interaction with the pore walls through hydrogen bonding between the liquid and the -OH group at the wall of the zeolite pore. As a result, an elevation in freezing/melting point was observed in both the liquids. However, the strength of the fluid-wall interaction is different due to the distinct nature of hydrogen bonding in these liquids. As a matter of fact, iso-propanol [CH₃CH(OH)CH₃] has intermolecular hydrogen bonding and strong attractive interfacial interaction with the pore

surface whereas, ethylene glycol [(CH₂OH)₂] experiences both intra- and inter-molecular hydrogen bonding, resulting in reduction in the strength of interfacial interaction towards the surface. The difference in the extent of fluid-wall interaction resulted in the different amounts of shift in the freezing/melting point in the two cases. The elevation in freezing/melting point of these liquids as revealed from PAS was corroborated with the NMR studies, wherein, spin-spin relaxation time was indexed to investigate the dynamics of the liquids. The sensitivity of relaxation process to the mobility of the molecules embodying the spins and hence, the intermolecular interactions can provide information about temperature mediated structural and dynamical changes in the liquid. The structural and dynamical information can then be used to index phase transitions.

In addition to shift in freezing/melting point of the liquids, thermodynamic properties (latent heat capacity, enthalpy), structural and dynamical properties (shear viscosity, mobility) also show deviation from the bulk behavior. There are experimental reports on the investigation of structure of confined phases using NMR and X-ray/neutron diffraction techniques, whereas, the dynamical properties have been studied using DRS, neutron scattering, solvation dynamics and NMR techniques. In this regards, nanoscale confinement of water has attracted considerable attention due to its relevance to fundamental physics, biological and geological processes as well as technological developments at nanoscale. For instance, water molecules confined in nanocavities of biomolecules play crucial role in regulating molecular structure [Zhou et al., 2004]. In the field of nanotribology and nanofluidics, behavior of molecularly thin water films influences nanomechanical dynamics of water [Holt et al., 2006; Khan et al., 2010]. It has been seen that nanoconfined water exhibits peculiar properties differing from the bulk. In this context, study of structural and dynamical properties of confined water has been an area of extensive research in order to understand the anomalous behavior of water in

nanoscale confinement. A lot of studies have been carried out in the context of structure and dynamics of confined water [Koga et al., 2001; Striolo et al., 2003; Mallamace et al., 2007] using variety of techniques and confining matrices. These studies mainly concern with the phase transitions and glass transition of water [Alba-Simionesco et al., 2006], nature of crystalline phases of ice formed inside the pores [Hummer et al., 2001], existence of disorder/amorphous regions within the pores etc. The anomalous behavior of water in confined systems has been attributed to the effect of surface interactions which modify the hydrogen-bonded network of water resulting in the formation of new phases and emergence of transitions otherwise, not prevailing in the bulk. In this context, we have studied structural and dynamical properties of water confined in saponite clay nanopores which act as one dimensional confining domain (referred as 2D confined water) using PAS, NMR and DRS. Water exhibits attractive interaction with the pore walls owing to the existence of hydrogen bonding between the water molecules and the silanol groups in addition, to the strong inter-molecular hydrogen bonding network. The effect of interfacial interaction on the phase behavior of confined water has been probed by indexing the variation in structure and dynamical properties. The comprehensive study of structural and dynamical properties of confined water has shown the presence of two transitions viz. above and below the bulk freezing temperature of water. This has been attributed to the existence of distinct regimes of water inside the pores undergoing transitions at different temperatures. The study has provided an insight into the structural and dynamical changes in confined water pertaining to the role of interaction energies between the water and the matrix. The presence of the transition at a temperature above the bulk freezing point of water, in addition to a transition below the bulk freezing point is the first report on the phase behavior of nanoconfined water.

Experimental and theoretical work in the area of confinement i.e. phase behavior in pores are beset with significant difficulties. On the experimental side, the morphology of confining matrix i.e. poor knowledge of the exact distribution of pore size, shapes, connectivity impose difficulties in the interpretation of the observed data. On the other hand, in theoretical work, simulating the exact morphology of the porous material considering the presence of impurities (might present in real system and can produce spurious result) and the presence of metastable states leads to significant deviation from the experimentally observed results. Despite a wealth of research, the overall view of the phenomena prevailing in the confined systems is still lacking. This field is experimentally and empirically driven and a lot work needs to be carried out in order to attain complete understanding of the effect of confinement. In the study of phase transitions in confined liquids, PAS has emerged as a sensitive technique to probe electronic-structural alterations following the phase transition.

1.8.2. Pore architecture of membranes

PAS is a well established and sensitive tool to characterize nanostructure in polymers by providing information about the pore size, its distribution and fraction of free volume nanoholes. These nanostructural properties are deterministic measures for various thermo-mechanical properties of the polymeric systems. The triplet Ps state (*o*-Ps) plays the key role in probing porous materials through its reduced lifetime and $3\gamma/2\gamma$ branching ratio when it is trapped in the pores. The *o*-Ps *pick-off* lifetime can be correlated to the size and distribution of pores using Tao-Eldrup equation and the fractional free volume, f_v in a polymer that can be calculated using average volume of nanoholes and *o*-Ps intensity as,

$$f_v = CI_3 \langle v_f(\tau_3) \rangle \quad (1.11)$$

where, C is a constant, I_3 is o -Ps intensity and $\langle v_f(\tau_3) \rangle$ is the average volume of nanoholes [Wang et al., 1990]. In addition to this, another important aspect in the characterization of nanoporous materials is to understand the pore growth mechanism which mainly deals with the length scale over which the pores are interconnected depending upon the porogen loading. This has important implication in the context of generation of porous matrices for various applications where the amount of porogen loading dictates not only the porosity but the network between the pores. The ability of Ps to diffuse within the porous network can be utilized to investigate pore architecture of the materials. Pore architecture refers not only to pore size and its distribution but, porosity (closed and open) and pore interconnectivity. The positron/Ps diffuses into the pores by colliding with the walls of the pores and annihilates therein. The annihilation profile in the material can provide information regarding the positron dynamics (diffusion) within the porous network. The annihilation characteristics i.e. S -parameter and $3\gamma/2\gamma$ branching ratio as a function of implantation energy of positrons are employed to evaluate positron/Ps mobility in the material taking into account its diffusion, trapping and annihilation. The mobility of positron/Ps is the direct measure of its diffusion length which can be correlated to the length scale of pore interconnection i.e. pore interconnectivity. These features of PAS have been used in the characterization of porosity in large variety of technologically relevant nanoporous materials. For example, porous structure in low- k dielectric thin films for microelectronics applications where control over porosity is one of the crucial factors in deciding the high speed and high integration chips for miniaturization of devices [Lynn et al., 2006; Gidley et al., 2007; Sun et al., 2002, Petkov et al., 2001]. In the area of membrane science, characterization of pore architecture of membranes used in separation science [Wang X. Y. et al., 2006], filtration [Baerdemaeker et al., 2007] and pervaporation [Huang et al., 2008] applications, is

crucial to determine the permeability and transport properties of the membrane. These studies have explored pore structure in terms of pore size, open and closed porosity, pore interconnectivity in membranes and thin films, pore structure analysis of hidden layers and asymmetric membranes that are otherwise, inaccessible to solvents and gases and characterization of multilayer films. Most of the PAS studies on the characterization of pore structure are focused on the identification of nanopores/nanoholes. In the present work, PAS has been utilized for the characterization of pore architecture in mesopores membranes (micron size pores). Though, PAS is not sensitive for the determination of micron size pores in the materials, however, Ps dynamics in the porous network can be utilized to analyze microstructural properties in the mesoporous systems. In this respect, Ps diffusion length is a sensitive index for the determination of length scale of pore interconnection (pore interconnectivity) in the membranes. In the present work, Ps diffusion length in supported liquid membranes (PTFE) and track-etched polycarbonate membranes with varying pore sizes in the range of microns has been calculated from the measured $3\gamma/2\gamma$ ratio as a function of positron implantation depth. Porosity at the surface has been measured by comparing $3\gamma/2\gamma$ ratio at lower implantation energies (surface region) as well as Ps diffusion length in pristine and gold capped membranes. Gold capping at the surface prevents Ps from escaping from the surface of the membrane. A large difference in $3\gamma/2\gamma$ ratio in the two cases is an indication of high open porosity and vice-versa. Pore interconnectivity together with porosity at the surface has provided a comprehensive picture of the pore structure in the studied mesoporous membranes. The measured pore architecture (pore interconnectivity/Ps diffusion length) of these membranes is then correlated with the permeability and transport properties of the membranes. The study has provided a new approach to utilize PAS for the

characterization of mesoporous membranes as well as identification of closed and interconnected pores present in the materials.

1.8.3. Nanostructure characterization in organic semiconductor thin films

Thin films of nanometer thickness constitute one of the classes of nanoscale materials. Similar to the case of confined fluids, properties of nanoscale thin films also differ from their bulk forms. The interaction between the substrate and the constrained thin film contribute to the observed differences in the properties. As an example, the change in T_g of free standing ultra thin polymer films [Forrest et al., 1996; Keddie et al., 1994] as well as supported polymer films [Jain et al., 2002] has been observed from plenty of studies. The constrained dynamics of molecular chain has been assigned as the main reason for the observed difference in T_g . In addition to the relaxation dynamics and thermo-physical properties of thin films, the structural and morphological properties are also observed to be affected due to the interaction potential/energy of the substrate. With the advancement in the area of science and technology, especially in microelectronic industry, thin films technology has emerged as the basic building block for all electronic devices. Miniaturization demands components of nanoscale dimensions. The structural properties hold the key role in dictating various properties and hence, performance of the devices. For example, defects control many optical and electronic properties in semiconductors, current density in superconductors, charge transport properties in materials etc. Therefore, for high efficiency and high performance devices, control over structural and morphological aspects is a prerequisite. The structure and morphology of nanoscale films are highly dependent on the deposition techniques and conditions (nature of substrate, its temperature etc.). In addition, interfaces between the various components of the device are crucial for its performance and hold the key to ascertain the working mechanism. For example, nature of interface determines the fate of excitons to be either

stabilized (for efficient LEDs) or destabilized (for efficient PVs) at the interface. Interfacial defects may act as traps for charge carriers and affect (lower) the conductivity. The structural characterization plays a pivotal role in thin film research and essential to realize perspectives for the next generation electronic industry. Thus, there is a need for fundamental understanding using nanoscale characterization techniques to probe bulk, surfaces, sub-surfaces and interfacial regions in thin films. There are numerous surface analytical methods for the characterization of surfaces and sub-surface regions like sputter-ion based X-ray photoelectron spectroscopy, secondary ion mass spectrometry etc. However, these techniques possess the limitation of being destructive in nature.

In this context, slow positron beam based spectroscopy has emerged as a sensitive, non-destructive defect characterization technique for nanoscale films. Implantation of monoenergetic positrons into the materials helps in probing the surface, sub-surface regions and buried interfaces. Together with the sensitivity of positron to defects of atomic order in materials has made beam based PAS a novel characterization tool in the area of thin film technology. There has been a plethora of work related to defect characterization in semiconductor thin films (single and multilayers) [Zhao et al., 1996; Brauer et al., 2002; Ferragut et al., 2010], thin high k-dielectric films on Si substrates [Uedono et al., 2007], metal-oxide semiconductor (MOS) [Uedono et al., 1988] and Si/SiO₂ interfaces [Kauppinen et al., 1997]. The vacancy defects, structural defects like grain boundaries and free volume, positron kinetics at the interfaces between different materials are some of the properties probed using slow positron beam spectroscopy. All these work relate to silicon or compound semiconductors materials.

In the present work, slow positron beam based spectroscopy has been utilized for microstructural characterization of nanoscale organic semiconductor (OSC) films. In contrast to the previous studies on inorganic semiconductors thin films, the present work

is the first report on the microstructural characterization of sub-surface regions and interfaces in nanoscale OSC films. The field of organic electronics has developed vastly in the past two decades due to its promise for low cost, light weight, flexible, versatility of chemical design and synthesis and ease of processing. However, charge mobility in OSC materials is far lower than the inorganic ones. Therefore, efforts are being made to achieve best possible mobility in these materials. Analogous to conventional inorganic semiconductors, the performance of OSC devices (organic field-effect transistor, organic light emitting diodes, photovoltaic cells etc) is directly related to structural properties like molecular packing, crystallinity, growth mode and purity. Various properties of organic devices viz. charge carrier mobility and opto-electronic property are highly dependent on the properties of both the active layer (OSC) and the interfaces between various organic and inorganic components of the devices. Since most of the organic molecules have large anisotropy in their shape and structure, good quality film is a challenge and essential in order to make best use of these molecules for organic electronic devices. The growth mode and orientation of molecules depends on the interaction between the substrate and the molecules as well as between two molecules. There are studies indicating the detrimental effect of structural defects on the opto-electronic properties of the devices [Zanfolim et al., 2010]. Therefore, in order to achieve best possible performance, it is critical to understand and characterize growth and nucleation modes of organic molecules under different conditions. In addition to molecular packing/orientation in active layers, interface properties are also crucial for high efficiency and stability of the devices. The charge transport across the interface between various organic and inorganic components (e.g. source/drain in OFETs) and light absorption/emission (OLEDs) characteristics of the device are believed to be influenced by structural and electronic properties of the interface. Interfacial properties can be tailored by wettability or adhesion between

different materials or modifying the electronic structure of the materials. For example, the dielectric interface (between dielectric and organic layer) is modified by polymers or self-assembled monolayers (SAM) which has influence on the growth behavior of OSC molecules. In the context of characterization of organic devices, depth profiling using slow positron beam has great potential owing to its capability to probe sub-surface regions and buried interfaces at nanoscale. Depth profile studies using slow positron beam open an avenue for the characterization of interfaces without the need of gate electrode in the case of electronic devices.

The present study mainly concentrates on the investigation of nanostructural variations as a function of varying deposition conditions (nature of substrate, deposition temperature and post deposition annealing) and the defect structure at the interfaces between different organic and inorganic components of multilayer heterostructures. Depth profile study in the case of single layer films has shown the influence of the nature of substrate and deposition temperature on the growth morphology of metal Phthalocyanine films. The *S*-parameter and positron diffusion length have been indexed to examine the structural variations. Defect depth profile study has indicated the presence of structural inhomogeneities across the depth in the case of annealed OSC films. Post deposition annealing is expected to improve the nanostructure (ordering of molecules) of the room temperature grown film. Deposition at lower temperatures is required in the case of materials which can decompose at higher temperatures. The study have indicated that post deposition annealing may not provide a defect free microstructure/homogeneously ordered films. Another interesting observation is the charge carrier mobility (determined from current-voltage characteristics) in OSC films which is seen to be comparable to positron mobility, evaluated from the diffusion length of positron in the films. Though the scattering mechanism of electron and positron are different, the dependence of mobility

(in both the cases) on structural defects enables comparison between the mobilities of the two particles. This property can be used to get a prior idea of the charge transport characteristic of the device by measuring the positron mobility in thin film without the actual device configuration (electrode deposition). In the case of heterostructures (different OSC materials viz. *p*- and *n*-type), the interface between organic-organic and inorganic-organic materials dictates charge conduction. The epitaxial relation between different materials results in structural defects which affects the conduction of charge across the interfaces. The ability of positron to get trapped in defects as well as at the interfaces has helped in characterizing interfaces in nanometer thin heterostructures. Possible effect of electric field present at these interfaces (especially organic-organic) has also been examined. In organic field-effect transistor, interface between the dielectric material and OSC is critical for the charge conduction between the source and drain. Dielectric surface modification allows controlling the structure and morphology of OSC film and the interfaces. The structural characteristics (defects/morphology) of the interface of the OSC film grown on silicon substrate with native and thermally grown oxide (SiO_2/Si) as well as surface modified SiO_2/Si have been studied. The influence of surface roughness on the structural characteristics of the grown films as well as interfaces has been examined.

CHAPTER-II

Experimental Techniques and Data Analysis (Positron annihilation spectroscopy)

Techniques in Positron annihilation spectroscopy

PAS comprises of different techniques which provide information about various properties of the material through energy and time domain measurements of annihilation γ -rays. These techniques differ primarily in the manner of detecting the γ -rays and subsequent analysis of the spectrum. Positron lifetime spectroscopy (PALS), Doppler broadening spectroscopy (DBS), Coincidence Doppler broadening spectroscopy (CDB), Age-momentum correlation (AMOC) and $3\gamma/2\gamma$ annihilation spectroscopy are the techniques in PAS. The conventional measurements using ^{22}Na source provide bulk information about the material whereas, depth dependent properties can be studied using slow positron beam. In this thesis, conventional PALS and DBS techniques are used for the study of phase transitions in nanodroplets and beam based DBS is mainly used for the study of microstructure of thin films and porous membranes. Details of these techniques and corresponding data analysis are described in this chapter. Other techniques used in the present thesis work include Nuclear magnetic resonance, dielectric relaxation spectroscopy, electrical conductivity (current-voltage) measurement, X-ray reflectivity and conventional characterization techniques *viz.* differential scanning calorimetry, Fourier transform infra-red spectroscopy, grazing incidence X-ray diffraction, thermogravimetric analysis and atomic force microscopy. These techniques are described in the relevant chapters.

2.1. Positron sources

2.1.1. Conventional techniques

The most suitable and widely used choice for conventional measurements is radio-isotope based sources. The choice of the source depends upon which PAS technique is used. ^{22}Na is the most common choice of radioisotope positron source in PALS and AMOC due to its relatively high positron yield of 90.4%, fairly long half-life (2.57 years)

and appearance of 1275 keV prompt γ -ray almost simultaneously with the emission of positron that serves as start signal in the PALS and AMOC experiments. The decay scheme of ^{22}Na is shown in Figure 2.1 [Firestone et al., 1999]. ^{22}Na is not the best choice for DBS as this technique does not require any prompt γ -ray which otherwise, adds to the background counts. However, it is the most commonly used source for PALS and DBS measurements.

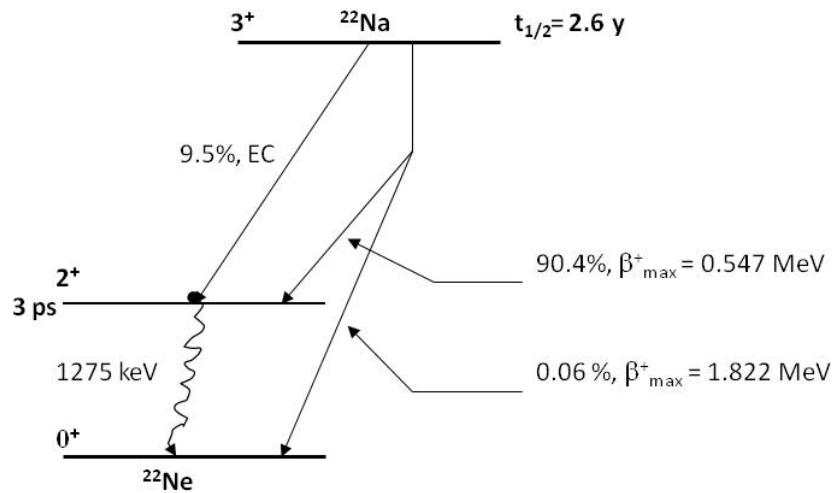


Figure 2.1: The decay scheme of ^{22}Na

^{22}Na positron source has been obtained from the Board of Radiation and Isotope Technology (BRIT), India in carrier free solution of $^{22}\text{NaCl}$. The solution of $^{22}\text{NaCl}$ was deposited drop by drop onto a 7.0 μm thick polyimide film (kapton[®]) till the required activity is achieved and the active area gets dried. The active area was covered with an identical film and edges were sealed with aluminium foil to prevent the leakage of activity. The activity of source used in PALS and DBS measurements was ~ 10 μCi . The positrons emitted from ^{22}Na source have an energy distribution which ranges from zero to 0.54 MeV and has maximum at 0.19 MeV as shown in Figure 2.2. The implantation profile of positrons in the sample is an exponentially decaying function based on experimental observations. According to this, the intensity of positrons at a depth x in the

sample is given by $I(x) = I(0) \exp(-\alpha x)$, where α is the absorption coefficient of the material for positrons and is given by $\alpha = (16 \pm 1) \rho E_{\max}^{-1.43} \text{ cm}^{-1}$ [Brandt and Paulin, 1977]. Here ρ is the density of the material in g/cc and E_{\max} (β_{\max}) is in MeV. The mean implantation depth of positron in the material is α^{-1} . Therefore, the range of positrons implanted into the sample has to be calculated prior its placement within the sample and accordingly the thickness of the sample should be chosen. In the study of nanodroplets, sealed source was embedded into the sufficient amount of powdered sample, ensuring no escape of positrons from the sample.

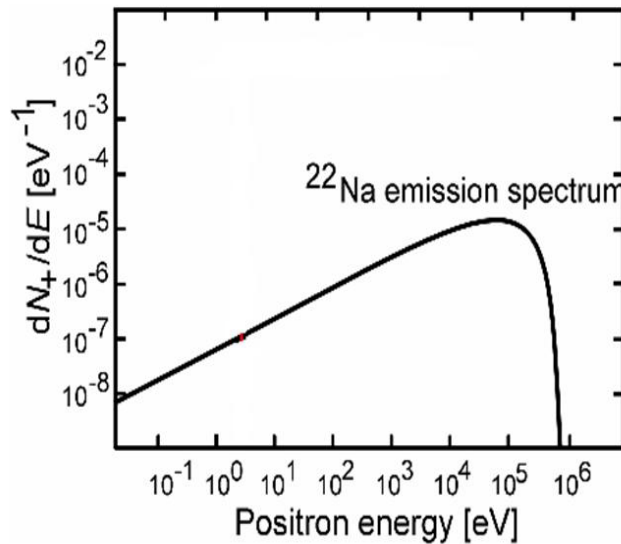


Figure 2.2: The positron energy spectrum in ^{22}Na Decay

2.1.2. Beam based techniques

For depth dependent measurements, positrons from slow positron beam were used which can provide monoenergetic positrons of varying energies. In the present thesis work, depth profile studies in organic semiconductor thin films (single and multilayer) and characterization of pore architecture in porous membranes were carried out using slow positron accelerator (beam) at Radiochemistry Division (SPARC), BARC, Mumbai

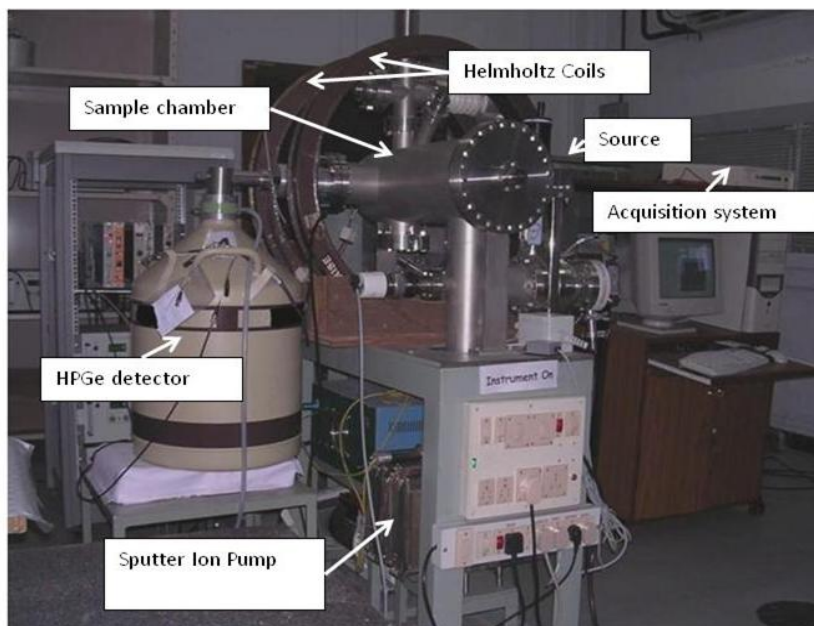


Figure 2.3: *Slow positron accelerator at Radiochemistry Division (SPARC), BARC, Mumbai.*

(Figure 2.3). The beam facility is based on radioisotope ^{22}Na (50 mCi) positron source. The monoenergetic beam of positrons is obtained by the combination of moderator, electric and magnetic field assembly and transported to the target chamber. The positrons emitted from radio-isotope are moderated using $1\ \mu\text{m}$ thick single crystal of tungsten, W [0 0 1], which has negative work function for positrons and thus, provides positron of energy equal to the work potential of tungsten. In the present beam, moderator is biased to a positive voltage, 200 V and subsequent focusing *via* electrostatic Einzel lens and transport with the help of magnetic field is optimized for 200 eV positrons. The focused beam of positron from Einzel lens is made to transport to the target with the help of magnetic field assembly comprising of bend solenoid and Helmholtz coils. The energy of positrons is varied by the application of negative voltage to the target. This beam can provide positrons in the energy range of 200 eV to 50 keV.

The implantation profile of monoenergetic positrons follows the Makhovian distribution, given as,

$$P(z) = m \frac{z^{m-1}}{z_o^m} \exp \left[- \left(\frac{z}{z_o} \right)^m \right] \quad (2.1)$$

where, z_o is the function of positron incident energy and given as, $z_o = 1.13 \langle z \rangle$, $\langle z \rangle$ is mean implantation depth of monoenergetic positrons of energy E is given as,

$$\langle z \rangle = \frac{A}{\rho} E^n \quad (2.2)$$

where, $\langle z \rangle$ is the mean implantation depth (nm) and ρ is the density of material (g/cc). The parameters A and n are material dependent constants. The parameters A and n are usually taken as 40 and 1.6, respectively.

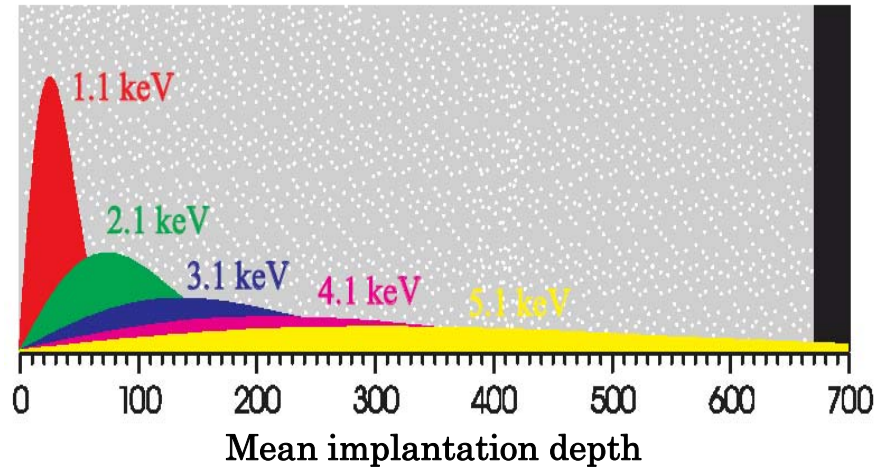


Figure 2.4: Positron implantation profile on a film of density 1 g/cc (figure taken from reference [Gidley et al., 2006])

The positron thermalization and diffusion lead to the observed implantation profile (Figure 2.4) which spreads from the surface to roughly twice the mean implantation depth. Due to the spread in implantation profile at higher incident positron energies, best resolution is achieved at low energies (shallow implantation depths).

2.2. Positron annihilation lifetime spectroscopy

2.2.1. Lifetime spectrometer

The lifetime of positron in the material is measured by the distribution of the events, each event being the time interval between the emission of 1.276 MeV photon (birth signal of the positron), emitted almost simultaneously with the birth of the positron and the emission of 0.511 MeV photon resulting from the annihilation of positron in the medium using fast-fast coincidence setup. A schematic of the fast-fast coincidence setup is shown in Figure 2.5. The fast-fast coincident setup employs a pair of scintillation detectors along with photo multiplier tubes (PMT), two constant fraction differential discriminators (CFDD), a time delay unit, a fast coincidence unit and a time-to-amplitude converter (TAC).

The source sample assembly was kept between the two scintillation detectors. The scintillators detectors are provided with photomultiplier tubes (PMT) for the processing of the signal. The energy and timing information are obtained from the same output of the PMTs using constant fraction differential discriminator (CFDD) unit. The 1276 keV and 511 keV γ -rays signifying the birth and annihilation (death) of positron, respectively, are picked up by two scintillation detectors. The timing *pick-off* signals are communicated to the TAC through CFDDs and the respective energy signals reach the coincidence unit through the single channel analyzers (SCAs) of CFDD. The coincidence unit checks for the 'genuineness' of the events and in the case of true coincident events, the TAC is strobed by the output pulse of coincidence unit to produce a signal which is equivalent to the time difference between the detection of 1276 keV and 511 keV γ -rays. The magnitude of this signal is converted to pulse height and recorded in a multi-channel analyzer [Pujari et al., 1992]. The time calibration of the multi channel analyzer was chosen depending on the range of the lifetimes required to be measured. Most of the work in this thesis required measuring Ps lifetime component (1-10 ns), therefore, time calibration used was 25 ps/channel. The time calibration of the spectrometer was

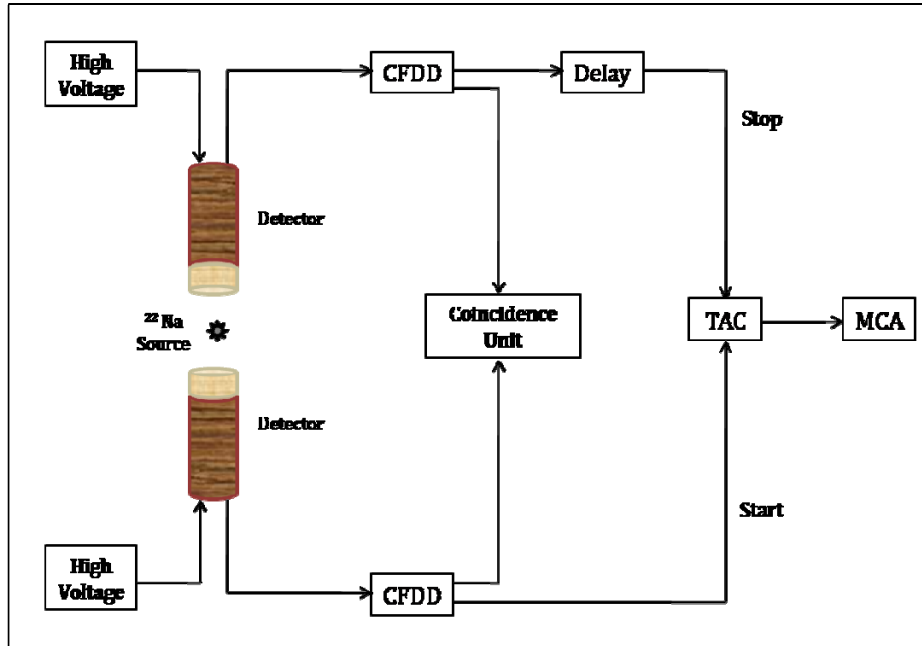


Figure 2.5: Block diagram of the positron lifetime spectrometer

performed from the measured lifetime spectrum of ^{60}Co γ -rays, keeping the discriminator levels of the CFDDs same as required for positron lifetime measurements using a ^{22}Na source. The delay on the stop detector signal was varied systematically using a nano second delay unit. The centroids of these peaks were plotted as a function of delay time introduced on the stop detector and slope of this line gives the time calibration of the spectrometer. The time calibration can also be calculated by dividing the TAC range (e.g. 50 ns) with number of channels in MCAs (e.g. 2K or 4K).

^{60}Co emits the two γ -rays of 1173 keV and 1332 keV within a time of less than 1 ps. These two γ -rays are assumed to be emitted simultaneously and the peak shape of the lifetime spectrum acquired for these two γ -rays is assumed to be Gaussian. The response function (time resolution) of the spectrometer is obtained by measuring the time difference between these two γ -rays. The lifetime spectrum of ^{60}Co is shown in Figure 2.6. The time resolution of the spectrometer is estimated from the width of this peak. The

time resolution of present spectrometer was of the order 285 ps with BaF₂ scintillations detectors.

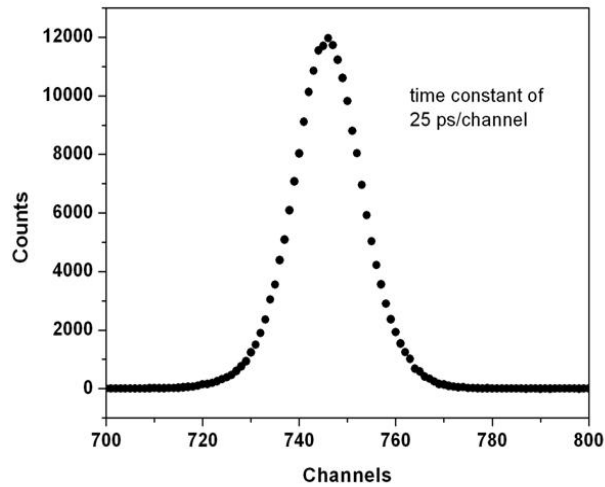


Figure 2.6: The lifetime spectrum measured using ⁶⁰Co γ -rays for obtaining the time resolution of the positron lifetime spectrometer.

2.2.2. Lifetime spectrum analysis

Positron lifetime spectrum consists of sum of decaying exponentials convoluted with the instrument's time resolution function. Each decaying exponential represents a positron state in the medium. Each spectrum consists typically a million counts to provide sufficient statistics for the extraction of lifetime components. The positron lifetime spectrum is given as,

$$F(t) = \sum_{i=1}^k \frac{I_i}{\tau_i} e^{-\frac{t}{\tau_i}} \quad (2.3)$$

where, $F(t)$ represents the number of counts at time t , k is the number of exponential decays, τ_i is the lifetime of the i^{th} component, I_i is the corresponding intensity and B is the constant background. The routine PATFIT-88 having programs RESOLUTION and POSITRONFIT have been used for the discrete lifetime components analysis [Kirkegaard et al., 1981 and 1989; Kirkegaard and Eldrup, 1972]. The positron lifetime spectrum defined by Eq. 2.3 is convoluted with the resolution function of the spectrometer which is

generally approximated by a sum of Gaussians or a Gaussian with exponential tails. A single Gaussian distribution, $G(t)$, centered at t_0 is generally used for the deconvolution is given as,

$$G(t) = \frac{1}{\sigma\sqrt{2\pi}} \exp\left[-\left(\frac{t-t_0}{2\sigma}\right)^2\right] \quad (2.4)$$

where, σ represents the standard deviation of the Gaussian and is related to full width half maximum (*FWHM*) of the Gaussian as,

$$FWHM = 2\sqrt{2 \ln 2} \sigma \quad (2.5)$$

The convoluted lifetime spectrum is represented as,

$$F(t) = \sum_{i=1}^k \frac{I_i}{2} \cdot \exp\left[-\frac{t-t_0 - \frac{\sigma^2}{4\tau_i}}{\tau_i}\right] \left[1 - \operatorname{erf}\left(\frac{1}{2\sigma\tau_i} - \frac{t-t_0}{\sigma}\right)\right] \quad (2.6)$$

The count distribution in lifetime spectrum is integration of the time interval into one fixed channel, represented as,

$$N(t) = \int_{t-\Delta t}^{t+\Delta t} F(t)dt + B \quad (2.7)$$

where, $N(t)$ is the number of counts in the channel corresponding to time ' t ', $2\Delta t$ is the channel constant and B is the constant background. The value of σ is taken from the fitted resolution function of ^{60}Co spectrum or it is determined from a reference spectrum like Silicon single crystal having a well defined positron lifetime (218 ps) using the routine RESOLUTION. The background in the above model is taken as the average counts per channel at the far end (no contribution from decaying exponential) of the lifetime spectrum. A list of parameters τ_i , I_i , t_0 , σ and B is obtained after the analysis using POSITRONFIT [Kirkegaard et al., 1989] model.

Source correction

The positron annihilation in the kapton foil (sandwiching the source) and within the source itself contribute to the lifetime spectrum and need to be subtracted from the spectrum to get the lifetimes corresponding to positron states in the material. The scattering of positrons from the sample also contributes to the fraction of positrons annihilating within the source [Djourelou and Misheva, 1996]. The source correction for the particular source used, can be calculated from the measured lifetime spectrum of a silicon sample using routine RESOLUTION. The lifetime of positron in silicon is fixed as 220 ps and the other obtained positron components are taken as the source components. For Kapton (7 μm thickness) one positron lifetime of 390 ps with 7 % intensity is generally obtained. The source correction thus obtained is used in POSITRONFIT while analyzing the actual lifetime spectrum of the sample.

2.3. Doppler broadening spectroscopy

2.3.1. Doppler broadening set up

A typical block diagram of Doppler broadening set up is shown in Figure 2.7. DBS involves measurement of energy spectrum of 511 keV annihilation γ -ray. High purity Germanium (HPGe) detector with best energy resolution has been employed for Doppler broadening measurements. The annihilation signal is amplified by the combination of preamplifier and spectroscopy amplifier and is fed into multi channel analyzer (MCA). The MCA was energy calibrated using the standard multi γ -ray sources of ^{152}Eu and ^{133}Ba . The energy resolution of the detection system was 2.0 keV at 1332 keV photopeak of ^{60}Co . For each Doppler broadening measurement approximately half a million counts were acquired under the 511 keV annihilation radiation.

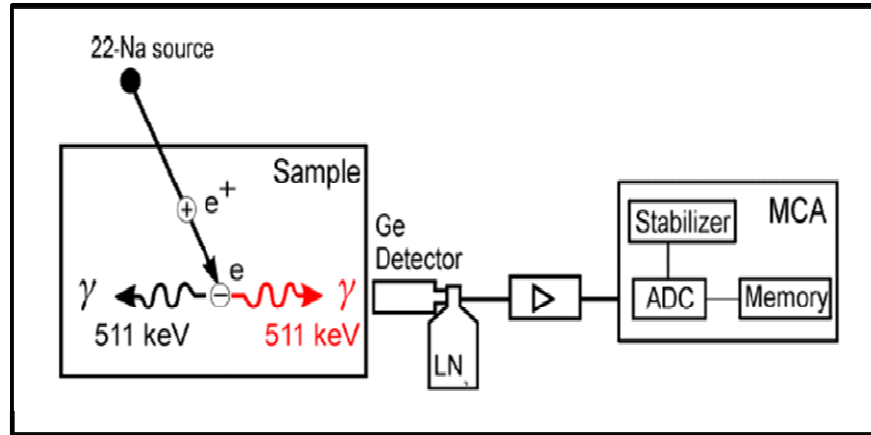


Figure 2.7: Block diagram of Doppler broadening spectroscopy set up

2.3.2. Data analysis

The Doppler broadened spectrum is generally convoluted with detector's resolution function (Gaussian function). However, for relative measurements, resolution function need not be deconvoluted from the spectrum. In the present work, the deconvolution of the detector resolution function was not carried out. The Doppler broadened spectrum is characterized in term of *line shape* and *wing* parameters, which contribute to low and high momentum distribution of the annihilation electrons, respectively. The *line shape* parameter, *S*-parameter and *wing* parameter, *W*-parameter were evaluated from the measured spectra using the program SP version 1.0 [SP-1] [Dryzek, SP 1.0; Dryzek and Quarles, 1996]. The apparent background on left of 511 keV is more compared to right, partly because of incomplete charge collection and scattering in the sample. Additional background contribution comes from the Compton scattering of 1276 keV γ -ray. In this program, the background is taken as a step function. The *S*-parameter is defined as the ratio of the central area (A_s) to the total area under the spectrum (A_t) as,

$$S = \frac{A_s}{A_t} = \frac{\int_{511-\Delta E}^{511+\Delta E} N(E)dE}{\int_{-\infty}^{+\infty} N(E)dE} \quad (2.8)$$

where, $N(E)$ represents the counts in the spectrum at energy E . The W -parameter is defined as the fractional area in the wing region of the Doppler broadened spectrum and signature of the annihilations with core electrons of the surrounding medium. It is defined as,

$$W = \frac{A_w}{A_t} = \frac{\int_{511-E_2}^{511-E_1} N(E)dE + \int_{511+E_1}^{511+E_2} N(E)dE}{\int_{-\infty}^{+\infty} N(E)dE} \quad (2.9)$$

The values of ΔE , E_1 and E_2 for evaluating S and W -parameters were chosen in such a way that the value of S -parameter is in the range of 0.50 or corresponding to 1.5 -1.9 keV broadening of the annihilation peak and the value of W -parameter is in the range of 10^{-2} [Campbell, 1977]. A schematic representation of evaluating the line shape parameters in the Doppler broadening spectroscopy is shown in Figure 2.8.

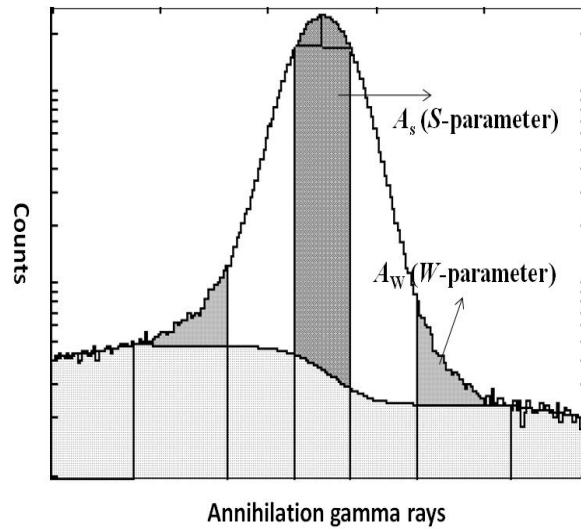


Figure 2.8: Schematic representation of evaluation of Doppler broadening parameters from DBAR spectrum

S-W correlation analysis

The simultaneous analysis of S and W -parameter (S - W correlation) helps in recognizing positron annihilation states in the materials [Clement et al., 1996]. The correlated measurement of S and W -parameters is sensitive to type and the nature of trapping site or defects in the material. Plotting S and W -parameters as a trajectory in the S - W plane and using positron energy as the running parameter, provides a powerful approach to interpret the depth profiling data especially in term of identification of trapping layers [Asoka-Kumar et al., 1994].

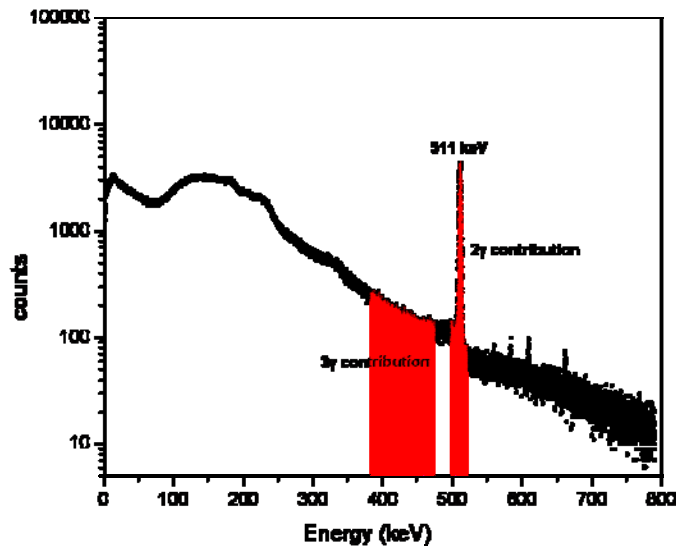


Figure 2.9: *The energy spectrum of positron/Pos annihilation*

$3\gamma/2\gamma$ ratio analysis

The $3\gamma/2\gamma$ ratio is calculated from the annihilation spectrum of positron and Ps. Annihilation into two photons (2γ) produces a peak at 511 keV and Compton scattered events from 0-341 keV. However, annihilation into three photons (3γ) produces a uniformly increasing energy distribution from 0-511 keV. Therefore, the total energy spectrum is a combination of 3γ and 2γ events as shown in Figure 2.9. The 2γ and 3γ contributions are evaluated from an energy window set around 511 keV and from the integrated counts within an energy window 385-485 keV, respectively. The $3\gamma/2\gamma$ ratio

profile is a sensitive index to characterize pore architecture of porous membranes with large size and interconnected pores [Gidley et al., 2006; Petkov et al., 2003].

2.4. Depth profiling using slow positron beam

Defect depth profiling in thin films (single and multilayers) and pore architecture in polymer membranes have been studied using slow positron beam at Radiochemistry Division, BARC, Mumbai. Doppler broadening measurement has been carried out as a function of positron incident energy to probe different depths of the samples. The energy of the positrons was varied by applying required negative bias voltage to the sample. The implanted positron follows Makhovian distribution in the sample [Schultz and Lynn, 1988]. The implanted positrons after thermalization, diffuse into the sample prior to the annihilation. The average distance traversed by the positron before annihilation is termed as positron diffusion length (L_+) which can be correlated to the mobility of positron. The positron mobility essentially refers to mean free path of positron in the system. The depth dependent Doppler broadening measurement (S and W -parameters) and $3\gamma/2\gamma$ ratio were used to evaluate positron/Ps diffusion length in the material. An HPGe detector having 30% efficiency and 2.0 keV resolution at 1332 keV (^{60}Co) placed at 90° to the target position and coupled to a 4k MCA was used for the measurements. The voltage applied to the target was varied and Doppler broadening spectra at different positron energies (implantation depth) were recorded. The line shape S -parameter calculated within ~ 2.0 keV energy window centered at 511 keV to the total photo peak area was evaluated as a function of positron energy. The S -parameter as a function of positron energy is termed as S - E profile of the sample. The wing parameter, W was evaluated from ~ 5.0 keV energy window in the wing region of Doppler broadened annihilation peak. The S and W -parameters with energy as a running parameter were used to get S - W correlation curve. The ratio of $3\gamma/2\gamma$ annihilation was evaluated as a function of depth from the annihilation

γ -ray spectrum. The ratio of integrated counts in the energy range 385 to 485 keV to total area under the photo peak of 511 keV was used to calculate $3\gamma/2\gamma$ ratio. The variation of $3\gamma/2\gamma$ with positron incident energy gives information about the fraction of positron/Ps reemitted from the sample at different depths. The curvature of $S-E$ and $3\gamma/2\gamma$ profile is used to evaluate mobility of positron/Ps in the material using variable energy fit analysis (VEPFIT) as discussed in the next section.

2.4.1. Variable Energy Positron Fit (VEPFIT) analysis

The depth dependent characteristics can be obtained by extracting relevant positron annihilation parameters as a function of depth or positron implantation energy. This is achieved by fitting $S-E$ or $3\gamma/2\gamma$ profile obtained from beam measurements using VEPFIT analysis [van Veen et al., 1990]. It involves solving positron diffusion equation (Eq. 2.10) taking into account the positron diffusion, trapping and annihilation in the medium. The positron diffusion equation is given as,

$$D^+ \frac{d^2 c(z)}{dz^2} - \frac{d}{dz} (v_d c(z)) + I(z) - \kappa_t n_t c(z) - \lambda_b c(z) = 0 \quad (2.10)$$

where, $c(z)$ is the time averaged positron density at a certain depth z below the solid surface, v_d is the drift velocity of positrons, $I(z)$ is the positron stopping rate at depth z , n_t is defect density, κ_t is rate constant for positron trapping at defects, λ_b is the bulk annihilation rate and D^+ is positron diffusion coefficient. The drift velocity, $v_d = \mu \zeta$, is the function of electric field ζ present in the sample and mobility μ of positron in the sample. The implantation profile of positrons is parameterized by Makhovian profile (Eq. 2.1).

The fast non-iterative calculation scheme is used to solve the diffusion equation to calculate the time averaged positron density in the medium. The average positron density is then used to extract diffusion length and the fraction of positrons annihilating at various

depths taking into account various boundary conditions for the diffusing positrons. The total fraction of positrons annihilating at a particular depth, $T_i(E_k)$ given as,

$$T_i(E_k) = \sum_{j=1}^n P_j(E_k) t_{ij} \quad (2.11)$$

where, t_i is the positrons that are surface-emitted or trapped in different depth intervals.

Using $T_i(E_k)$ values, S -parameter as a function of positron energy E_k is defined as,

$$S(E_k) = \sum_i^n S_i T_i + T_{surf} S_{surf} \quad (2.12)$$

Different models have been provided in VEPFIT analysis to fit the data for variety of material characteristics. The choice of input parameters varies depending upon the model chosen. In the case of thin films/heterostructures, Model # 5 is mainly used which can provide S -parameter, L_+ and layer thickness for each layer of the system. In the present work, model# 5 has been used to fit S - E profile in organic semiconductor (OSC) thin films wherein, multilayers were chosen to fit the data. This has not only provided positron annihilation parameters in each layer but also, helped in the identification of interfaces between various layers of the multilayer system. The inputs for the fitting analysis were S -parameter as a function of energy (S - E profile), guess value of S -parameter, L_+ , layer boundary and density of each layer. The semi-linear fitting procedure is carried out to fit the experimentally measured S - E profiles through an iterative procedure. In the case of pore architecture study in polymer membrane, instead of S - E , $3\gamma/2\gamma$ profiles were used for the fitting procedure to obtain Ps diffusion length which was then correlated to pore architecture of the porous membrane.

Other conventional characterization techniques like X-ray diffraction, Fourier transform infra-red spectroscopy, thermogravimetric and evolved gas analysis and differential calorimetric scanning have been used for nanodroplets study. The structural and dynamical properties of confined fluids have been studied using nuclear magnetic

resonance and dielectric relaxation spectroscopy. The experimental details are described in chapter III. In the case of pore architecture study in membranes, scanning electron microscopy has been used for surface characterization. The transport properties of the membranes have been investigated from the permeability of Am^{+3} and Pu^{+3} ions through the membranes. In OSC thin film study, atomic force microscopy and grazing incidence X-ray diffraction have been used for the investigation of surface morphology and crystallinity, respectively. The electrical properties have also been measured using current-voltage (I - V) characteristics to calculate mobility of charge carriers in the films. In addition to defect depth profiling using slow positron accelerator, electron density profiling using X-ray reflectivity has also been carried out for the investigation of nanostructure in organic semiconductor thin films. The experimental details are described in chapter V.

CHAPTER-III

Nanodroplets: Phase transitions in nanoconfined fluids

Nanoconfinement significantly affects structural and dynamical properties of the fluids owing to the combined effect of reduced dimensionality, surface forces and finite size. This includes nature of phase transition (first order vs. continuous), direction of shift in freezing/melting point, origin of hysteresis, structural change of condensed phase and effect on thermodynamical parameters. In this context, shift in the freezing/melting behavior of fluids confined in nanodomains has been a subject of research for the last few decades. Classical thermodynamics (Gibbs-Thomson equation) has been invoked to explain the observed shifts in the freezing/melting point of confined fluids. However, in the limit of small and highly inhomogeneous systems (nanopores), a deviation from Gibbs-Thomson equation has been observed. This has been attributed to; (i) extremely high surface to pore volume ratio, (ii) not well defined surface energy and, (iii) deviation of melting enthalpy and density of the phases from their bulk values. Therefore, in nanodomain, it is important to consider the surface/interfacial effects through a description of the confined phase at the molecular level. The main stimulus behind the ongoing research in the field has been to explore the effect of pore size, its geometry and interfacial interactions on the properties of confined phases. In addition, emergence of new phases/properties at nanoscale, otherwise not prevailing in the bulk has also attracted the attention in this area.

Numerous studies have been carried out to explore the effect of pore size, interfacial interaction between confining matrix and the confining phase. However, a clear picture of the contribution of fluid-wall interaction separated from the finite size effect on the freezing/melting properties has not been evolved in any of these studies. It may be due to the reason that the relative contributions of geometrical confinement and the fluid-wall interaction are difficult to separate. Also, the topology of the confining matrix plays a crucial role in addition to these effects. Different techniques have been

employed to study the phase transitions and properties of confined fluids. For example, thermodynamic properties are mainly studied using calorimetry, diffraction techniques for structure and density while scattering and relaxation spectroscopy for dynamical properties. However, the existence of inhomogeneous phases, density variation and most important, the small amount of sample (confined fluid) put limitation and complexities to interpret the results. Hence, the comprehensive study using variety of techniques and confining geometries are required to get better insight into the phenomena.

In this context, positron/Ps has emerged out as a sensitive and in situ probe to study the phase behavior of confined fluids. Together with the ability of positron/Ps to probe very small pores, the *pick-off* rate of *o*-Ps is sensitive to surface chemistry, change of density and free volume following freezing/phase transition. When the pores are filled with liquid, *pick-off* rate depends on the electron density as well as effective surface tension of the confined fluid. In addition, when the volume fraction of the pores is high, a significantly larger part of positron will interact with the liquid (or the solid, following freezing) leading to an alteration in the intensity and life-time of *o*-Ps. Phase transitions are manifested in the change in momentum distribution too, which can be indexed using Doppler broadening *S*-parameter (solid and liquid state annihilation have different momentum distribution). Free positron is also expected to behave like Ps and hence, can be used to index phase transitions especially in the case when Ps yield is low.

In addition to positron annihilation spectroscopy (PAS), different techniques in nuclear magnetic resonance (NMR) have also been widely used to monitor the dynamics of fluid molecules trapped in the pores or adsorbed on surfaces. The dynamical information can be utilized to study the phase transition behavior of confined fluid molecules. The spin-spin relaxation time (T_2) and chemical shift analysis are mainly used to index phase transitions. The spin relaxation process is governed by the average

distance between the spins, which, in a fluid, is determined by the state of mobility of the molecules embodying the spins. In a porous medium, fluid molecules are in various states of compartmentalization owing to various pore sizes, and their rigidity (mobility) is affected in various degrees by the temperature of the surroundings. If the molecular motion is fast, the effectiveness of spin-spin interaction is diminished, owing to the averaging of the spin-spin dipolar interaction, and the resulting T_2 is long. On the other hand, when molecules are rigid, as in the pores whose size is comparable to that of the molecules, or when the temperature is sufficiently low, the averaging is not so effective and T_2 becomes very short. T_2 in fluid state is about two to three orders of magnitude longer than that in the rigid or frozen state, if the pore size is sufficiently large compared to the size of the molecule. If the majority of fluid molecules are in the state of high mobility, the measurement of T_2 yields an exponential decay of magnetization. On the other hand, fluids bound in small pores often exhibit non-exponential decay arising from a combination of different fluid components that are identifiable only by the states of molecular mobilities they are in. Moreover, in the case of relatively rigid molecules, the presence of strong dipolar interaction may also lead to a Gaussian decay. Hence, relaxation time measurement is a sensitive probe to study the phase behavior of confined liquid. In addition, the sensitivity of chemical shift to local magnetic field induced by electronic currents surrounding the molecules is also used as an index to examine the variation of intermolecular interactions and hence, can provide structural information.

The present study mainly aims at understanding the contribution of fluid-wall interaction on the freezing/melting properties of confined liquids. Different techniques viz. PAS, NMR and dielectric relaxation spectroscopy (DRS) have been used to investigate structural and dynamical features associated with the phase behavior of confined fluids. For this, two types of organic liquids viz. ethylene glycol and

isopropanol, differing in the nature of hydrogen bonding were confined in ZSM 5 nanopores (pore size $\sim 5\text{\AA}$). The strength of the interaction between liquid molecules and the confining wall is different, but the topology and the pore size remain identical. Isopropanol [$\text{CH}_3\text{CH}(\text{OH})\text{CH}_3$] has inter-molecular hydrogen bonding and strong attractive interfacial interaction with the pore surface whereas, ethylene glycol [$(\text{CH}_2\text{OH})_2$] experiences both intra- and inter-molecular hydrogen bonding, resulting in the reduction in the strength of interfacial interaction towards the surface. PAS and NMR have been used to investigate change in the freezing/melting point of these liquids under the nanoscale confinement.

The effect of confinement on the phase behavior of water confined in slit like pores of saponite clay has also been studied. Water confined in a nanoscale environment exhibits peculiar properties differing from the bulk such as confined water is unable to grow into a crystalline structure and remains in liquid state becoming increasingly viscous as temperature approaches glass transition. In such a metastable supercooled state, anomalies in thermodynamic properties are seen, showing a power law divergence at a singular temperature $\sim 228\text{ K}$. At very low temperature water can exist in amorphous glassy form and show different amorphous phases depending upon the temperature and pressure. The anomalous behavior of water in confined systems has been attributed to the effect of surface interactions which modify the hydrogen-bonded network of water resulting in the formation of new phases and emergence of transitions otherwise, not prevailing in the bulk. Confinement of water in nano domains is therefore, sometimes regarded as a trick to experimentally assess the bulk water properties within the inaccessible low-temperature region and may provide answers to many open questions concerning the properties of supercooled water. In addition, anomalous dynamical properties have also been observed for supercooled water. In this context, cross over from

non-Arrhenius to Arrhenius behavior at low temperature is a subject of intense debate. Initially, this behavior has been assigned to *fragile-to-strong* transition (FST) of supercooled water. However, recent studies have indicated that the existence of a dynamic cross over is not restricted to water, but, other supercooled liquids as well [Mattson et al., 2009; Hedstrom et al., 2007]. The structural α and β relaxations are also invoked to explain the observed FST [Swenson et al., 2006].

Despite a wealth of research, complete understanding of the origin of such anomalous behavior of confined water is still missing. Understanding the phase behavior, as well as structural and dynamical properties of water, is complex and requires more studies with a variety of confining matrices having a range of pore sizes and different geometries. In addition to this, sensitivity of different techniques can be utilized for a comprehensive study to probe properties of water confined in nanoscale. In the present work, PAS, NMR and DRS together with other conventional characterization techniques have been used to investigate the structural and dynamical aspects associated with the phase behavior of water confined in clay nanopores (interplatelet space). The water confined in interplatelet space is confined only in one-direction (say z-direction) and allowed to move in the other two directions i.e. it can be considered as one-dimensional confined system referred to as 2D confined water.

3.1. Sample preparation

3.1.1. Ethylene glycol and isopropanol confined in ZSM 5 zeolite

Commercially available ZSM 5 zeolite ($\text{SiO}_2/\text{Al}_2\text{O}_3=30$, surface area $380 \text{ m}^2\text{gm}^{-1}$ and pore volume $0.22 \text{ cm}^3\text{gm}^{-1}$) and analytical grade ethylene glycol and isopropanol have been used. No dehydration of ethylene glycol was carried out. ZSM 5 zeolite sample was heated at 573K under vacuum for 7-8 hours to remove adsorbed air and moisture. It was cooled to room temperature and sufficient volume of ethylene glycol/isopropanol, as

the case may be, was injected into the sample (in vacuum) with a syringe so that the entire sample was covered with liquid. The liquid-sample mixture was kept overnight for homogeneous adsorption of liquid into the pores. The sample was then evacuated at room temperature using rotary pump for 10-15 minutes to remove the excess liquid /vapor at bulk surface of the sample.

3.1.2. Saponite clay

Saponite clay containing Mg^{2+} as octahedral cations and Al^{3+} substituting Si^{4+} in the tetrahedral sheet ($Mg^{2+}/Al^{3+}/Si^{4+}$) has been synthesized using microwave assisted radiation heating [Trujillano et al., 2011]. The saponite clay formula targeted was $[Si_7M^{III}_1] [M^{II}_6] O_{20} (OH)_4 [Na_1] \cdot n H_2O$, where $M^{III}=Al^{+3}$, and $M^{II}=Mg^{+2}$. The mixture of sodium silicate with divalent and trivalent cations was prepared in the molar ratios of: $Si/M^{II}=7:6$ and $Si/M^{III}=7:1$. The pH of the reaction mixture was maintained at 10.3 by adding NaOH and $NaHCO_3$. The resultant gel obtained was sealed in a 100 mL Teflon reactor and treated hydrothermally in a microwave furnace at $180^\circ C$, for 7h. The synthesized clay material was washed with de-ionized water to remove the unreacted residues followed by drying at $80^\circ C$ in oven. Saponite is a smectite type of clay having an alumino-silicate layer structure where polymeric sheets of SiO_4^{4-} tetrahedra are linked to the sheets of alumina octahedra. The layers or sheets possess a net framework negative charge, originating from the isomorphous substitution of Si^{4+} by Al^{3+} or Fe^{3+} in the tetrahedral sheets, and by cation substitutions (e.g., Mg^{2+} , Ni^{2+} , Fe^{2+}) in the octahedral sheets. The net anionic framework charge on the sheets is compensated by the presence of suitable charge balancing cations existing in their hydrated forms in interplatelet space. The as-synthesized clay is the hydrated form with water confined between the interplatelet spaces wherein, water is associated with the platelet surface and interplatelet

cations forming hydration layer around the cations. The schematic of typical smectite clay is shown in Figure 3.1.

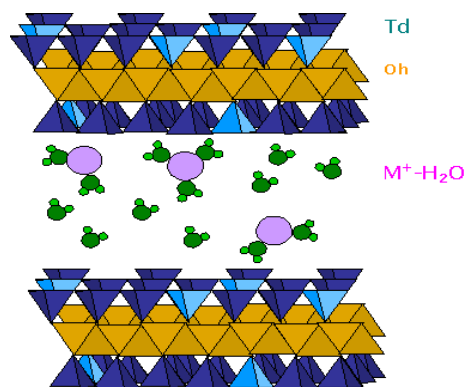


Figure 3.1: Schematic of typical smectite clay (T_d : tetrahedral; O_h : octahedral)

3.2. Experimental techniques

PAS and NMR techniques have been used for the study of phase behavior of Ethylene glycol and isopropanol confined in ZSM 5 zeolite and water confined in saponite clay. In addition to this, in the case of confined water study, X-ray diffraction, thermogravimetric and evolved gas analysis (TG-EGA), attenuated total reflection-Fourier transform infra-red spectroscopy (ATR-FTIR), differential scanning calorimetry (DSC) and dielectric relaxation spectroscopy (DRS) have also been carried out.

3.2.1. X-ray Diffraction

Water confined in saponite clay

The interplatelet spacing of as-synthesized saponite clay has been determined from X-ray diffraction. The measurement was performed using PANalytical MRD system with Cu K_α radiation of wavelength 0.15418 nm. The 2θ scan was carried out from 2° to 70° . The interplatelet spacing of saponite clay obtained from (001) Bragg peak was 15.4 Å. The interplatelet spacing of 15.4 Å includes thickness of the rigid clay platelets and interplatelet distance.

3.2.2. Thermogravimetric and Evolved Gas Analysis (TG-EGA)

Water confined in saponite clay

TG-EGA measurement was carried out using Netzsch Thermobalance (Model No.: STA 409 PC Luxx) coupled to Bruker Fourier transform infra-red (FTIR) system (Model No.: Tensor 27) via a heated Teflon capillary. Simultaneous TG-EGA measurements were carried out individually on accurately weighed samples (about 100 mg) in inert atmosphere by heating from room temperature to 500 K at a heating rate of 10 K min⁻¹. The flow rate of high purity nitrogen was maintained at 100 mL min⁻¹ to transport the volatile products. Nitrogen was also used as a protective gas to the thermobalance at a flow rate of 20 mL min⁻¹.

FTIR system used for the identification of evolved gases through the measurement of IR absorbance in the mid IR region (400 – 4000 cm⁻¹) was equipped with liquid nitrogen cooled MCT detector and low-volume gas cell (8.7 mL) with a 123 mm path length and KBr windows. The adapter head of thermobalance, transfer line and sample cell were heated to a constant temperature of 473 K to avoid condensation of low volatile compounds. FTIR compartment was continuously purged by high purity nitrogen and molecular sieves/silica gel was used to minimize the water and carbon dioxide background in the recorded spectra. The resolution of the collected spectra was set to 4 cm⁻¹ and co-addition of 32 scans per spectrum with a scan speed of 20 kHz was applied. As a consequence, spectra were recorded with a temporal resolution of about 2.5 s, depending on the integration methods.

3.2.3. Attenuated total reflection- Fourier transform Infra-red spectroscopy (ATR-FTIR)

Water confined in saponite clay

A PIKE MIRacle™ Attenuated total reflection (ATR) accessory equipped with a single reflection diamond ATR crystal was used for the analysis of solid samples. The MIRacle accessory was fitted with a high pressure clamp, providing intimate contact between the sample and ATR crystal. The MIRacle ATR accessory utilizes a pre-aligned, pinned-in-place crystal plate design enabling easy exchange of ATR crystal for sampling optimization. FTIR spectrometer (Bruker Tensor 27) was equipped with KBr beamsplitter, DLaTGS (deuterated L-alanine doped triglycene sulphate) detector, sealed and desiccated to minimize purge effects. The samples were placed over ATR crystal and maximum pressure was applied using the slip-clutch mechanism. All spectra were collected at 4 cm^{-1} spectral resolution using sample and background collection time of one minute each. FTIR data analysis was done using Opus (version 6.0) software from Bruker.

3.2.4. Differential scanning calorimetry (DSC)

Water confined in saponite clay

DSC measurements in temperature modulated and unmodulated (conventional) mode were carried out in temperature range from 298-198 K. The conventional scanning was performed by METTLER TOLEDO Thermal Analysis system using argon gas (flow rate 60 ml min^{-1}) in the DSC cell purge. The scanning speed was fixed at 2.0 K min^{-1} . The temperature modulated measurements were carried out using METTLER TOLEDO Thermal Analysis system using argon gas (flow rate 60 ml min^{-1}) in the DSC cell purge. The system allows heating or cooling scans in the modulated DSC regime. The samples were weighed and placed into standard Al sample pans with crimped lids. A matching empty sample pan with crimped lid was used as the reference. The scanning was performed by first cooling the samples from room temperature down to 198 K and then starting the heating ramp to room temperature at a rate 2 K min^{-1} . In order to obtain

accurate and reproducible results, three experimental parameters, underlying heating rate, modulation amplitude and modulation period were carefully selected. The modulation period was varied from minimum value of 15 seconds to maximum value of 30 seconds with modulation amplitudes of 1 K (+/- 0.5 K).

3.2.5. Positron annihilation spectroscopy

3.2.5a. Ethylene glycol and isopropanol

Temperature dependent positron lifetime and Doppler broadening measurements were carried out in the temperature range from room temperature to 245 K in the case of ethylene glycol and from 210 to 170 K in the case of isopropanol, in both cooling and heating cycle. For low temperature measurements, the sample (powdered form and hermetically sealed) along with the source ($\sim 8 \mu\text{Ci}$ deposited on thin Kapton foil) was mounted on the cold head of APD closed cycle helium refrigerator. Temperature variation was carried out in 1 K interval with an accuracy of ± 0.01 K. Doppler broadened annihilation radiation measurements were carried out using an HPGe detector having resolution of 1.8 keV at 1332 keV photo peak of ^{60}Co . The shape parameter, namely, S -parameter defined as the ratio of the number of counts falling in a fixed energy window centered at 511 keV to the total number of counts, was evaluated. The experiments were repeated in different samples (both cooling and heating cycle) and the reproducibility of the data was seen to be good in both the liquids confined in zeolite. Positron annihilation lifetime measurements were carried out using BaF_2 scintillation detectors in a fast-fast coincidence system. The time resolution measured with a ^{60}Co source was 300 ps and the time calibration was 25 ps per channel. Data analysis was carried out using PATFIT program [Kirkegaard et al., 1981 and 1989; Kirkegaard and Eldrup, 1972].

3.2.5b. *Water confined in saponite clay*

Low temperature positron lifetime and Doppler broadening measurements were carried out in the same experimental set up (APD closed cycle helium refrigerator) and the sample geometry as for ethylene glycol and isopropanol. The temperature variation was carried out in the range of 200-300 K in both heating and cooling cycles. The temperature variation was carried out in 2 K interval with an accuracy of ± 0.01 K. Doppler broadened annihilation radiation measurements were carried out using an HPGe detector having resolution of 2.2 keV at 1332 keV photo peak of ^{60}Co and the variation of S -parameter was measured. Positron annihilation lifetime measurements were carried out using BaF_2 scintillation detectors in a fast-fast coincidence system. The time resolution measured with a ^{60}Co source was 295 ps and the time calibration was 25 ps per channel. Data analysis was carried out using PATFIT program.

3.2.6. Nuclear magnetic resonance

NMR measures the absorption of electromagnetic radiation during the transition from spin states of atomic nuclei. In NMR experiments, a constant strong magnetic field H leads to splitting of energy levels of the nuclei depending upon the spin states. The energy difference between the two levels is given by,

$$\Delta E = \frac{\gamma \hbar H}{2\pi} \quad (3.1)$$

where, γ is a constant termed as gyromagnetic ratio of the nucleus defined as,

$$\gamma = \frac{q}{2m} \quad (3.2)$$

where, q and m represent the electronic charge and mass of the nucleus, respectively. An oscillating field B_1 applied to the sample leads to absorption of energy, resulting in excitation of the nuclei. The energy absorbed by a given nucleus, ΔE depends on the local

magnetic field experienced by the nucleus. The local magnetic field is the resultant of applied field and the field created by electron current in the molecular orbital. Therefore, resonance frequency or ΔE depends on the electronic environment, and consequently on the structural properties of the sample. The variation of interaction between the nuclei due to any phase transition can be detected from the change in structural and dynamical properties of the system which can be derived from chemical shift measurement and the analysis of relaxation time.

3.2.6a. Chemical shift and relaxation time

The chemical shift (δ) is defined as the variation of NMR resonance frequencies of the same kind of nucleus, due to the variation of electronic distribution. It is measured as the resonance frequency of the nucleus relative to a standard. The total magnetic field experienced by a nucleus includes local magnetic field induced by the electronic currents in the molecular orbitals which vary depending upon the local geometry (bond angle, length, bonding partner etc.).

The radio frequency, RF (equal to the energy difference between the two levels) applied to the sample causes spins to flip and redistribute among the two energy levels. The energy absorbed by the nuclear spins induces a voltage that can be detected by a suitably tuned coil of wire, amplified and the signal is displayed as free induction decay (*FID*). The relaxation process eventually returns the spin system to thermal equilibrium, which occurs in the absence of any perturbing RF pulses. The two relaxation processes are; spin-lattice (or longitudinal relaxation time, T_1) and spin-spin (or transverse relaxation time, T_2) relaxation. T_1 measures how fast the magnetization relaxes back along the z -axis, whereas, T_2 measures how fast the spins exchange energy in the transverse (xy) plane. There are several mechanisms by which molecular motions can influence nuclear relaxation; direct interaction with the nearby nuclei (dipole-dipole),

chemical shift effects, quadrupole interaction and j - j coupling. Different pulse sequences are employed to measure relaxation times. Pulse sequence is the set of RF pulses applied to the sample to produce a specific form of NMR signal.

In the present work, 90° *FID* pulse and spin-echo pulse sequences are used to measure T_2 . In the 90° *FID* pulse sequence, net magnetization is rotated down into the xy plane with a 90° pulse. The net magnetization vector begins to precess about z -axis. The decay time is determined from the *FID* curve. The *FID* is an observable NMR signal generated by non-equilibrium nuclear spin magnetization precessing about the magnetic field direction. The non-equilibrium magnetization can be induced generally by applying a pulse of resonance frequency (90° pulse as mentioned above) close to the Larmor frequency of the nuclear spin. In the spin-echo pulse sequence, initial 90° pulse rotates the magnetization into y -direction. Due to inhomogeneous magnetic field, spins fan out in the xy plane with a loss of phase coherence. A 180° pulse applied after time τ , results in phase coherence along the negative y -direction producing a signal called echo after time 2τ . Following the spin-echo, phase coherence will again be lost but can be regained with another 180° pulse. T_2 can be obtained from the amplitudes of the decaying echoes.

3.2.6b. *Static and Magic angle spinning*

NMR spectral lines obtained in static measurement from a liquid specimen are much narrower than that in the solids. This difference in the behavior arises from the static anisotropic interactions to which the nuclei are subjected in the solid state. By contrast, in liquids the rapid isotropic motion of the nuclei average out the anisotropic interactions and effectively remove them from the spectrum. These anisotropic interactions include chemical shift anisotropy, dipolar coupling and quadrupole interactions. The rotation/spinning of the solid specimen so as to mimic the rotation of nuclei as in liquids can help in averaging out the anisotropic interactions in the solids.

Rapid rotation about an axis inclined to an angle (magic angle) to the direction of magnetic field can remove anisotropic part of chemical shift anisotropy and dipolar coupling and a narrower spectrum can be obtained.

In a strong magnetic field, the dipolar coupling between the nuclei depends on the orientation of internuclear vector with the applied magnetic field, given as,

$$D \propto (3 \cos^2 \theta - 1) \quad (3.3)$$

where, θ is the angle between the internuclear vector and the direction of applied magnetic field and D is the dipolar coupling constant which tends to zero at $\theta = 54.7^\circ$ known as the magic angle. In the magic angle spinning measurement, specimen is spinned at an angle of 54.7° with respect to field direction. In the present work, magic angle spinning (MAS) has been used in the case of water confined in saponite clay. The effect of MAS on improving spectral resolution is evident from the Figure 3.2.

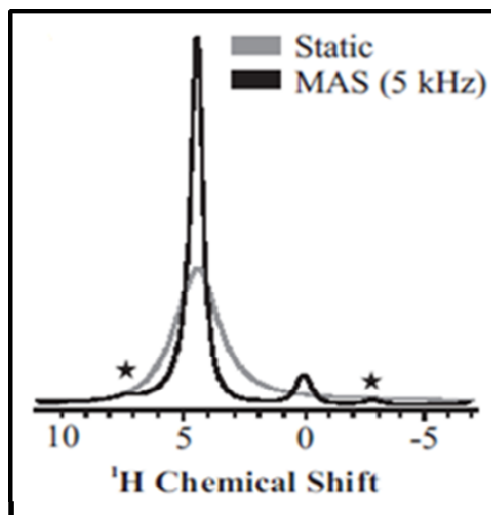


Figure 3.2: One-Dimensional ^1H spectrum of water confined inside clay nanopores, when the sample is static (grey) and spinning at 5 kHz at magic angle (black) inside the 700 MHz NMR spectrometer. The peak at 0 ppm in MAS spectrum corresponds to Si-OH group in the clay platelets. Peaks with stars on top of them are MAS side bands of the water and Si-OH peaks.

3.2.6c. Ethylene glycol and isopropanol

^1H NMR studies were carried out at a resonance frequency of 42.53 MHz with a Bruker MSL100 NMR spectrometer and at 9.97 kOe using a field-dial controlled Varian V7400 electromagnet. All the samples were sealed under argon atmosphere in glass tubes. A Bruker temperature controller was used to vary the sample temperature. The spin-spin relaxation time (T_2) has been measured by Hahn-echo method using the pulse sequence $90^\circ\text{-}\tau\text{-}180^\circ$ signal acquisition, which eliminates the effect of magnetic field inhomogeneity on T_2 decay. 90° pulse length was set at 2.1 μs and τ values were varied between 0.5 – 30 ms. The intensity of the resonance spectrum for a particular component of the fluid in which the nuclear spins experience a certain kind of interaction, is given by,

$$I_{2\tau}(i) = I(i) \exp\left(-\frac{2\tau}{T_2(i)}\right)^{m_i} \quad (3.4)$$

where $I_{2\tau}(i)$ is the intensity corresponding to the i^{th} component of the resonance spectrum after a time 2τ after 90° pulse, and m_i is 1 for exponential and 2 for Gaussian decay. $I(i)$ are the fractional intensities of the components having spin-spin relaxation times $T_2(i)$. The total intensity of the spectrum is given by,

$$(I_{2\tau})_{\text{total}} = \sum_i I_{2\tau}(i) \quad (3.5)$$

T_2 decay curves for ethylene glycol was decomposed into two distinct Gaussian decays whereas, three Lorentzian decay curves were employed to decompose T_2 decay curve in the case of isopropanol.

3.2.6d. Water confined in saponite clay

Solid-state ^1H NMR measurements were performed at a magnetic field of 16.43 T (700 MHz of ^1H Larmor frequency) using Bruker AVIII NMR spectrometer. 4 mm triple-

resonance probe was used for static and MAS experiments. Clay samples in the form of fine powder were packed in 4 mm rotors using ceramic caps to perform low temperature studies. All chemical shifts were referenced with respect to ^1H chemical shift of Si-OH groups in clay fixed to 0 ppm at 298 K. Chemical shift of ^{79}Br in KBr sample was used for temperature calibration in static as well as spinning samples. The transverse spin-spin relaxation time T_2^* (T_2') was measured in the temperature range 325-240 K. T_2^* values were calculated by measuring the full width at half maximum of water peak obtained from 1D spectrum of static and spinning clay sample obtained with just a 90° pulse. T_2' measurements were carried out by monitoring peak height in 1D ^1H spectrum of clay recorded after a spin-echo. The observed ^1H peak height was plotted as a function of spin-echo duration to obtain transverse dephasing curves. These curves were then fitted to a single-exponential decay function to obtain transverse dephasing times (T_2' values).

3.2.7. Dielectric relaxation spectroscopy

In dielectric relaxation experiments collective polarization of all the polar molecules in the sample is measured. The dielectric relaxation time provides the measure of the time taken by a system to reach the final polarization after an electric field is switched on (or off). The technique measures the dielectric response i.e. complex dielectric function $\varepsilon^*(\omega)$ of the system under study. The complex dielectric function, $\varepsilon^*(\omega)$ can be decomposed into real and the imaginary parts as,

$$\varepsilon^*(\omega) = \varepsilon'(\omega) - \varepsilon''(\omega) \quad (3.6)$$

The real $\varepsilon'(\omega)$ and imaginary $\varepsilon''(\omega)$ parts represent the storage and loss part, respectively for a relaxation process. Different molecular theories of dielectric relaxation process provide microscopic understanding of the relaxation phenomena existing in the system. The dependence of $\varepsilon^*(\omega)$ on angular frequency originates from different factors, (i)

microscopic fluctuations of molecular dipoles, (ii) the propagation of mobile charge carriers (translational diffusion of electron, holes or ions), and (iii) the separation of charges at the interfaces which give rise to additional polarization. The sensitivity of dielectric relaxation to intermolecular interactions and its ability to monitor cooperative processes at molecular level help in the investigation of properties of individual constituents of the system and hence, derivation of macroscopic bulk properties.

3.2.7a. *The dielectric constant and polarization*

The static dielectric constant (relative permittivity) of a material is given by,

$$\varepsilon = \frac{C}{C_o} \quad (3.7)$$

where, C is the capacitance of a parallel plate capacitor with the space between the plate filled with a dielectric material and C_o is the capacitance with vacuum in between the plates. The permittivity of the material depends on the polarisability of the molecules in between the plate. The polarization of the medium is a function of frequency of the applied electric field and is defined as,

$$P = \varepsilon_o(\varepsilon - 1)E \quad (3.8)$$

where, ε_o is the dielectric permittivity of vacuum and is equal to $8.854 \times 10^{-12} \text{ Fm}^{-1}$ and E is the applied electric field. The total polarizability is the sum of electronic, atomic and orientation (in case of polar medium) polarization. The applied field leads to polarization of the medium by displacing the charge distribution/aligning the dipoles in a direction parallel to the field. Each of these mechanisms has a characteristic resonant or relaxation frequency.

3.2.7b. *Relaxation Times*

Dielectric relaxation is a consequence of the movement of dipoles or electric charges due to the changing electric field. Dielectric relaxation processes lie in a wide range of characteristic times, 10^5 - 10^{-12} s and is denoted by,

$$\tau = \frac{1}{2\pi\nu_{\max}} \quad (3.9)$$

where, τ is the characteristic relaxation time and ν_{\max} is the resonance frequency of the relaxation process. Relaxation processes are characterized by a peak in the imaginary part (ϵ'') and a step-like decrease of the real part (ϵ') of the dielectric function. The relaxation processes are usually analyzed by using model functions. In the present work, a general model function introduced by Havriliak and Negami (H-N function) [Havriliak and Negami, 1966 & 1967], has been used to analyze the dielectric response of the system under study. The H-N function is defined as,

$$\epsilon''(\omega) = \frac{\sigma_{DC}}{\epsilon_o} \omega^{-n} + \text{Im} \left[\frac{\Delta\epsilon}{[1 + (i\omega\tau)^\alpha]^\beta} \right] \quad (3.10)$$

where, $\omega = 2\pi f$, $\Delta\epsilon = \epsilon_S - \epsilon_\infty$, where, ϵ_S and ϵ_∞ are static and high frequency limiting values of the dielectric constant, respectively, σ_{DC} is the conductivity contribution, τ is the relaxation time and n , α and β are empirical exponents with values between 0 and 1.

3.2.7c. Instrumentation and measurement technique

Using a sinusoidal electric field, $E^* = E_o \exp(i\omega t)$ with angular frequency ω and at field strength within the linear response (for most materials $E_o \leq 10^6$ Vs⁻¹), the dielectric function is derived by measuring the complex impedance $Z^*(\omega)$ of the sample, defined as,

$$\epsilon^* = \frac{j^*(\omega)}{i\omega\epsilon_o E^*(\omega)} = \frac{1}{i\omega Z^*(\omega)C_o} \quad (3.11)$$

where, $j^*(\omega)$ is the complex current density. Fourier correlation analysis in combination with impedance analysis has been used to evaluate amplitude and the phase of $Z^*(\omega)$. The schematic of the measurement technique is shown in Figure 3.3.

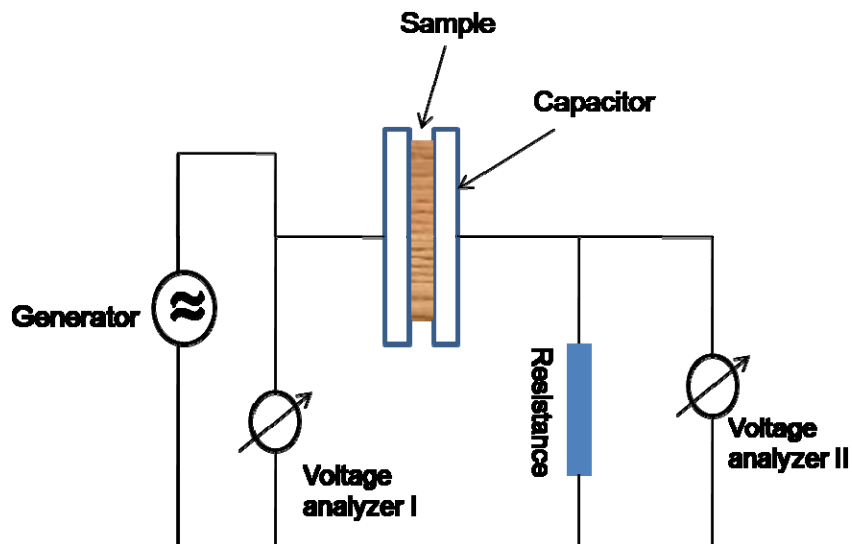


Figure 3.3: *The schematic of the measurement of dielectric response*

3.2.7d. *Water confined in clay*

For nanoconfined water in saponite clay, the dielectric measurements were performed using a Novocontrol Alpha AN impedance analyzer over a frequency range of 10 Hz to 1 MHz at several temperatures in the range of 190-298 K. The sample in powder form was placed between the two gold-coated electrodes in a parallel plate capacitor configuration with a thin annular Teflon spacer for insulation. Sample was first cooled to 190 K and the measurements were performed while slowly bringing the temperature to 298 K using the Novocontrol Quatro nitrogen gas cooling/heating cryosystem. The temperature was constant within ± 0.5 K during each measurement of the dielectric constant and loss. The similar measurement has been performed for dry saponite obtained by heating the hydrated sample at 493 K in vacuum.

I. Freezing/melting behavior of ethylene glycol and isopropanol confined in ZSM 5

3.3. Results and Discussion

3.3.1. Ethylene glycol and isopropanol confined in ZSM 5

3.3.1a. PAS results

The change in positron/Ps annihilation parameters (S -parameter, o -Ps *pick-off* lifetime and intensity) as a function of temperature is indicative of phase transition. In the present case, S -parameter, o -Ps *pick-off* lifetime (τ_p) and intensity (I_p) as a function of temperature have been used to identify phase transition in ethylene glycol and isopropanol confined in ZSM 5. The variation in S -parameter with temperature during cooling and heating cycle for confined ethylene glycol is shown in Figure 3.4. It is seen that during cooling cycle S -parameter initially decreases with the decrease in temperature and a sharp discontinuity in S -parameter is seen around 270 K. Below 270 K, S -parameter decreases and a second discontinuity is seen coinciding with the bulk freezing temperature 260 K. In the heating cycle, interestingly, S -parameter change is significant at the bulk freezing temperature and muted at 270 K. The temperature dependence of I_p and τ_p for ethylene glycol are shown in Figure 3.5. Both these parameters show discontinuities at 270 K and 260 K during the cooling cycle. The transition at 270 K may be attributed to the freezing of ethylene glycol confined in nanoscopic pores (micropores) of ZSM 5, which is 10 K above the bulk freezing temperature (260 K). However, the values of τ_p in Figure 3.5 remain at about 1.1 ns both in liquid (above 270 K) and solid (below 260 K) phase in contrast to ~ 2.3 ns expected in bulk liquid in this temperature range. This implies either no bubble formation or the volume available for Ps trapping must be similar in either phase. The origin of the available space may be the covolume associated with ethylene glycol molecules. A gross average of $\sim 26 \times 10^{-3} \text{ nm}^3$ for the covolume of a number of organic molecules would result in a life-time of 1.1 ns, in excellent agreement with the measured o -Ps life-time. If the present correlation is correct,

then it implies that the confined ethylene glycol molecules (*i*) are in an arrangement too rigid for Ps to form a bubble and (*ii*) maintain their covolume over the temperature range studied. The observed intensity of 15% at 280 K (Figure 3.5) in contrast to 22% in bulk liquid suggests that either a large fraction of positron/Ps is localized in the liquid or there is contribution from the zeolite bulk. However, the role of solvation phenomenon of electrons in the liquid and its influence on the Ps yield cannot be ignored.

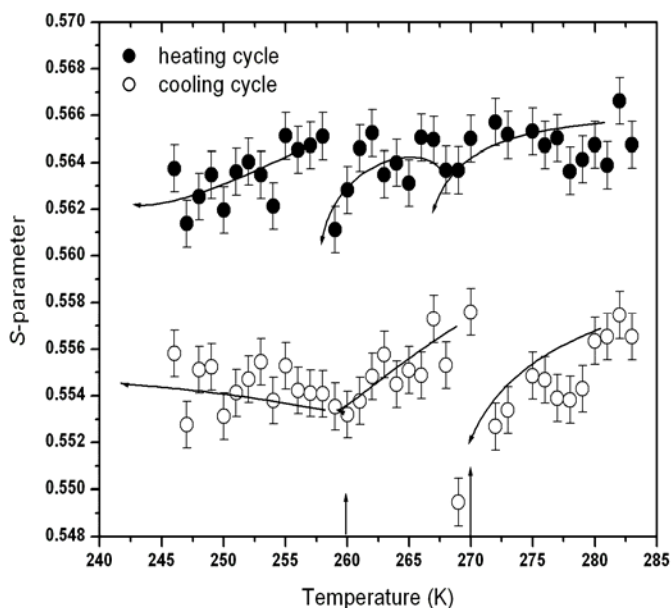


Figure 3.4: The Variation of S -parameter with temperature during cooling and heating cycle for ethylene glycol in ZSM-5. The solid lines are for eye-guide.

The *pick-off* intensity (I_p) response (in Figure 3.5) is observed to be quite different from the response of S -parameter (in Figure 3.4). It is seen that unlike S -parameter, I_p initially increases with the decrease in temperature till the discontinuity at the first phase transition temperature 270 K. Immediate below 270 K, I_p shows a drop at 268 K, which signifies the inhibition of Ps formation after the completion of liquid to solid phase transformation in nanopores. Below 268 K, S -parameter is seen to decrease slowly till 260 K, which is essentially due to the behavior of liquid trapped in mesopores. At 260 K (bulk freezing point of ethylene glycol), a second discontinuity in I_p , τ_p , as well as S -

parameter profile has been observed, which can be ascribed to the freezing of ethylene glycol present in the mesopore and bulk of the ZSM 5 matrix. Below the bulk freezing temperature, S -parameter does not show any change at least down to 245 K. Hence, I_p and τ_p below the bulk freezing temperature were not measured.

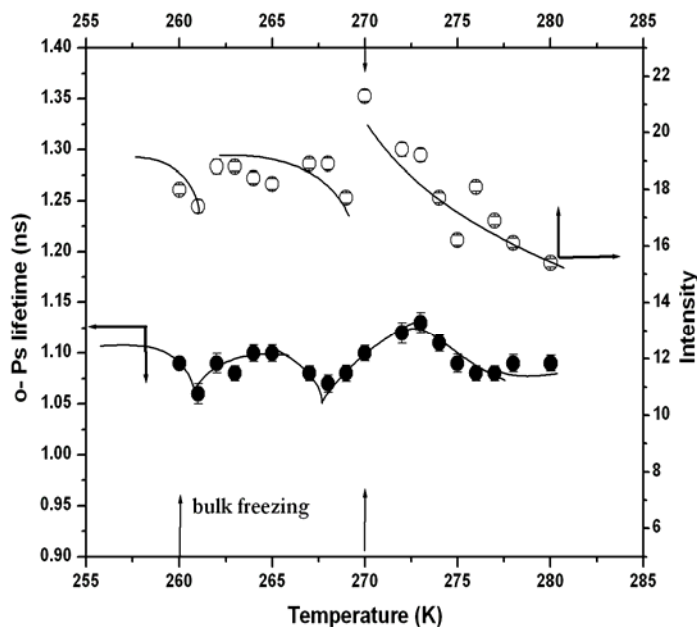


Figure 3.5: The variation of pick-off lifetime (τ_p) and intensity (I_p) during cooling cycle for ethylene glycol in ZSM-5. The solid lines are for eye guide.

One interesting observation (Figure 3.4 & 3.5) is the contrasting behavior of S -parameter and I_p . In bulk liquid, upon cooling, the intensity decreases. In general, S -parameter follows the trend of the intensity. The contrasting behavior observed in the present case, therefore, can be ascribed to the possible detrapping of positron/Ps leading to broader momentum distribution and concomitant decrease in S -parameter. However, the role of free positron annihilation in sampling the altered physical state as well as interface cannot be discounted.

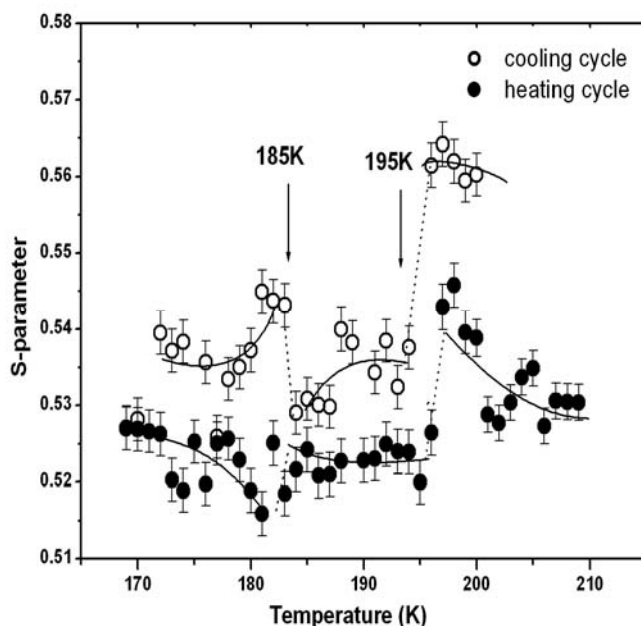


Figure 3.6: The variation of S -parameter with temperature during cooling and heating cycle for isopropanol in ZSM-5. The solid lines are for eye guide.

The variation of S -parameter during cooling and heating cycle in isopropanol confined in ZSM 5 is shown in Figure 3.6. It is seen that S -parameter, I_p and τ_p (in Figure 3.7) profiles exhibit quite different features from the case of ethylene glycol (Figure 3.4 and 3.5). During cooling cycle, S -parameter shows a sharp drop near 195 K. I_p and τ_p profile also show an abrupt change in the slope in the temperature range 199-195 K, which illustrates that the phase transition starts near 199 K and continues to 195 K. Below 195 K, the profile of S -parameter, I_p and τ_p show almost constant behavior before the second transition occurs at the bulk freezing point 185 K. It is to be noted that I_p is very small (5%) and τ_p (2.5 ns) is very close to that of the bulk liquid. It was argued that in the case of ethylene glycol there could be contribution to I_p from the zeolite bulk and similar contribution should be seen in the case of isopropanol too. However, this seems very unlikely keeping in mind the low P_s yield. Therefore, solvation of electrons in these liquids can be invoked to explain the yields. It is known that the solvation time in ethylene glycol is very short as compared to isopropanol. In the event of a shallow

potential electron trap the electron can be picked up by the positrons giving higher Ps yield, a process known as anti-inhibition. In the case of isopropanol, on the other hand, this is not possible due to slower solvation kinetics and consequently the yield is low. Further, the higher life-time of Ps under confinement indicates that Ps atom is able to create a hole around itself in the confined isopropanol.

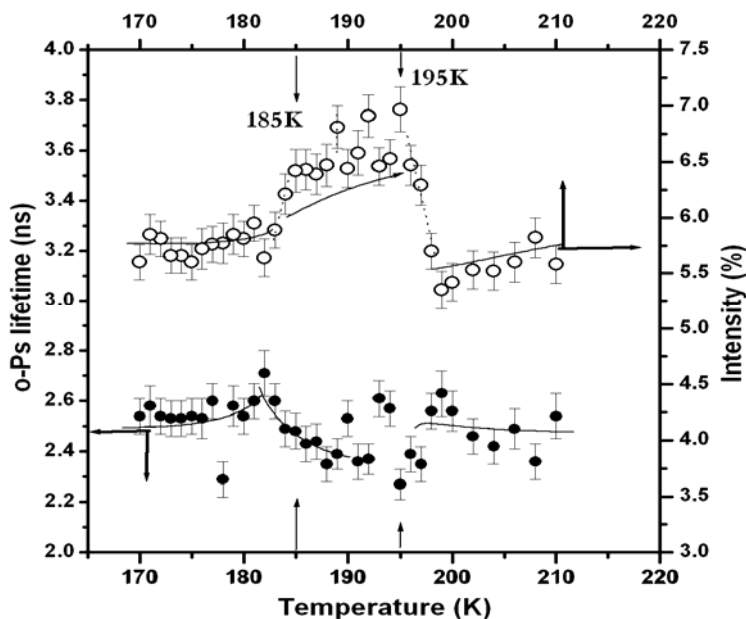


Figure 3.7: The variation of pick-off lifetime (τ_p) and intensity (I_p) during cooling cycle for isopropanol in ZSM-5. The solid lines are for eye guide

An elevation in the freezing/melting behavior is observed in both the cases. This is unlike the case of benzene confined in similar matrix i.e. ZSM 5 [Dutta et al., 2008] wherein, a depression was observed. This has been attributed to the role of interfacial interaction (fluid-wall) in these cases. The fluid-wall interaction is attractive in the case of ethylene glycol and isopropanol unlike benzene, which experiences weakly attractive/repulsive interaction with the pore wall. This clearly indicates the role of interfacial interactions on the direction of the shift in freezing/melting point. The different behavior of S -parameter, I_p and τ_p signifies that the nature of phase transition in isopropanol is different from that of ethylene glycol. The major reason behind this

dissimilarity is the difference in the nature of hydrogen bonding in ethylene glycol and isopropanol molecules, which makes the interfacial interaction different. It is already mentioned that ethylene glycol has both inter- and intra-molecular hydrogen bonding, whereas isopropanol has only inter-molecular hydrogen bonding. Hence, under confinement, isopropanol experiences more attractive interaction with the pore wall. This causes the extent of elevation $\left(\frac{\Delta T}{T_{freezing}}\right)$ in phase transition temperature higher in the case of isopropanol. It is observed that the elevation in phase transition temperature in ethylene glycol is only 3.8%, whereas in isopropanol it is around 7.5% relative to their respective bulk freezing temperature. Although, the pore size in both the cases remains same, it is only the distinct interfacial interaction or the surface energy which plays crucial role to make the phase transition behavior quite different. In isopropanol, since the molecules strongly interact with the pore surface, the mobility of the molecules near the pore surface decreases very fast with the decrease in temperature. This may also be one of the reasons for the different behavior of S -parameter, τ_p and I_p across the phase transition temperature in the two cases.

3.3.1b. NMR results

Figure 3.8 shows the variation of spin-spin relaxation times originating from the protons of the molecules confined primarily in the nanopores. A typical decay curves for ethylene glycol in ZSM 5 taken at 267 and 240 K, respectively is shown in Figure 3.8. In the temperature range 230-300 K, T_2 decay is expressed as a sum of at least two distinct components exhibiting Gaussian decay. As a typical example, the deconvolution into two components ($I(1)$ & $I(2)$) for 267 K decay curve is shown in the inset of Figure 3.8. The temperature dependence of the fractional intensities of the two components and their characteristic times are shown in Figures 3.9 and 3.10, respectively.

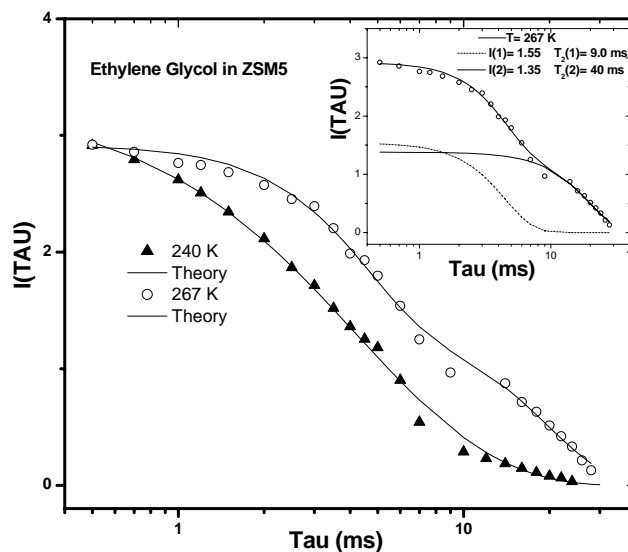


Figure 3.8: Decay of NMR signal intensity for ^1H spin-spin relaxation in ethylene glycol in ZSM-5 at 267 and 240 K. Inset: two distinct fractional intensities ($I(1)$ and $I(2)$) of spin-spin relaxation time (T_2) are shown at 267 K.

The characteristic time ($T_2(1)$) for $I(1)$ component is in the range of 5 ms and that of $I(2)$ component ($T_2(2)$) is around 30 ms, showing a decreasing trend with the decrease in temperature. The obtained time scales indicate that both the components are in the fluid state, but with different physical environment. The shorter component $T_2(1)$ (Figure 3.10) is ascribed to fluid molecules close to the pore wall. The molecules away from the pore walls would exhibit relatively longer $T_2(2)$ because of the higher mobility like the bulk fluid. $T_2(1)$ is almost temperature independent, however, gradual decrement in $T_2(2)$ is ascribed to slowing down of the molecular motion due to lowering of temperature. The two components are present at about equal intensities at room temperature and down to about 270 K. Below this temperature, $I(1)$ begins to increase at the expense of other component, indicating a transition from a higher to a lower mobility state (similar discontinuity in the S -parameter is seen at this temperature). This means that fluid pore wall surface interaction starts to percolate towards the centre of the pore facilitating the gradual increase in the number of molecules interacting with pore wall. This process

continues down to 260 K (bulk freezing point of ethylene glycol). From 260 K, the intensity of the component with shorter T_2 ($I(1)$ component) starts to dominate and finally around 235 K, $I(2)$ component i.e. that with longer T_2 reduces to 10% of the total intensity of the resonance line.

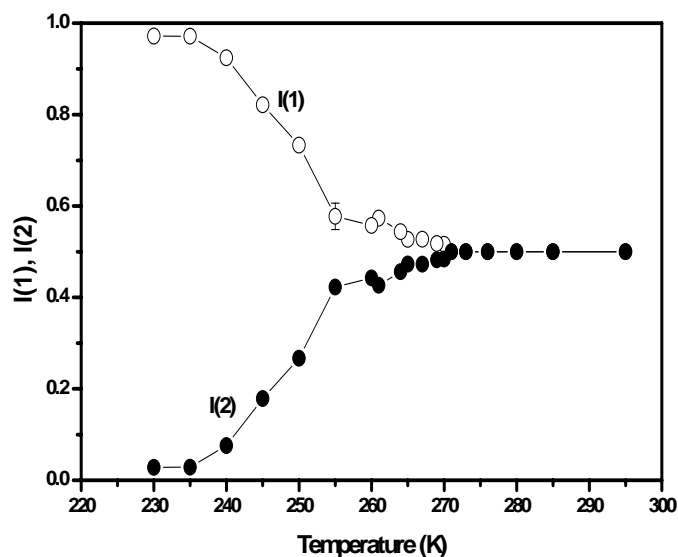


Figure 3.9: Temperature variation of fractional intensities of the molecular components having two different mobilities observed in 1H NMR of ethylene glycol in ZSM-5.

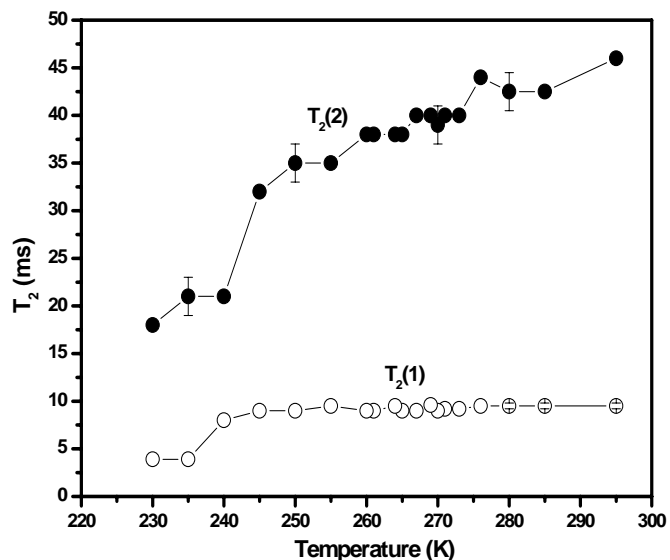


Figure 3.10: 1H spin-spin relaxation time (T_2) at various temperatures of the molecular components with two different mobilities in ethylene glycol in ZSM-5.

Shorter T_2 component as explained before indicates the presence of strong surface bonded molecules. The other component having longer T_2 shows the existence of molecules free to move, but still close enough to the surface so that the surface interaction becomes dominant at about 10 degrees above the bulk freezing point, when the molecular motion is slowed down. It may be said that the part of adsorbed ethylene glycol that exhibits fluidity at room temperature, experiences a gradual decrease in mobility below 270 K. Probably, the high degree of compartmentalization prevents the occurrence of a long range crystalline order at a sharply defined temperature as it happens in a bulk fluid. A possible reason for this could be the pore size in the present case (0.5-1.3 nm), which is comparable to the molecular size, and much smaller compared to other porous materials with a larger pore size (6 - 50 nm) where definite signature of the crystalline state has been observed upon freezing [Gussoni et al., 2004].

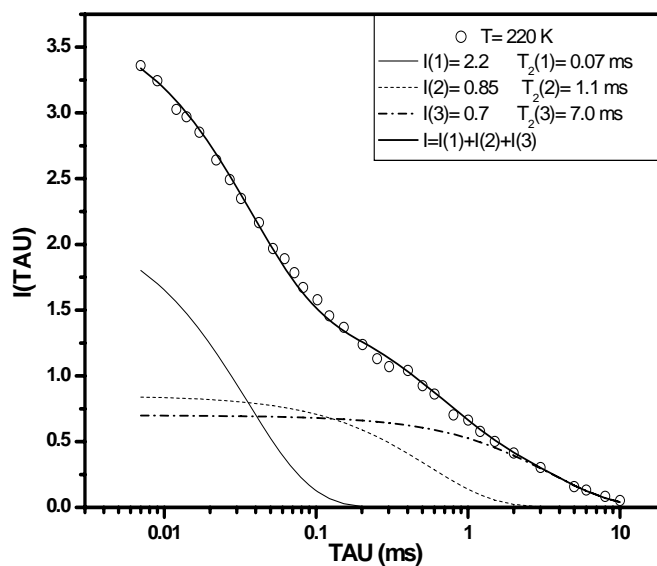


Figure 3.11: Decay of NMR signal intensity for ^1H spin-spin relaxation in isopropanol at 220 K.

In the case of isopropanol, T_2 decay in the temperature range 295-200 K, could be satisfactorily expressed as a sum of three components exhibiting Lorentzian decay. Figure 3.11 shows a typical example of one such fitting at 220 K. The temperature dependence

of the fitting parameters, $I(i)$ and $T_2(i)$ is shown in Figures 3.12 and 3.13. The values of T_2 , which are about 0.07 ms, 1.0 ms, and 5.0 ms, do not show appreciable change with temperature. The component having the shortest T_2 (0.07 ms) remains dominant, at about 70 %, throughout the temperature range. This component indicates the presence of isopropanol molecules rigidly bonded inside the pores via strong surface interaction. The component having such a small value of T_2 has not been seen in ethylene glycol, signifying weaker interaction of ethylene glycol with the pore surface. The intermediate and long components of T_2 in isopropanol signify the presence of molecules having relatively higher mobility. Below about 200 K, the component with the longest T_2 is gradually diminished, and no longer obtained below 190 K, which is indicative of gradual freezing of molecular mobility, or a phase transition of molecules away from the pore surface.

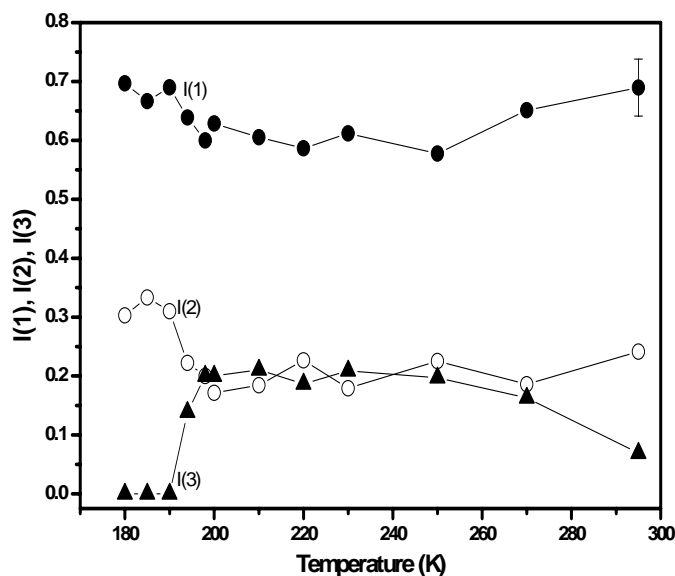


Figure 3.12: Temperature variation in fractional intensities of the molecular components with three different mobilities observed in ^1H NMR of isopropanol in ZSM-5.

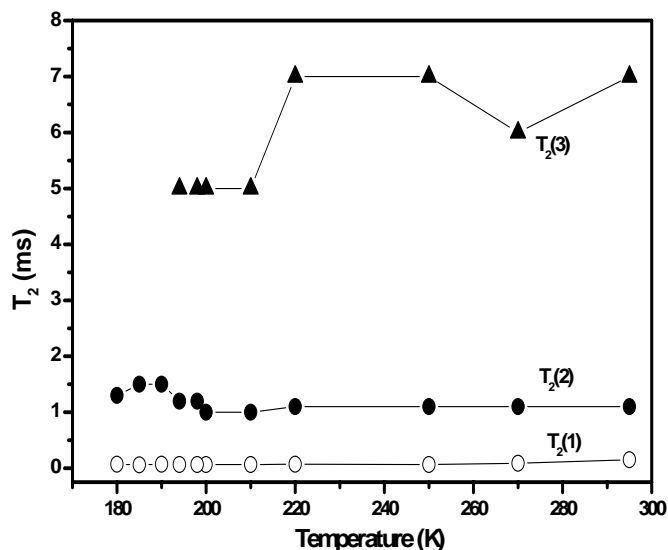


Figure 3.13: ^1H spin-spin relaxation time (T_2) at various temperatures of the molecular components with three different mobilities in isopropanol in ZSM-5.

3.3.1c. Discussion

PAS and NMR measurements in ethylene glycol and isopropanol thus, explored the nature of the phase transition of two liquids having different liquid-substrate interfacial interaction within the confinement. The structures of the quasi-solid state of ethylene glycol and isopropanol near or below their bulk freezing temperatures depend on the relative strength of the interaction within the molecules as well as between the molecules and the pore wall. The oxygen atoms present on the surface of the void space of ZSM 5 enhances the effect of the interfacial hydrogen bonding, which provides a strong spatial correlation and supports the propagation of surface induced order to the molecules at the centre of the pore. The fluid molecules having strong interaction with the surface of the pore are generally arranged in a layer structure [Morineau, et al., 2003; Abragam et al., 1961]. Hence, the present situation facilitates the layer like configuration of strongly hydrogen bonded molecules like isopropanol. The ethylene glycol, on the other hand, which shows comparatively weaker interfacial hydrogen bonding due to presence of strong intra-molecular hydrogen bonding, is expected to have inhomogeneous phases

with globular structure as observed in case of benzene in silica pores by Dutta et al. [Dutta et al., 2008]. An inhomogeneous phase with partial crystalline domain is also reported by Radhakrishnan et al. and Bartkowiak et al. using Monte Carlo simulation method in the context of freezing of nitrobenzene in silica [Radhakrishnan et al., 2000; Bartkowiak et al., 2001].

**II. Phase transitions of water confined in clay
nanopores**

3.3.2. Water confined in saponite clay

3.3.2a. TG-EGA results

The presence of water in the clay sample was confirmed and the amount was determined by monitoring the evolved water from the samples using simultaneous TG-EGA measurements. Figure 3.14a shows the mass (%) change in the clay samples as a function of temperature while the inset shows the extracted IR spectrum of the corresponding evolved gas at 423 K. The as-synthesized saponite clay shows 22% mass loss whereas the sample heated at 493 K for 15 hrs shows no mass loss in the temperature range 298-500 K (Figure 3.14a). This indicates that as-synthesized clay (hydrated) contains 22% water whereas no water is present in the heated sample (dry clay). The inset FTIR spectrum of the evolved gas confirms the presence of water in the as-synthesized clay sample through 1506 and 3600 cm^{-1} IR bands corresponding to H–O–H bending and stretching vibrations, respectively. Hence, the respective mass loss corresponds to the amount of water present in the clay sample. The desorption temperature (T_{desorb}), is the maximum obtained by differentiating the mass-temperature curve with respect to temperature, defines the maximum rate of desorption of liquid from the sample. The differentiated mass-temperature (DW) profile can be used to identify different adsorption sites for the liquid inside the matrix [Yudasaka et al., 2005]. In the present case, DW profile is seen to be asymmetric as shown in Figure 3.14b and the desorption behavior of water is obtained by deconvoluting DW profile. DW profile has been deconvoluted into two peaks (Figure 3.14b) which indicate two adsorption sites or two regimes of water (distinctly bonded water molecules confined within the clay nanopores).

We have analyzed the manner in which 22% water is distributed in the clay nanopores. The diameter of a water molecule is 0.275 nm and external surface area of

saponite used is $315 \text{ m}^2/\text{g}$. A dense monolayer close to the wall surface requires 7 mM of water per gram of saponite.

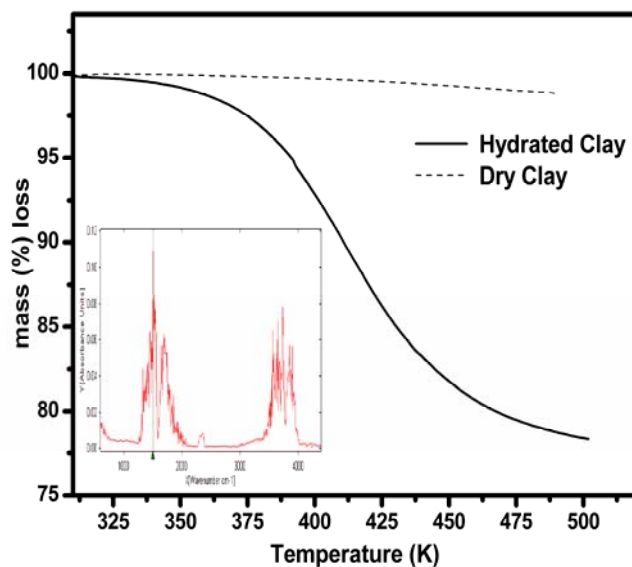


Figure 3.14a: Mass (%) loss as a function of temperature (mass-temperature curve) for dry and hydrated clay as measured from TG-EGA. Inset shows FTIR spectrum of the evolved gas.

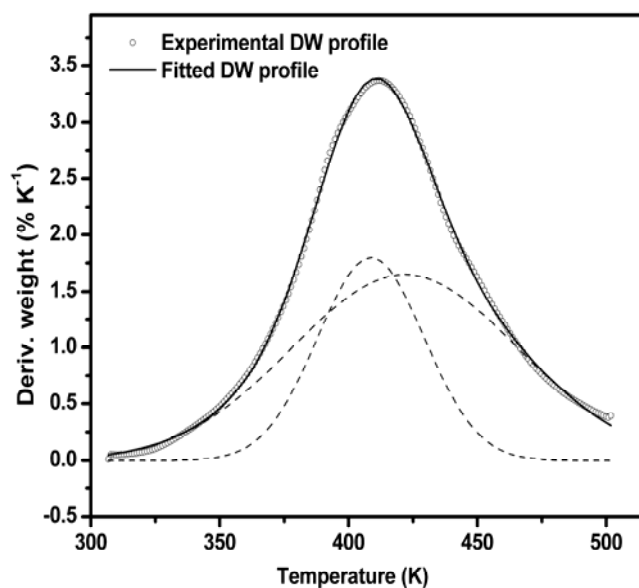


Figure 3.14b: DW profile for hydrated clay as obtained from mass-temperature curve.

For 22% water confined in the pores, the amount of water is 12 mM per gram of saponite, which is about twice the amount required for the densely packed monolayer. This shows that 22% water in saponite would form two water layers on the surface of the platelets. The interplatelet spacing of 15.4 Å as obtained from XRD measurement in as-synthesized clay includes thickness of rigid clay platelets and interplatelet distance. Considering the interplatelet spacing of clay, not more than two layers can be accommodated between the platelets. Neutron scattering studies in vermiculite clay by Skipper [Skipper et al., 1991] has shown that water in interplatelet spaces is associated with the platelet surface and interplatelet cations forming hydration layer around the cations. Each water molecule in the coordination sphere directs one of its hydrogen atoms towards the platelet to form hydrogen-bond with the surface oxygen atom. However, the exact position of cations within the platelets could not be deduced from these experiments and there is no reason to assume that cations would lie only midway between the clay platelets. Therefore, it can be assumed that out of the total water molecules, few molecules are attached to the cations as well as the platelet surface. These water molecules are more bound as compared to the relatively free water molecules which do not form hydrogen-bond with the platelet surface but can be hydrogen-bonded to other water molecules in the close vicinity.

3.3.2b. ATR-FTIR results

Figure 3.15 shows ATR-FTIR spectra of hydrated and dry clay. The spectra show different vibrational modes of water confined in clay nanopores in the hydrated sample. The vibrational modes observed at 1641 and 3000-3600 cm^{-1} correspond to OH-bending and OH-stretching (OHS) modes of water, respectively. The band at 970 cm^{-1} is attributed to the combination of OH-libration (686 cm^{-1}) and OHS (3000-3600 cm^{-1}) bands of water. The vibrational mode involving stretching motion of the intramolecular OH-bond is

sensitive to the strength of the hydrogen-bonding between the water molecules. Within a sample, especially in confined geometries, there may exist a variety of molecules that are differently coordinated to each other. With this in mind, we have deconvoluted OHS spectrum into four Gaussian components (as shown in the inset of Figure 3.15) viz. (a) 3110 cm^{-1} , (b) 3230 cm^{-1} , (c) 3425 cm^{-1} and (d) 3600 cm^{-1} , coming from well established studies of OHS vibrational spectrum of water [Brubach et al., 2005; Mallamace et al., 2007]. The low frequency contributions 3110 and 3230 cm^{-1} are attributed to hydrogen-bonded water molecules. The component at 3110 cm^{-1} confirms the presence of confined water in the form of tetrahedrally coordinated water clusters and 3230 cm^{-1} corresponds to symmetric OH vibrations observed in liquid water [Mallamace et al., 2007; Kittaka et al., 2009]. The components at higher frequencies 3425 cm^{-1} and 3600 cm^{-1} correspond to less hydrogen-bonded molecules. These frequencies are close to that of water molecules existing in the form of dimer or multimer water, respectively.

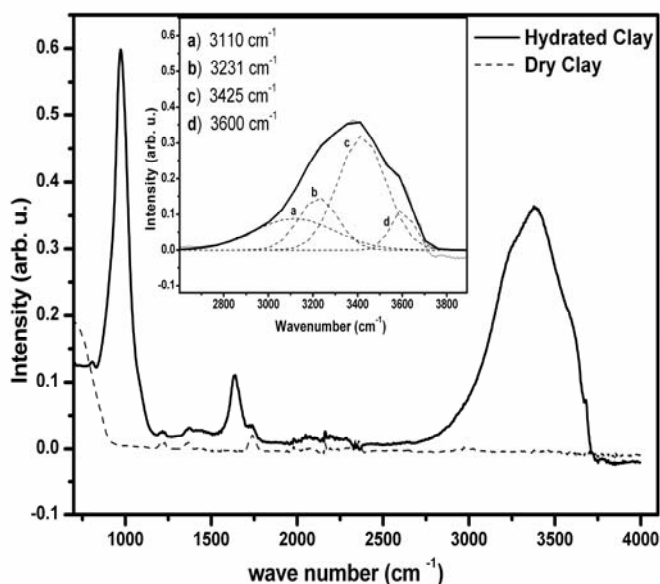


Figure 3.15: ATR-FTIR spectra of dry and hydrated clay. Inset shows the deconvoluted OHS band of water ($3000\text{-}3600\text{ cm}^{-1}$). OHS band is deconvoluted into four peaks (a, b, c and d).

3.3.2c. DSC results

Figure 3.16 shows the conventional DSC curves for hydrated and dry clay in the temperature range 200-298 K in the cooling and heating scans. In the hydrated clay, a peak at $T \sim 230$ K is observed during the cooling scan which becomes broader and shifts to higher temperature during the heating scan. No transition peak is observed in dry clay throughout the temperature range. Therefore, the peak observed in hydrated clay at $T \sim 230$ K is attributed to the freezing/melting or a similar phase transition of the confined water. The broad nature of the peak does not allow us to determine the onset of transition temperature and indicates that the phase transition spreads over a wide temperature range. The presence of low temperature peak has been observed for water confined in variety of porous media [Kozlowski et al., 2012; Schreiber et al., 2001; Tombari et al., 2005] and attributed to the depression in the freezing/melting behavior of water. The apparent specific heat capacity C_p for water confined in clays calculated by Kozlowski et al. using modulated DSC indicated the presence of partial freezing/inhomogeneous phases [Kozlowski et al., 2012]. However, different thermal characteristics have been observed in different materials. In the present study, the observed low temperature peak may be attributed to a low-temperature phase transition involving partial freezing of the confined water.

The C_p of confined water is calculated by subtracting C_p of dry clay from the C_p of hydrated clay as measured in temperature modulated mode and is shown in the inset of Figure 3.16. The C_p of confined water is seen to be lower than the bulk water ($4.18 \text{ Jg}^{-1}\text{K}^{-1}$). This could be a manifestation of the effect of confinement as also suggested by Kozlowski [Kozlowski et al., 2012]. It is also observed that the obtained C_p increases with the decrease in temperature and shows a maximum at ~ 230 K corresponding to the low-temperature phase transition of confined water. The increase in C_p is an indicative of more

configurational contribution to heat capacity than the contribution from vibrational and anharmonic modes. Changes in the average coordination and short range order in the structure of liquid contribute to the configurational part of heat capacity. Therefore, the variation of C_p as a function of temperature reveals structural changes in confined water whereas, the low-temperature peak can be assigned to the partial freezing of confined water molecules.

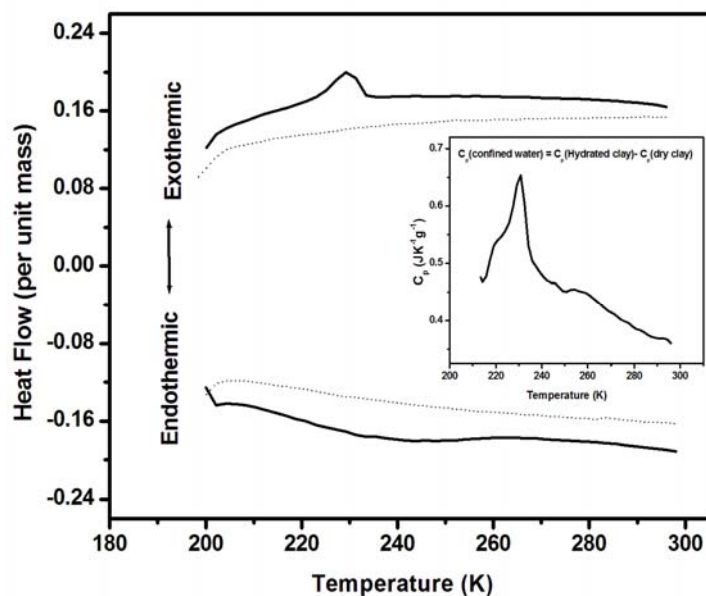


Figure 3.16: Heat flow per unit mass in dry and hydrated clay in cooling and heating scans. The inset shows the apparent heat capacity (C_p) of confine water obtained by subtracting C_p of dry clay from the hydrated clay.

3.3.2d. PAS results

Positron lifetime measurements have been carried out at room temperature for hydrated and dry clay samples. The lifetime spectrum for the hydrated clay could be decomposed into three life-time components; however, four components were obtained for the dry clay. The measured life-times and intensities are shown in Table 3.1. The presence of only one Ps like state (long component) in a system with confined fluids as compared to two distinct Ps like states in the absence of confining fluid has been

observed by others too [Kajcsos et al., 2000; Dutta et al. 2006]. In the context of present work, the observed result reveal localization of positron/Ps in nanoconfined water in clay.

Table 3.1: Positron lifetime and intensities at room temperature for the hydrated and dry clay sample

Sample	τ_1 [ns]	I_1 [%]	τ_2 [ns]	I_2 [%]	τ_3 [ns]	I_3 [%]	τ_4 [ns]	I_4 [%]
Hydrated clay	0.226 (± 0.009)	38.42	0.490 (± 0.017)	43.63	2.115 (± 0.024)	17.94	-----	-----
Dry Clay	0.200 (± 0.016)	28.06	0.439 (± 0.015)	54.5	1.86 (± 0.066)	10.12	10.75 (± 0.200)	7.3

Figures 3.17 and 3.18 show the variation of S -parameter as a function of temperature for dry and hydrated clay, respectively. The S -parameter profile for dry clay (Figure 3.17) shows insignificant variation unlike the hydrated clay (Figure 3.18) which shows distinct features over the studied temperature range in cooling as well as heating cycle. The change of slope/discontinuity in S -parameter profile as a function of temperature is indicative of phase transition of liquid confined in nanodomains [Dutta et al., 2006 & 2008]. In the present context, the absence of variations in S -parameter profile in the dry clay shows that the features seen in the hydrated clay are signatures of phase transition of water confined in clay nanopores. Two phase transitions have been observed for the confined water viz. above (high-temperature transition, HTT) and below (low-temperature transition, LTT) the bulk freezing temperature (Figure 3.18) of water (273 K). The HTT and LTT range from 286-274 K and 254-240 K, respectively. Figure 3.18 also shows S -parameter profile for the heating cycle showing the presence of both the transitions in addition to a marked hysteresis for HTT. The hysteresis behavior of confined liquids has been observed by others and is explained on the basis of thermodynamical stability of the phases taking into account surface energy barriers

[Morishige et al., 1999]. The origin of hysteresis observed in the present study could be the inhomogeneities brought out by the strong surface interactions as well as the effect of confining geometry [Brun et al., 1977; Vanfleet et al., 1995; Gross et al., 1997].

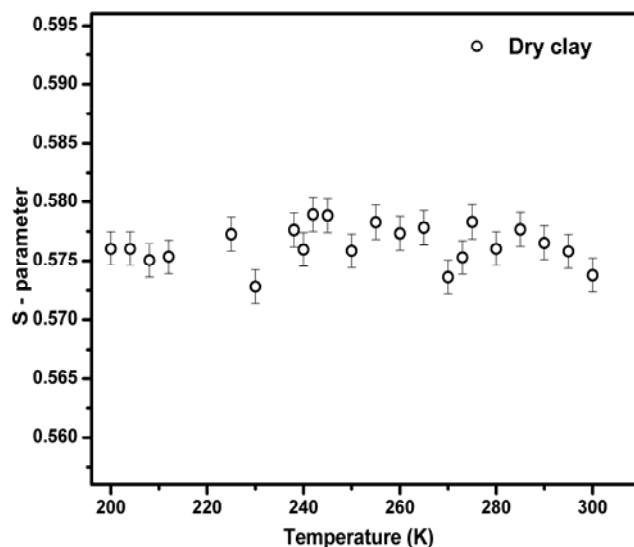


Figure 3.17: Variation of S -parameter with temperature for dry clay.

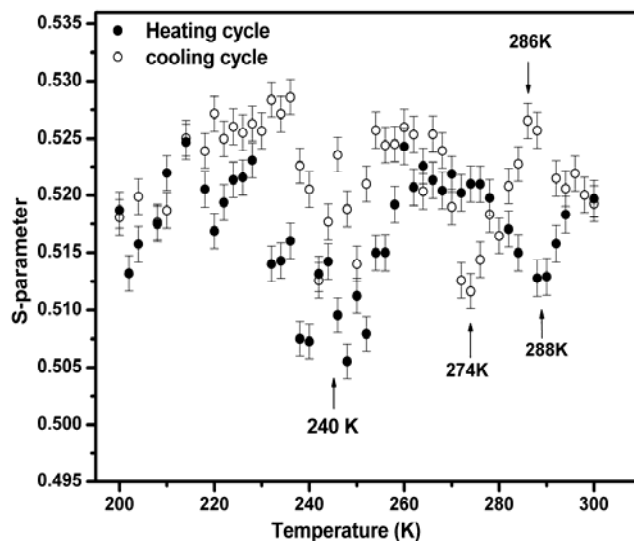


Figure 3.18: Variation of S -parameter with temperature for hydrated clay in cooling (\circ) and heating (\bullet) cycle.

The variation of o -Ps pick-off life-time (τ_3) and intensity (I_p) as a function of temperature for hydrated clay are shown in Figure 3.19. It is seen that τ_3 increases to a maximum value (around $T \sim 268$ K) after the completion of HTT, and, the corresponding

intensity I_p decreases significantly followed by a marginal increase that remains nearly constant upto the lowest temperature studied. No significant change in τ_3 and I_p are seen at LTT unlike S -parameter. However, it is interesting to note that I_p remains constant around 11% till the lowest temperature studied. Figure 3.20 shows the change in free volume ($f_v = (4\pi/3)*r^3$) with temperature, where r is the radius of the free volumes as calculated from τ_3 using Tao-Eldrup equation [Tao, 1972 and Eldrup et al., 1981],

$$\tau_3 = \frac{1}{2} \times \left(1 - \frac{r}{r + \Delta r} + \frac{1}{2\pi} \sin\left(\frac{2\pi r}{r + \Delta r}\right) \right)^{-1} \quad (3.12)$$

where, Δr is the empirical electron layer thickness (0.166 nm). The significant variation of f_v suggests nanostructural alterations with temperature.

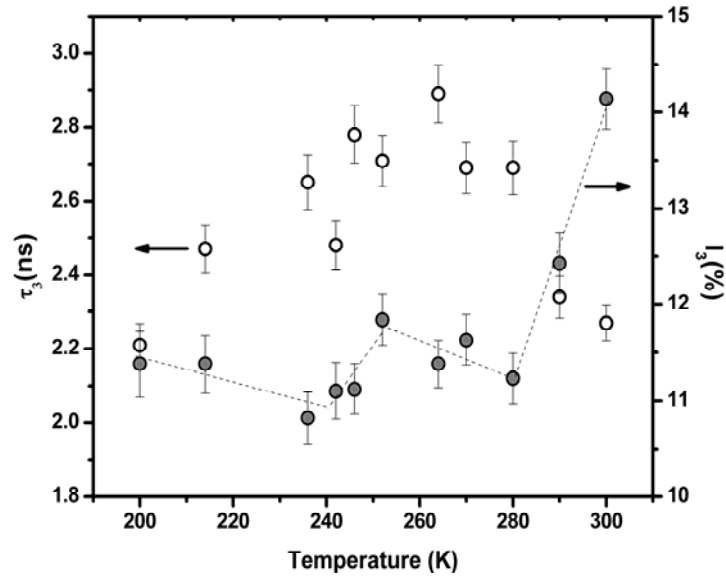


Figure 3.19: Variation of *o*-Ps pick-off lifetime (τ_3) and intensity (I_p) as a function of temperature.

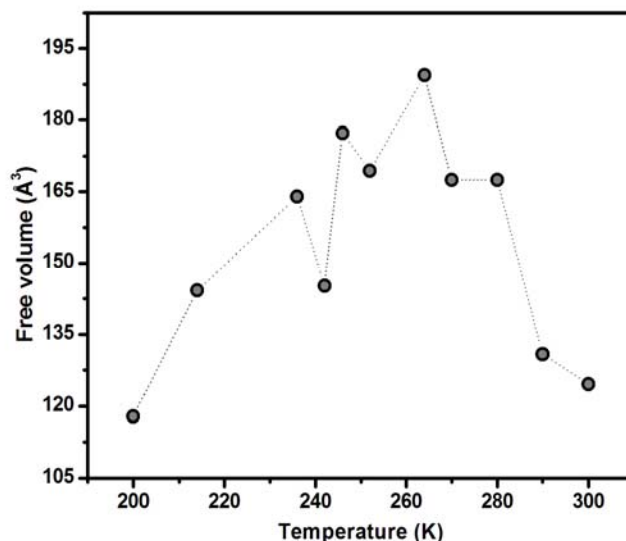


Figure 3.20: Variation of free volume (f_v) with temperature. Error bar lies within the symbols.

The presence of two phase transitions, above and below the bulk freezing point of water, is the first report on the phase behavior of nanoconfined water. Phase transition below the bulk freezing temperature of water has been observed by many authors for water confined in different geometries and assigned to supercooled water [Bruni et al., 2011; Mallamace et al., 2006]. However, the transition seen at elevated temperature (HTT) in the present study is observed for the first time for water confined in clay nanopores. The shift in freezing/melting behavior has been explained on the basis of nature of fluid-wall interaction [Miyahara et al., 1997; Radhakrishnan et al., 2002]. It has been shown that the attractive interaction with the wall surface results in the elevation of the freezing point, whereas, depression is observed in the case of repulsive (less attractive) interaction. On this basis, we feel that the observed HTT (above bulk freezing point), represents phase transition associated with the water molecules hydrogen-bonded to cations as well as platelets surface (bound water). However, the concurrent presence of a transition below the bulk freezing point (LTT) of water evidently reveals existence of different regimes of confined water. In order to get further insight into these transitions both NMR and DRS studies have been carried out as detailed in the latter section.

It is seen that the positron annihilation parameters viz. S -parameter, τ_3 and I_p are sensitive to phase transitions in confined systems and explore nanostructural alterations following the transitions. The studies on phase transition of confined liquids have always shown anomalous changes in S -parameter, τ_3 and I_p near the transition. The onset of transition is marked by a decrease in S -parameter similar to the present observation. The completion is associated with the minimum in S -parameter which increases on further cooling to a value similar to that at the onset of transition. This is explained on the basis of structural inhomogeneities existing in the confined systems which include the presence of inhomogeneous phases due to partial freezing, agglomeration or clustering of molecules and the appearance of more surfaces and interfaces due to freezing [Dutta et al., 2006 & 2008]. In addition, positron/Ps dynamics in the confined system viz. trapping/detrapping and annihilation from delocalized states are also invoked to explain the S -parameter and τ_3 behavior.

While the two observed transitions are associated with significant change in electron momentum distribution as reflected in S -parameter, it is interesting to note the variation in free volume, f_v . It significantly increases below HTT, reaches a maximum (~268 K) and decreases till the lowest temperature studied. The variation of S -parameter and f_v at HTT suggest rearrangement of water molecules leading to structural ordering of molecules near the surface. This ordering results into a new phase (configuration) with large open/free volumes. On the other hand, at LTT, the variation in f_v is not as pronounced as S -parameter. Electron momentum distribution seems to be a more sensitive index as compared to electron density associated with this transition. Although the exact reason for this behavior is not known, a possible reason could be the fact that S -parameter provides a composite information on p -Ps, free positron and o -Ps states unlike o -Ps lifetime (free-volume size). An empirical viscosity-free volume correlation i.e. $\eta = A \exp$

($1/f_v$) suggested by Miller indicates an inverse relation between f_v and η [Miller et al., 1963]. Therefore, the observed variation in f_v (monotonic decrease) indicates increase in the viscosity of water as temperature is lowered. This behavior corresponds to supercooled liquids which become increasingly viscous as temperature approaches glass transition, T_g (T_g of water is lower than the lowest temperature studied in the present case). It is also to be noted that I_p reduces to 11% below HTT and remains nearly same till the lowest temperature studied (even below LTT). This indicates that confined water does not completely freeze to crystalline ice at LTT. On the basis of these observations, we conjecture that the LTT is associated with the supercooled water molecules.

3.3.2e. NMR results

NMR measurements have been performed in static and MAS mode for hydrated clay sample. A single broad peak observed in static case is resolved into two distinct peaks in MAS case coming from the confined water molecules (around 4 ppm) and Si-OH groups (around 0 ppm) as shown in Figure 3.21. The confined nature of water trapped inside the clay nanopores is the reason behind the extremely broad NMR peak of water observed in static case. Anisotropic interactions like chemical-shift anisotropy and dipolar-dipolar interactions are strong under these conditions. Partial averaging of these interactions by MAS leads to narrower NMR peak of water.

Isotropic chemical-shifts, δ , of nuclei like protons reflect the kind of electronic environment experienced by them in a system. Any changes in the local electronic environment of these nuclei will be accompanied by chemical-shift changes. Water molecules form an extensive hydrogen-bonding network with each other. It has been generally observed that the strength of this network weakens (lengthening of hydrogen-bonds) with increase in temperature [Yamaguchi et al., 2001]. This change has a direct influence on the ^1H chemical-shifts of the water molecules, which for example, can

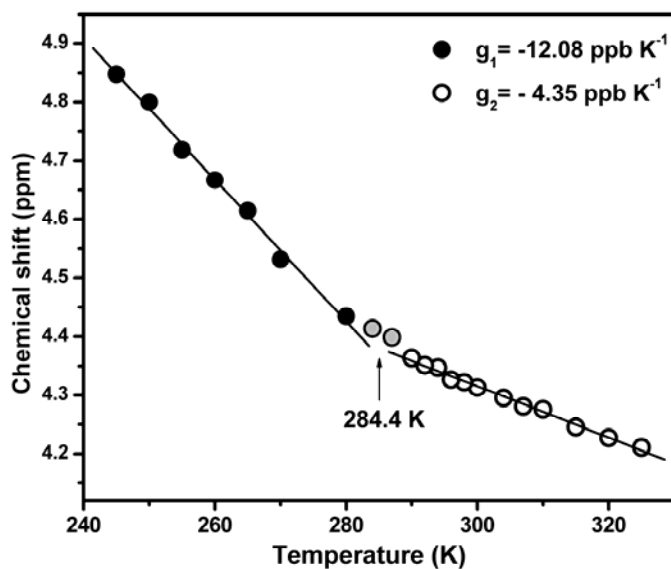


Figure 3.21: ^1H chemical shift (δ) of water as a function of temperature when the clay sample is spinning at 5 kHz at magic angle inside NMR spectrometer. Temperature dependence data from 245–280 K and 290–325 K is fitted to two independent straight lines, yielding temperature coefficient (g) values of -12.08 and -4.35 ppb K^{-1} .

change by -11.9 ppb K^{-1} in the case of bulk water [Wishart et al., 1995]. One can thus obtain information about the kind of structural environment experienced by a water molecule by monitoring δ as a function of temperature. Thus, a careful examination of δ as a function of temperature can provide details of the thermal evolution of water configurations in terms of local hydrogen-bonded geometry, especially in supercooled regime. ^1H δ obtained from MAS spectra of water trapped inside clay nanopores, plotted as a function of temperature, is shown in Figure 3.21. The temperature dependence of δ (temperature coefficient, g) could not be fitted to a single straight line in this case. Water molecules yield different values of g viz. -12.08 ± 0.4 and -4.35 ± 0.1 ppb K^{-1} when temperature is varied from 245 to 280 and 290 to 325 K, respectively. It is seen that the chemical-shift between 280 and 290 K could not be fitted to either of the straight lines. This indicates that the water molecules trapped inside the clay nanopores undergo significant changes in their hydrogen-bonding network when the temperature is lowered

from 290 to 280 K. Moreover, g values in these two regimes reveal that the trapped water resembles bulk-like water (in terms of hydrogen-bonding network) at lower temperatures ($T < 280$ K), while it exists as a less mobile liquid at higher temperatures ($T > 290$ K) as indicated by high g value of -4.35 ppb K^{-1} . This region corresponds to the HTT, observed in positron annihilation studies.

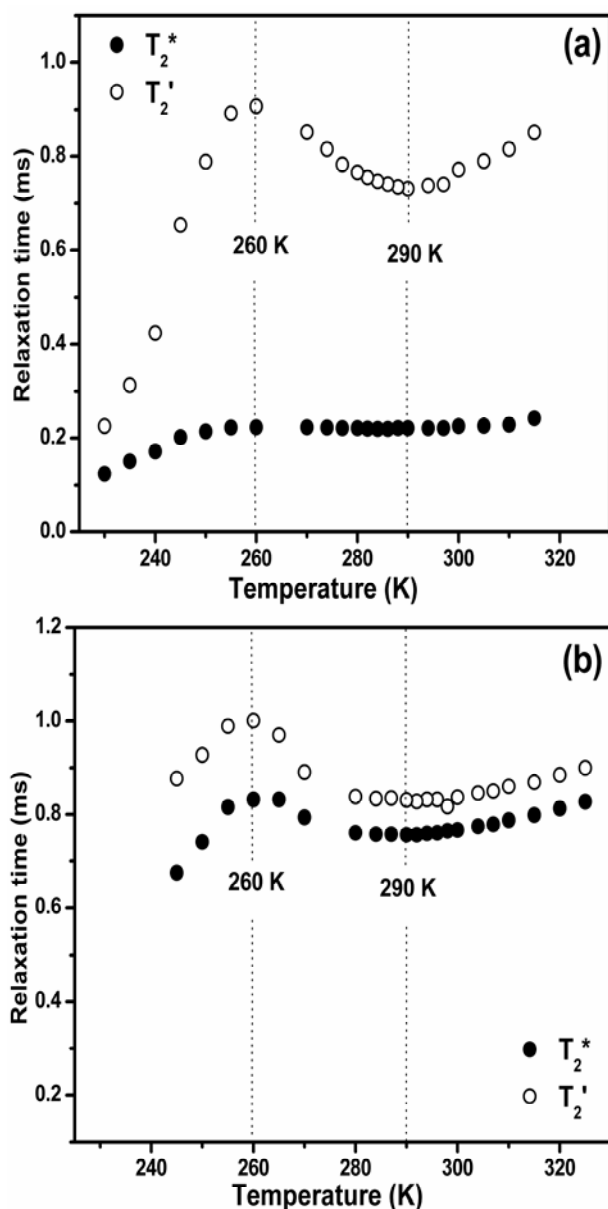


Figure 3.22: Transverse relaxation times (T_2^* and T_2') of water as a function of temperature when clay sample is (a) static and (b) spinning at 5 kHz at magic angle inside NMR spectrometer. Dotted lines in both the plots indicate inflection points in the measured T_2' values as a function of temperature.

Figure 3.22 shows the variation of T_2^* and T_2' values with temperature in static (Figure 11a) and MAS (Figure 11b) modes. All the curves show two inflection points, near 290 and 260 K. These inflection points are seen to be more pronounced in the case of T_2' values obtained from the static mode. The variation of T_2^* and T_2' at 290 and 260 K are indicative of change in dynamical properties of water and can be associated with the phase transition of confined water. The transition at 290 K can be associated with the change in local hydrogen-bonding network of water molecules as indicated by the change in the value of temperature coefficient of ^1H chemical-shift which leads to a structural rearrangement of water molecules resulting in a network having bulk-like configuration.

We now correlate the changes observed in the structural and dynamical properties of water confined in the clay nanopores as indicated by temperature coefficients (g) and transverse relaxation times (T_2^* and T_2'), respectively. At higher temperatures ($T > 290$ K), water exists as a less mobile liquid, with each molecule experiencing a strong hydrogen-bonding network ($g = -4.35$ ppb K^{-1}). The lowering of temperature in this region decreases the mobility of water molecules and, as a result, transverse relaxation times are shortened. The slow rise of transverse relaxation times when the temperature is lowered from 290 to 260 K can be explained on the basis of partial freezing/immobilization of water molecules resulting into two different regimes of molecules whose relaxation times differ significantly.

The water molecules close to the platelet surface (hydrogen-bonded to the surface as well as cations) get immobilized due to relatively attractive interaction with the surface as compared to the molecules away from the surface. The relaxation time of these immobile molecules falls off rapidly as compared to other molecules. The water molecules which are away from the surface (relatively less bound) have mobility akin to molecules present in bulk water as indicated by g value (-12.1 ppb K^{-1}) and hence, yield

much longer relaxation times. This scenario can be well understood from Figure 3.23, wherein, eye guide (solid and dashed) indicate two regimes I and II of water molecules representing faster relaxation of water molecules near the platelet surface and slower relaxation due to the molecules away from the platelet surface, respectively. The resultant of two relaxation processes results in the slow rise of $T_2'(T_2^*)$ from 290 to 260 K. As the temperature is lowered further, the overall relaxation time is dominated more and more by the water molecules in the regime II (bulk-like phase). Below 260 K, decrease in transverse relaxation time indicates decrease in the mobility of water due to the decrease in temperature.

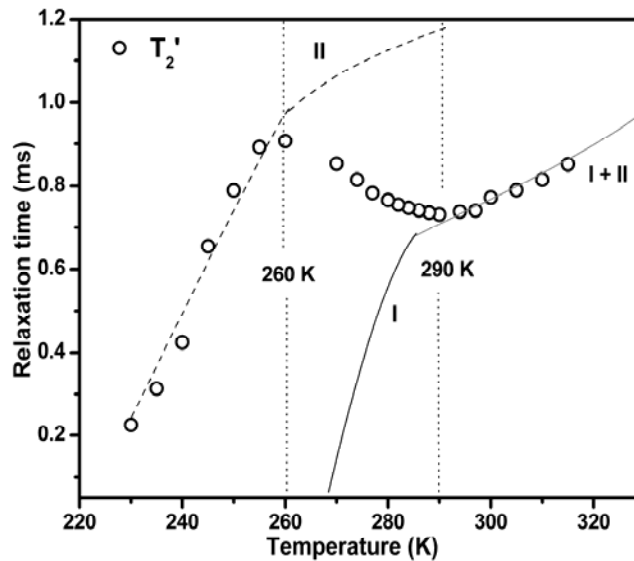


Figure 3.23: Transverse relaxation time (T_2') of water as a function of temperature obtained in the static mode. Solid and dashed lines (eye guides) represent the likely scenario of the freezing phenomenon of water layers.

3.3.2f. DRS results

Figure 3.24a and 3.24b show the three-dimensional plots of frequency (f) and temperature dependence of the measured dielectric loss i.e. imaginary part of permittivity ($\epsilon''(f)$) in hydrated and dry clay, respectively. The dielectric response of the two samples are significantly different throughout the studied temperature range.

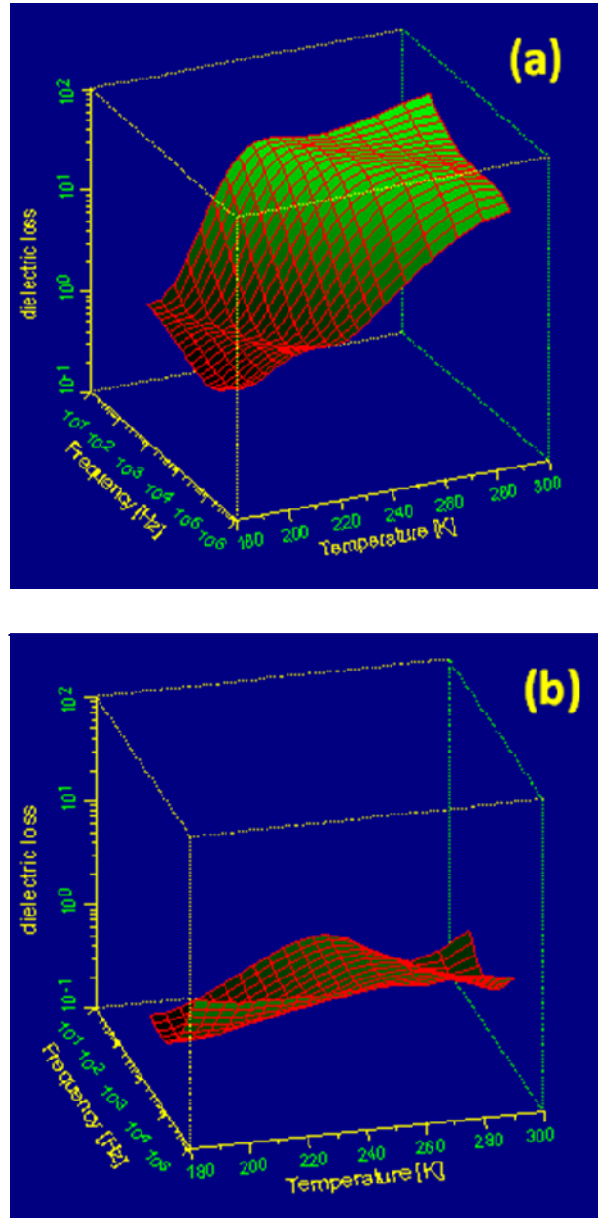


Figure 3.24: Three dimensional representation of temperature and frequency dependence of imaginary part of the dielectric permittivity ($\epsilon''(f)$) or dielectric loss for (a) hydrated and (b) dry clay.

Figure 3.25 shows the dielectric response at $T = 278$ K for both the samples, which indicates different relaxation processes in the two cases. The strong loss peak near 10^6 Hz is present in both the samples and does not show any temperature dependence. This peak is also present in the dielectric response of empty cell with the Teflon spacer,

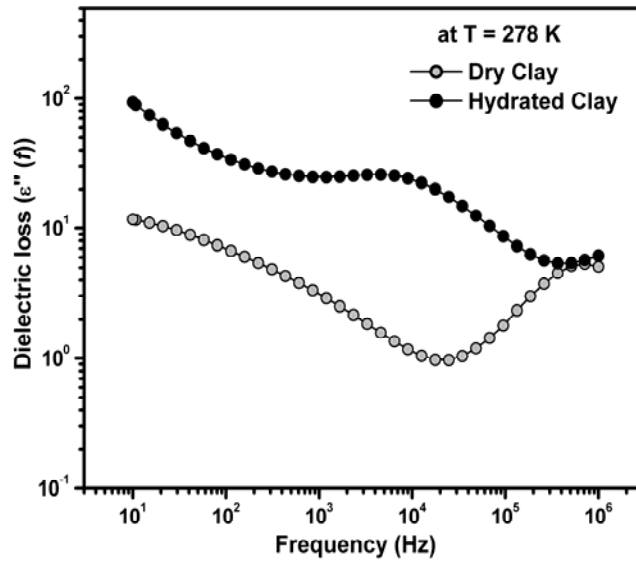


Figure 3.25: Dielectric response of hydrated and dry clay at $T = 278$ K.

and we, therefore, attribute it to the empty cell with spacer. In addition to high frequency loss peak (10^6 Hz), two more relaxation processes are seen in the dielectric response of hydrated clay. The large loss peak (*main relaxation process*) shows strong temperature dependence whereas, the weak peak (*secondary relaxation process*) is seen to be swamped by the presence of the *main relaxation process* above 210 K and hence, could not be discerned from the dielectric response in the temperature range 300-220 K (Figure 3.24). Therefore, the present study mainly concentrates on the *main relaxation process*. The peak due to *main relaxation process* observed in hydrated clay is clearly absent in the dry clay. This suggests that the *main relaxation process* arises from the water molecules confined in the clay. This peak shifts to higher frequencies with the increase in temperature (Figure 3.24a), and at 278 K it is located at about 10^4 Hz (Figure 3.25). The dipolar rotation of liquid water molecules is a fast process, of the order of 10^{-12} seconds and this time scale lies beyond the limits of detection of our instrument. Thus, the processes responsible for the *main relaxation peak* are most likely a combination of interfacial polarization involving water molecules and conductivity effects. The low

frequency dispersion is observed in both the samples and is ascribed to conductivity contribution from the sample. It may also be noted that the weak loss feature at lower temperatures in dry clay is qualitatively different from that observed in hydrated clay, and must therefore, have a different origin. Further analysis of the *main relaxation process* to obtain relaxation times has been carried out by fitting the dielectric response curves ($\epsilon''(f)$ vs. f) with the sum of a power law (d.c. conductivity) and a well known Havriliak-Negami (HN) function,

$$\epsilon''(\omega) = \frac{\sigma_{DC}}{\epsilon_0} \omega^{-n} + \text{Im} \left[\frac{\Delta\epsilon}{[1 + (i\omega\tau)^\alpha]^\beta} \right] \quad (3.13)$$

where, $\omega = 2\pi f$, $\Delta\epsilon = \epsilon_S - \epsilon_\infty$, where, ϵ_S and ϵ_∞ are static and high frequency limiting values of the dielectric constant, respectively, ϵ_0 is the permittivity of free space, σ_{DC} is the conductivity contribution, τ is the relaxation time and n , α and β are empirical exponents with values between 0 and 1. As an example of this fitting, the dielectric loss spectrum of the hydrated clay at 250 K is shown in Figure 3.26.

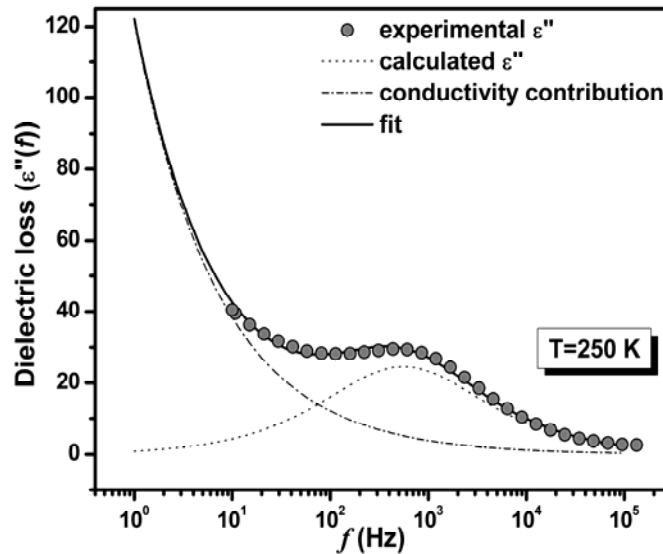


Figure 3.26: Dielectric response ($\epsilon''(f)$ vs. f) for hydrated clay at 250 K. The solid line represents the fit to the response using sum of power law and HN function; dotted and dash-dot curves represent the main relaxation process and d.c. conductivity contribution, respectively.

The *main relaxation process* is the only dominant relaxation observable at this temperature and is shown with a dotted curve along with the conductivity contribution. For the spectra at temperatures below 210 K, two HN functions are required to fit the dielectric response. However, due to small amplitude of *second relaxation process* at low temperatures (below T=210 K) it could not be discerned from the response curve.

In the case of dry clay, the only relaxation process apart from the low frequency dispersion shows weak loss in the temperature range 298-210 K. This process is seen to be different from that observed in hydrated clay, and shows Arrhenius temperature dependence of relaxation time over the studied temperature range. The activation energy of this process is found to be $E_A \approx 0.72$ eV, which is higher than that for the process observed in hydrated clay (Table 3.2, discussed below). The origin of this process is not clear but this feature is not observed in hydrated clay where it might have been swamped by low frequency dispersion.

The relaxation time τ corresponding to the *main relaxation process* in hydrated clay shows strong temperature dependence over the range 298-210 K. The plot of temperature dependence of τ is given in Figure 3.27. It is interesting to note that the relaxation time, τ follows Arrhenius behavior at temperatures below 240 K and a non-Arrhenius behavior above 240 K. In fact, above 240 K, the behavior could be very well approximated by a Vogel-Fulcher law (see below). The temperature dependence of τ for the *main relaxation process* are fitted as,

$$\tau(T) = \tau_o \exp\left(\frac{E_a}{k_B T}\right) \quad \text{for } T \leq 240 \text{ K} \quad (3.14)$$

$$\tau(T) = \tau_o \exp\left(\frac{BT_o}{(T - T_o)}\right) \quad \text{for } T \geq 240 \text{ K} \quad (3.15)$$

where, E_a is activation energy, k_B is Boltzmann constant, T is the temperature, B is a dimensional normalization factor, τ_0 is a pre-exponential factor and T_o is Vogel-Fulcher (VF) temperature. The best fit values for the Arrhenius and VF behavior are tabulated in Table 3.2.

Table 3.2: Fitting parameters for hydrated clay; Arrhenius fit ($T < 240$ K) and Vogel-Fulcher fit ($T > 240$ K).

Arrhenius Fit		Vogel-Fulcher Fit	
Parameter	Value	Parameter	Value
E_a	0.257 eV	E	0.027 eV
τ_0	7.17×10^{-9} s	τ_{VF}	5.34×10^{-7} s
----	----	T_{VF}	200 K

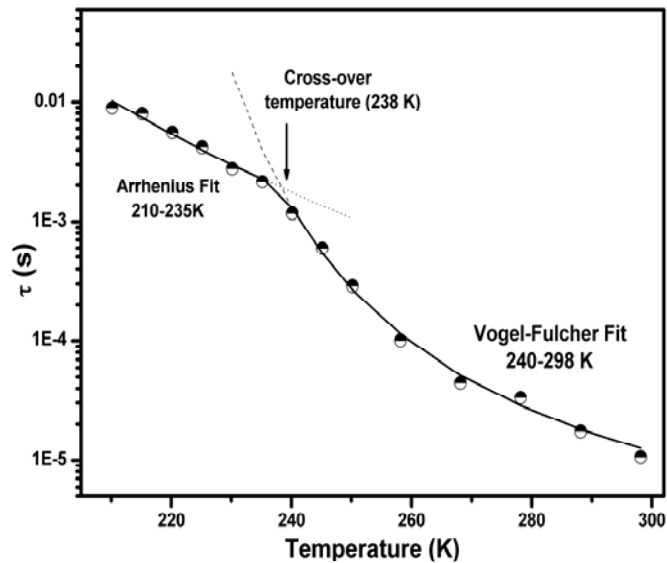


Figure 3.27: Temperature dependence of relaxation time (τ) for the main relaxation process in hydrated clay, fitted to Arrhenius (210-235 K) and Vogel-Fulcher (240-300 K) functions.

The variation of relaxation time with temperature shows that the dynamics of water confined in clay nanopores shows a cross over from non-Arrhenius to Arrhenius

temperature dependence around 240 K. However, the values of the relaxation times are much slower than those reported for rotational dynamics of water molecules [Swenson et al., 2000; Bergman et al., 2000] and hence cannot be attributed to these processes. As mentioned earlier, this relaxation may be a combination of interfacial polarization and conductivity effects involving the water molecules. Even so, the cross over from one type of temperature dependence to another, as observed in Figure 3.27, suggests a transition. This change in behavior near 240 K matches well with the low-temperature transition observed in our positron annihilation study. Since conductivity effects are likely to be dominant in liquid water as compared to frozen water, we may infer that substantial amount of liquid water exists above 240 K. On this basis, we may conjecture that the observed cross over at 240 K is related to the partial freezing of supercooled water which results in the change in conductivity contribution owing to the frozen phase of water.

3.3.2g. Discussion

Two phase transitions viz. above (HTT) and below (LTT) the bulk freezing temperature of water have been observed for water confined in clay nanopores. PAS is seen to be sensitive to both the transitions unlike other techniques. While DSC and DRS are not sensitive to HTT, NMR provides the strongest evidence of structural and dynamical changes associated with this transition. As discussed earlier, two layers of water molecules can be accommodated between the clay platelets. These water molecules exist in two different regimes, molecules hydrogen-bonded to platelet surface as well as cations are more bound as compared to the molecules away from the surface [Skipper et al., 1991]. Based on our earlier studies, HTT is expected to be associated with the molecules experiencing more attractive interactions with the surface of the platelets. NMR study reveals that HTT is associated with the structural rearrangement of water molecules as reflected in the variation of ^1H chemical-shift with temperature. The change

of slope of chemical-shift with temperature (g) from -4.35 to -12.08 ppb/K around 284.4 K indicates alteration in hydrogen-bonded network of water molecules. The increase in τ_3 and S -parameter below HTT signify structural alterations in terms of increase in free volume/open space and is consistent with NMR observation. The transverse relaxation time measured in NMR reveals change in dynamical properties of water molecules at HTT. The slow rise around 290 K (near HTT) is explained on the basis of different relaxation times which have arisen due to the existence of different regimes of confined water (discussed earlier). This has been correlated to the immobilization of water molecules (faster relaxation) close to the platelet surface (bound molecules) as compared to the slower relaxation of molecules away from the platelet surface. It is also to be noted that a marked hysteresis is observed for HTT in PAS owing to thermal stability of the phases at the surface. On the basis of NMR and PAS results, HTT is expected to be associated with the phase behavior of water molecules bound to the platelet surface i.e. immobilization of these water molecules together with the structural rearrangement of confined water. Below HTT, rest of the water molecules tend to form hydrogen-bonded network and behave as bulk-like phase as reflected from the variation of ^1H chemical-shift with the decreasing temperature ($g = -12.08$ ppb/K).

The presence of LTT is observed from PAS, DSC and DRS. This transition can be related to water molecules forming hydrogen-bonded network similar to bulk water ($g = -12.08$ ppb/K). The S -parameter has shown significant change at this transition unlike f_v , I_p and ^1H chemical-shift. The change in S -parameter can be explained on the basis of alteration in electron momentum distribution owing to the change in the phase behavior of water at this temperature. The significant and nearly constant value of I_p (~11%) shows that the confined water does not freeze till the lowest temperature studied. In DSC, a peak has been observed corresponding to LTT. This low temperature peak has been attributed

to the depression in freezing/melting point of confined water by many authors. However, its correspondence to incomplete freezing has been explained by Kozłowski et al. Though DRS is sensitive to relaxation dynamics of molecules (dipolar relaxation), in the present case, the measured relaxation time corresponds to the combination of interfacial polarization and conductivity contribution from the sample. This relaxation process shows a cross over from non-Arrhenius to Arrhenius behavior around 240 K. The observed cross over in the behavior of relaxation time can be correlated to change in the phase behavior which results in the change in conductivity contribution of the sample. Though no clear evidence for any structural or dynamical change for confined water is observed at LTT, the results from PAS, DSC and DRS indicate incomplete freezing and/or depression in freezing /melting point of confined water.

3.4. Conclusions

Phase transitions in nanodroplets (ethylene glycol and isopropanol confined in ZSM 5 and, water confined in saponite clay) have been studied using different techniques *viz.* PAS, NMR and DRS. The structural and dynamical properties were indexed to probe the phase transitions. The effect of fluid-surface interfacial interaction on the freezing/melting point of confined ethylene glycol and isopropanol was examined. An elevation in the freezing/melting point was seen and attributed to the attractive interaction between the liquids and wall of the confining geometry (ZSM 5). However, the strength of the (attractive) interaction has significant influence on the extent of the shift, as clearly seen from different degree of shifts in the two cases. The strong interaction in the case of isopropanol owing to inter-molecular hydrogen bonding resulted in higher degree of shift in contrast to ethylene glycol where, due to both inter- and intra molecular hydrogen bonding the effective interaction with the surface is weaker.

The phase behavior of nanoconfined water in slit like pores of saponite was studied. The effect of strong hydrogen bonding between water molecules as well as water molecules and the surface of platelet strongly influence the structural and dynamical properties of confined water. Two phase transitions *viz.* above (HTT) and below (LTT) the bulk freezing temperature of water were observed and attributed to different regimes of confined water (role of interfacial interactions). The presence of HTT is the first report on the phase behavior of nanoconfined water. The structural and dynamical parameters suggest that HTT involves structural modification in terms of hydrogen-bonded network and dynamic arrest/immobilization of water molecules close to the platelet surface owing to attractive interaction with the surface. On the other hand, LTT is conjectured to be associated with the partial freezing of confined water as evident from PAS, DRS and DSC. The present study mainly highlights the effect of role of interfacial interaction on the phase transition of confined liquids.

CHAPTER-IV

Pore architecture of membranes

Membranes based processes are an active area of interest for scientific community engaged in developing new membranes and understanding the microscopic aspects of their transport mechanism. Membrane processes are broadly divided on the basis of the intrinsic pore sizes in liquid as well as gas permeation based separation schemes. For example, reverse osmosis, pervaporation as well as gas separation schemes have pore sizes below 0.8 nm while nanofiltration of liquid or gas separation using ceramic membranes have pore sizes in the range of 0.8 to 1.5 nm. Ultrafiltration for liquid permeation refers to pore sizes 2-60 nm, whereas membranes with pore sizes larger than 60 nm are used in microfiltration processes. In the dense and homogeneous polymer membranes with pore sizes smaller than 1 nm, the mechanism is primarily known as solution-diffusion model where the permeability is given as the product of diffusion coefficient and solubility of liquid or gas, as the case may be, in the polymer matrix [Baker et al., 2004].

Hydrophobic supported liquid membranes (SLMs) having pore sizes larger than 100 nm provide a nice alternative to conventional liquid-liquid extraction process such as solvent extraction [Luque et al., 2000; Allen et al., 1999 and Baker et al., 1977]. In recent years, SLMs have received considerable attention for the recovery of metallic ions from waste water streams due to its characteristics such as low energy consumption, high selectivity and rapid extraction capacity factor. SLM extraction is based on three phase system with an organic phase sandwiched between two aqueous phases (inset Figure 4.1) [Joensson et al., 1992, Barcelo et al., 1997 and van de Merbel et al., 1993]. The organic phase containing the metal ion selective extractant and solvent is immobilized in a porous hydrophobic membrane. This membrane acts as an intermediary separating the feed phase, which contains the species to be removed, and the stripping phase in which the species to be transferred is recovered [Reyes-Aguilera et al., 2008]. As in solvent

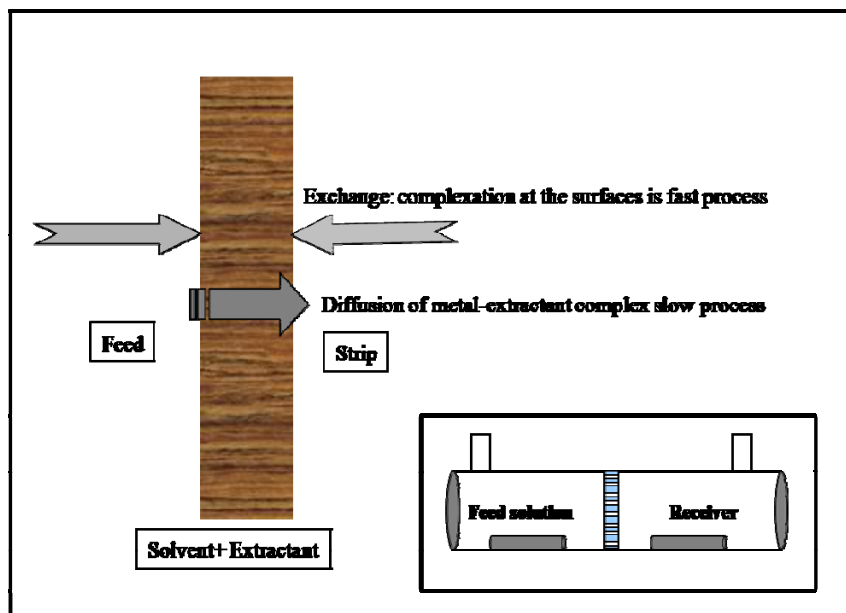


Figure 4.1: SLM based three phase extraction system.

extraction, the extractant is responsible for the extraction of the species of interest; in this case, however, the extraction and recovery processes are carried out simultaneously, with the advantage that, unlike solvent extraction, SLM uses minimum quantities of organic phase [Valenzuela et al., 1993], which allows the use of highly selective extractants and diminishes the risk of environmental contamination at the same time. The transport mechanism that dictates this process has two steps (i) the exchange of metal ion in the feed side which is a fast process and (ii) the diffusion of metal-extractant complex which is a slow process, primarily Fickian in nature. Overall, the mechanism is solution-diffusion in nature as described earlier for the dense homogeneous phase, only difference being that the solubility term is equivalent to the fast exchange process at the surface. The diffusion of the metal-extractant complex (Fickian) across the membrane thickness is similar to that used in the dense homogeneous phase (Figure 4.1).

Membrane permeability and transport properties are governed by the structural characteristics like pore architecture of the membrane which essentially refers to pore

size, its distribution, pore fraction, porosity and pore interconnectivity. There are a host of techniques such as small angle X-ray/neutron scattering (SAXS/SANS), gas absorption techniques, ellipsometric porosimetry, electron microscopy that can characterize the size as well as pore fraction, however, they fail to evaluate the extent of pore interconnectivity. In this regard, positron annihilation spectroscopy (PAS) can be used as a probe to characterize pore architecture not only in terms of pore size, pore size distribution, pore fraction, porosity (open/closed) but also to evaluate the pore interconnectivity through the evaluation of positron/Ps mobility in porous materials. Essentially, the mean free path of Ps in the pores gives an idea about the length scale over which pores may be interconnected thus providing a complete idea about the pore architecture. Figure 4.2 represents the positron/Ps behavior in a porous membrane containing closed, open and interconnected pores. Positron injected into the porous system forms Ps and then diffuses within the porous network by making collisions with the walls of the pores. In the event of highly porous network or in vacuum, annihilation from the intrinsic triplet state (3γ annihilation) is enhanced. Ps escaping into the vacuum (3γ annihilation) is a telltale indicator of highly porous (open porosity) and interconnected network. The technique involves slow positron beam depth profiling to obtain annihilation profile in the porous membrane, which is used to evaluate Ps diffusion/mobility within the porous network. The $3\gamma/2\gamma$ ratio is mainly used to characterise porosity or Ps reemission from surfaces [Petkov et al., 2001 and 2003; Gidley et al., 2006] through the evaluation of Ps diffusion length inside the membrane using VEPFIT analysis.

In the present work, polytetrafluoroethylene (PTFE) SLMs and track etched polycarbonate (PC) membranes have been studied for their pore architecture using slow positron beam depth profiling. The $3\gamma/2\gamma$ profile has been utilized as a measure of

porosity and interconnectivity of pores through Ps diffusion length in the membranes obtained by fitting the profiles. A correlation between the pore architecture and permeability of metal ions through the membranes (PTFE) has been observed.

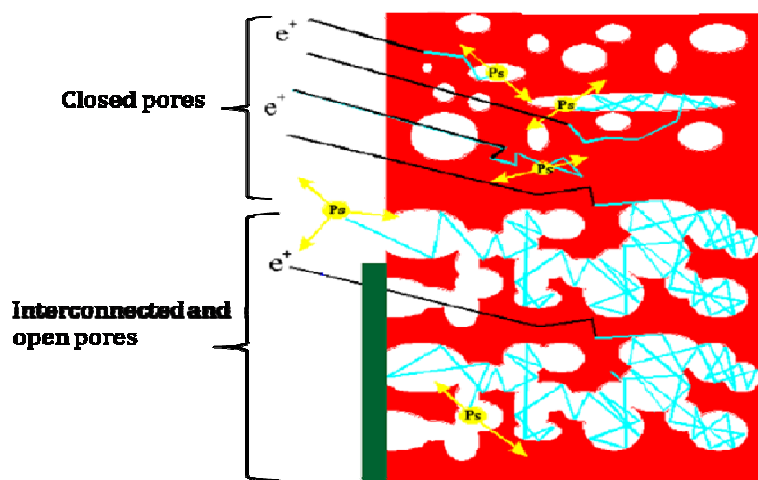


Figure 4.2: Schematic of positron/Ps behavior in a porous membrane containing closed, open and interconnected pores [Gidley et al., 2006].

4.1. Materials

Two varieties of commercially available macroporous membranes *viz.* PTFE SLMs (70 μm) and track etched PC membranes (25 μm) with quoted pore size in the range of 0.2-5 μm and 0.03-0.2 μm , respectively have been studied for their pore architecture. The membrane surface has been coated with 10 nm gold diffusion layer deposited by vacuum evaporation. The track etched PC membranes were obtained from Whatman Asia Pacific Private Ltd. These membranes were formed by the bombardment of medium mass charged particles with sufficient energy to perforate 10 μm polycarbonate sheets in the charged particle accelerator. After irradiation with charged particles, these membranes were subjected to chemical etching to form cylindrical pores having desirable diameter. The pores formed in these membranes have straight cylindrical shape.

4.2. Experimental Techniques

4.2.1. Conventional characterization of the membranes

Polytetrafluoroethylene Supported liquid membranes

The densities of PTFE membranes with pore size 0.2 (A), 0.45 (B), 1.2 (C) and 5 μm (D) were 0.84, 0.70, 0.55 and 0.56 g/cc, respectively. Membrane porosity (ϕ) is the fraction of the total membrane volume that is porous, and was calculated from the densities (d) of the membrane and its compact form as [Baker et al., 2004],

$$\Phi = 1 - (d_{\text{membrane}} / d_{\text{compact}}) \quad (4.1)$$

The solvent uptake method was also used to calculate the porosity by measuring the sorbed fraction of solvent. For this, membranes were soaked with dodecane and the weight difference of the dry and dodecane sorbed membranes was measured. The linear relation between the porosity and sorbed fraction showed that there is no swelling of the membranes and it can be used as a measure of the porosity of the membranes. The calculated porosity using Eq. 4.1 and the sorbed fraction of dodecane are given in Table 4.1.

Table 4.1: *Physical parameters of PTFE membrane A, B, C and D.*

Membrane	Quoted pore size (μm)	Density (g/cc)	Porosity	Sorbed fraction
A	0.2	0.84	.618	.603
B	0.45	0.70	.681	.704
C	1.2	0.55	.750	.787
D	5.0	0.56	.745	.806

The sorbed fraction was seen to be consistent with the calculated total porosity. Scanning electron microscopy (SEM) measurements for characterizing the surface morphology

were carried out in back scattering mode with 1200X magnification. The chemical nature of the membranes (impurities if any) was examined by attenuated total reflection infra red spectroscopy (ATR-FTIR). A PIKE MIRacle™ Attenuated total reflection (ATR) accessory equipped with a single reflection diamond ATR crystal was used for the analysis. The MIRacle accessory was fitted with a high pressure clamp, providing intimate contact between the sample and ATR crystal. The samples were placed over ATR crystal and maximum pressure was applied using the slip-clutch mechanism.

4.2.2. Small angle X-ray scattering

Polytetrafluoroethylene Supported liquid membranes

SAXS is a powerful non-destructive technique to investigate structural features on the length scale ranging from one to hundred nanometers. SAXS measurement was carried out to investigate the presence of mesoscopic structure in the membranes. It was done using small goniometer mounted on 12 kW Rigaku rotating anode X-ray generator with CuK α radiation. Intensities were measured by transmission method using scintillation counter with pulse height analyzer. Intensity ($I(q)$) was recorded as a function of wave vector transfer, $q (= 4\pi\sin\theta/\lambda)$, 2θ being scattering angle and λ is the wave length of incident X-ray, ($\lambda = 0.154$ nm) in the steps of scattering angle 2θ . The measured intensities were corrected for absorption and slit smearing effects [Schmidt et al. 1960].

4.2.3. Positron annihilation lifetime spectroscopy

Polytetrafluoroethylene Supported liquid membranes

The conventional positron annihilation lifetime (PALS) measurements were carried out using a pair of plastic scintillation detectors with a fast-fast coincidence system with time resolution of ~ 220 ps under 10^{-2} torr vacuum. Measurements were

carried out using a ^{22}Na source in sandwich configuration. Several pieces of the membranes A, B, C or D as the case may be, were taken on either side to ensure that positrons annihilate in the sample. The life-time spectra were fitted using routine PATFIT-88 program [Kirkegaard and Eldrup, 1989].

4.2.4. Doppler broadening and $3\gamma/2\gamma$ annihilation radiation measurements

Polytetrafluoroethylene Supported liquid membranes and polycarbonate membranes

Beam based Doppler broadening and $3\gamma/2\gamma$ annihilation radiation measurements were carried out as a function of positron incident energy (200 eV- 20 keV) in pristine and gold coated membranes, as the case may be. A 30% relative efficiency High purity germanium (HPGe) detector with a resolution of 2 keV at 1332 keV of ^{60}Co was used for Doppler broadening and $3\gamma/2\gamma$ annihilation measurements. Spectra with 5×10^5 counts were acquired at each energy. The detector placement was perpendicular to the beam and ~ 3 cm away from the sample. For Doppler broadening measurements, the ratio of integral counts within a ~ 1.8 keV energy window, centered at 511 keV and the total photopeak area was used to measure the S -parameter. The energy spectra were used to calculate $3\gamma/2\gamma$ ratio which measures the self annihilation of Ps from its triplet state (o -Ps). Counts in the energy region 383 keV to 475 keV and 497 keV to 522 keV in full energy spectra were taken as 3γ and 2γ annihilation contributions, respectively. The obtained $3\gamma/2\gamma$ profiles were fitted using VEPFIT to determine the diffusion length of Ps in the membranes.

4.2.5. Transport properties (permeability of metal ions)

Transport properties of PTFE SLMs were studied in terms of permeability of metal ions *viz.* Am^{+3} and Pu^{+3} through these membranes. The membrane containing the extractant N,N,N',N'-tetraoctyl diglycolamide (TODGA) in dodecan solvent separates

the two compartments viz. the feed chamber containing the metal ions (in 0.1 M HNO₃) and the receiver chamber (0.1 M HNO₃). Both the chambers were stirred continuously using a magnetic stirrer and known concentration of tracer (Am⁺³ and Pu⁺³) was added to the feed compartment. The concentration of these tracers were monitored (using liquid scintillation counting) in the receiver compartments as a function of time. The permeability coefficients (P_t) were calculated using the expression [Bansal et al., 2005],

$$\ln(C_{f,t}/C_{f,o}) = -(Q/V_f) P_t \quad (4.2)$$

where, $C_{f,t}$ and $C_{f,o}$ are the concentration of the metal ion in the feed phase at time ' t ' and at the starting of the experiment, respectively, V_f is the feed volume and Q is the effective membrane area. Q is expressed as the product of the geometrical surface area (A) and the porosity (ϕ).

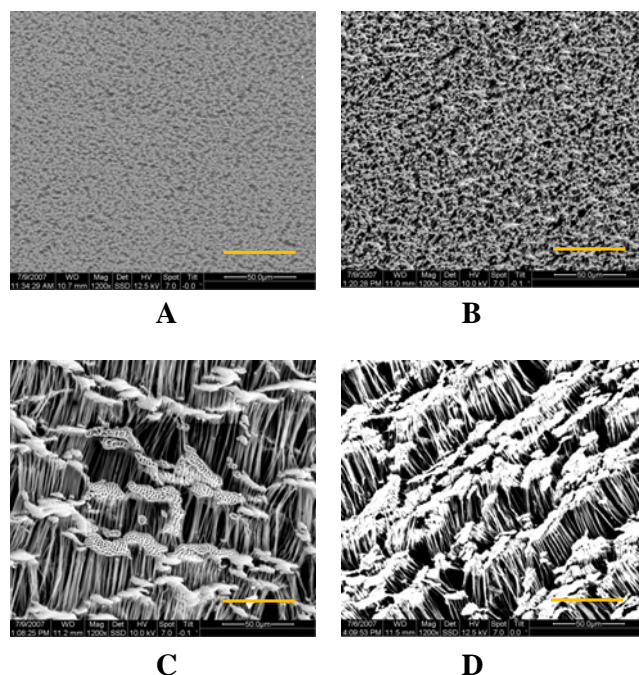


Figure 4.3: SEM images of PTFE SLMs with pore sizes as; A (0.2 μm), B (0.45 μm), C (1.2 μm) and D (5.0 μm). Yellow line indicates 50 μm length scale.

4.3. Results and discussion

4.3.1. Polytetrafluoroethylene Supported liquid membranes

4.3.1a. *Surface morphology and chemical nature*

Surface morphology of the membranes as characterized by SEM is shown in Figure 4.3. SEM images show that these membranes have different surface morphology and can be categorized into two classes. Membranes A and B show granular structure with small pores, whereas membranes C and D show fibre like structure with large open pores. The porosity data (Table 4.1) for the membranes is seen to be consistent with the morphology. Figure 4.4 shows the ATR-FTIR spectra for all the membranes. The presence of only two peaks at 1275 cm^{-1} and 1205 cm^{-1} characteristics of PTFE corresponding to C-C and C-F bonds ensures that there are no other chemical impurities that might influence the Ps formation probabilities.

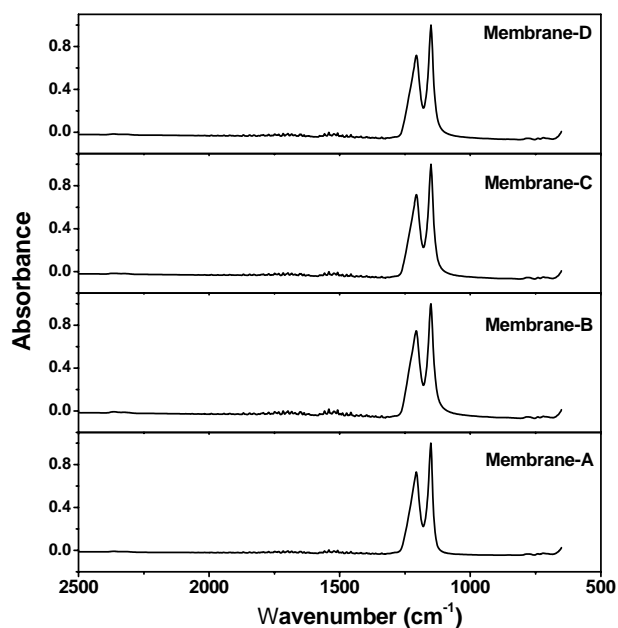


Figure 4.4: ATR-FTIR spectra of PTFE SLMs.

4.3.1b. *Small angle X-ray scattering*

Experimental corrected SAXS profiles are shown in Figure 4.5. The profiles for all the membranes are seen to be similar and vary as q^{-4} in the high- q region suggesting smooth surface for the scattering objects (pores in the present samples). The SAXS

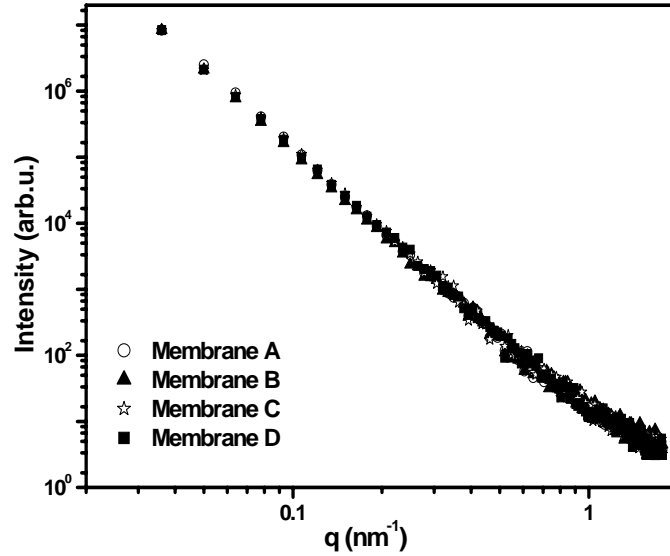


Figure 4.5: *Experimental corrected SAXS profiles.*

intensity $I(q)$ from an ensemble of pores or particles having uniform shape and polydispersity in size can be expressed as [Gunier et al., 1955 and, Glatter et al., 1982],

$$I(q) = C \int P(q, R) N(R) (V(R))^2 dR \quad (4.3)$$

where, C is independent of ' q ' but depends on the scattering length density contrast between the solid matrix and pore and, number density of the pores. $P(q, R)$ is square of the scattering form factor for particle of radius R . The expression for $P(q, R)$ for spherical scattering objects is [Gunier et al., 1955 and, Glatter et al., 1982],

$$P(q, R) = \left[\frac{3(\sin(q, R) - qR \cos(q, R))}{(q, R)^3} \right]^2 \quad (4.4)$$

where, $V(R)$ is volume of the pore of radius R and $N(R)$ is the pore radii distribution function. The limits of integration depend on the q -range of the profiles. For log-normal distribution, $N(R)$ is given by [Aitchison et al., 1957],

$$N(R) = \frac{1}{\sqrt{2\pi\sigma^2 R^2}} \exp \left[-\frac{[\ln(R/R_o)]^2}{2\sigma^2} \right] \quad (4.5)$$

where, R_o and σ are parameters of the distribution. Figure 4.6 shows fit to the data for membrane A (quoted pore size 200 μm) and the pore size distribution (inset). From the fitted parameters, the mean radius ($\langle R \rangle$) of the pores is estimated using the relation, $\langle R \rangle = R_o \exp(\sigma^2/2)$ whereas, the variance in the distribution is given by, $w = [\langle R^2 \rangle - \langle R \rangle^2]^{1/2}$. The size of the pores as estimated by SAXS is, $\langle R \rangle = 38.3$ nm and $w = 29.5$ nm. It has been observed that all the membranes contain pores of 38.3 nm size.

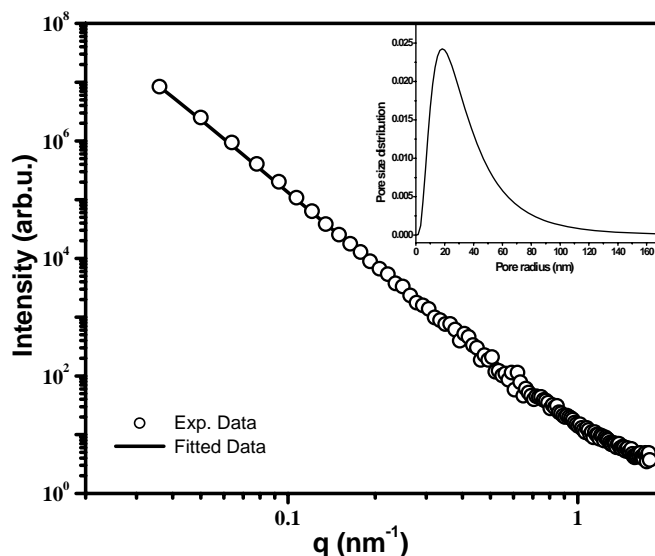


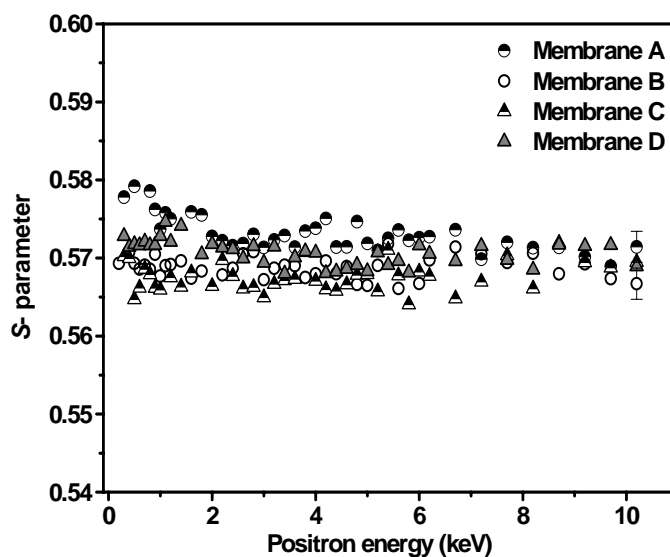
Figure 4.6: Fit to the experimental SAXS profile for membrane A; inset shows the obtained pore size distribution.

4.3.1c. Positron annihilation life time spectroscopy

PALS measurement has been deliberately carried out with small time dispersion to evaluate the smaller pores (free-volume) as, 39 nm (measured from SAXS) and the quoted larger pores would yield the near saturation life-time of *o*-Ps i.e. 142 ns. Pick-off *o*-Ps life-time (τ_3), intensity (I_3) and average pore size estimated using TE equation (Eq. 1.5) are given in Table 4.2. It is seen that Ps intensities and life time are nearly equal in all the membranes and all the membranes contain pores in the range of 0.26-0.29 nm.

Table 4.2: *o*-Ps life time, Intensity and calculated pore size (PALS measurement)

Membranes	<i>o</i> -Ps pick-off lifetime, τ_3 (ns)	Intensity, I_3 (%)	Radius (nm)
A	1.92	5.99	0.28
B	1.76	6.22	0.26
C	1.98	7.03	0.29
D	1.82	5.59	0.27

**Figure 4.7:** The *S*-parameter profile for pristine PTFE SLMs. Error on the data is indicated on one of the data points in the figure.4.3.1d. Doppler broadening and $3\gamma/2\gamma$ annihilation spectroscopy

The *S*-parameter and $3\gamma/2\gamma$ ratio as a function of positron energy (depth) for all the membranes (as received/pristine) are shown in Figure 4.7 and 4.8, respectively. The *S*-parameter profiles are seen to be flat and no significant difference has been observed for membranes A, B, C and D. This is similar to the behavior of *S*-parameter in nonporous PTFE. Flatness of the profiles in the present case may also be due to the highly porous nature of the membranes. It is, therefore, not useful in elucidating any information on Ps

mobility. The $3\gamma/2\gamma$ profile (Figure 4.8), on the other hand, shows distinct changes with positron incident energy as well as between the membranes. The profiles carry information about the Ps mobility and fitted using VEPFIT to extract Ps diffusion length (L_+). The fit to the experimental data, represented by solid lines is shown in Figure 4.9. The diffusion lengths are seen to be 39, 102, 72 and 107 nm for membrane A, B, C and D, respectively. The obtained diffusion length in the case of membrane C and D are seen to be very small in spite of the large size of pores as compared to membrane A and B. It is seen from SEM that membrane C and D have different morphology compared to A and B. Also, the porosities in the former are larger. From the measured Ps diffusion length it is seen that although there is a sharp increase in L_+ going from A to B, the values for C and D seem to be underestimated considering the porosity and morphology.

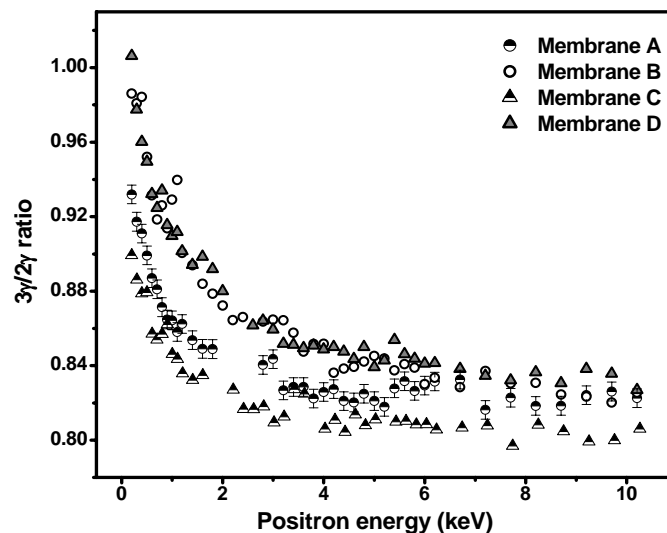


Figure 4.8: *The $3\gamma/2\gamma$ profiles for pristine PTFE SLMs. Error on the data is same for all the membranes and is shown for one of the membranes in the figure.*

In order to get a better understanding in to this aspect, $3\gamma/2\gamma$ profile for the membranes B and C (one membrane from either category) with a surface diffusion layer of gold (10 nm) has been measured. This prevents Ps from escaping in to the vacuum that

might modify $3\gamma/2\gamma$ profile. The $3\gamma/2\gamma$ profile for goldcoated and the pristine membranes (B and C) are compared in Figure 4.10.

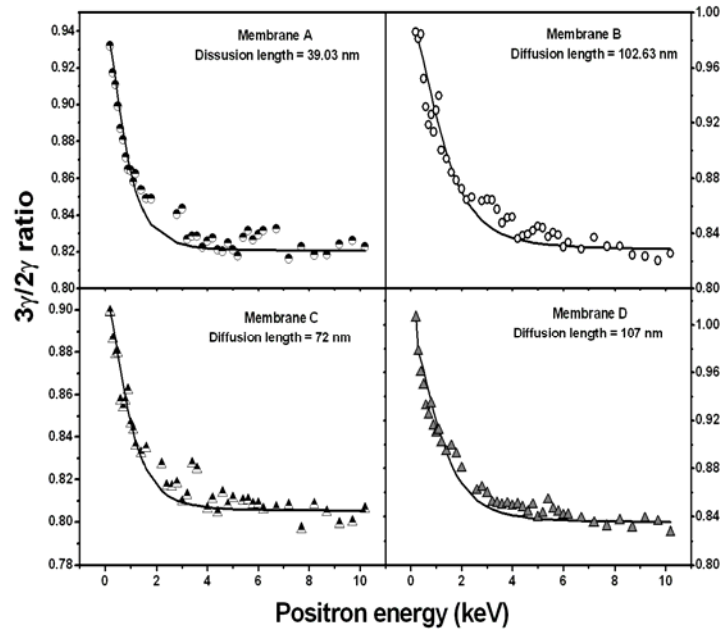


Figure 4.9: VEPFIT analysis of $3\gamma/2\gamma$ ratio for PTFE SLMs. Solid lines represent fit to the experimental data.

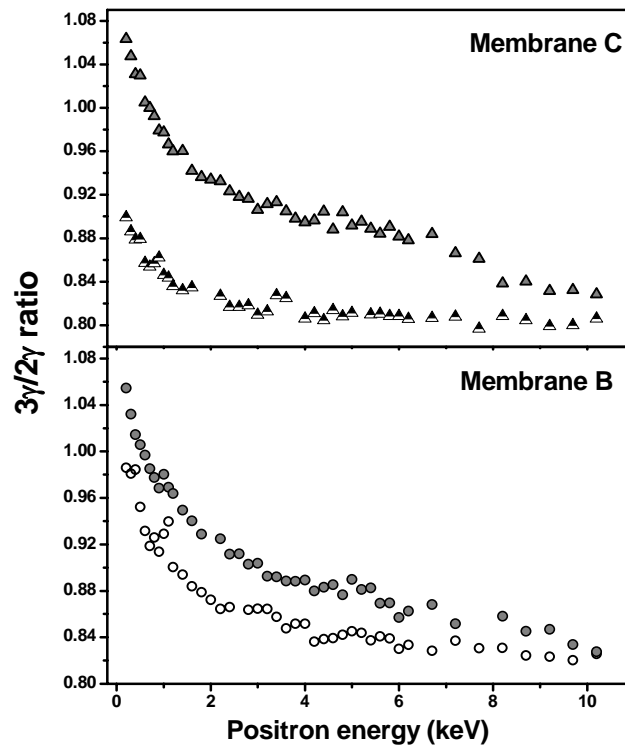


Figure 4.10: $3\gamma/2\gamma$ profiles for Pristine and goldcoated PTFE (soild symbols) membranes B and C.

At thermal velocity, Ps can travel a substantial distance away from the surface prior to annihilation. Considering the experimental arrangement (detector perpendicular to sample), Ps escape from the membrane surface due to open surface porosity has resulted in the decrease in 3γ detection leading to decrease in $3\gamma/2\gamma$ ratio in the surface region. In the case of membrane C, the open porosity on the surface seems to be much higher than the membrane B as reflected from the large difference in $3\gamma/2\gamma$ ratio (surface region) in the former. The fitting of $3\gamma/2\gamma$ profiles obtained in the case of goldcoated membranes show much higher L_+ viz. 400 and 3000 nm for B and C, respectively as compared to 102 and 72 in the corresponding pristine membranes. By preventing Ps to escape from the surface and make them coral within the membrane reveals the true picture of the pore architecture of the membranes. The L_+ is related to the mean free path of Ps and hence, measure of pore interconnectivity. The obtained L_+ indicate that pore interconnectivity is much higher in the case of fibrous membranes (C and D) as compared to membrane A and B having granular structure.

4.3.1.e. Permeability of metal ions and transport properties

Figure 4.11 shows the permeability of Pu^{+3} and Am^{+3} for all the four membranes (A, B, C and D) with TODGA as extractant, *n*-dodecan as solvent and nitric acid in feed as well as receiver cells. A systematic decrease in permeability is seen from A to D (i.e. increase in pore size) under identical condition. Similar trend has also been seen in earlier studies on the permeation of UO_2^{2+} through identical PTFE SLMs [Mohapatra et al., 2006 and Lakshmi et al., 2004]. It is known that permeability is proportional to ϕR^2 (R being radius of pore) and inversely proportional to the thickness of the membrane [Baker, 2004]. The latter being identical in all the membranes, the permeability should have been highest in the case of membrane D contrary to what is observed in the present study.

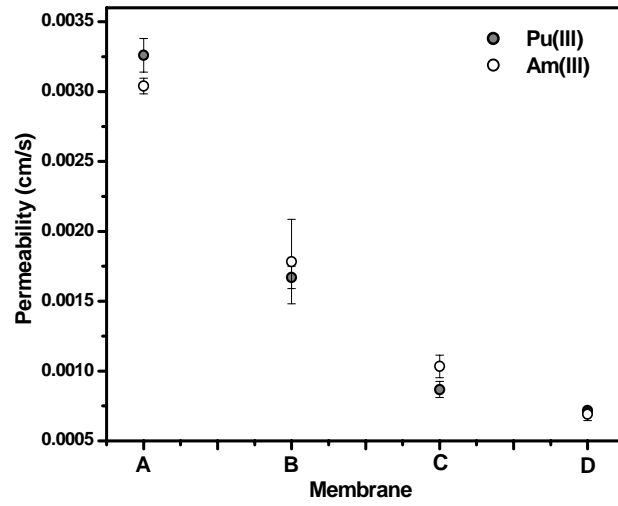


Figure 4.11: Permeability of Pu (III) and Am (III) through PTFE membranes.

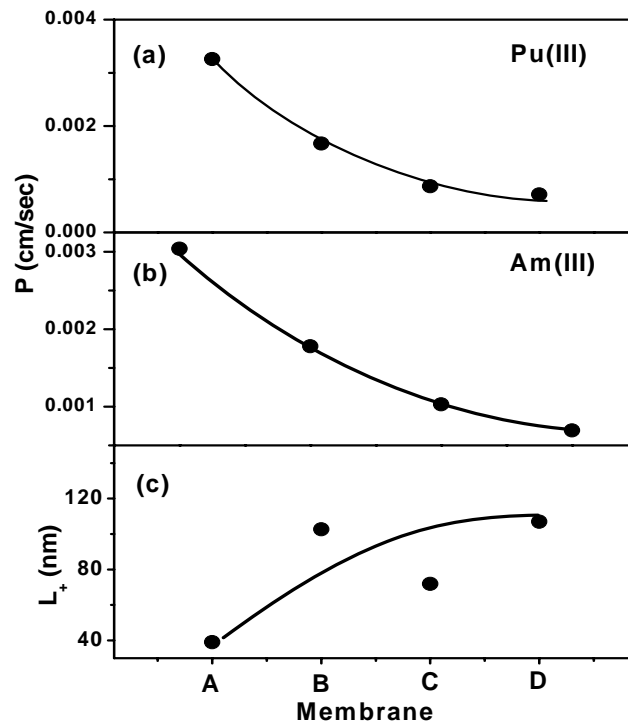


Figure 4.12: Correlation between Permeability of ions in PTFE membranes and P_s diffusion length.

An inverse correlation between the permeability and L_+ has been observed for PTFE SLMs (Figure 4.12) i.e. higher the L_+ , lower is the permeability. A systematic increase in L_+ can be ascribed to increase in pore interconnectivity or pore overlap, resulting in enhancement in the mean free path of the Ps atom. Such interconnection of pores provides alternative path to the diffusing metal ion complex which could be longer than the thickness of the membrane it has to travel to reach the receiver compartment. Overall this would result in increase in the time taken by the metal ions to permeate through the membrane resulting in decrease in permeability. In the parlance of membrane science this is referred to as tortuosity. Permeability scales inversely with tortuosity i.e. higher the tortuosity lower is the permeability [Baker et al., 2004]. Pore interconnectivity is the main microscopic reason for the increase in the tortuosity in a membrane as evident from the measured L_+ . The large pore interconnectivity is seen to have deleterious effect on the permeability (inverse relation between the two) of metal ions through the membrane.

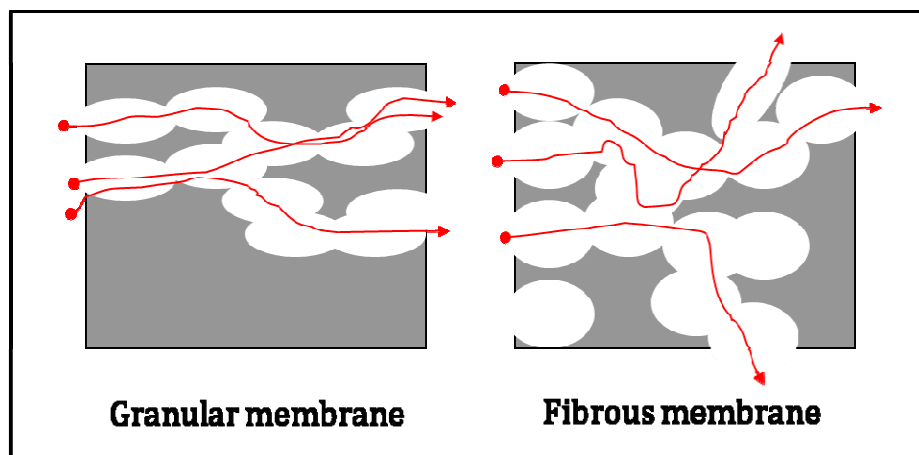


Figure 4.13: *Impression of pore architecture in porous membranes.*

Collating all the information from conventional as well as positron beam studies, an impression of pore architecture of the studied membranes (granular and fibrous) is depicted in Figure 4.13. As seen, pore overlap increases in the case of fibrous membrane

having large size pores, resulting in large interconnectivity between the pores. Also, fibrous membrane have high open porosity. The solid lines represent the path taken by the metal ion complex across the membrane. Pore overlap (interconnection) is seen to provide alternative tortuous path to metal ions resulting in lowering of permeability.

4.3.2. Track etched polycarbonate membranes

4.3.2a. Surface morphology

Figure 4.14a shows the SEM image of one of the track etched nuclepore PC membranes showing the presence of cylindrical through and through pores. Distinct morphology of track etched PC membrane as compared to fibrous membrane (PTFE SLM) having highly interconnected pores is clearly evident from Figure 4.14b. In the present study PC membranes with pore size 0.03, 0.2 and 0.4 μm are named as membrane 1, 2 and 3, respectively.

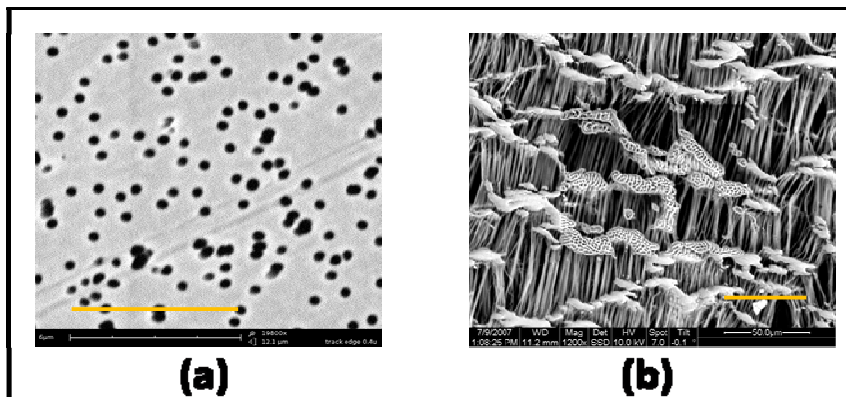


Figure 4.14: SEM images of (a) track etched PC and, (b) fibrous PTFE SLM. Yellow lines indicates the length scale of measurement; (a) 6 μm ; (b) 50 μm

4.3.2b. Doppler broadening and $3\gamma/2\gamma$ annihilation spectroscopy

The variation of S -parameter as a function of positron energy for membranes 1-3 are shown in Figure 4.15. The S -parameter profile is almost featureless throughout the energy range owing to the highly porous nature of the membranes. As the pore size is large (order of μm) in these membranes, o -Ps *pick-off* annihilation is expected to be

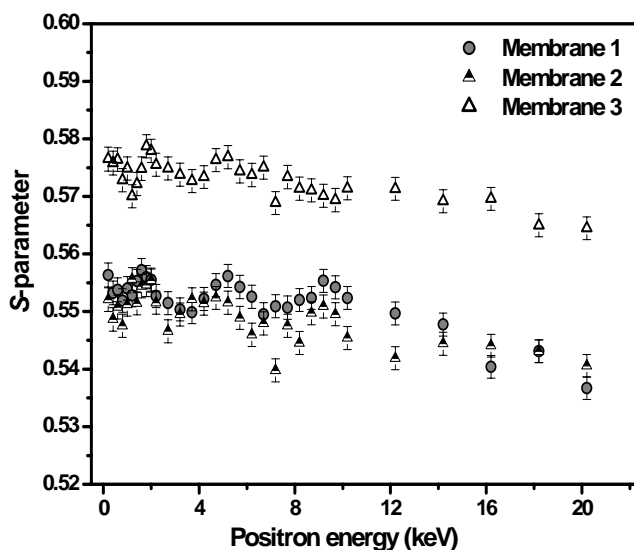


Figure 4.15: The S -parameter profile for pristine track etched PC membranes; Membrane 1 ($0.03 \mu\text{m}$), Membrane 2 ($0.2 \mu\text{m}$) and Membrane 3 ($0.4 \mu\text{m}$).

insensitive to the pore sizes and most of the o -Ps annihilate by 3γ annihilation. The energy spectroscopy ($3\gamma/2\gamma$), which directly senses the formation and complete history of long-lived 3γ decay of o -Ps, is seen to be a more sensitive technique for the investigation of pore architecture in these membranes. In addition, similar to earlier observation in PTFE SLMs, open porosity due to large pore size may modify the $3\gamma/2\gamma$ profiles and hence, corresponding goldcoated membranes are also studied in order to get true picture of pore architecture in these membranes. The $3\gamma/2\gamma$ profiles for PC membranes are shown in Figure 4.16 indicating distinct variation between the membranes. The quantitative analysis for the observed variations is carried out by evaluating L_+ using VEPFIT. The L_+ obtained by fitting the $3\gamma/2\gamma$ profiles are 55, 30 and 76 nm for membrane 1, 2 and 3, respectively. No systematic trend in L_+ is seen with the increase in the pore size. Based on our earlier observations (PTFE SLMs), for large size pores (micron range) and highly porous membranes, the escape of Ps from the surface modifies the profiles resulting in underestimation of L_+ . In such cases, true pore architecture can be obtained by capping the membrane surface with gold layer to prevent Ps escape from the surface. The S -

parameter and $3\gamma/2\gamma$ profile for goldcoated PC membranes are shown in Figures 4.17 and 4.18, respectively. No significant variation is S -parameter with depth has been observed owing to the porous nature of the membranes and hence, it cannot be used to elucidate any information about the pore architecture. However, it indicates that Ps yield in all the membranes is same. On the otherhand, $3\gamma/2\gamma$ profiles for goldcoated membranes show distinct behavior as compared to their pristine forms. The measured L_+ for goldcoated membrane 1, 2 and 3 are 375, 255 and 330 nm, respectively.

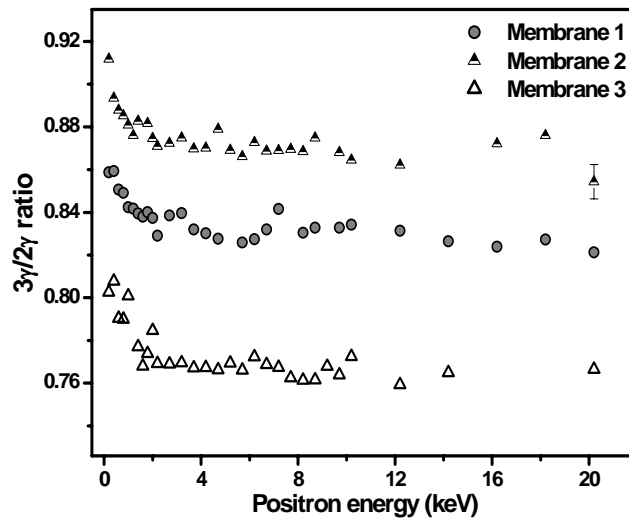


Figure 4.16: $3\gamma/2\gamma$ profiles for pristine track etched PC membranes.

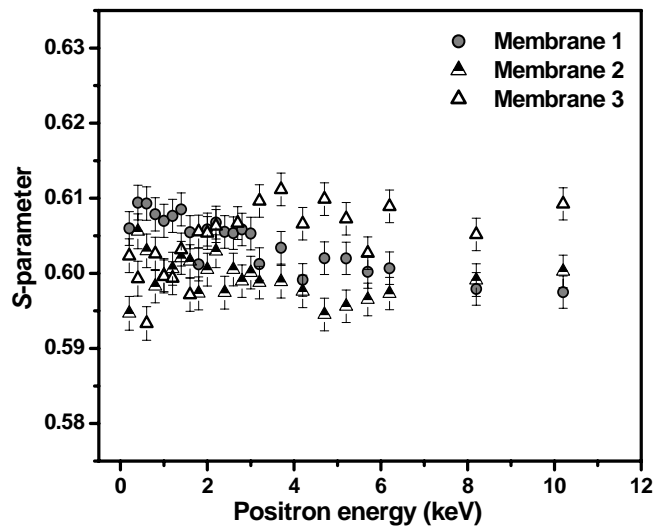


Figure 4.17: The S -parameter profile for goldcoated PC membranes.

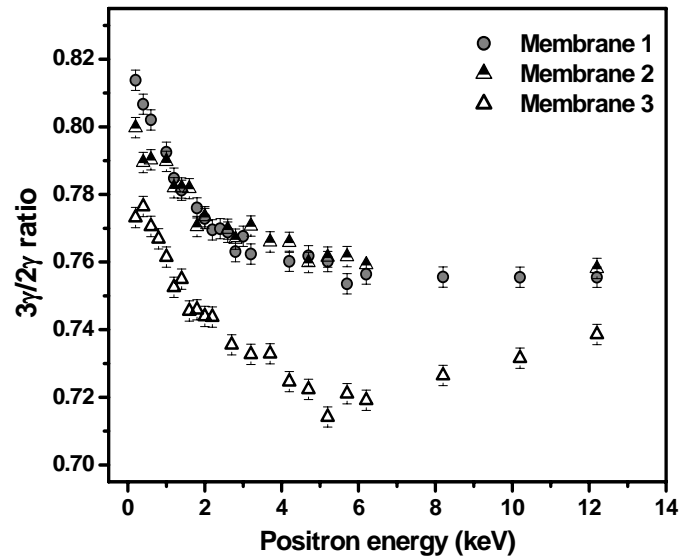


Figure 4.18: $3\gamma/2\gamma$ profiles for goldcoated PC membranes.

As also observed in PTFE SLMs, the profile obtained in the case of goldcoated membranes represent the true reflection of pore architecture of the membranes. It is seen that the obtained L_+ is much larger than the pore size in the case of membrane 1 in contrast to membranes 2 and 3 where, L_+ is of the order of the pore size. This indicates that pores in the membrane 1 are highly interconnected as compared to membrane 2 and 3, where cylindrical through and through pores are present. The L_+ is related to the cross section of pores in the latter case. Also, a marginal difference in $3\gamma/2\gamma$ ratio at the surface has been observed for pristine and goldcoated membranes depicting open porosity.

It is also to be noted that the obtained L_+ in the case of track etched PC membranes are much smaller than that in fibrous PTFE SLMs indicating distinct microstructure of the membranes especially in terms of pore interconnection. The fibrous membranes show higher degree of pore interconnectivity (large L_+) than the track etched PC membranes where cylindrical through and through pores are present.

4.4. Conclusions

The pore architecture of supported liquid PTFE and track etched PC membranes having micron size pores have been studied using PAS. Slow positron beam depth profiling has been utilized to evaluate Ps mobility (diffusion length) in these membranes defined by the mean free path of Ps in the system. This has been utilized to evaluate pore architecture in terms of pore interconnectivity in these membranes. Ps diffusion length, a measure of length of interconnection of the pores is evaluated from the $3\gamma/2\gamma$ profiles using VEPFIT analysis. The high open porosity at the surface has been seen to modify $3\gamma/2\gamma$ profiles due to the escape of Ps from the surface and do not represent the true pore architecture. Capping the surface of the membrane with thin gold layer prevents the escape of Ps from the surface and hence, gives a true reflection of the pore architecture of the membranes. In the case of PTFE SLMs, high interconnectivity has been observed for the fibrous class of the membrane (C and D) as compared to the granular (A and B). An inverse correlation between the pore interconnectivity and the permeability of metal ions through SLMs has been observed. High interconnectivity results in decrease in permeability. The increase in tortuosity due to large interconnectivity is responsible for the decrease in permeability. On the otherhand, in the case of track etched PC membranes having through-and-through cylindrical pores, the interconnectivity between the pores is seen to be less than the PTFE SLMs. It is also observed that, in the case of less interconnected but large size pores, Ps diffusion length is a measure of cross section rather than length of the pores. PAS is one of the best probes to measure pore sizes in the range of 0.1-1 nm. However, for polymeric systems having large size and interconnected pores, slow positron beam depth profiling provide an approach to measure pore architecture of the membrane especially in terms of open porosity and length of interconnection between the pores. The pore architecture of the membrane is the

microscopic origin of the transport properties of the membranes. The study demonstrates the advantages of positron beam characterization of pore interconnectivity in the design/development of membranes with tailored transport properties.

CHAPTER-V

Nanostructure characterization in Organic Semiconductor thin films

Organic thin film devices are the primary building block for the next generation organic electronics. Owing to the dependence of electronic, optical and even magnetic properties on the structure and morphology of the films, the ordered, smooth and defect free surfaces are prerequisite for achieving high performance electronic devices [Stadlober et al., 2006; Offerman et al., 2002]. The growth behavior of OSC molecules depends on the nature of substrate, its temperature, deposition technique, rate of deposition and post deposition annealing treatment [Karan et al, 2007; Miller et al., 2005; Forrest et al., 1997; Nonaka et al., 1995]. There have been number of studies using variety of techniques addressing the growth behavior and its effect on the performance of organic devices [Don Park et al., 2007; Koch et al., 2007]. For example, nature and temperature of the substrate affects the growth mode of organic molecules. The interaction between the substrate and the molecules as well as between the two molecules dictates molecular arrangement. When substrate-molecule interaction dominates, stacking of the molecules will be edge-on. However, molecules stack in face-on manner if molecule-molecule interaction is dominant [Debnath et al., 2008]. In addition to this, heteroepitaxy between different materials results in translational and orientational domains, which are the sources of disorder/defects at the interfaces between different materials [Brutting et al., 2008]. These defects may influence charge transport properties of the devices. Therefore, optimization of growth parameters/conditions and the characterization of structural properties are very relevant to organic electronic industry. Several techniques are used for structural characterization of these devices. For instance, AFM and SEM are often used for the characterization of surface morphology [Chowdhury et al., 2012; Virkar et al., 2010], sputter-ion based X-ray photoelectron spectroscopy (XPS) [Hong et al., 2012; Liu et al., 2011] and secondary ion mass spectrometry (SIMS) for compositional characterization [Chang et al., 2012], near-edge

X-ray absorption fine structure (NEXAFS) for bond orientation and chemistry of the film and Grazing incidence X-ray diffraction (GIXRD) for crystal structure. However, destructive nature (sputter-ion XPS, SIMS) and limited depth profiling capability (GIXRD) impose limitations on the utilization of these techniques for the characterization of organic devices. In addition, only few techniques are available which can provide defect structure of the film and interfaces. AFM and SEM are sensitive to structural defects, but these are local probes for the characterization of surface morphology only and cannot provide information about the nanostructure of buried layers and interfaces.

Depth profiling using slow positron beam has emerged as a sensitive technique for the characterization of defect microstructure in thin films. The sensitivity of positrons to get trapped in low electron density regions enables study of open volume defects and vacancies. Together with the ability to monoenergize positrons helps in probing defect microstructure at different depths of the sample. In the present work, the technique has been employed for the first time for defect depth profiling in OSC thin films. The growth behavior and surface morphology in OSC thin films are mainly characterized by AFM and SEM. However, there are no studies related to depth dependent defect microstructure in these films especially, interfacial microstructure which requires either layer by layer sputtering or growth of monolayers. The defect microstructure of different layers and interfaces in actual device configuration cannot be probed by these techniques due to the destructive nature of the techniques. In this context, defect depth profiling is useful to investigate structural inhomogeneities as well as interfaces in organic devices.

In the present work, defect depth profiling has been carried out in OSC thin films under different growth parameters to examine the nanostructure of the films. Positron annihilation parameters (S -parameter and diffusion length) are indexed to represent the nanostructural variations as a function of growth parameters. In the case of films

subjected to post-deposition annealing, depth profiling has been seen to be sensitive to structural inhomogeneities in the direction normal to the surface of the film. Depth profile study has also enabled identification of buried interfaces i.e. interfaces between organic-organic and organic-inorganic materials in heterostructures. No other technique has been seen to be sensitive to defect/disorders present in these interfaces.

The growth behavior of organic molecules depends on the interaction between the molecules and the dielectric surface. The surface energy/roughness of dielectric strongly influences the nucleation and growth of molecules, grain size, molecular ordering and crystalline structure. These factors are crucial for the mobility of charge carriers in organic devices. Interface engineering has been employed to modify dielectric surface (substrate) using self assembled monolayer in order to improve the growth behavior of OSC to achieve high charge mobility. The present study pertains to the investigation of defect microstructure of the interface between dielectric substrate (modified/unmodified)/OSC layer and its effect on the charge carrier mobility. The above study using positron beam has been corroborated with other conventional characterization techniques like AFM, GIXRD and X-ray reflectivity (XRR).

5.1. Material and sample preparation

In this work, metal phthalocyanines (MPcs) have been used as OSC materials. Phthalocyanines (Pc's) are a class of planar aromatic organic compounds which exhibit semiconductor properties. Their thermal and chemical stability makes them very suitable material for organic electronic devices [Ribeiro et al., 2000; Prince et al., 2001]. MPcs have planar (within 0.3 Å) molecular structure, as schematically shown in Figure 5.1. The parent molecule, hydrogenated Pc, with chemical formula $C_{32}H_{18}N_8$, has 2 hydrogen atoms in the center of the ring, and 16 surrounding the molecule. The two hydrogen atoms are replaced by a metal atom in case of MPcs. The replacement of central metal

atom and side group modifies the electronic properties of Pcs. For example CuPc is a *p*-type organic semiconductor but the replacement of 16 hydrogen by fluorine makes the molecule (F₁₆CuPc) *n*-type.

Thin films of different MPcs have been used as organic semiconductor materials in the present work. The effect of substrate temperature and thickness of the film on the nanostructure of the films have been studied for Iron-Phthalocyanine (FePc). FePc films of thicknesses 50, 100 and 140 nm have been grown on ITO-glass substrate by molecular beam epitaxy technique using RIBER make model EVA32 system. These films have been deposited using an effusion cell loaded with 97% pure α -FePc powder (Aldrich make) at substrate temperature of 200°C. The above method has also been utilized for the deposition of FePc films at two different temperatures *viz.* 30°C and 300°C.

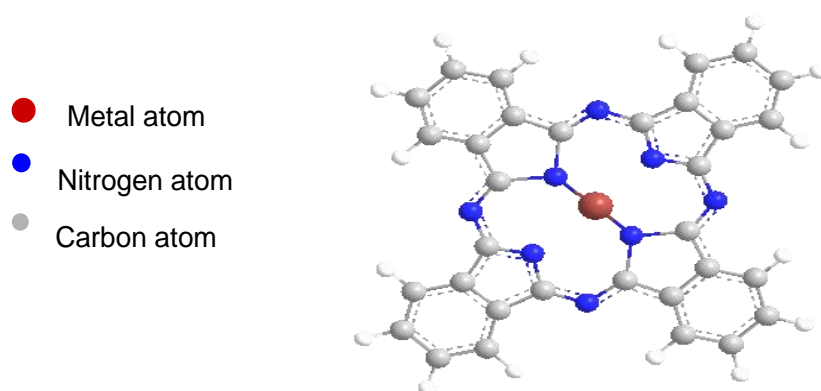


Figure 5.1: *The structure of Metal Phthalocyanine molecule.*

The effect of post-deposition annealing has been studied for cobalt-phthalocyanine (CoPc) film grown on quartz substrate by thermal evaporation using Hind high Vac thermal evaporation system (model no-12A4T) under vacuum better than 10⁻⁶ mbar. The substrate is cleaned by sonication with trichloroethylene, acetone and methanol separately for 5 minutes each before the deposition. The film is deposited at room temperature at the deposition rate of 0.2-0.3 Å/sec. The thickness of the film as measured by quartz crystal monitor is 200 nm. The grown film has been subjected to post-

deposition annealing treatment at temperatures 140 and 200°C in a vacuum oven for 1 hour in a vacuum better than 10^{-3} mbar.

For the study of interfacial characteristics in OSC heterostructures, single layer and multilayer films of *n*-type (copper-hexadecafluoro-phthalocyanine, F₁₆CuPc) and *p*-type (cobalt-phthalocyanine, CoPc; FePc and zinc-phthalocyanine, ZnPc) OSC materials have been prepared on quartz substrate by thermal evaporation using Hind high Vac thermal evaporation system (model no-12A4T) under vacuum better than 10^{-6} mbar. The substrate is cleaned by sonication with trichloroethylene, acetone and methanol separately for 5 minutes each before the deposition. Films have been deposited at the substrate temperature of 100° C and the deposition rate of 0.2 Å/sec. The thickness of single layer films of *n*-type (F₁₆CuPc) and *p*-type (CoPc) material is 80 nm thick. The multilayer structures comprise bilayer of *p-n* (CoPc- F₁₆CuPc) and *p-p* (FePc- ZnPc) type and trilayer of *n-p-n* (F₁₆CuPc- CoPc-F₁₆CuPc) type OSC materials. The thickness of each film in bilayer and trilayer structures is 60 nm and 30 nm, respectively. The thickness of the films has been measured by quartz crystal monitor.

Interface engineering of dielectric surface (SiO₂/Si) has been carried out using self assembled monolayers (SAM) of trichlorosilane *viz.* phenylhexyltrichlorosilane (PTS) and octadecyltrichlorosilane (OTS) differing in the tail group and chain length. Highly doped *n*-type (100) Si wafer has been used as a substrate and the gate dielectric SiO₂ of 200 nm thickness has been deposited thermally. For modifying SiO₂ with SAM of OTS, silicon substrates with SiO₂ layer has been first cleaned in Piranha solution (2:1 v/v H₂SO₄ and H₂O₂) to obtain OH terminated surface and then immersed in freshly prepared 0.5 mM OTS solution in toluene for 16 hours in an argon filled glove box (relative humidity and oxygen < 1 ppm). For the preparation of PTS (phenylhexyltrichlorosilane) SAM, SiO₂ substrates has been immersed in freshly prepared 0.25 mM

phenylhexyltrichlorosilane (PTS) solution in toluene for 3 hours. Thickness of the monolayers (OTS ~2.6 nm; PTS~1.4 nm) has been measured using ellipsometry. CuPc films have been grown on native oxide SiO₂ (3-4 nm)/Si, thermally grown oxide SiO₂ (200 nm)/Si and SAM modified SiO₂ (200 nm)/Si substrates using thermal evaporation using Hind high Vac thermal evaporation system (model no-12A4T) under vacuum better than 10⁻⁶ mbar. The deposition rate has been maintained at 0.5-1 Å/s and thickness of the films is about 30 nm, as measured by quartz crystal monitor. The schematic of different SAM (PTS and OTS) and SAM modified substrate with a grown OSC layer is shown in Figure 5.2.

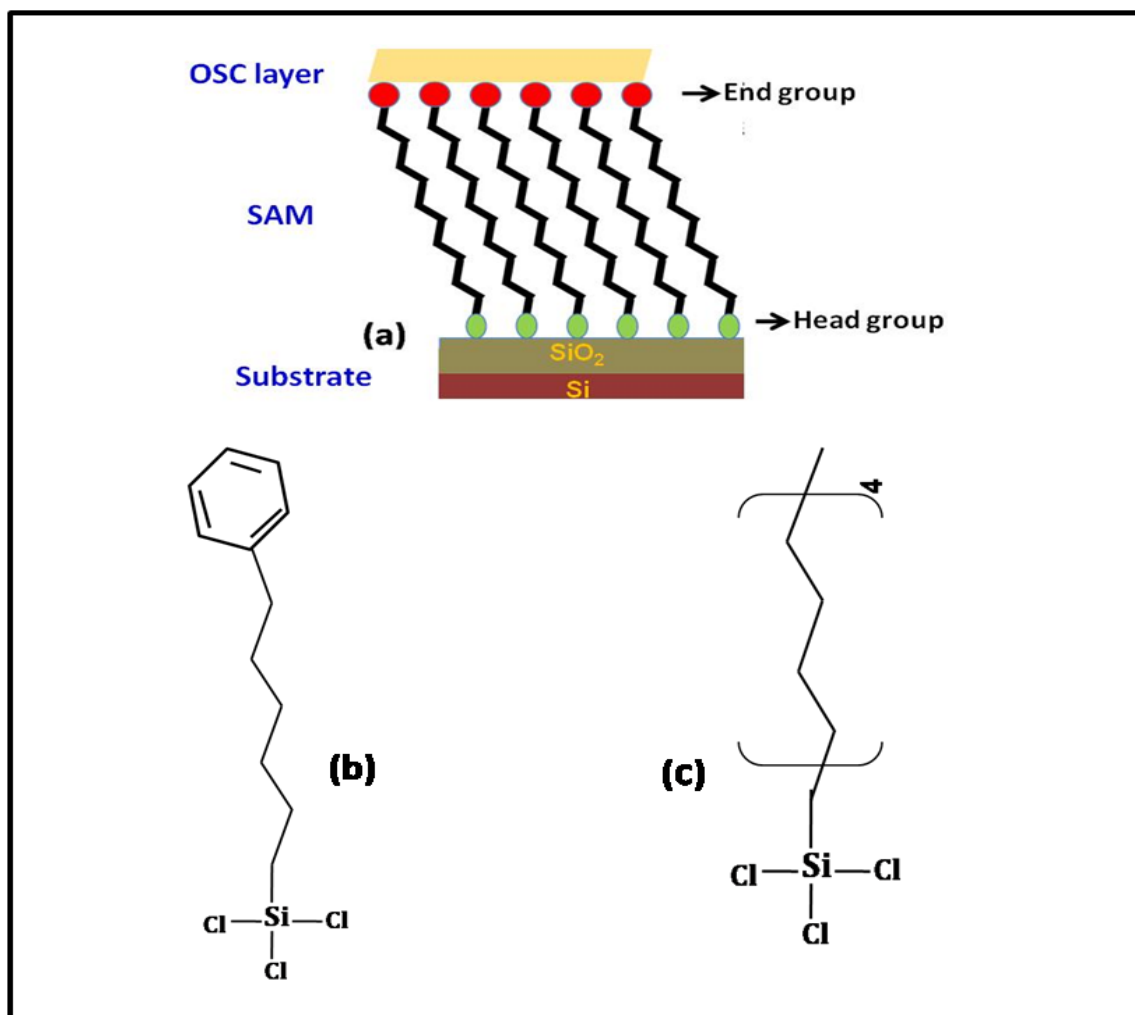


Figure 5.2: Schematic of (a) OSC grown on self assembled monolayer (SAM) modified SiO₂/Si substrate; (b) PTS; (c) OTS.

5.2. Experimental Techniques

5.2.1. Grazing incidence X-ray diffraction (GIXRD)

The nature of the grown films (crystallinity) has been determined using GIXRD. The measurements have been carried out using PANalytical MRD system using Cu K α radiation of wavelength 0.15418 nm in out of plane geometry. The measurements have been performed at small grazing angles (0.2° to 1°) with a high resolution theta-2-theta scan ranging from 0° to 15° in the step size of 0.0001° to examine the crystalline nature of the films. However, in the case of heterostructures (multilayer films), measurements are performed at varying grazing angles so as to probe the multilayer system as a function of depth. The high resolution theta-2-theta scan ranging from 0° to 30° in the step size of 0.0001° is carried out at each grazing angle.

5.2.2. Atomic force microscopy (AFM)

The surface morphology of the films have been characterized using AFM in tapping/non-contact mode. The measurements are performed using a NT-MDT solver model instrument with 50 μ m scanner head and silicon nitride tip with a scanning speed of about 1 Hz. The growth mode of CuPc molecules grown on SiO₂ (200 nm)/Si at room temperature and 225°C have been examined by depositing only one or two monolayers (~ 2 nm) of CuPc on the modified substrate.

5.2.3. Doppler broadening spectroscopy

Depth profiling has been carried out using Doppler broadening spectroscopy using slow positron accelerator at Radiochemistry Division, Bhabha Atomic Research Centre, Mumbai. The depth dependent Doppler broadening measurements have been carried out in the positron energy ranging from 200 eV to the maximum of 20 keV. A high purity germanium detector with a resolution of 2.0 keV at 1332 keV photopeak of ⁶⁰Co has been

used for Doppler broadening measurements and approximately half a million counts are acquired under 511 keV photopeak at each energy. The Doppler broadened annihilation γ -radiation has been characterized by line shape parameters S and W . The S -parameter mainly reflects the change due to positron annihilation with electrons having low momentum distribution, whereas, W -parameter reflects the annihilation from electrons with high momentum distribution. The ratio of integral counts within ~ 2.0 keV energy window centered at 511 keV to the total photo peak area has been used to evaluate S -parameter, whereas, W -parameter is evaluated from the energy window of ~ 5 keV in the wing region of 511 keV photopeak. The S - W correlation has been examined to identify the nature and type of defects in multilayers. VEPFIT analysis has been used to fit S -parameter profiles as a function of energy of the positrons to evaluate S -parameter and positron diffusion length in the layers and interfaces, as the case may be. Positron mobility in organic layers has also been calculated from the fitted value of positron diffusion length.

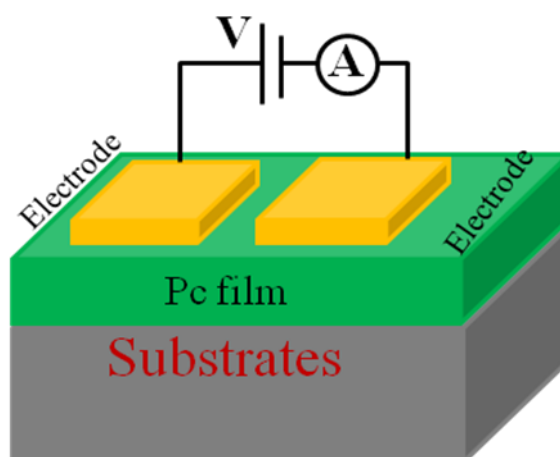


Figure 5.3: A schematic of in-plane charge transport measurement geometry.

5.2.4. Current-voltage measurement (J - V characteristics)

The current density-voltage (J - V) measurements have been carried out using two probe in-plane electrode geometry as shown in Figure 5.3. Two planar gold electrodes of

length 3 mm, width 2 mm separated by 12 μm are thermally deposited onto the films using a metal mask and silver wires are attached to the gold pads with silver paint. J - V measurements are carried out using Keithley 6487 picoammeter/ voltage source and computer based data acquisition system.

5.2.5. X-ray reflectivity (XRR)

When X-ray beam falls on a surface it undergoes total external reflection below certain critical angle (θ_c). Above θ_c , X-ray starts penetrating inside the layer and the reflectivity of the sample falls off with a slope depending on the incidence angle and the roughness of the interface. The oscillation on the reflectivity spectrum above θ_c (generally known as the Kiessig oscillations) is due to the finite thickness of the layer. The reflectivity pattern is obtained from the interference of monochromatic X-rays that are reflected from the different interfaces of the layered structure, owing to the changes in refractive indices of the layers. When used in specular (angle of incidence=angle of reflection) mode, XRR can provide information regarding the structure of the layers through an electron density profile in a direction normal to the surface [Pietsch et al., 1993; Xia et al., 2004]. In this configuration these experiments probe the electronic density that is roughly homogeneous in the horizontal plane but varies in a deterministic way along the vertical depth of the sample. In general, the thickness of the film can be obtained from the frequency of oscillations, while the slope of the curve gives the roughness of the interface.

X-ray reflectivity measurements have been carried out using CuK_α radiation (1.54 Å) on a computer-controlled reflectometer (Kristalloflex 710 D X-ray generator (SIMENS) and D5000 diffractometer). The complex index of refraction for X-rays is given by,

$$\eta = 1 - (r_e \rho_e \lambda^2 / 2\pi) - i (\mu \lambda / 4\pi) \quad (5.1)$$

where, r_e ($= 2.818$ fm) is the classical electron radius; ρ_e is the electron scattering length density of the material (in \AA^{-2} units), λ is the incident wavelength (in this case: Cu K_α , 1.54\AA) and μ is the absorption coefficient. Since η is usually < 1 , total external reflection of X-rays will occur at the surface of the material under study for grazing incident angle θ smaller than the critical angle θ_c , whose value depends on the electron density. Therefore, the value of θ_c is specific to a material. Above the critical angle, X-rays can penetrate the material up to a depth determined mainly by the absorption coefficient. In the case of a single thin film on a substrate, for $\theta > \theta_c$, reflection occurs at both the air/film and film/substrate interfaces due to differences in refractive indices or electron densities of the layers (called density contrast). The combination of both these reflections results in interference fringes. Such interference patterns are recorded as a function of momentum transfer q (\AA^{-1}) perpendicular to the reflecting surface, where $q = (4\pi / \lambda) \sin \theta$. The lessening or absence of interference fringes in a reflectivity pattern can be attributed to variations like surface/interface roughening, interdiffusion or formation of interface layers. In order to obtain meaningful information from the measured reflectivity, the experimentally obtained data is fitted with a computer generated theoretical model, from which one can derive depth-dependent scattering length density (SLD) profile of the sample. The fitting parameters used which ultimately define the sample are thickness, electron density and roughness for each layer. Thus, it is obvious that SLD, which is the product of number density per unit volume of the constituents and the Thomson scattering length for X-rays, contains significant information for the characterization of a material, especially with respect to vertical depth.

5.3. Results and Discussion

5.3.1. Effect of substrate temperature and thickness of the film

5.3.1a. Surface morphology and crystallinity

The effect of deposition temperature (substrate) and thickness of the film on the nanostructure has been studied for FePc thin films. The crystalline nature and surface morphology of the films have been characterized using GIXRD and AFM. Figure 5.4 shows the GIXRD pattern of FePc films (100 nm) deposited at two different substrate temperatures (30°C and 300°C). It is seen that the films grown at substrate temperature of 30°C and 300°C are amorphous and crystalline, respectively. The films grown at higher temperature shows crystalline nature owing to the sufficient energy provided to the molecules to get arranged in an ordered manner on the substrate. To study the effect of thickness, FePc films of varying thicknesses (50, 100, 140 nm) have been grown at a substrate temperature of 200°C (all are crystalline films).

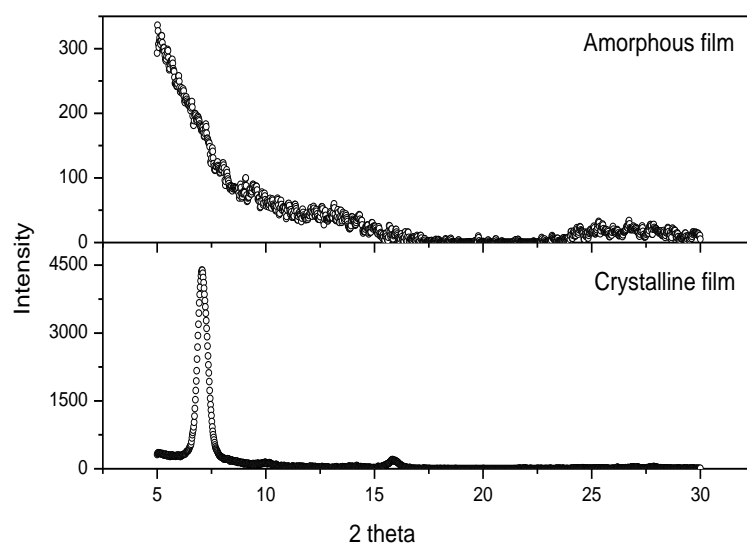


Figure 5.4: GIXRD pattern for FePc films grown on ITO-glass substrate at 30°C (amorphous) and 300°C (crystalline).

AFM images and the corresponding height profiles of crystalline FePc films grown at 200°C are shown in Figure 5.5, depicting significant difference in the morphology of the films. The film of lowest thickness (50 nm) has shown columnar growth of molecules, leaving a large open volume $\sim 1\mu\text{m}$ between the columns (as depicted from AFM height profiles). However, at higher thicknesses, a transition from

columnar to granular arrangement has been observed. The free open space between the molecules at lower thickness gets filled by other molecules with the increase in the film thickness resulting in random growth of the grains.

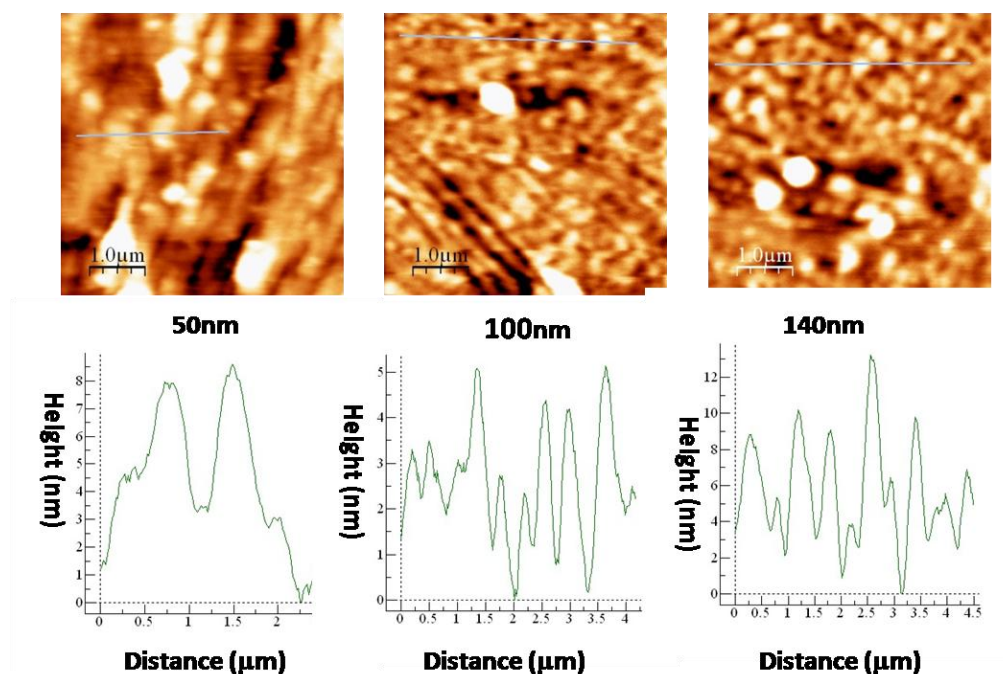


Figure 5.5: AFM images and height profiles of FePc films.

5.3.1b. Doppler broadening spectroscopy

The nanostructure variation in the films has been probed by defect depth profiling using slow positron accelerator. Doppler broadening S -parameter as a function of implantation depth of the positrons (S - E profile) has been measured for all the films. The S - E profile has been fitted using VEPFIT analysis to evaluate bulk S -parameter and positron diffusion length in the films. Figure 5.6 shows S - E profiles for FePc films grown at 30 and 300°C representing amorphous and crystalline nature, respectively. The higher value of S -parameter for amorphous film shows the presence of more free volume or grain boundaries as compared to the crystalline film. The S - E profile is almost flat in the case of amorphous film depicting large number of defects or voids throughout the film. These defects act as trapping site for positrons and thus restricting the diffusion of

positrons in the film (very short positron diffusion length). On the other hand, the crystalline film shows lower S -parameter in FePc layer as compared to amorphous film. This indicates that crystalline film has only fewer sites for positron trapping with comparatively closed packed structure.

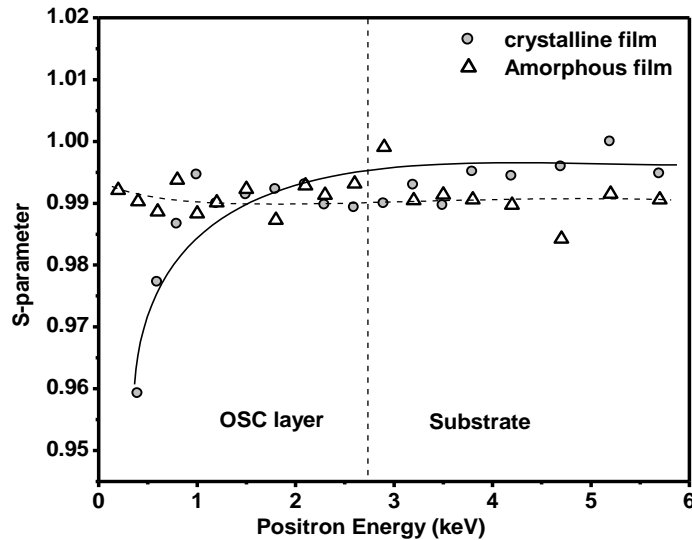


Figure 5.6: The S -parameter profile for 100 nm thick amorphous and crystalline FePc films grown at 30 and 300° C, respectively.

S - E profiles for the films with varying thicknesses are shown in Figure 5.7. The profiles clearly indicate the crystalline nature of the films. The S -parameter at the substrate is normalized to 1 and the profiles are fitted using VEPFIT analysis to determine S -parameter and positron diffusion length (Table 5.1). This helps in the identification of nanostructural variations in the films. The S -parameter at the surface and in the bulk of FePc layer of the films has been seen to be increasing with the increase in thickness of the films (Table 1). The positron diffusion length is nearly identical for 50 and 100 nm films, unlike 140 nm film where, a small but significant (reproducible) decrease has been seen. The increase in S -parameter and decrease in positron diffusion length have indicated the increase in trapping sites for positrons with the increase in the thickness of the films.

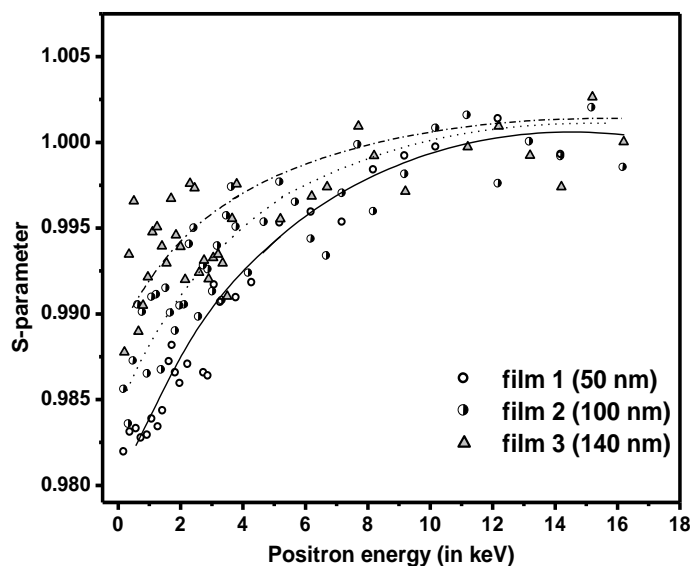


Figure 5.7: The *S*-parameter profile for FePc films of different thicknesses.

Table 5.1: *S*-parameter and diffusion length (L_+) of positron in FePc layer calculated by VEPFIT.

Film thickness (nm)	Surface <i>S</i> -parameter	Bulk <i>S</i> -parameter	Positron diffusion length (nm)
50	0.9815	0.9836	17.84 ± 6.96
100	0.9839	0.9909	17.63 ± 5.86
140	0.9902	0.9942	14.61 ± 6.64

5.3.1c. Discussion

As the film thickness increases, molecular arrangement changes from columnar (rod like) to granular kind with random grain growth resulting in the increase in grain boundaries. This signifies that the arrangement of molecules and hence, the morphology of the film depends on the interaction between the substrate and the molecules as well as between the two molecules. When substrate-molecule interaction dominates stacking of the molecules will be edge-on. However, molecules stack in face-on manner if molecule-molecule interaction dominates [Debnath et al., 2008].

The grain boundaries between the columnar grains in 50 nm film are found to be 1 μm in size as reflected from AFM height profile measurement. However, the lowest value of S -parameter for 50 nm film implies that at lower thickness, columnar arrangement of molecules has lesser defects as compared to higher thicknesses where molecules arrange with random grain growth. However, it may also be noted that the micron size inter-columnar space in 50 nm film as observed through AFM cannot be probed by the positrons. As the film thickness increases, the inter-granular space is filled by FePc molecules, leading to more interfaces which act as positron trapping sites. This has resulted in the increase in S -parameter and decrease in Positron diffusion length with the increase in the thickness of the films.

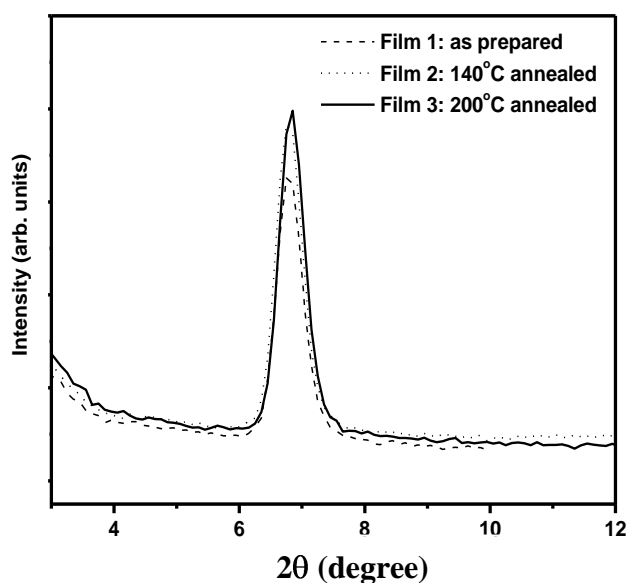


Figure 5.8: GIXRD pattern of CoPc films

5.3.2. Effect of post deposition annealing treatment

5.3.2a. Surface morphology and crystallinity

GIXRD has been used to examine the crystalline nature of CoPc film before and after annealing at two different temperatures (140 and 200°C). Figure 5.8 shows GIXRD pattern of as-deposited (film 1) and annealed films (film 2: 140°C and film 3: 200°C). The sharp Bragg peak at 6.8° indicates the crystalline nature of the films. This peak

corresponds to (200) peak of α -CoPc phase. No phase transformation of CoPc has been observed at the studied annealing temperatures (140 and 200°C).

The surface morphology of the film has been studied using AFM. Figure 5.9 represents AFM images and typical height profiles for the film 1-3. AFM image for film 1 shows smooth island-like structure as also depicted from the broad nature of the height profile. On the other hand, distinct morphological features start to appear when the film is annealed at higher temperatures. The high temperature annealing leads to the formation of grains as clearly seen in AFM images of film 2 and 3. A more homogeneous distribution of grains has been observed for 200°C annealed film (film 3) as reflected from the sharp oscillatory behavior of the height profile as compared to film 2. The rms roughness values for film 1, 2 and 3 are seen to be 3.12, 4.25 and 3.08 nm, respectively. This indicates that formation of grains initially increases the roughness of the film.

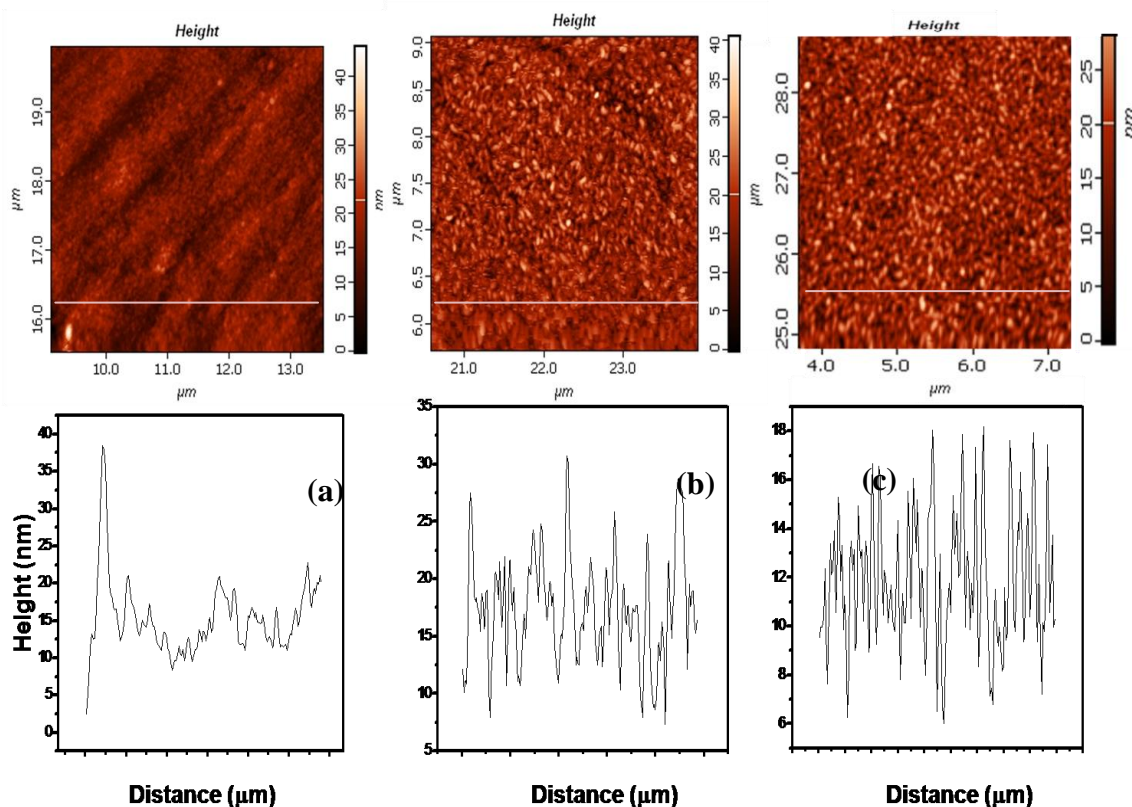


Figure 5.9: AFM images of CoPc films: (a) as-prepared; (b) annealed at 140°C; (c) annealed at 200°C

5.3.2b. Doppler broadening spectroscopy

The variation of S -parameter, as a function of positron implantation energy (S - E profile) for as-deposited and annealed films (film 1-3) are shown in Figure 5.10. At higher positron energies ($E > 6$ keV) S -parameter for all the films corresponds to quartz substrate. The S -parameter profile for as-deposited (film 1) and film annealed at 140°C (film 2) are identical, the latter having lower S -value corresponding to OSC region. The flat response of S -parameter at lower energies for film 1 and 2 indicates the presence of large number of trapping sites or defects in the film. The low value of S -parameter in film 2 has been attributed to the change in the morphology of the film due to post deposition annealing. The S -parameter profile for film 3 is seen to be noticeably different than the film 1 and 2 (Figure 5.10). The profile shows enhancement in S -value at a certain depth in the region corresponding to the OSC film. The enhancement in S -parameter indicates the presence of more defects or disorder at the corresponding depth. The quantitative analysis of the observed differences in S -parameter profiles has been carried out using VEPFIT as discussed in the following section.

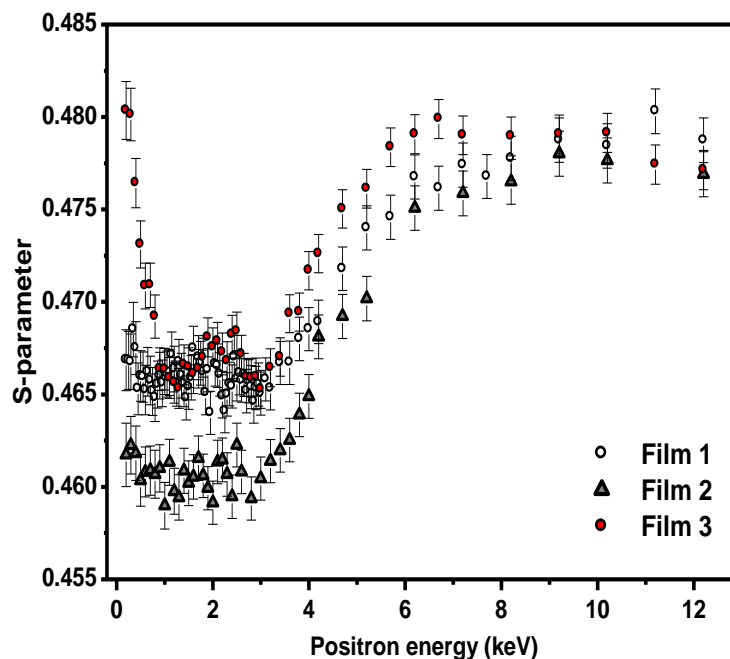


Figure 5.10: S -parameter profiles for Film 1: as-prepared; Film 2: annealed at 140°C and Film 3: annealed at 200°C .

5.3.3c. VEPFIT analysis

A quantitative analysis of the nanostructural variations in the films has been carried out by indexing S -parameter and diffusion length of positrons (L_+) in the films, obtained by fitting the S -parameter profiles using VEPFIT analysis [van Veen et al., 1990]. It has been observed that profiles for film 1 and 2 are best fitted using two layers in contrast to four layers in the case of film 3. The two layers in film 1 and 2 correspond to OSC layer and the substrate. However, in film 3, in addition to substrate, the OSC layer is divided into three distinct layers. The graphical representation of different layers and corresponding S -values for all the films is shown in Figure 5.11. The fitted values of S -parameter and L_+ for these layers and corresponding thicknesses are given in Table 5.2 (a, b). S -parameter and L_+ for the substrate have been obtained by fitting the experimentally observed S -parameter profile of the substrate (measured separately). The obtained L_+ for substrate was 20 nm and is used as a fixed parameter for the fitting procedure in the case of OSC films (film 1-3).

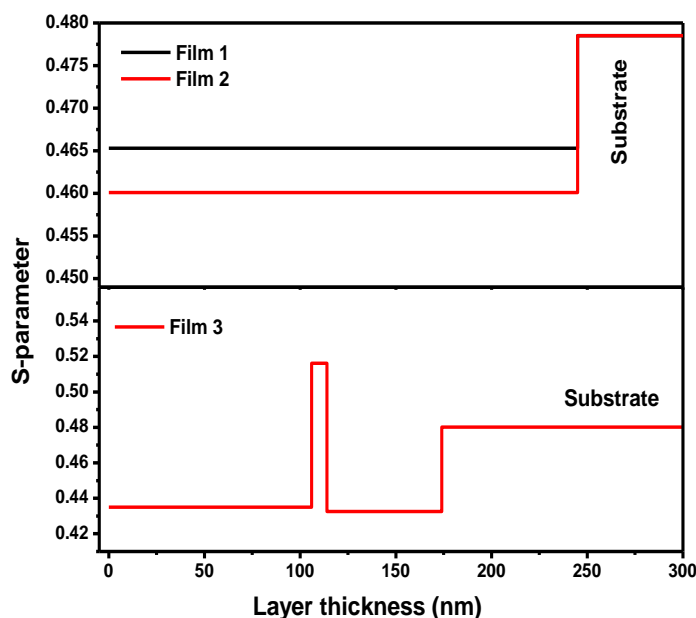


Figure 5.11: VEPFIT fitted S -parameter corresponding to different layers of the films.

Table 5.2a: VEPFIT analysis: Two layer fitting results for film 1 and 2.

	S_1	L_{+1} (nm)	ρ_1 (g/cc)	x_1^* (nm)	S_2	L_{+2} (nm)	ρ_2 (g/cc)
Film 1	0.4653±0.0002	1.0	1.76	245± 12	0.4785 (fixed)	21 (fixed)	2.60
Film 2	0.4601±0.0002	3.0	1.76	247± 10	0.4785 (fixed)	21 (fixed)	2.60

* x_1 is the layer boundary or width of OSC layer in film 1 and 2

Table 5.2b: VEPFIT analysis: four layers fitting results for film 3.

	Layer 1	Layer 2	Layer 3	Layer 4 (substrate)
Width of the layer	106	8	60	----
S	0.4350 ±0.004	0.5162 ± 0.006	0.4326 ± 0.003	0.4801 (fixed)
L_+ (nm)	40	4.8	10	18 (fixed)
ρ (g/cc)	1.76	1.65	1.76	2.6

The high S -parameter and short L_+ for film 1 and 2 indicate disorder or the presence of large number of defects in the films. In the film 3, however, distinct nanostructure is clearly revealed from the presence of three OSC layers in contrast to only single OSC layer in film 1 and 2. Three layers as observed from the fitting in film 3 have different S -parameter and L_+ (Table 5.2b), indicating inhomogeneous nature of the film along the direction normal to the surface. The S -parameter value for layers 1 and 3 of film 3 are lower than that of film 1 and 2. The corresponding L_+ are also seen to be higher than that observed in film 1 and 2. The reduction in S -parameter and increase in L_+ indicate lesser defects in these layers (reduction in the number of defects in the film after annealing at 200°C). In contrast, layer 2 of film 3 has highest S -parameter and short L_+ , indicating the

presence of more defects as compared to layer 1 and 3. The fitting of S -parameter profile has revealed the presence of a region with more defects or disorder (layer 2) in film 3 indicating structural inhomogeneity across the depth of the film.

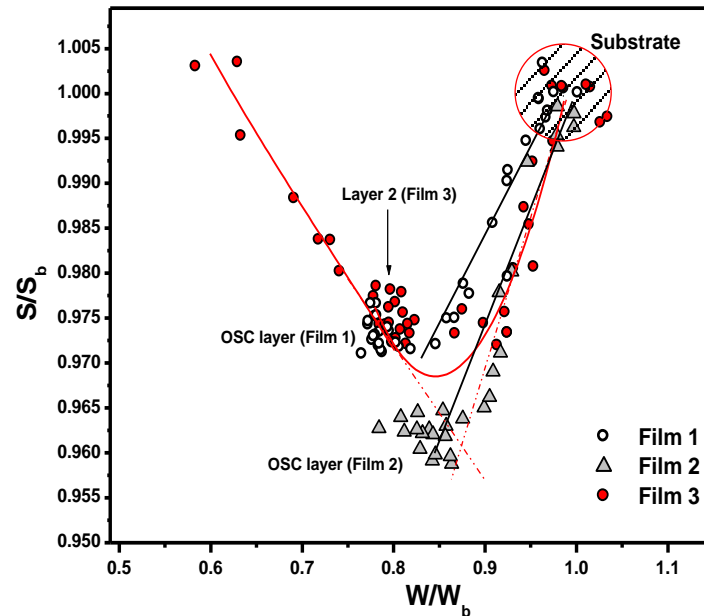


Figure 5.12: S - W curves for CoPc films; solid lines represent the slope of (S, W) points of respective films.

5.3.2d. S - W Analysis

Figure 5.12 represents S - W plot of all the films with positron implantation energy as the running parameter. S - W correlation analysis provides another qualitative way to identify different trapping layers through the characterization of (S, W) coordinates instead of S -values. The S - W analysis is also sensitive to the nature and type of defects and can help in identifying the location of the layers in the system. The convenience of the interpretation of S - W plot stems from the linearity property of S and W which is the consequence of the particular choice of their definition [Schultz et al., 1988; Asoka-Kumar et al., 1995]. The (S, W) points lie on the straight line in the case of both film 1 and 2 (shown by solid line in Figure 5.12) unlike a curved trajectory in film 3. The straight line (film 1 and 2) connects (S, W) points of substrate (marked in the Figure 5.12) and the respective OSC layer and thus, reveals two distinct layers (OSC and substrate) in

the case of film 1 and 2. In contrast, a curved trajectory shows the presence of more than two layers [Clement et al., 1996]. The curved trajectory is seen to exhibit two straight parts (dotted lines in Figure 5.12) indicating trapping in two distinct layers, whereas, the intersection/deviation of trajectory from straight line path reveals the presence of another trapping layer. The presence of three layers could be easily identified from (S , W) plot, however, S - E profile for film 3 has shown the presence of four layers. It is to be mentioned that all the trapping layers can be identified from S - W plot provided (S , W) points for any of the layers do not lie on the straight line joining other layers. The (S , W) points corresponding to layer 2 of film 3 (marked in Figure 5.12) lie on one of the straight lines and therefore, could not be established from (S , W) trajectory. The location of (S , W) point for layer 2 of film 3 indicates that layer 2 corresponds to OSC film region, not the interface between OSC and the substrate. This supports the observed inhomogeneity in the nanostructure of film 3 i.e. distinct three layers configuration for film 3.

5.3.2e. Depth profiling using X-ray reflectivity

The nanostructure variations in the films have also been studied by obtaining depth profile of electron density using XRR. The XRR profiles corresponding to film 1-3 are shown in Figure 5.13 (a-c) along with the fitted profiles (solid lines). A detailed analysis of the film structure with respect to its thickness, density and roughness has been achieved by using a genetic algorithm based fitting program which generated a theoretical model to explain the experimental data. Fitted electron SLD profiles are shown in Figure 5.14 (a-c) in units of \AA^{-2} . Periodic oscillations in the reflectivity profile are seen in the case of film 1 (inset of Figure 5.13a). These oscillations, known as Kiessig oscillations, are obtained from the interference of monochromatic X-rays that are reflected from top and bottom of the film (i.e. surface and film/substrate interface, respectively), owing to the refractive indices contrast between the film and the substrate. The period of these

oscillations allows one to determine thickness of the film. The fitted thickness of the as-deposited film (film 1) is 188 nm with a SLD of $1.49 \times 10^{-5} \text{ \AA}^{-2}$ which corresponds to physical density of 1.74 g/cc and a surface roughness of 0.8 nm (Figure 5.14a). Annealing at 140°C does not show any major change in the density of the film (film 2). The only signature of annealing at 140°C is reflected as increase in surface roughness to 3.2 nm at the film-air interface.

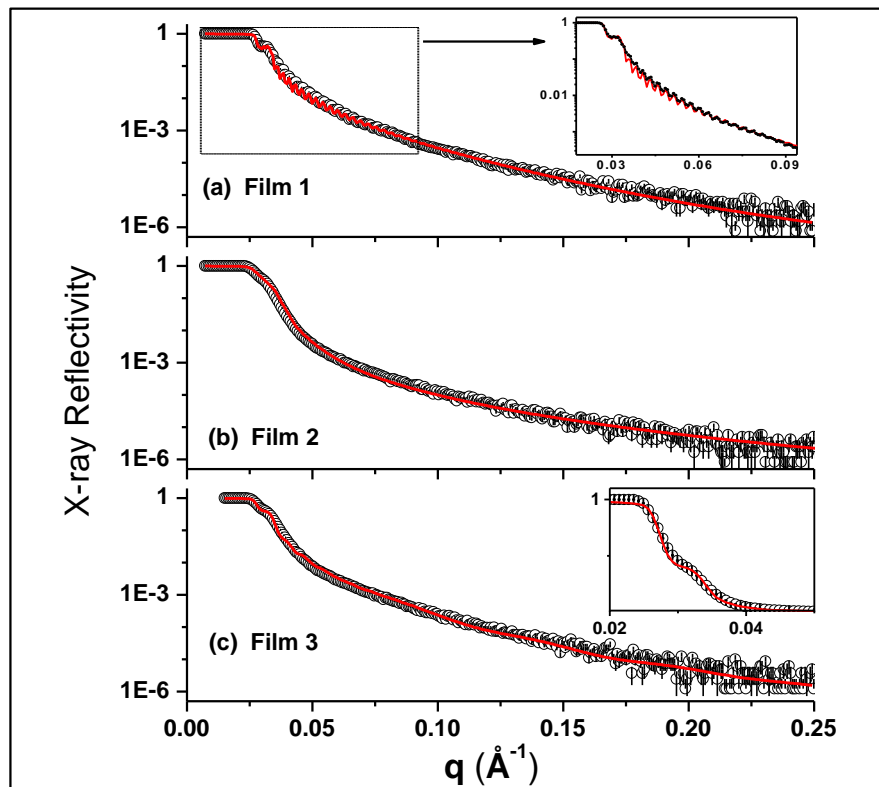


Figure 5.13: Fits (continuous lines) to the XRR data (open circles) of as-deposited and annealed films. Top panel (a) highlights the specific features obtained for Film 1. Middle panel (b) shows absence of these features in Film 2 and increased roughness. Bottom panel (c) shows the best fit for Film 3 obtained with a 3-layer model.

The increased roughness also reduces the amplitude of Kiessig oscillations. The difference in the XRR data of film 2 and film 3 are marginal, but the feature appearing in the experimental data (film 3) at low q region as shown in the expanded scale in the inset of Figure 5.13c cannot be accounted for single layer model. We observe that the XRR

data for film 3 could be best fitted by means of a 3-layer model for the CoPC film. The fit shows a 3-layer configuration represented by two layers of similar density sandwiching a thin layer of relatively lower density, manifested as a dip in the SLD profile (Figure 5.14c). The presence of three layers in film 3 is consistent with the slow positron beam depth profile study. The outer two layers (layer 1 and 3) have density similar to that of film 1. All the fitted parameters for films 1-3 are given in Table 5.3.

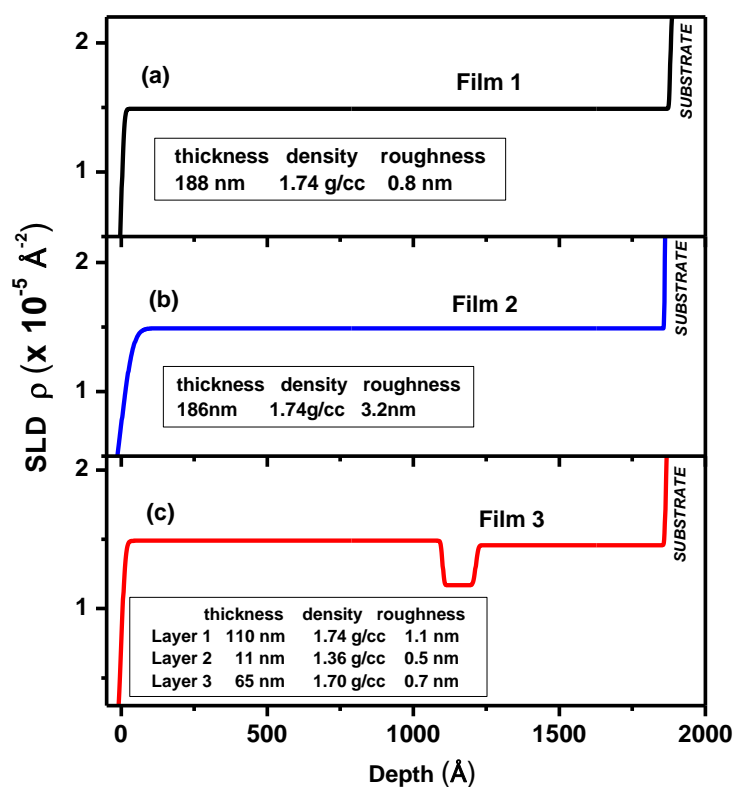


Figure 5.14: Comparison of SLD profiles of (a) as-deposited (Film 1; black line), (b) film annealed at 140 °C (Film 2; blue line) and (c) film annealed at 200 °C (Film 3; red line). Respective fitted parameters are indicated.

A marginal shrinkage in the thickness of film 2 and 3 (total thickness) has also been observed. The low density layer (layer 2) in film 3 approximately at a depth of 110 nm has a density of 1.36 g/cc. The SLD plot in Figure 5.14c and the S -parameter plot in Figure 5.11 corroborate the possibility that defect density is large in this low density layer. It is also to be noted that there is excellent match between XRR analysis and

VEPFIT analysis with respect to the location and width of the low density layer (Table 5.2 and 5.3).

Table 5.3: XRR fitting parameters for film 1 and film 3.

	Layers	Thickness (nm)	Electron scattering length density (\AA^{-2})	Roughness (nm)
As-prepared (Film 1)	single layer	188	1.49E-5	0.8
	layer 1	110	1.49E-5	1.1
Annealed at 200°C (Film 3)	layer 2	11	1.17E-5	0.5
	layer 3	65	1.46E-5	0.7

5.3.2e. Discussion

The morphology and nanostructure of CoPc film is seen to be influenced by post deposition annealing at temperatures 140 and 200°C owing to the role of surface energy and molecule-substrate interactions on the growth and orientation of molecules. The annealing results in transition from island-like structure (room temperature deposited film) to a granular form. The grains formed due to annealing (140°C) get arranged in a more orderly manner with subsequent annealing at higher temperature (200°C). The annealing at 140°C is seen to increase the surface roughness (AFM and XRR) of the film which is attributed to the interpenetrating network of molecules due to the formation of grains. However, the ordered and homogeneous distribution of grains at higher temperature annealing (200°C) results in decrease in the roughness of the film. In addition to the variation in the morphology of the films due to annealing, significant variation in the depth dependent nanostructural characteristics have been seen from the *S*-parameter profiles. Although annealing at 140°C modifies the morphology significantly (island-like to granular), *S*-parameter profile for film 2 (140°C annealed) show only a marginal

difference as compared to film 1 (as-deposited). The beginning of the formation of grain like structure is coupled with large number of defects (grain boundaries) in the film due to the non uniform distribution of grains. As a result of the presence of defects/more grain boundaries, a short L_+ has been observed in film 2. This is also consistent with the increase in the roughness of film 2. On the other hand, annealing at 200°C has significantly modified the nanostructure of the film as revealed from defect depth profiling using slow positron beam and electron density XRR profiling. Depth profiling has indicated the inhomogeneity in the nanostructure in the case of film 3. The presence of a region (layer) with disorder or more defects (high S -parameter and short L_+) has been seen in film 3 unlike other films. This layer is sandwiched between the two layers with lesser defects as revealed from their low S -values (calculated using VEPFIT). XRR study has also confirmed the presence of this layer having low SLD as compared to other layers. High temperature annealing improves the nanostructure of the film by rearranging the molecules in a more orderly and homogeneous manner and thereby, minimize the defects/disorder in the film. However, in the present case, high temperature annealing resulted in inhomogeneity in the nanostructure across the depth as indicated by the presence of a layer with disorder or more defects. This might be due to the incomplete annealing out of the defects probably due to the large thickness of the film (200 nm). This reveals that although post deposition annealing improves the structural characteristics of the film, the depth dependent nanostructure analysis is essential to examine the homogeneity which is essential for better device performance. The present study highlights the ability and sensitivity of slow positron beam and XRR for nanostructural characterization in thin OSC films which are otherwise, difficult to be probed non-destructively by any other technique. It is seen that annealing may not ensure homogeneity throughout the bulk of the film. This necessitates evaluation of defect

structure to ensure best device performance since structural inhomogeneities affect device performance by lowering the mobility of charge carriers.

5.3.3. Defect profiling in organic semiconductor heterostructures

5.3.3a. Grazing incidence X-ray diffraction

The crystalline nature and d -spacing have been determined from GIXRD in single and multilayer films. All the films show sharp diffraction peak indicating the crystalline nature of the films. The d -spacing has been determined from the diffraction peak using Bragg's formula. Figure 5.15 shows the GIXRD pattern for the single layer (n and p -type) OSC films. The d -spacing for p -type OSC material (CoPc) is 13.497Å (2θ -angle 6.55°) and that of n -type OSC material (F₁₆CuPc) is 14.083Å (2θ -angle 6.22°).

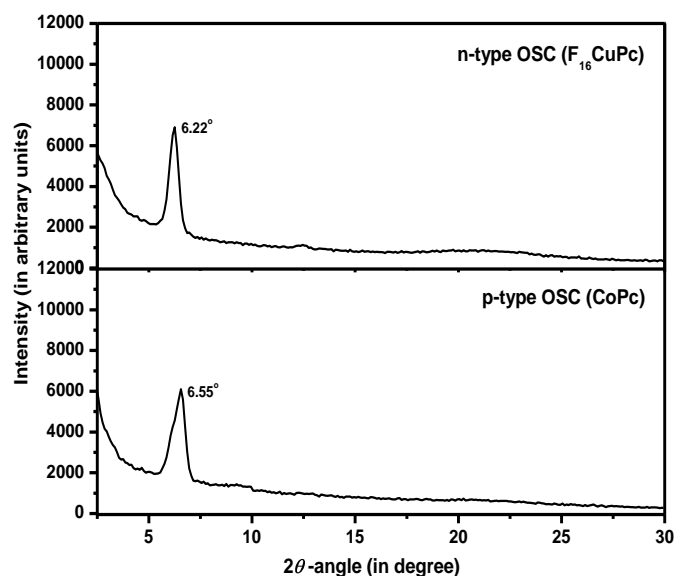


Figure 5.15: GIXRD pattern for single layer films of n and p -type OSC materials on quartz substrate.

In bilayer structures (p - n and p - p), different layers have been probed by varying the grazing angle. Figure 5.16 shows the GIXRD pattern for p - n and p - p bilayers performed at grazing angles corresponding to OSC layers and the interfacial region between the two organic materials (n and p -type, as the case may be). In the case of p - n bilayer (Figure

5.16) two peaks obtained at different 2θ -angles correspond to p and n -type OSC materials. The 2θ -angles (d -spacings) for p and n -type materials are 6.62° and 6.22° , respectively consistent with the single layer films of the same material. The dashed line (Figure 5.16) corresponds to the organic-organic interface region i.e. it samples both the layers. In the case of p - p bilayer (Figure 5.16), sharp peaks have been obtained at different 2θ -angle values for the grazing angles corresponding to p -type OSCs used in this bilayer. The 2θ -angles for the peaks are 6.87° and 6.80° and the d -spacing are 12.77\AA and 12.93\AA , respectively. The p -type OSC materials used in p - p bilayer are different (FePc and ZnPc) from that used in p - n bilayer and single layer p -type film (CoPc). This has resulted in different values of 2θ -angles (d -spacing) in p - p bilayer.

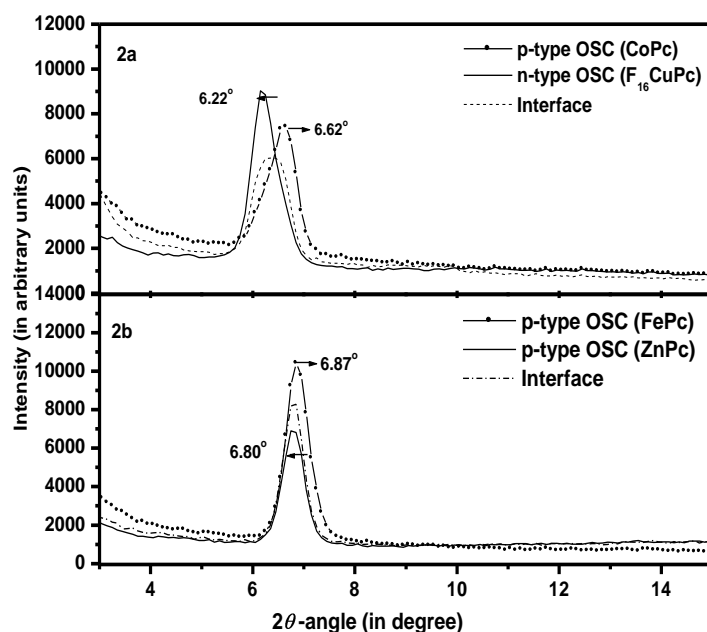


Figure 5.16: GIXRD pattern for bilayer films of p - n and p - p -type OSC materials on quartz substrate.

5.3.3b. Doppler broadening spectroscopy

Defect depth profiling has been carried out in all the films to study the nanostructural variations as a function of depth of the films. The S -parameter variation as a function of positron energy for single layer films of n and p -type OSCs are shown in Figure 5.17 and 5.18. A non-monotonic change in the S -parameter profile as a function of

depth of the film has been seen. The high value of S -parameter at a given depth is a signature of the presence of defects in that region. The single layer films of n and p -type OSC on quartz comprise of an interface between organic and inorganic (substrate) materials. The increase in S -parameter reflects the interfacial characteristics between the film and the substrate. The high value of S -parameter at the interface indicates the presence of open volume defects/ domains (trap centers) and reveals the structural variations between organic and inorganic materials (substrate) as indicated by the subsequent fall in S -parameter. The epitaxial relation between the film and the substrate is important in crystallographic sense as well as for growth behavior. The organic molecules have large anisotropy and internal degrees of freedom due to low symmetry and extended size. The effect of size difference of unit cells of organic molecules and the inorganic substrate as well as molecule-substrate interaction lead to translational and orientational domains, which are the sources of disorders [Brutting et al., 2008]. In addition, growth of the films is accomplished by the interplay of molecule-molecule and molecule-substrate interaction [Debnath et al., 2008].

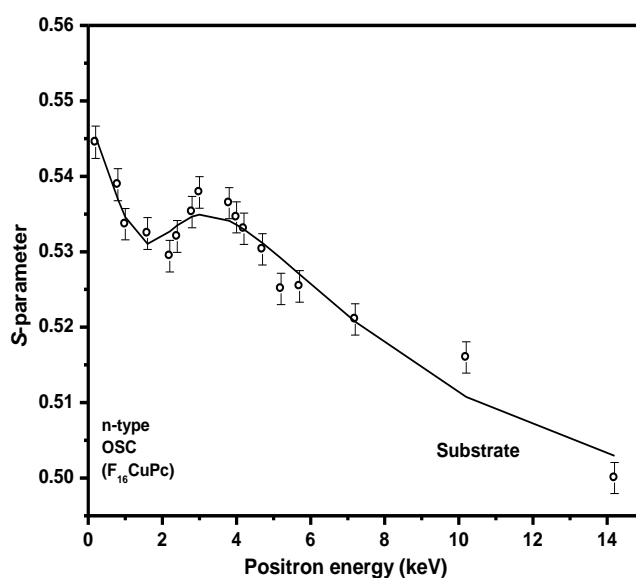


Figure 5.17: The S -parameter profile for single layer film of n -type OSC material. The solid line represents the best fit to data using VEPFIT.

Similar enhancement in S -parameter has been observed in the case of p - n and p - p bilayers corresponding to organic-organic and organic-inorganic (substrate) interfaces, as the case may be (Figure 5.19 and 5.20). The increase in S -parameter has been seen at the organic-inorganic interfaces in both the bilayers (p - n and p - p) similar to the observation in single layer films. However, there is a marked difference in S -parameter profiles in the region corresponding to organic layers. The region corresponding to organic-organic interface in the two types of heterostructures show different features.

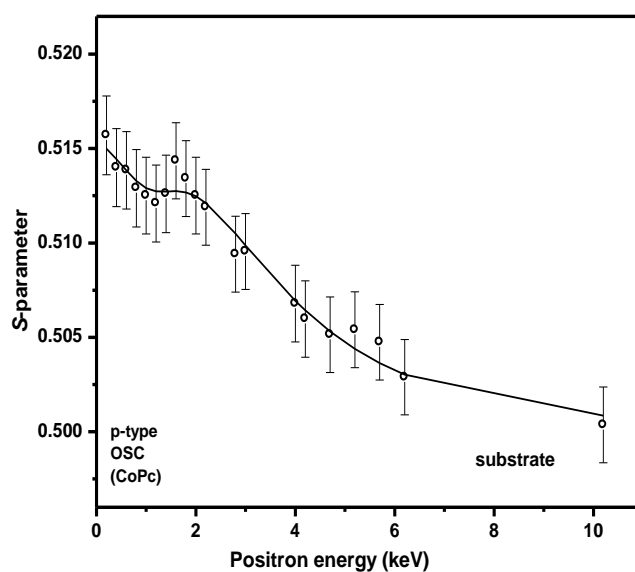


Figure 5.18: The S -parameter profile for single layer film of p -type OSC material. The solid line represents the best fit to data using VEPFIT.

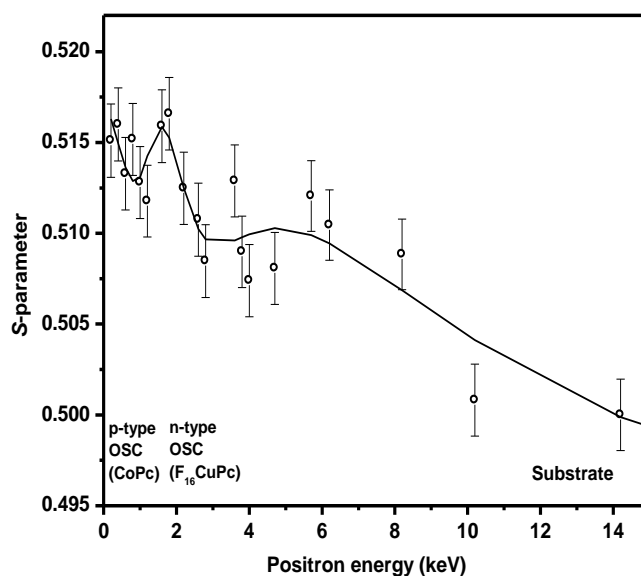


Figure 5.19: The S -parameter profile for p - n bilayer. The solid line represents the best fit to data using VEPFIT.

The S -parameter shows sharp increase at a depth corresponding to the interface between p and n -type OSCs (in p - n bilayer), which is absent in the case of p - p interface (in p - p bilayer) that shows a smoothly varying S -parameter profile. It is to be noted that p - n interface has an intrinsic electric field due to the difference in the energy level of different organic materials which is directed in the beam direction unlike the p - p interface in p - p bilayer. In addition to this, the difference in d -spacing for the constituents in p - n bilayer is larger compared to that of p - p bilayer (GIXRD measurement). The intrinsic electric field and incoherency/lattice mismatch at the interface which can produce defects due to local molecular ordering at the junction as well as strain at the interface in p - n bilayer as compared to p - p bilayer may be responsible for the enhancement in S -parameter at the interfaces.

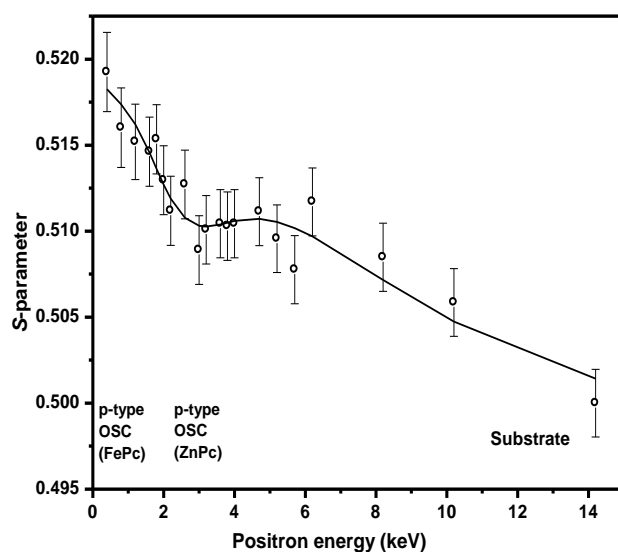


Figure 5.20: The S -parameter profile for p - p bilayer. The solid line represents the best fit to data using VEPFIT.

The S -parameter profile for n - p - n heterostructure is shown in Figure 5.21. The n - p - n trilayer comprises of two organic-organic (n - p and p - n) and organic-inorganic (n -type OSC and substrate) interfaces. The S -parameter profile shows similar features as observed in the case of p - n bilayer i.e. enhancement of S -parameter at all the interfaces. The enhancement in S -parameter at the organic-organic interfaces in p - n and n - p - n

heterostructures is expected to be a cumulative effect of the presence of defects and intrinsic electric field. However, positron diffusion modeling in the presence and absence of electric field is suggestive of the fact that electric field across the interface need not necessarily help localize positrons at the interfaces, a discussion on which is given in latter section.

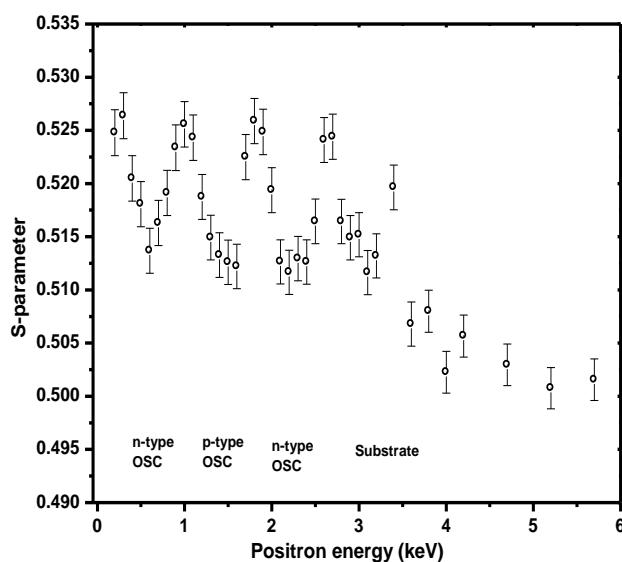


Figure 5.21: The S -parameter profile for n - p - n trilayer.

5.3.3c. S - W Analysis

S -parameter profiles for single and multilayers (n , p , p - n , p - p and n - p - n) have indicated the presence of interfaces with significant defects at the junction of different organic as well as organic and inorganic materials. However, the type and nature of defects at the interfaces have been discerned from S - W analysis which involves simultaneous analysis of S and W parameters and helped in recognizing positron annihilation states in the system.

The S - W curve for p - p and p - n bilayers is shown in Figure 5.22. The S and W values have been normalized with respect to quartz substrate. Each S and W value corresponds to a particular depth of the sample. The quartz substrate has been represented by $S=W=1$. The S - W curves for p - p and p - n bilayers have shown different slopes which

indicated the presence of different type of defects in these heterostructures. In the case of p - n bilayer, S - W points corresponding to different depths lie on the line L2 (shown in Figure 5.22) indicating the presence of similar type of defects throughout the bilayer. However, defects at organic-organic interface are more as compared to bulk layer. Similarly, in the case of p - p bilayer, only one kind of defects exist throughout the depth, however, the S - W curve (line L1) has shown the absence of interface between p -type materials.

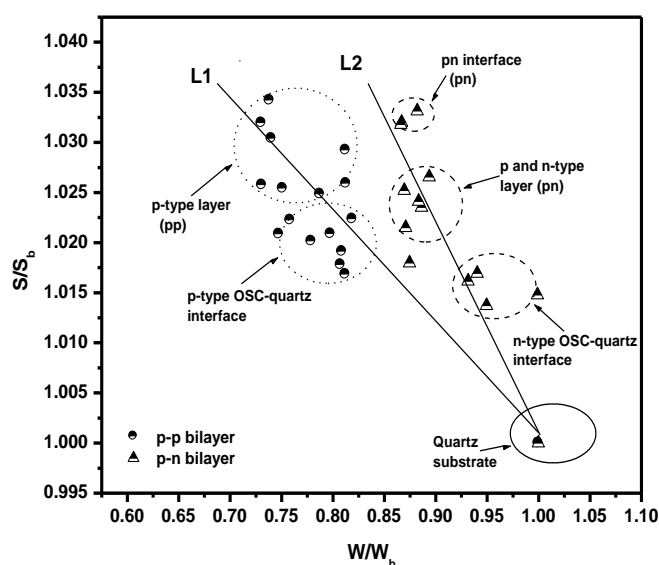


Figure 5.22: S - W correlation for p - n and p - p bilayers.

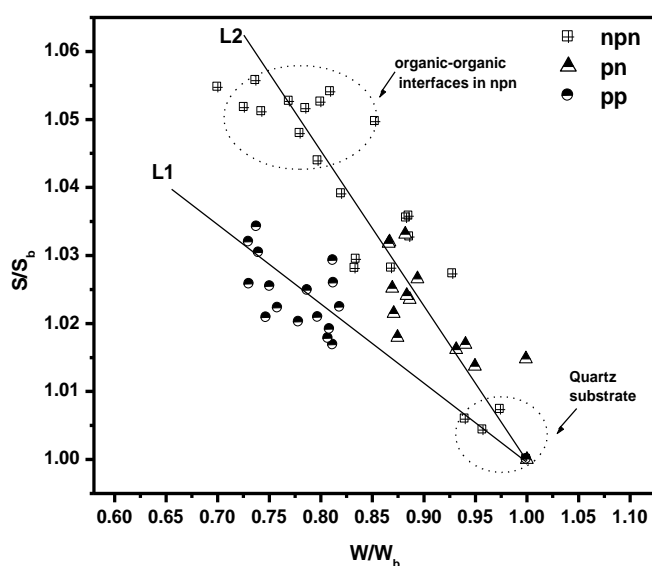


Figure 5.23: S - W correlation for p - n , p - p and n - p - n multilayers.

Figure 5.23 shows the S - W curves for p - p , p - n and n - p - n together. It has been seen that the slope of S - W curves of p - n and n - p - n multilayer is same, but different from p - p bilayer which indicated that the nature of defects in p - n and n - p - n is similar and distinct from p - p bilayer. The difference in the nature of defects in these multilayers is due to the presence of different organic materials (n and p -type). The S - W curve for n - p - n trilayer has shown the presence of more defects at the organic interfaces as compared to p - n bilayers. This has been attributed to different morphology of the layers owing to the different thickness of the layers in p - n and n - p - n multilayers. The S - W mapping has revealed the effect of organic materials as well as thickness of layers on the defect microstructure in multilayers.

5.3.3d. VEPFIT analysis

Depth dependent S -parameter profiles have been fitted using VEPFIT analysis to evaluate the S -parameter and positron diffusion length for different layers of the heterostructures. Figures 5.17-5.20 show the fitting data for S -parameter profiles of single layer as well as bilayers (p - n and p - p type). The solid lines in the figures are the fitted lines to the data. In case of single layer films (n and p), the fitting has been done by considering three layers, wherein, the additional layer corresponds to an interface between the OSC material (p or n) and the quartz substrate. The fitted values of layer S -parameter, diffusion length and layer thickness are shown in Table 5.4. The bulk S -parameter corresponding to the annihilation in quartz substrate has been normalized to a value of 0.5 for all the films (single as well as multilayer). The diffusion length of positrons in quartz substrate has been determined by fitting the S -parameter profile measured in quartz. The diffusion length of positron in quartz has been seen to be in the range of 300-500 nm which is taken as a fixed parameter in all the fittings. It has been observed that a good fit to the data required very short diffusion length of positron and

nanometers thick interface layer. The diffusion length in organic layers and the interfaces have been seen to be in the range of 30-40 nm and 0.2 nm, respectively. The S -parameter has been seen to be highest for the interface layer. The high value of S -parameter and short diffusion length (~ 0.2 nm) for the interface layer is indicative of the presence of defects at the interface as compared to bulk layers. The mean depth of the interface (90-100 nm) obtained from VEPFIT has been seen to be higher as compared to the film thickness (80 nm) in both the cases. This appears to be due to the effect of higher diffusion coefficient of positrons on the substrate that leads to a broader implantation profile.

Table 5.4: Fitted values of S -parameter and positron diffusion length (L_+) in single layer of n and p -type OSCs.

Sample	Layer 1		Layer 2		Layer 3	
	S1	$L_+(1)$ (nm)	S2	$L_+(2)$ (nm)	S3	$L_+(3)$ (nm)
n-type	0.51198	30	0.54468	0.2	0.5000	320
p-type	0.50742	35	0.51533	0.2	0.5000	110

Table 5.5: Fitted values of S -parameter and positron diffusion length (L_+) in p - n and p - p bilayers.

Sample	Layer 1		Layer 2		Layer 3		Layer 4		Layer 5	
	S1	$L_+(1)$ (nm)	S2	$L_+(2)$ (nm)	S3	$L_+(3)$ (nm)	S4	$L_+(4)$ (nm)	S5	$L_+(5)$ (nm)
pn type	0.48532	37	0.54303	0.1	0.44971	62	0.51752	0.2	0.4970	500
pp type	0.51625	31	--	--	0.506181	27	0.51619	0.2	0.4970	350

In the case of *p-n* bilayer, a good fit has been obtained by considering five layers. The additional layers correspond to the interfaces between the organic-organic and organic-inorganic materials. On the other hand, in case of *p-p* bilayer, only four layers are required to fit the data indicating the absence of interface between the two *p*-type organic materials. The fitted values of *S*-parameter for all the layers including the interfaces and diffusion length of positrons at the interfaces are shown in Table 5.5. The *S*-parameter values in organic bilayers are seen to be different from that obtained for single layers. This is due to the difference in the morphology of the films in single layer and bilayer structures owing to the differences in their thickness [Debnath et al., 2008]. The *S*-parameter at interfaces has been seen to be higher than the bulk layers as observed in single layer films as well. The diffusion length of positrons in organic layers is in the range 30-40 nm except for the *n*-type layer in *p-n* bilayer. On the other hand, very short diffusion length has been obtained at all the interfaces. The high value of *S*-parameter and short diffusion length of positrons at interfaces ($\sim 0.1-0.2$ nm) are indicative of the presence of defects at the interfaces as compared to bulk of the layers. Interestingly, the thickness of interface between *p* and *n*-type OSC is ~ 0.2 nm, which is of the order of bond length in organic molecules. The positron diffusion length in *n*-type layer in *p-n* bilayer is 62 nm which is higher than the value obtained for other organic layers. It is to be noted that the presence of electric field at *p-n* interface has not been taken into account while fitting the data, due to the lack of knowledge on the exact value of electric field, normally evaluated from current-voltage characteristics and in-situ spectroscopic measurements. The enhanced diffusion length of positron in the *n*-type layer could be a manifestation of the drift of positrons due to the intrinsic electric field at the interface leading to over estimation of diffusion length.

In the case of *n-p-n* trilayer, fitting could not be done due to the presence of large number of layers (seven layers) including the interfaces between organic materials. However, sharp features in experimental *S*-parameter profile are indicative of interfaces between *p* and *n*-type materials similar to that observed in *p-n* bilayer. It may be mentioned that the electric field at the two organic interfaces (*n-p* and *p-n*) is in the opposite direction. We believe, this has effectively improved the depth resolution especially for the middle layer (*p*-type) owing to the modification of implantation profile.

5.3.3e. Analysis of the effect of intrinsic electric field and defects at the interfaces (VEPFIT modeling)

The fitting parameters obtained through VEPFIT analysis reflect the cumulative effect of defects and the intrinsic field at the interfaces. In order to understand the effect of defects and the intrinsic electric field at the organic-organic interfaces on the positron systematics, VEPFIT has been used to model the multilayer system. To mimic the present system, two layers of OSCs with an interface in between have been considered. The *S*-parameter value of each layer is chosen on the basis of fitting results obtained from VEPFIT analysis on the actual *p-n* bilayer system. The model system consists of a top *p*-type layer, followed by an interface layer and *n*-type layer of infinite thickness. The presence of defects has been represented by high *S*-parameter and short diffusion length of positrons at the interface. Similarly, the absence of defects is represented by taking the interface layer *S*-parameter and diffusion length identical to that of the top layer. Different scenarios have been considered to examine the effect of defects and the electric field, individually or in tandem, as the case may be on the *S*-parameter profile.

The modeled *S*-parameter profiles have been shown in Figure 5.24 which represents the case for the presence or absence of defects at the interface layer in the absence of any electric field. It has been observed that the *S*-parameter profile, similar to

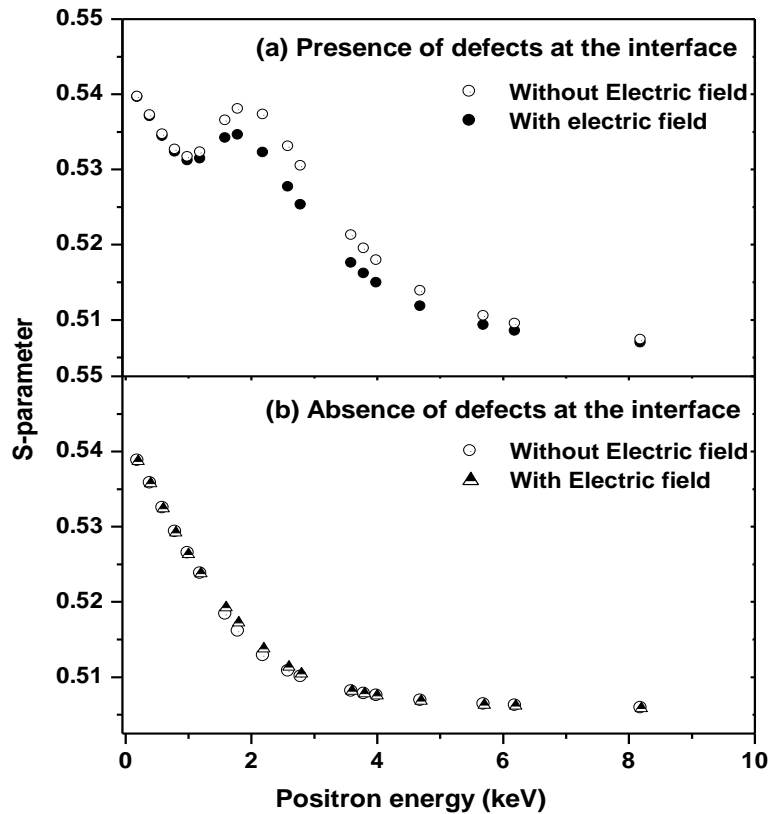


Figure 5.24: *S-parameter profiles for a p-n heterostructure as obtained from Positron diffusion modeling considering different scenarios for the effect of defects and electric field at the interface.*

the experimentally obtained profile (with a marked increase at the organic-organic interface), cannot be generated without taking into consideration the defects at the interface. Figure 5.24a shows the effect of electric field at the interface in the presence of defects. Presence of electric field in the direction of the beam (in the present case) drifts the positrons away from the interface, consequently reducing the stopped positron fraction in this region and increasing the fraction of positrons annihilating in the bottom layer. Effectively, positrons see the bottom layer at lower implantation energy or depth leading to the observed profile. It may be mentioned that the electric field has marginally but distinctly modified the profile keeping the effect of defects (positron trapping at the interface) dominant. Figure 5.24b indicates that the electric field alone cannot generate the observed profiles (experimental) in the absence of defects at the interface. The

modeling has clearly shown that the presence of defects due to epitaxial relation between the materials is the dominant feature leading to enhanced trapping of positrons at the interface. The electric field, on the other hand, facilitates diffusion of positrons away from the interface in the direction of the field.

5.3.3f. Mobility of positrons and charge carriers in OSC layers

The mobility of positrons in a medium is dependent on its microstructure due to the tendency of positrons to get trapped at the structural defects. The positron diffusion length obtained from VEPFIT analysis has been used to calculate positron mobility in OSC layers. The positron diffusion length L_+ and diffusion coefficient D_+ are related as,

$$L_+ = \sqrt{D_+ \tau} \quad (5.2)$$

where, τ is positron lifetime in the material. The diffusion coefficient can be used to calculate positron diffusion mobility in the material using Nernst-Einstein relation,

$$D_+ = \mu_+ k_B T / e \quad (5.3)$$

where, μ_+ is positron diffusion mobility, k_B is Boltzman's constant, T is temperature and e is electronic charge. Coincident Doppler broadening studies have shown that positron/Ps do not interact with the metal ion in phthalocyanines [Ito et al., 2000]. The positron lifetime in bulk of phthalocyanine has been reported in the range 0.290-0.330 ns [Ito et al., 2000]. The positron diffusion coefficient has been calculated using Eq. (4), taking into account the positron diffusion length of 35 nm as calculated from VEPFIT analysis and positron lifetime as 300 ps. The diffusion mobility (μ_+) of positron estimated using Einstein's relation (Eq. (5.3)) has been seen to be 1.6 cm²/Vs.

The mobility of charge carriers has been measured from J - V characteristics in organic layers. The J - V measurement in n -type OSC single layer film is shown in Figure 5.25. At low voltage, J - V characteristics represents ohmic conduction. At higher voltages

the transport mechanism is space charge limited conduction (SCLC) where the charge transport is governed via deep traps existing in the organic layers. These deep traps can be generated due to the presence of structural defects in the organic layers [Samanta et al., 2008]. J - V characteristics in SCLC region is given by,

$$J = \frac{9\varepsilon_0\varepsilon_r\mu\theta}{8d^3}V^2 \quad (5.4)$$

where, ε_0 is the permittivity of free space, μ is the charge carrier mobility, ε_r is the static dielectric constant of the material and θ is described as ratio of density of free carriers to the density of total charge carriers, i. e. $\theta = p/(p+p_t)$ where, p is the free carrier density and p_t is the density of trapped carriers. In the presence of defects the value of θ is less than 1 and approaches to a maximum value of 1 in the absence of any defect.

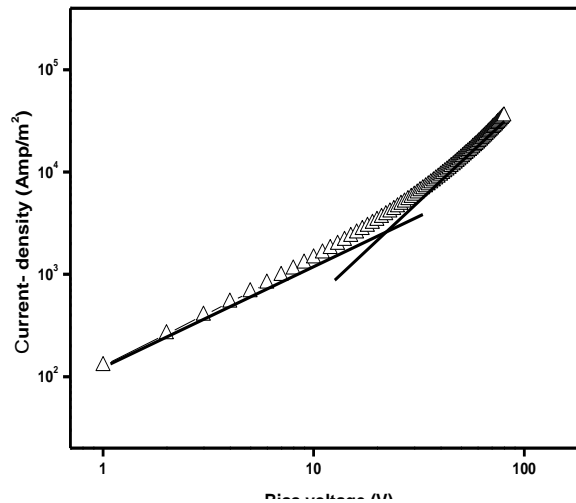


Figure 5.25: Current density-voltage (J - V) characteristics in single layer OSC film.

Using the slope of J - V plots for n -type OSC single layer film and the literature value of $\varepsilon_0\varepsilon_r$ as 2.43×10^{-11} F/m, the effective mobility of charge carriers, $\mu\theta$ in organic layer has been calculated as $3.5 \text{ cm}^2/\text{Vs}$, which represents the lower limit of charge mobility in organic layers. The effective mobility ($\mu\theta$) of charge carriers decreases with the increase in defect density of the medium. The mobility of positrons which is also strongly

dependent on the structural defects in the materials has been seen to be comparable to the effective mobility ($\mu\theta$) of charge carriers determined from the J - V characteristics.

It is an interesting observation and it offers the possibility to determine defect (trap) density and charge conductivity in organic thin films by measuring the positron mobility. It may, however, be mentioned that the dynamic behavior of positron and charge carrier are different in a medium due to the difference in the scattering mechanism and nature of delocalization of their wave functions. Therefore, more studies on variety of OSC materials are necessary to ascertain stronger correlation between positron mobility and effective mobility of charge carriers.

5.3.4. Interface engineering: Modification of dielectric surface using self assembled monoayers (SAM)

5.3.4a. Crystallinity and Surface morphology of the films

The crystalline nature of CuPc films grown on thermally grown oxide (200 nm) SiO₂/Si substrates (SiO₂(200 nm)/Si) and self assembled monolayer, SAM (PTS and OTS) modified SiO₂(200 nm)/Si has been investigated using GIXRD (Figure 5.26). The Bragg peak at 2θ angle 6.98° corresponds to α -CuPc phase. The presence of peak indicates the crystalline nature of the films, although, the degree of crystallinity varies in the films. The sharpness of the peaks in both the SAM modified cases is seen to be higher than the unmodified substrate indicating better crystallinity in the former as compared to the latter. The full width at half maximum (FWHM) calculated by fitting the peaks for unmodified, PTS and OTS modified substrates are 0.285, 0.227 and 0.21, respectively. The low intensity and broadness of the peak in CuPc grown on SiO₂(200 nm)/Si shows low degree of crystallinity as compared to SAM modified cases. No significant difference in the crystalline behavior in PTS and OTS modified cases are seen.

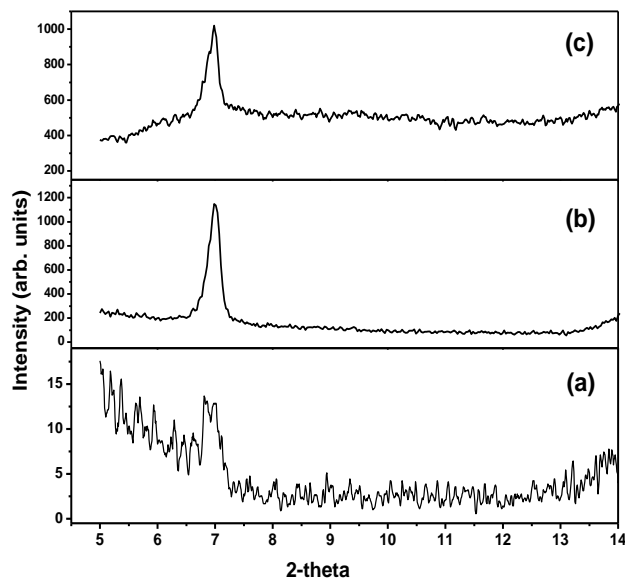


Figure 5.26: GIXRD pattern of CuPc films grown on unmodified and SAM modified substrates; (a) $\text{SiO}_2(200 \text{ nm})/\text{Si}$; (b) $\text{PTS}/\text{SiO}_2(200\text{nm})/\text{Si}$; (c) $\text{OTS}/\text{SiO}_2(200 \text{ nm})/\text{Si}$

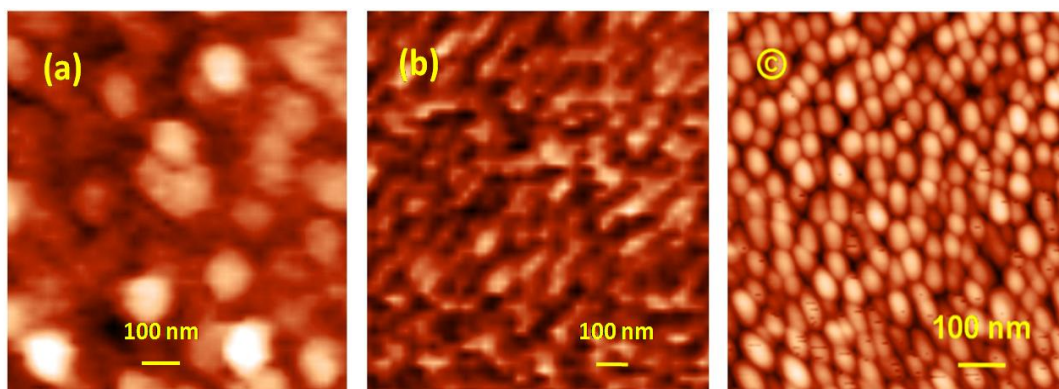


Figure 5.27a: AFM images of CuPc films (30 nm) grown on unmodified and SAM modified substrates; (a) $\text{SiO}_2(200 \text{ nm})/\text{Si}$; (b) $\text{PTS}/\text{SiO}_2(200\text{nm})/\text{Si}$; (c) $\text{OTS}/\text{SiO}_2(200 \text{ nm})/\text{Si}$

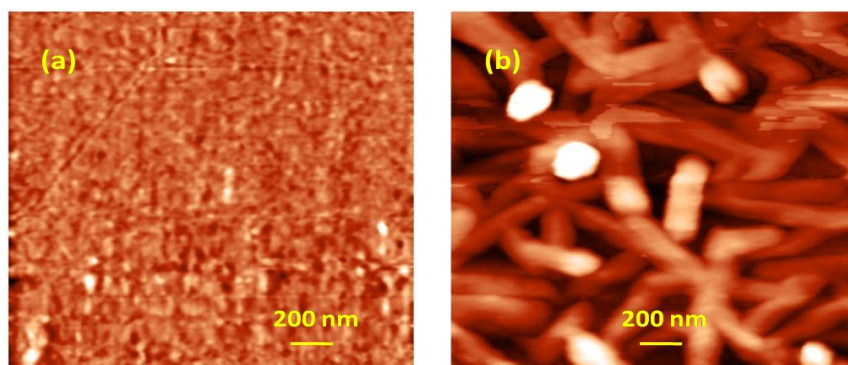


Figure 5.27b: AFM images of CuPc films ($\sim 2 \text{ nm}$) grown on $\text{SiO}_2(200 \text{ nm})/\text{Si}$ substrate at (a) Room temperature; (b) 225°C temperature

Figure 5.27a shows the AFM images of 30 nm CuPc film grown on unmodified and SAM (PTS and OTS) modified SiO₂(200 nm)/Si substrates. The film grown on unmodified substrate shows granular morphology with ~ 100 nm size grains. On the otherhand, the films grown on PTS and OTS modified substrates show elongated structures and granular morphology with smaller size and more crystalline grains, respectively. Figure 5.27b shows morphology of the interface between CuPc and SiO₂(200 nm)/Si substrate for the films grown at room temperature and 225°C obtained by growing ~2 nm CuPc layer on the substrate. The film grown at 225°C shows fiber like structures with large open voids between the fibers whereas room temperature grown film shows 2D layer like growth mode.

5.3.4b. Depth profiling using slow positron beam

(i) OSC film grown on SiO₂/Si dielectric substrates

The variation of *S*-parameter as a function of positron implantation energy for CuPc film grown at room temperature on native oxide (3-4 nm) and thermally grown oxide (200 nm) SiO₂/Si substrates, designated as *native* SiO₂/Si and SiO₂(200 nm)/Si, respectively is shown in Figure 5.28. The profile above 1.2 keV positron energy corresponds to the substrate *S*-parameter in each case. The difference in *S*-parameter profiles between 3-9 keV energy has been attributed to different thickness of oxide layers in the two cases beyond which *S*-parameter monotonically approaches to crystalline silicon. The energies below 1.2 keV correspond to the grown OSC films (30 nm). A significant difference in the profile has been observed above 550 eV in the two cases (Figure 5.29), represented by increase in *S*-parameter value in the case of film grown on SiO₂(200 nm)/Si. This is followed by a slight decrease in *S*-parameter and finally reaching to the substrate *S*-parameter value.

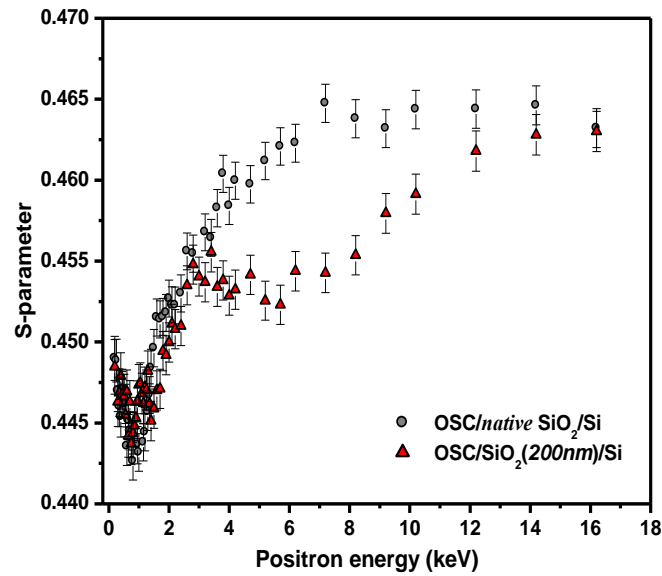


Figure 5.28: *S-E profile for CuPc film grown on native and thermally grown oxide silicon substrate.*

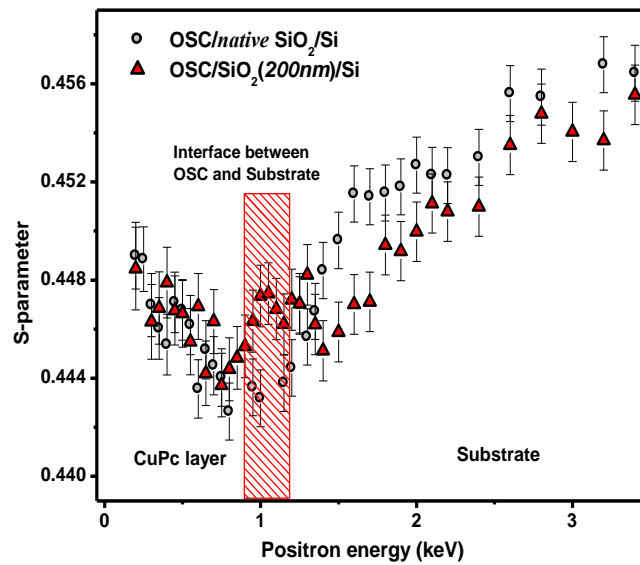


Figure 5.29: *S-E profile for CuPc film grown on native and thermally grown oxide silicon substrate; patterned region indicates the interface between OSC layer and substrate*

On the other hand, film smoothly varying S -parameter profile reaching the substrate S -parameter value at higher energies. The difference in S -parameter profiles in the two cases (below 1.2 keV) corresponds to the interface region between OSC layer and the substrate (as evaluated from relation, z (nm) = $40 * E^{1.6} / \rho$). The increase in S -parameter at

the interface in the case of film grown on $\text{SiO}_2(200 \text{ nm})/\text{Si}$ unlike *native* SiO_2/Si indicates more defects/disorder at the interface between OSC layer and the substrate in the former. The surface roughness is high in the case of thermally grown oxide layer as compared to the native oxide. The high surface roughness leads to more defects/disorder at the interface between the film and the substrate.

It is seen that the films grown at higher substrate temperature show ordered growth of molecules as compared to lower temperatures. Figure 5.30 shows the S -parameter profiles for OSC films grown on $\text{SiO}_2(200 \text{ nm})/\text{Si}$ at room temperature and 225°C . For visual clarity, the S -parameter for the film grown at 225°C has been raised to a certain value keeping the profile same. The S -parameter profiles show noticeable difference in the region corresponding to the interface between OSC film and the substrate. The increase in S -parameter at the interface in the room temperature grown film shows the presence of more defects in contrast to the film grown at 225°C . It is to be noted that though the film grown at room temperature shows 2D layer like growth (AFM study), the presence of large number of defects could not be identified by AFM.

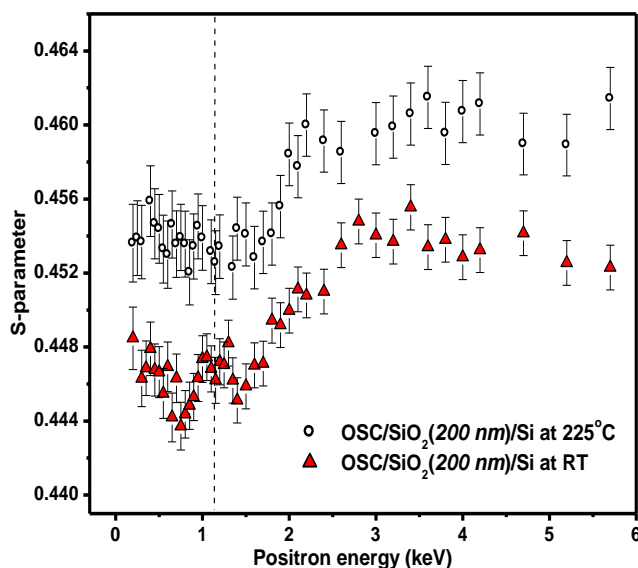


Figure 5.30: S - E profile for CuPc film grown on $\text{SiO}_2(200 \text{ nm})/\text{Si}$ at temperatures; room temperature (RT) and 225°C .

(ii) OSC film grown on SAM modified SiO_2/Si dielectric substrates

Figure 5.31 shows the S -parameter profile (S - E) of OSC film (CuPc) grown on SAM (PTS) modified $\text{SiO}_2(200 \text{ nm})/\text{Si}$ and unmodified $\text{SiO}_2(200 \text{ nm})/\text{Si}$ dielectric substrates. The S -parameter profiles show distinct feature at implantation energy corresponding to the interface between OSC layer and the substrate. The observed variation in S -parameter at the interface indicates the presence of defects/disorders in unmodified substrate as compared to SAM modified substrates which show smoothly varying S -parameter profiles. This is clear indication of reduction in surface roughness of the substrate due to SAM modification.

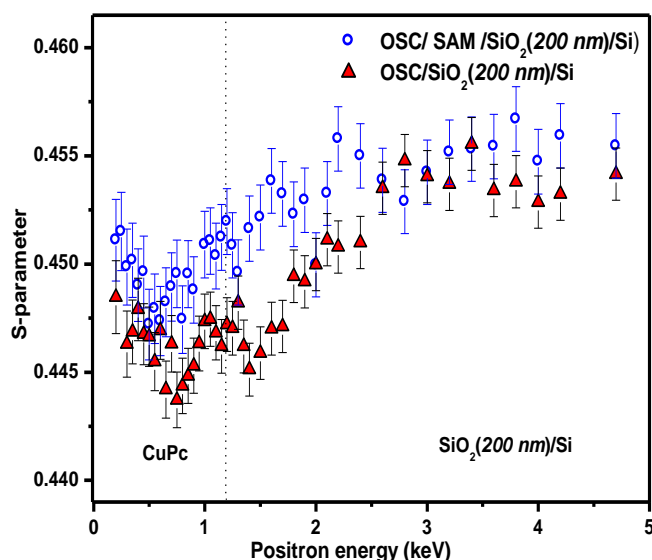


Figure 5.31: S - E profile for CuPc films grown on $\text{SiO}_2(200 \text{ nm})/\text{Si}$ and SAM (PTS) modified $\text{SiO}_2(200 \text{ nm})/\text{Si}$ substrates.

Similar characteristics have been seen for OTS modified substrate too. The dielectric substrate modification using SAM alters the surface energy owing to the difference in the tail groups viz. $-\text{C}_6\text{H}_5$ and $-\text{CH}_3$ in PTS and OTS, respectively which influences the growth behavior/mode of OSC molecules. The influence of surface energy on the growth behavior of OSC molecules has been studied for two different SAMs viz. PTS and OTS. Figure 5.32 shows S -parameter profiles for CuPc film grown on PTS and OTS modified

substrates. Only a slight difference in S -parameter profile has been observed for the two cases though the interfacial morphology and growth mode as observed by AFM shows distinct growth behavior of the molecules.

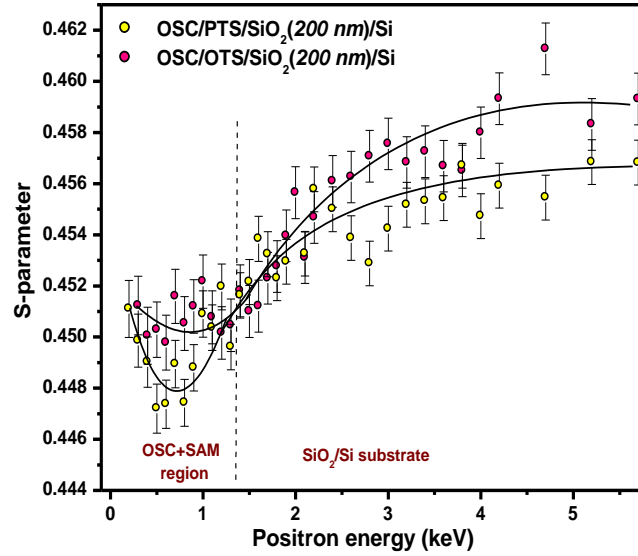


Figure 5.32: S - E profile for CuPc films grown on SAM (PTS and OTS) modified substrates.

5.3.4c. Field effect mobility of charge carriers

The field effect mobility of charge carriers has been determined from the electrical characterization of organic field effect transistor (OFET) with SiO₂/Si dielectric (modified and unmodified). The transfer characteristics of OFETs on PTS and OTS modified and unmodified SiO₂ (200 nm)/Si substrates are shown in Figure 5.33.

The field effect mobility of holes (μ_p) in saturation region has been extracted from the plot of $I_D^{1/2}$ versus V_G using the equation,

$$I_D = \frac{WC_i}{2L} \mu_p (V_G - V_T)^2 \quad (5.5)$$

where, L and W are length and width of the channel, C_i is the capacitance per unit area of the dielectric, I_D is drain current, V_G is gate voltage and V_T is the threshold voltage.

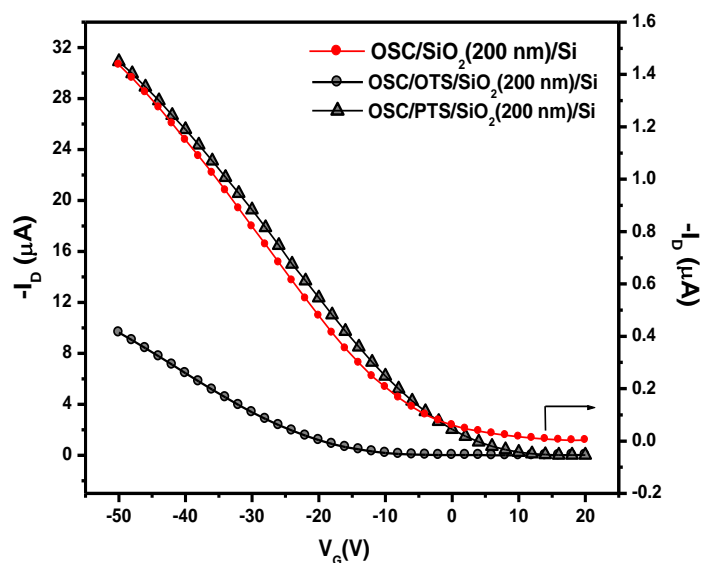


Figure 5.33: Transfer characteristics of OFETs on unmodified and SAM modified $\text{SiO}_2(200 \text{ nm})/\text{Si}$

The calculated μ_P for unmodified, PTS and OTS modified $\text{SiO}_2(200 \text{ nm})/\text{Si}$ devices are 0.0009, 0.02 and 0.01 cm^2/Vs , respectively. This shows that the performance of OFETs on modified substrates is better than the unmodified one. The lowest mobility in the case of unmodified $\text{SiO}_2(200 \text{ nm})/\text{Si}$ as compared to PTS and OTS modified substrate is attributed to structural defects at the interface in the former. These defects act as charge traps and thereby reduce the charge mobility through the channel formed at the interface. On the other hand, growth behavior has influence on the mobility as revealed from the different mobilities in PTS and OTS. The 2D like layer by layer growth (in the case of PTS) is known to result in improved charge mobility as compared to 3D growth which can give rise to voids in the film with large number of grain boundaries (hinder the charge transport) [Hwang et al., 2006].

5.3.4d. Discussion

The morphology of OSC at the dielectric/semiconductor interface is crucial for better device performance (charge conduction). The interfacial properties especially, nucleation and growth of OSC, grain size, molecular ordering, alignment and crystalline

structure are influenced by the surface characteristics of the dielectric viz. surface energy and roughness. Surface roughness leads to disordered arrangement of molecules resulting in more defects at the interface as observed in the case of CuPc grown thermally grown 200 nm oxide SiO₂/Si substrate. The *native* oxide SiO₂/Si substrate has lower surface roughness as compared to thermally grown oxide which leads to better growth of molecules in the former. SAM modification reduces the surface energy and roughness resulting in ordered growth of the molecules. It is seen that although OSC film grown on PTS and OTS modified substrates show crystalline nature and smooth interfacial characteristics as reflected from the *S-E* profile, the charge mobilities are different in the two cases. Since the channel is formed close to the dielectric/semiconductor interface, surface properties play a crucial role in regards to the initial coverage of OSC molecules on the substrate. OTS promoted 3D like growth of molecules with more grain boundaries as compared to 2D like layer by layer growth in PTS case. The hindrance on charge transport due to the presence of void/grain boundaries in 3D growth reduces the mobility. The study highlights the role of surface energy/roughness on the growth behavior of OSC as well as the dependence of mobility on the growth mode of the molecules.

5.4. Conclusions

Defect depth profiling using slow positron beam has been carried out for nanostructure characterization in thin OSC films. The morphology and nanostructure of the films depend on the growth parameters viz. substrate temperature, deposition rate, thickness of the film etc. In this regards, nanostructure of FePc films grown at different temperatures and varying thickness have been studied. The observed variations have been attributed to the role of molecule-substrate interaction which affects the growth behavior of OSC. For instance, the film grown at room temperature shows more disorders as compared to the one grown at higher temperature and distinct morphology has been

observed for different thickness of the films. In order to improve the morphology of the films grown at room temperature, post deposition annealing treatment has been carried out. Though annealing has been seen to improve ordering of OSC molecules, inhomogeneity in the nanostructure has been observed. A region of more defects/disorders has been identified at a certain depth of the film after post deposition annealing at 200°C. This has been attributed to incomplete annealing out of the defects. Depth profiling studies using XRR is seen to be consistent with the above observation.

Defect depth profiling at the junction of different materials i.e. interfaces in organic heterostructures comprising of junction between different organic and inorganic materials have been studied using slow positron beam. The epitaxial relation between different materials having different lattice parameters results in mismatch at the interfaces giving rise to disorders/defects. The sensitivity of *S*-parameter has been utilized to identify defects in these buried interfaces which otherwise are difficult to be examined by other techniques. The mobility of charge carriers has been measured in OSC films and seen to be comparable to positron mobility owing to the dependence of both on structural defects in the film. The technique, therefore, can be used to characterize organic devices at early stage of fabrication and can give preliminary knowledge of trap density and charge conductivity in organic layers. The nanostructure of interfaces between OSC and dielectric substrate has been studied for CuPc films grown on SAM modified SiO₂(200 nm)/Si and its effect on charge mobility has been studied. The ordered growth of molecules on modified substrate results in higher mobility as compared to unmodified substrate. The alteration in surface energy (roughness) due to SAM modification results in better ordering which in turn increases the mobility of charge carriers. Defect depth profiling using slow positron beam has been seen to be a sensitive technique to

characterize the nanostructure of buried interfaces and layers. This opens an avenue in electronic industry for the characterization of devices in actual configuration.

SUMMARY

Positron annihilation spectroscopy (PAS) is a powerful nuclear probe to study open volumes and defects in solids. It is known as one of the sensitive defect spectroscopic techniques due to the propensity of positron to get trapped in low electron density regions like free volume hole, voids, vacancy defect etc. PAS involves positron and Ps (bound state of positron and electron) as probes to identify atomic order defects in solids and free volumes in polymers, respectively. PAS comprises of different techniques which provide information about various properties of the material through energy and time domain measurements of annihilation γ -rays. Different techniques in PAS are positron lifetime spectroscopy (PALS), Doppler broadening spectroscopy (DBS), Coincidence Doppler broadening spectroscopy (CDB), Age-momentum correlation (AMOC) and $3\gamma/2\gamma$ annihilation spectroscopy. The positron lifetime (inverse of the annihilation rate) is correlated to the size of the defect and the corresponding intensity to defect concentration. Doppler broadening of annihilation radiation carries information about the momentum distribution of annihilating electron-positron pair. The underlying manifestations in positron defect spectroscopy are the increase in the lifetime of positron upon localization in the defect because of the lowering of electron density as compared to bulk and narrowing of the momentum distribution (measured from the Doppler broadening of annihilation γ -rays) when positron is trapped in the defect. In soft condensed matter like polymers and biomaterials, *o*-Ps *pick-off* lifetime enables probing the nanostructural properties viz. free volume distribution and correlated properties such as glass transition, mechanical strength and stability.

The present work highlights the sensitivity and capability of positron annihilation spectroscopic (PAS) techniques to probe atomic and molecular level properties in nanoscale materials. Two categories of nanoscale materials viz. porous matrices and nanoscale thin films have been studied in the present work. PAS has been utilized to

study variety of properties ranging from phase transition of nanoconfined liquids to the characterization of nanostructure of porous membranes and thin films. The sensitivity of positron annihilation parameters to electron density and electron momentum distribution helps in identifying minute structural alterations following the phase transitions. An elevation in the freezing/melting point has been observed in ethylene glycol and isopropanol confined in ZSM-5 nanopores which has been attributed to the role of surface interactions between the liquids and wall of the pores. Interestingly, the extent of the shift has been seen to be different in the two cases owing to the difference in the strength of interaction between the liquid and the wall surface pertaining to distinct nature of hydrogen bonding in these liquids. PAS study has been corroborated with NMR wherein, dynamics of the molecules (spin-spin relaxation) has been utilized to index phase transitions. The different time scale for relaxation indicates different physical environment of the molecules pertaining to different interfacial interactions in these cases. The structural and dynamical properties have been probed to investigate the phase behavior of nanoconfined water in saponite clay (slit-like pores) using PAS, NMR and DRS. An experimental evidence of a new phase transition (above the bulk freezing point of water) in nanoconfined water, in addition to the low-temperature transition in supercooled water has been reported. The study reveals it to be a structural rearrangement of water molecules associated with modification of hydrogen-bonded network. Evidence has also suggested the dynamical arrest/immobilization of water layer near the clay platelet surface (bound water molecules) to be associated with this transition. The above study on phase behavior of liquids confined in nanopores provides evidence of the role of surface interactions on the phase transitions of liquids.

Positron/Ps diffusion length in the material has been utilized to examine the pore architecture of microporous membranes. For larger pore size, lifetime analysis is

insensitive due to the saturation of *o*-Ps lifetime (142 ns). Ps diffusion length evaluated from $3\gamma/2\gamma$ profiles has been indexed as a measure of the length scale of interconnection of pores in the membranes. The comparison of $3\gamma/2\gamma$ ratio in pristine and gold capped membranes has helped in examining the true pore architecture of the membranes by preventing Ps escape from the surface of the membranes owing to high open porosity. In the case of supported liquid PTFE membranes, the pore architecture of membranes has been correlated to the transport properties of the membranes in terms of the permeability of different ions through the membranes. An inverse relation has been seen between the permeability and Ps diffusion length indicating the decrease in permeability with the increase in the length scale of pore interconnection. In the case of track etched polycarbonate membranes, Ps diffusion length obtained in the case of gold capped membranes has been seen to provide length scale of interconnection for smaller pores as well as cross-section of the pores for larger pores indicating small degree of interconnection in the latter case. The study demonstrates the advantages of positron beam characterization of pore interconnectivity in the design/development of membranes with tailored transport properties.

The sensitivity or localization of positron in the low electron density region enables identification of defects/disorders in materials. This capability has been utilized for the characterization of nanostructure of thin OSC films. Depth profiling using slow positron accelerator has been used for the characterization of defect microstructure in these films as a function of different growth parameters like deposition temperature, thickness of the films and post deposition annealing temperature. The bulk *S*-parameter and positron diffusion length evaluated from VEPFIT analysis have been indexed for the analysis of defect/disorders. The effect of interaction between the molecules and substrate on the growth modes has been observed, as revealed from the variation of the

nanostructure of the films grown at different temperatures and of varying thicknesses. The post deposition annealing has been seen to modify the morphology of room temperature deposited film from island like to granular form as seen from AFM. However, inhomogeneity in the nanostructure i.e. a region with more defects/disorder as compared to rest of the film has been observed from PAS as well as XRR. Defect depth profiling has also been carried out for characterizing buried interfaces between different organic (*p* and *n*-type) and inorganic materials (*p* or *n*-type and substrate) in OSC heterostructures. The study reveals the effect of heteroepitaxy between different materials which leads to more defects/disorder at the interfaces between different materials. Interface engineering using self assembled monolayer has been employed to minimize defect/disorder at the interface between OSC and substrate. The mobility of positron determined from the measured positron diffusion length has been seen to be comparable to charge carrier mobility in OSC thin films. This has significant implication towards the determination of charge mobility in OSC materials without the actual device configuration. Depth profiling using slow positron accelerator opens an avenue for the characterization of nanostructure of organic devices.

BIBLIOGRAPHY

A

1. Abragam, A. *The Principles of Nuclear Magnetism*, Oxford, 1961.
2. Aitchison, J. and Brown, J. A. C., **1957**. *The Lognormal Distribution*, Cambridge University Press, Cambridge (Eds).
3. Alba-Simionesco, C.; Coasne, B.; Dosseh, G.; Dudziak, G.; Gubbins, K. E.; Radhakrishnan, R.; Silwinska-Bartkowiak, M., **2006**. *J. Phys.: Condens. Matter*, 18, R15.
4. Alba-Simionesco, C.; Dosseh, G.; Dumont, E.; Geil, B.; Morineau, D.; Frick, B.; Teboul, V., and Xia, Y., **2003**. *Eur. Phys. J. E* 12, 19.
5. Allen, S. D.; and Lyman, L. R., **1999**. United States Patent, Patent number 5910259.
6. Anderson, C. D., **1933**. *Phys. Rev.* 43, 491.
7. Asoka-Kumar, P.; Lynn, K. G., and Welch, D. O., **1994**. *J. App. Phys.* 76, 4935.

B

8. Baerdemaeker, J.; Boussu, K.; Djourelov, N.; Vad der Bruggen, B.; Dauwe, C.; Weber, M., and Lynn, K. G., **2007**. *Phys. Stat. Solidi (c)* 10, 3804.
9. Baker, R. W.; Tuttle, M. E.; Kelly, D. J.; Lonsdale, H. K., **1977**. *J. Mem. Sci.* 2, 213.
10. Baker, R. W., **2004**. "Membrane technology and applications" California, John Wiley & Sons Ltd.
11. Bandzuch, P.; Kristiak, J.; Sausa, O., and Zrubcova, J., **2000**. *Phys. Rev. B.* 61(13), 8784.
12. Bansal, B.; Chen, X. D. and Hossain., Md. M., **2005**. *Chem. Eng. Proc.* 44, 1327.

13. Bansil, A.; Pankaluoto, R.; Rao, R. S.; Mijnaerends, P. E.; Długosz, W.; Prasad, R., and Smedskjaer, L. C., **1988**. *Phys. Rev. Lett.* 61, 2480.
14. Barcelo, D., and Hennion, M.-C., **1997**. “Trace Determination of Pesticides and their Degradation Products in Water” *Techniques and Instrumentation in Analytical Chemistry*, Vol.19. Elsevier, Amsterdam.
15. Bartos, J.; Sausa, O.; Kristiak, J.; Blochowicz, T., and Rossler, E., **2001**. *J. Phys.: Condens. Matter* 13, 11473.
16. Barut, G.; Pissis, P.; Plester, R., and Nimtz, G., **1998**. *Phys. Rev. Lett.* 80, 3543.
17. Bergman, R.; Swenson, J.; Borjesson, L.; Jacobsson, P., **2000**. *J. Chem. Phys.* 113, 357.
18. Brandt, W., and Dupasquier, A., **1983**. “Positron solid state Physics”, North-Holland, Amsterdam.
19. Brandt, W., and Paulin, R., **1977**. *Phys. Rev. B.*, 15, 2511
20. Brauer, G.; Anwand, W.; Skorupa, W.; Revesz, A.G., and Kuriplach, J., **2002**. *Phys. Rev. B* 66, 195331.
21. Brubach, J. B.; Mermet, A.; Filabozzi, A.; Gerschel, A.; Roy, P., **2005**. *J. Chem. Phys.* 122, 184509.
22. Brun, M.; Lallemand, A.; Quinson, J.-F.; Eyraud, C., **1977**. *Thermochim. Acta* 21, 59.
23. Bruni, F.; Mancinelli, R.; Ricci, M. A., **2011**. *Phys. Chem. Chem. Phys.* 13, 19773.
24. Brutting, W., **2008**. *Physics of Organic semiconductors*, WILEY-VCH Verlag GmbH & Co. KGaA, Weinheim.

C

25. Campbell, J. L., **1977**. *Appl. Phys.*, 13(4), 365.

26. Chan, L. P.; Lynn, K. G., and Harshman, D. R., **1992**. *Internat. J. of Mod. Phys. B* 6(11), 617.
27. Chang, C.-J.; Changb, H. -Y.; Youb, Y. -W.; Liaob, H. -Y.; Kuo, Y. -T.; Kao, W. -L.; Yena, G. -J.; Tsaia, M. -H.; Shyue, J. -J., **2012**. *Anal. Chim. Act.* 718, 64.
28. Cheng, S. Z. D.; Wu, Z. Q., and Wunderlich, B., **1987**. *Macromolecules* 20, 2802.
29. Chowdhury, A.; Biswas, B.; Majumder, M.; Sanyal, M. K.; Mallik, B., **2012**. *Thin Solid Films* 520, 6695.
30. Clement, M.; de Nijs, J. M. M.; Balk, P.; Schut, H.; van Veen, A., **1996**. *J. App. Phys.* 79, 9029.
31. Couchman, P. R., and Jesser, W. A., **1977**. *Nature* 269, 481.

D

32. Dalnoki-Veress, K.; Jones R. A. L., and Cory, R. A. **2001**. *Phys. Rev. E.* 63, 031801.
33. Dauwe, C.; van Waeyenberge, B., and Balcaen, N., **2003**. *Phys. Rev. B* 68, 132202.
34. Debnath, A. K.; Samanta, S.; Singh, A.; Aswal, D. K.; Gupta, S. K.; Yakhmi, J. V.; Deshpande, S. K.; Poswal A. K. and C., Surgers, **2008**. *Physica E* 41, 154.
35. Defay, R.; Prigogine, I.; Bellemans, A., and Everett, D. H., **1966**. *Surface tension and Adsorption* (New York: Wiley).
36. Dirac, P. A. M., **1930**. *Proc. Camb. Phil. Soc.* 26, 361.
37. Dirac, P. A. M., **1935**. *The Principles of Quantum Mechanics*, Oxford University Press.
38. Djourellov, N., and Misheva, M., **1996**. *J. Phys: Condens. Matter* 8, 2081

39. Don, Y. P.; Lim, J. A.; Lee, H. S.; Cho, K., **2007**. *Mater. Today* 10, 46.
40. Dryzek, J., and Quarles, C. A., **1996**. *Nucl. Instr. Meth. A* 378, 337.
41. Dryzek, J., SPversion 1.0, Downloaded from
<http://www.Positronannihilation.net/software.html>
42. Dryzek, J.; Pamula, E., and Blazewicz, S., **1995**. *Phys. Status Solidi A* 151(1), 39.
43. Duffy, J. A., and Alam, M. A., **2000**. *Langmuir* 16, 9513.
44. Duplatre, G., and Billard, I., **2003**. in *Principles and Applications of Positron and Positronium Chemistry*, Jean, Y. C.; Mallon, P. E., and Schrader, D. M., (Eds.)
World Scientific, London, p. 253.
45. Dutta, D.; Sachdeva, A., and Pujari, P. K., **2006**. *Chem. Phys. Lett.* 432, 116.
46. Dutta, D.; Pujari, P. K.; Sudarshan, K., and Sharma, S. K., **2008**. *J. Phys. Chem. C*
112, 19055.

E

47. Eldrup, M.; Lightbody, D., and Sherwood, J. N., **1981**. *Chem. Phys.* 63, 51.
48. Evans, R., and Marini B. M., **1987**. *J. Chem. Phys.* 86, 7138.

F

49. Ferragut, R.; Calloni, A.; Dupasquier, A., and Isella, G., **2010**. *Nano. Res. Lett.* 5,
1942.
50. Ferrell, R. A., **1957**. *Phys. Rev.* 108, 167.
51. Firestone, R. B.; Baglin, C. M., and Frank Chu, S. Y., **1999**. *Table of isotopes*, 8th
Edition, Wiley-Interscience.
52. Forrest, J. A.; Dalnoki-Veress, K.; Stevens, J. R., and Dutcher, J. R., **1996**. *Phys.*
Rev. Lett. 77, 2002.
53. Forrest, S. R., **1997**. *Chem. Rev.*, 97, 1793.

54. Forrest, S. R.; Burrows, P.E., **1997**. *Supramolecular Science* 4, 127.
55. Fretwell, H. M.; Duffy, J. A.; Clarke, A. P.; Alam, M. A., and Evans, R., **1996**. *J. Phys.: Condens. Matter* 8, 9613.

G

56. Gebauer, J.; Krause-Rehberg, R.; Prokesch, M., and Irmischer, K., **2002**. *Phys. Rev. B* 66, 115206.
57. Gidley, D. W.; Peng, H. G., and Vallery, R. S., **2006**. *Ann. Rev. Mater. Res.* 36, 49.
58. Gidley, D. W.; Vallery, R. S.; Liu, M., and Peng, H. –G. **2007**. *Phys. Stat. Solidi (c)* 4, 3796.
59. Glatter, O. And Kratky, O., **1982**. “*Small Angle X-ray Scattering*”, Academic Press, London.
60. Grosse, K.; Ratke, L.; Feuerbacher, B., **1997**. *Phys. Rev. B* 55, 2894.
61. Gunier , A. and Fournet, G. (B.C. Walker trans.), **1955**. *Small Angle X-rays*, Wiley, New York.
62. Gussoni, M. et al., **2004**. *Mag. Res. Imaging* 22, 877.

H

63. Havriliak, S., and Negami, S., **1966**. *Polym. Sci. C* 16, 99.
64. Havriliak, S., and Negami, S., **1967**. *Polymer* 8, 161.
65. Hedström, J.; Swenson, J.; Bergman, R.; Jansson, H.; Kittaka, S., **2007**. *Euro. Phys. J. Special Topics* 141, 53.
66. Holt, J. K.; Park, H. G.; Wang, Y.; Stadermann, M.; Artyukhin, A. B.; Grigoropoulos, C. P.; Noy, A.; Bakajin, O., **2006**. *Science* 312, 1034.

67. Hong, J. -Y.; Chang, Y. -M.; Chuang, C. -H.; Li, K. -S.; Jhang, Y. -C.; Shiu, H. -W.; Chen, C. -H.; Chiang, W. -C.; and Lin, M. -T., **2012**. *J. Phys. Chem. C* 116, 21157
68. Huang, S.-H.; Hung, W. -S.; Liaw, D.-J.; Li, C. -L; Kao, S. -T.; Wang, D. -M.; Guzman, M. De; Hu, C. _C; Jean, Y. C.; Lee, K. -R. and Lai, J. -Y., **2008**. *Macromolecules* 41, 6438.
69. Hummer, G.; Rasaiah, J. C.; Noworyta, J. P., **2001**. *Nature* 414, 188.
70. Hwang, D. K.; Lee, K.; Kim, J. H.; Im, S.; Park, J. H.; Kim, E., **2006**. *Appl. Phys. Lett.* 89, 093507.

I

71. Ito, K.; Ujihira, Y.; Yamashita, T., and Horie, K., **1998**. *J. Polymer Sci. B* 36, 1141.
72. Ito, K.; Ujihira, Y.; Yamashita, T., and Horie, K., **1999a**. *Polymer* 40, 4315.
73. Ito, K.; Ujihira, Y.; Yamashita, T., and Horie, K., **2000**. *J. Polymer Sci. B* 38, 922.
74. Ito, Y. and Suzuki, T., **2000**. *Radiat. Phys. Chem.* 58, 743.

J

75. Jackson, C. L., and McKenna, G. B., **1996**. *Chem. Mater.* 8, 2128.
76. Jain, T. S., and de Pablo J. J., **2002**. *Macromolecules* 35, 2167.
77. Jean, Y. C.; Mallon, P. E., and Schrader, D. M., (Eds.) **2003**. *Principles and Applications of Positron and Positronium Chemistry*, World Scientific, London.
78. Joënsso, J. Aî., Mathiasson, L., **1992**. *Trends Anal. Chem.* 11, 106.

K

79. Kajcsos, Z.; Duplâtre, G.; Liskay, L.; Billard, I.; Bonnenfant, A.; Azenha, E.; Lázár, K.; Pál-Borbély, G.; Caullet, P.; Patarin, J.; Lohonyai, L., **2000**. *Radiat. Phys. Chem.* 58, 709.
80. Karan, S.; Mallik, B., **2007**. *Solid State Comm.* 143, 289.
81. Kauppinen, H.; Corbel, C.; Liskay, L.; Laine, T.; Oila, J.; Saarinen, K.; Hautojärvi, Barthe, P.; M-F., and Blondiaux, G., **1997**. *J. Phys.: Condens. Matter* 9, 10595.
82. Keddie, J. L.; Jones, R. A. L., and Cory, R. A., **1994**. *Faraday Discuss.* 98, 219.
83. Khan, S. H.; Matei, G.; Patil, S.; Hoffmann, P. M., **2010**. *Phys. Rev. Lett.* 105, 106101.
84. Kilburn, D., **2008**. *Appl. Phys. Lett.* 92, 033109.
85. Kimmich, R., **2002**. *Chem. Phys.* 284, 253.
86. Kirkegaard, P., and Eldrup, M., **1972**. *Comp. Phys. Comm.* 3, 240.
87. Kirkegaard, P., and Eldrup, M., **1991**. *Comput. Phys. Commun.*, 17, 401.
88. Kirkegaard, P.; Eldrup, M.; Mogensen, O. E., and Pedersen, N. J., **1981**. *Comp. Phys. Comm.* 23, 307
89. Kirkegaard, P.; Pedersen, N. J., and Eldrup, M., **1989**. PATFIT-88: A data-processing system for positron annihilation spectra on mainframe and personal computers, RISO-M-2740, RISO National Laboratory, Denmark.
90. Kittaka, S.; Sou, K.; Yamaguchi, T.; Tozaki, K.-i., **2009**. *Phys. Chem. Chem. Phys.* 11, 8538.
91. Koch, N., **2007**. *Chem. Phys. Chem.* 8, 1438.
92. Koga, K.; Gao, G. T.; Tanaka, H., and Zeng, X. C., **2001**. *Nature* 412, 802.
93. Kozłowski, T., **2012**. *Cold Reg. Sci. Tech.* 78, 89.

94. Krause-Rehberg, R., and Leipner, H. S., **1999**. *Positron annihilation in semiconductors: Defect studies*, Springer-Verlag Berlin Heidelberg New York.

L

95. Lakshmi, D. S.; Mohapatra, P. K.; Mohan, D.; Manchanda; V. K., **2004**. *Desalination* 163, 13.
96. Liu, C. -P.; Wang, W. -B.; Lin, C. -W.; Lin, W. -C.; Liu, C. -Yi.; Kuo, C. -H.; Lee, S. -H.; Kao, W. -L.; Yen, G. -J.; You, Y. -W.; Chang, H. -Y.; Jou, J. -H.; Shyue, J. -J., **2011**. *Organic Electronic* 12, 376.
97. Luque, M.; Luque-Pérez, E.; R'ios, A.; and Valcárcel, M., **2000**. *Anal. Chim. Act.* 410, 127.

M

98. Makkonen, I.; Snicker, A.; Puska, M. J.; Mäki, J.-M., and Tuomisto, F., **2010**. *Phys. Rev. B.* 82, 041307(R).
99. Mallamace, F.; Broccio, M.; Corsaro, C.; faraone, A.; Liu, L.; Mou C-Y.; Chen, S-H., **2006**. *J. Phys: Condens. Matt.* 18, S2285.
100. Mallamace, F.; Broccio, M.; Corsaro, C.; Faraone, A.; Majolino, D.; Venuti, V.; Liu, L.; Mou, C.-Y.; Chen, S.-H., **2007**. *Proc.Natl. Acad. Sci.* 104, 424.
101. Mallamace, F.; Branca, C.; Broccio, M.; Corsaro, C.; Mou, C.-Y.; Chen, S.-H., **2007**. *Proc. Nat. Acad. of Sci. U. S. A.* 104, 18387.
102. Mallon, P. E., **2003**, in *Principles and Applications of Positron and Positronium Chemistry*, Jean, Y.C.; Mallon, P.E., and Schrader, D.M., (Eds.) World Scientific, London, p. 253.

103. Mattson, J.; Jacobsson, R. B. P.; and Borjesson, L., **2009**. *Phys. Rev. B* 79, 174205.
104. Merbel, N.C. van de; Hageman, J. J.; Brinkman, U. A. Th., **1993**. *J. Chromatog.* 634, 1.
105. Miller, A. A., **1963**. *J. Chem. Phys.* 38, 1568.
106. Miller, C.W.; Sharoni, A.; Liu, G.; Colesniuc, C. N.; Fruhberger, B. ; Schuller, I. K., **2005**. *Phys. Rev. B* 72, 104113.
107. Miranda, L. A. de; Mohallem, N. D. S., and Magalhaes W. F. de, **2006**. *Appl. Surf. Sci.* 252, 3466.
108. Miranda, R.; Ochoa, R., and Huang, W. F., **1993**. *J. Mol. Catal.* 78, 67.
109. Miyahara, M., and Gubbins, K. E. **1997**. *J. Chem. Phys.* 106, 2865.
110. Mogensen, O. E., **1974**. *J. Chem. Phys.* 60, 998.
111. Mogensen, O. E., **1988**. *Electrochim. Acta.* 33, 1203.
112. Mogensen, O. E., **1989**. *Chem. Phys. Lett.* 163, 145.
113. Mohapatra, P. K.; Lakshmi, D. S.; Mohan, D.; Manchanda, V. K., **2006**. *Separation and Purification Tech.* 51, 24.
114. Morineau , D.; Alba-Simionesco, C., **2003**. *J. Chem. Phys.* 118, 9389.

N

115. Nonaka, T.; Nakagawa, Y.; Mori, Y.; Hirai, M.; Matsunobe, T.; Nakamura, M.; Takahagi, T.; Ishitani, A.; Lin, H.; Koumoto, K., **1995**. *Thin Solid Films* 256, 262.

O

116. Offerman, S. E.; van Dijk, N. H.; Sietsma, J.; Grigull, S.; Lauridsen, E. M.; Margulies, L.; Poulsen, H. F.; Rekveldt, M.T.; van der Zwaag, S., **2002**. *Science* 298, 1003.
117. Ore, A., and Powell, J. L., **1949**. *Phys. Rev.* 75(11), 1696.

P

118. Petkov, M. P.; Wang, C. L.; Weber, M. H.; Lynn, K. G., and Rodbell, K. P., **2003**. *J. Phys. Chem. B* 107, 2725.
119. Petkov, M. P.; Wang, C. L.; Weber, M. H.; Lynn, K. G.; Rodbell, K. P., **2003**. *J. Phys. Chem. B* 107, 2725.
120. Petkov, M. P.; Weber, M. H., and Lynn, K. G. **2001**. *Appl. Phys. Lett.* 79, 3884.
121. Petkov, M. P.; Weber, M. H.; Lynn, K. G.; Rodbell, K. P., **2001**. *App. Phys. Lett.* 79, 3884.
122. Pietsch, U.; Hoehne, U.; Moehwald, H., **1993**. *Langmuir* 9, 208.
123. Prince, B. J.; Williamson, B. E.; Reeves, R. J., **2001**. *J. Luminesc.* 93, 293.
124. Pujari, P. K.; Dutta, T.; Tomar, B. S., and Das, S. K., **1992**. *Report: BARC/1992/E/043*.

R

125. Radhakrishnan, R.; Gubbins, K. E.; Sliwinska-Bartkowiak, M. **2000**. *J. Chem. Phys.* 112, 11048.
126. Radhakrishnan, R.; Gubbins, K. E., and Sliwinska-Bartkowiak, M., **2002**. *J. Chem. Phys.* 116, 1147.

127. Reyes-Aguilera, J. A.; Gonzalez, M. P.; Navarro, R.; Saucedo, T.I.; Avila-Rodriguez, M., **2008**. *J. Mem. Sci.* 310, 13.
128. Ribeiro, A. O.; Biazotto, J. C.; Serra, O. A., **2000**. *J. Non-Crystalline Solids* 273

S

129. Samanta, S.; Singh, A.; Debnath, A. K.; Aswal, D. K.; Gupta, S. K. ; Yakhmi, J. V.; Singh, S.; Basu, S.; and Deshpande, S. K., **2008**. *J. App. Phys.* 104, 073717.
130. Schmidt, P.W. and Hight, R. Jr., **1960**. *Acta Cryst.* 13, 480.
131. Schneider, H.; Seeger, A.; Siegle, A.; Stoll, H.; Castellaz. P., and Major, J., **1997**. *Appl. Surf. Sci.* 116, 145.
132. Schrader, D. M., and Jean, Y. C., (Ed) **1988**. *Positron and Positronium chemistry* Elsevier, New York.
133. Schreiber, A.; Ketelsen, I.; Findenegg, G. H., **2001**. *Phys. Chem. Chem. Phys.* 3, 1185.
134. Schultz, P. J. and Lynn, K. G., **1988**. *Rev. Mod. Phys.* 60, 701.
135. Schwinberg, P. B.; VanDyck, R. S. Jr., and Dehmelt, H. G., **1981**. *Phys. Rev. Lett.* 47, 1679.
136. Seeger, A., **1974**. *Appl. Phys.* 4, 183.
137. Siegel R. W., **1980**. *Ann. Rev. Mater. Sci.* 10, 393.
138. Skipper, N. T.; Soper, A. K.; McConnell, J. D. C., **1991**. *J. Chem. Phys.* 94, 5751.
139. Sliwinska-Bartkowiak, M.; Dudziak, G.; Sikorski, R.; Gras, R.; Radhakrishnan, R.; Gubbins, K. E. **2001**. *J. Chem. Phys.* 114, 950.
140. Slotte, J.; Saarinen, K.; Salmi, A.; Simula, S.; Aavikko, R., and Hautajarvi, P., **2003**. *Phys. Rev. B* 67, 115209.

141. Smedskjaer, L. C.; Liu, J. Z.; Benedek, R.; Legnini, D. G.; Lam, D. J.; Stahulak, M. D.; Claus, H., and Bansil, A., **1998**. *Physica C* 156(2), 269.
142. Stadlober, B.; Haas, U.; Maresch, H.; Haase, A., **2006**. *Phys. Rev. B* 74, 165302.
143. Striolo, A.; Chialvo, A. A.; Gubbins, K. E., and Cummings, P. T., **2005**. *The J. Chem. Phys.* 122, 234712.
144. Suzuki, N.; Hirade, T.; Saito, F., and Hyodo, T., **2003**. *Rad. Phys. Chem.* 68, 647.
145. Swenson, J.; Bergman, R.; Howells, W. S., **2000**. *J. Chem. Phys.* 113, 2873.
146. Swenson, J.; Jansson, H.; Bergman, R., **2006**. *Phys. Rev. Lett.* 96, 247802.

T

147. Tao, S. J., **1972**. *J. Chem. Phys.* 56, 5499.
148. Thomson, W., **1871**. *Phil. Mag.* 42, 448.
149. Tombari, E.; Salvetti, G.; Ferrari, C.; Johari, G. P., **2005**. *J. Chem. Phys.* 122, 104712.
150. Tuomisto, F.; Pelli, A.; Yu, K. M.; Walukiewicz, W., and Schaff, W.J., **2007**. *Phys. Rev. B.* 75, 193201.
151. Tuomisto, F., **2008**. *App. Surf. Sci.* 255, 54.

U

152. Uedono, A.; Tanigawa, S., and Ohji, Y., **1988**. *Phys. Lett. A* 133, 82.
153. Uedono, A.; Naito, T.; Otsuka, T.; Ito, K.; Shiraishi, K.; Yamabe, K.; Miyazaki, S.; Watanabe, H.; Umezawa, N.; Chikyow, T.; Ohdaira, T.; Suzuki, R.; Akasaka, Y.; Kamiyama, S.; Nara, Y., and Yamada, K., **2007**. *Japan. J. Appl. Phys.* 46, 3214.

V

154. Valenzuela, F. L. and Basualto, C. F., **1993**. *Minerales* 48, 23.
155. van Veen, A.; Schut, H.; Vries, J. De; Hakvroot, R.A., and Ijpma, M.R., **1990**. *AIP conf. Proc.*, 218, 171.
156. Vanfleet, R. R.; Mochel, J. M., **1995**. *Surf. Sci.* 341, 40.
157. Virkar, A. A.; Mannsfeld, S.; Bao, Z.; Stingelin, N., **2010**. *Advanced Materials* 22, 3857.

W

158. Wang, C. L.; Weber, M. H. and Lynn, K. G., **2006**. *J. Appl. Phys.* 99, 113514.
159. Wang, X. Y.; Willmore F. T.; Raharjo, R. D.; Wang X. C. ; Freeman, B. D.; Hill A. J., and Sanchez, I. C., **2006**. *J. Phys. Chem. B* 110, 16685.
160. Wang, Y.Y.; Nakanishi, H., and Jean, Y.C., **1990**. *J. Polym. Sci., Part B: Polym. Phys.*, 28, 1431.
161. West, R.N., **1973**. *Adv. Phys.*12, 263.
162. Wilkinson, N. J.; Alam, M. A.; Clayton, J. M.; Evans, R.; Fretwell, H. M., and Usmar, S. G, **1992**. *Phys. Rev. Lett.* 69, 3535.
163. Wishart, D.; Bigam, C.; Yao, J.; Abildgaard, F.; Dyson, H. J.; Oldfield, E.; Markley, J.; Sykes, B., **1995**. *J. Biomol. NMR* 6, 135.

X

164. Xia, W.; Minch, B. A.; Carducci, M. D.; Armstrong, N. R., **2004**. *Langmuir* 20, 7998.

Y

165. Yamaguchi, Y.; Yasutake, N.; Nagaoka, M., **2001**. *Chem. Phys. Lett.* 340, 129.
166. Yudasaka, M.; Fan, J.; Miyawaki, J.; Iijima, S., **2005**. *J. Phys. Chem. B* 109, 8909.

Z

167. Zanfolim, A. A.; Volpati, D.; Olivati, C. A.; Job, A. E., and Constantino, C. J. L., **2010**. *J. Phys. Chem. C* 114, 12290.
168. Zeyada, H. M.; El-Nahass, M. M., **2008**. *Appl. Surf. Sci* 254, 1852.
169. Zheng, W., and Sindee, L. S., **2007**. *J. Chem. Phys.* 127, 194501.
170. Zhou, R.; Huang, X.; Margulis, C. J.; Berne, B. J., **2004**. *Science* 305, 1605.
171. Zubiaga, A.; Garcia, J. A.; Plazaola, F.; Zuñiga-Perez, J., and Muñoz-Sanjose, V., **2011**. *J. of Phys: Conference Series* 265, 012004.